









UNIVERSITÀ DEGLI STUDI DELL'AQUILA

DIPARTIMENTO DI Scienze Fisiche e Chimiche

Dottorato di Ricerca in **SCIENZE FISICHE E CHIMICHE**

Curriculum _____

XXXVII ciclo

Titolo della tesi

Modeling of Radiation-Molecule Interaction in Nanophotonic Environments

SSD PHYS-04/A

Dottorando

Raju Adhikary

Coordinatore del corso

Prof. Massimiliano Aschi

Tutor

Dr. Andrea Marini

Co-Tutor

Prof. Massimiliano Aschi

a.a. 2023/2024

Acknowledgement

I would like to express my heartiest gratitude to my supervisor, Andrea Marini, for his constant guidance and support. *Grazie, Prof.!* Your kindness, courage, passion and dedication to science have inspired me from day one of this journey. Beyond science, I am grateful for all the insightful conversations shared outside the office.

I would also like to thank my co-supervisor, Massimiliano Aschi, for all the help, support, and encouragement. I am grateful for the profound question-answer sessions throughout my tenure—working with you has been a privilege.

Special thanks to Isabella Daidone, Carino Ferrante, Paola Benassi, Antonio Mecozzi, and Alessandro Ciattoni for their support and thoughtful discussions.

To my collaborators—Andrea Toma, Francesco Tani, Jens Biegert, Hatice Altug, Patrice Genevet, Samira Khadir, Shamaem Khushhali, Samudra Roy, and Francesco Di Stasio—thank you for your invaluable support and contributions. It has been a privilege to work with such outstanding personalities.

Many thanks to all the faculty of the Department of Physical and Chemical Sciences at the University of L'Aquila for their constant encouragement.

Special thanks to Ambaresh Sahoo for his guidance, company, and patiently addressing all the ifs and buts. *Dhonyobad, Ambaresh Da,* for standing by me in all moments.

To my talented group members—Matteo V., Matteo S., Leone D. M., Davide T., Andrea A., Giovanna S., Somasree P., Federico P., Ashis P., and Luca A.—thank you for making this journey memorable. I am blessed to work with such amazing individuals. *Grazie mille, Luca*, for the precious moments we shared.

I am thankful to all my dear friends—Subhankar, Arundev, Chinmay, Anirud-

dha, Partha, Arkadip, Kushal, Divyanshu, Amit, Swati, Dipshikha, Mitali, Saad, Sourabh, Paban Da, Satya Da, Atash Da, Partha Da, Pabitra, Suman, Rajat, Rajashree, and Malabika—for various help. I am grateful to Dipika for all the support—thank you for being there through thick and thin. Thanks to Atul, Manas, Phanindra, Megha, Divya, Meghashyam, Dipanjan Da, Biswajit Da, Pawan, Ansh, Nandini Di, Sayak Da, Ritabrata Da, and Soumen Da—your presence brought warmth and joy to my life here in L'Aquila.

My heartfelt thanks to the professors of the Physics Department at NIT Durgapur, where the first footprints of my journey into research were marked.

Lastly, I would like to thank my family. I am indebted to my parents for everything. You are my strength!

Finally, and above all, I am forever grateful to the University of L'Aquila and Twisted-Nano for giving me the opportunity to pursue my Ph.D.

Abstract

Chirality, the property characterized by broken mirror symmetry, is a widespread trait of nature, manifested in the twist of galaxies to the handedness of molecules. Enantiomers, the two mirror counterparts of a chiral molecule, exhibit distinct biochemical properties, making chiral sensing crucial in pharmaceutical and biomedical industries. Current state-of-the-art techniques are effective for macroscopic operational volume; however, they lack real-time compatibility and are inefficient for lab-on-a-chip integration platforms. This work advances a step forward toward improving the sensitivity of enantiomeric excess detection by exploring chiroptical interactions in nanophotonic environments, utilizing realistic pharmaceutical drugs. The radiation-molecule interactions are demonstrated through a perturbative theory in the density matrix formalism, and the microscopic molecular observables are evaluated through a robust computational method combining Molecular Dynamics (MD), Time-Dependent Density Functional Theory (TDDFT) and quantum chemical calculations. We observe that Surface-Plasmon Polariton (SPP)s at the noble metal interface can significantly enhance circular dichroism differential absorption by chiral samples. Additionally, we investigate enhanced vibrational circular dichroism offered by Localised Surface Plasmon Resonance (LSPR)s in plasmonic nanostructures embedding chiral mixtures. Thanks to intense near-fields produced by SPPs and LSPRs, we attain significant enhancement of chiroptical signal in an nl-volume chiral sample, paving a way to design highly sensitive, laboratory-friendly, innovative chiral sensors.

List of abbreviations

AZO Aluminum-Doped Zinc Oxide

ATR Attenuated Total Internal Reflection

BACRs Bi-Anisotropic Constitutive Relations

BCs Boundary Conditions

CD Circular Dichroism

CDDA Circular Dichroism Differential Absorption

CP Chiral Parameter

CS Chiral Sample

DFT Density Functional Theory

EC Electron Correlation

ED Essential Dynamics

EWFD Electromagnetic Wave Frequency Domain

FT Fourier Transform

GGA Generalized Gradient Approximation

HF Hartee-Fock

IR Infrared

ITO Indium Tin Oxide

LCP Left Circular Polarization

LDA Local Density Approximation

LP Linear Polarization

LSP Localized Surface Plasmon

LSPR Localized Surface Plasmon Resonance

MD Molecular Dynamics

MIR Mid-Infrared

MM Molecular Mechanics

ORD Optical Rotatory Dispersion

PBCs Periodic Boundary Conditions

PME Particle Mesh Ewald

PMM Perturbed Matrix Method

QC Quantum Center

QM Quantum Mechanics

RCP Right Circular Polarization

RDP Relative Dielectric Permittivity

RMP Relative Magnetic Permeability

SPP Surface-Plasmon Polariton

TDDFT Time-Dependent Density Functional Theory

TE Transverse Electric

TM Transverse Magnetic

UV Ultraviolet

VCD Vibrational Circular Dichroism

VCDDA Vibrational Circular Dichroism Differential Absorption

XC Exchange-Correlation

Contents

Acknowledgements **I**

Abstract **III**

List of abbreviations **IV**

1 Introduction **1**

1.1 Thesis aspects and objectives. 6

1.2 Outline. 7

1.3 Fundamentals of electromagnetism 11

1.4 Plane wave, polarization and Stokes parameters. 14

1.5 Chiroptical activity in chiral media. 17

1.5.1 Bi-anisotropic media. 18

1.5.2 Optical rotatory dispersion. 19

1.5.3 Circular dichroism. 21

1.6 Plasmonic nanomaterials 24

1.6.1 Surface plasmon polariton. 24

1.6.2 Localized surface plasmon. 26

2 Physical Chemistry Modeling of Spectroscopic Properties of Chiral Drug Solutions **28**

2.1 Introduction. 29

2.2 Molecular Interactions. 30

2.3 Classical Molecular Dynamics. 33
2.4 Electronic Structure Theory. 37
2.4.1 Hartree-Fock Equations. 38
2.4.2 Post-Hartee-Fock Methods. 40
2.4.3 Density Functional Theory. 41
2.4.4 Time-Dependent Density Functional Theory. 44
2.4.5 Linear response (Weak perturbation). 45
2.5 Quantum Mechanics/Molecular Mechanics. 47
2.6 Perturbed Matrix Method. 49
2.6.1 Atom based expansion. 52
2.7 Modeling of absorption spectra. 55
2.8 Electronic structure of chiral drugs 57
2.8.1 MD-Simulation details. 58
2.8.2 Essential Dynamics: analysis of MD trajectory. 60
2.8.3 Unperturbed quantum chemical calculations. 62
2.8.4 Absorption spectra and ensemble averages of molecular observables. 63
2.9 Concluding remarks. 65

3 Chiroptical Light-Matter Interactions 66
3.1 Introduction. 67
3.2 Fundamental concepts. 68
3.2.1 Density operator: definition and temporal evolution. 69
3.2.2 Lindblad operator. 72
3.3 Multilevel chiroptical interaction. 73
3.3.1 Induced dipole moments. 77
3.3.2 Averaging over molecular orientation. 78
3.3.3 Microscopic response. 80

3.3.4 Macroscopic response. 81
3.3.5 Constitutive relations. 83
3.4 Enantioselective properties. 84
3.5 Concluding remarks. 85

4 Enhancement of Circular Dichroism Spectroscopy by Surface Plasmon Polaritons 87

4.1 Introduction. 88
4.2 Optical properties of metals. 90
4.3 SPPs at a single interface. 94
4.4 SPP excitation. 97
4.4.1 Prism coupling. 98
4.5 Interaction of radiation with Reparixin in water. 100
4.5.1 Electronic and vibrational structure of Reparixin in water. . 101
4.5.2 Macroscopic bi-anisotropic response of Reparixin in water. . 104
4.6 Plasmon enhanced CD spectroscopy. 109
4.6.1 Otto coupling scheme. 110
4.6.2 Kretschmann coupling scheme. 119
4.6.3 Reflected polarization dynamics. 125
4.7 Results and discussions. 128
4.8 Concluding remarks. 129

5 Enhanced Vibrational Circular Dichroism of Plasmonic Nanostructures Embedding Chiral Drugs 130

5.1 Introduction. 131
5.2 Theoretical framework. 132
5.2.1 Achiral nanoshell. 134
5.2.2 Chiral naoshell. 136
5.2.3 Green function for coupled wave equations in chiral media. . 138

5.3 Dipolar excitation in electrostatic limit. 142
5.3.1 Scattering of nanoshell upon circular polarization excitation. 143
5.3.2 Power dissipation and absorption cross section. 146
5.3.3 Polarizability of nanoshell surrounding chiral media 148
5.4 Plasmon-enhanced VCD of chiral drug solutions. 149
5.5 Results and discussions. 152
5.6 Concluding remarks. 157

6 Conclusions **158**
6.1 List of publications. 161

Bibliography **162**

List of Figures

1.1 Thesis outline 8
1.2 Propagation of polarized light 20
1.3 Schematic representation of CD and ORD 23
1.4 Schematic illustration of SPP 25
1.5 Schematic illustration of LSP 27

2.1 Bond length, bending angle and dihedral angle 30
2.2 Intramolecular interactions 32
2.3 Schematic of a simple molecular system 37
2.4 Schematic representation of QM/MM 46
2.5 Flowchart of computational method 59
2.6 Dynamics of chiral drug solution 61
2.7 UV-spectra of considered molecular systems 63

3.1 Schematic of laboratory and molecular frame 79
3.2 Reflection of polar and axial vectors 85

4.1 Illustration of free electron gas model 91
4.2 plane-wave propagation in metal 93
4.3 SPP propagation at metal-dielectric interface 94
4.4 SPP dispersion at metal-air interface 96
4.5 Excitation of SPP 97
4.6 SPP dispersion at metal-prism interface 99

4.7 Vibronic structure of aqueous Reparixin 102
4.8 Electronic polarizability of aqueous Reparixin 106
4.9 Bi-anisotropic optical parameters of aqueous Reparixin 109
4.10 Schematic of plasmon-enhanced CD in the Otto coupling 110
4.11 TM absorbance and CDDA in the Otto coupling 118
4.12 TM absorbance and CDDA in the Kretschmann coupling 119
4.13 Reflected polarization dynamics in the Otto configuration 126
4.14 Reflected polarization dynamics in the Krteschmann configuration . 126
4.15 CDDA enhancement factor 127

5.1 Schematic of spherical core-shell structure 134
5.2 Schematic of plasmonic nanostructures embedding chiral sample . . 149
5.3 RDP of AZO and water 150
5.4 Vibronic structure of aqueous Ladarixin 151
5.5 Bi-anisotropic optical parameters of aqueous Ladarixin 153
5.6 absorption cross-section of Type-1 and Type-2 geometries 154
5.7 VCD enhancement factor 156

Chapter 1

Introduction

The discovery of Molecular Chirality in 1848 and demonstrations of Enantioselectivity in 1857 by Louis Pasteur unveiled a new window of research and eventually led to an understanding of many fascinating phenomena. A few decades later, in 1886, Arnaldo Piutti's discovery of Enantioselectivity at Biological Receptors triggered further research on chirality in drugs. Pasteur introduced the term *'dissymmetry'* and Lord Kelvin [1] first thought of the terms *'chiral'* and *'chirality'* in 1894. In his words:

> *" I call any geometrical figure, or group of points,'chiral', and say that it has chirality if its image in a plane mirror, ideally realized, cannot be brought to coincide with itself."*

Eventually, Kelvin's terminology of chirality became equivalent to Pasteur's findings on dissymmetry concepts in subsequent contexts of crystallography, optics, and chemical structuralism. In terms of temporal and spatial symmetry, Barron [2] defined chirality in a more comprehensive manner: "true chirality is exhibited by systems that exist in two distinct enantiomeric states that are interconverted by space inversion, but not by time reversal combined with any proper spatial rotation." The origin of the word chiral is a Greek word that means 'hand'—a prototypical example of a chiral entity. From a historical perspective, chiral twin

structures, "enantiomorphs," are typically assigned left/right handedness due to the connection with the word hand.

Nature displays a large spectrum of chiral elements. The straightforward example, human hands, are very similar but not identical; in fact, one cannot align the key features of both hands across all axes regardless of orientation. More importantly, the specific hand has a certain role in daily life. The structure of DNA, amino acids, tendrils of trees, and snails are other examples of chirality in the natural world. Overall, chirality is a widespread trait of nature. Over many centuries, relief from human disease relied on folk medicines [3, 4] obtained from various natural substances, plants, and animals, but of course without the knowledge of a proper scientific basis until the 1800s. Even to date, people still use many ancient natural products for medical purposes. Modifying those therapeutics, a handful of new medicines have been developed as well. However, toxicity and other negative side effects were a major concern at that time.

The mirror image isomers of a chiral molecule are called "enantiomers". They have similar atomic composition and connectivity, but the presence of chiral elements (e.g., chiral center, chirality axis, or chiral plane) prevent them from superimposing on each other. Enantiomers can be specified adopting three common conventions. First, the Cahn-Ingold-Prelog priority rules [5] classify the enantiomers in R/S, meaning rectus (right in Latin) and sinistral (left in Latin). This approach is based on the spatial arrangement of atoms around the chiral center. Another way to categorize enantiomers is based on the interaction with light. According to this method enantiomers are identified as (+) or (-). Additionally, the D/L system is used to distinguish left- and right-handed biomolecules, respectively. Throughout this work, the R/S convention is adopted to indicate enantiomers. Naturally, chiral molecules tend to exist in single enantiomeric form. For example, the protein building blocks (amino acids) in living organisms are left-handed chiral, except glycine. Conversely, natural sugars are mostly right-handed chiral.

Also, many naturally available antibiotics and steroids are in single enantiomeric form. However, regardless of such typical biasness in nature, it is important to distinguish the opposite enantiomers because they exhibit unique interactions and dramatic functional dissimilarities in living organisms.

Often, we find that one enantiomer is beneficial for a particular pharmacological application while the other enantiomer possesses toxic behavior. In fact, a racemic mixture where both enantiomers are present in equal amounts exhibits different pharmacodynamic properties in comparison with single-enantiomeric features. For example, it has been reported that the R-enantiomer of the drug thalidomide is therapeutically useful while the S-enantiomer causes birth defects [6]. In turn, the medical properties of a drug are significantly affected by the contamination of the wrong enantiomer, emphasizing the necessity of enantiomeric imbalance detection. One such example is methamphetamine, also known as methylamphetamine. L-methamphetamine was employed as a relatively mild active ingredient in nasal decongestants in the United States [7]; conversely, D-methamphetamine strongly stimulates the nervous system and hence can cause a high risk of addiction and abuse [8] by drug addict. In addition, a racemic mixture of d-ketamine and l-ketamine has been utilized in pain relief and anesthesia purposes, although it may exhibit hallucinogenic side effects [9]. Therefore, precise chiral sensing is crucial for the pharmaceutical industry, especially in new drug development.

Chiral sensing plays a major role in many biomedical applications like drug discovery [10, 11], biosensing [12, 13], and DNA delivery [14, 15]. Also, in material science [16, 17] and nanotechnology [18, 19], chiral recognition holds significant involvement. The pioneering work of Biot in 1817 was the pivotal observation of chiroptical activity. He found that several natural compounds, for instance, the oils of turpentine, camphor, sucrose, and tartaric acid in a non-crystalline state produce the rotation of polarized light. Later, these findings had a great impact

on the discovery of chirality by Pasteur. The development of chiral sensing evolved along a long path in parallel with the modern scientific detection approach and became more precise over time. The foundation of chiral-optical activities relies either on dichroism, or circular birefringence. Circular Dichroism (CD) is the measure of unequal absorption by a chiral molecule upon excitation by left and right circularly polarized light. In addition, the chiral molecule rotates the plane of linearly polarized light, a phenomenon known as Optical Rotatory Dispersion (ORD). Such unique interactions with polarized light make optical methods suitable for chiral sensing. CD-spectroscopy is a commonly used technique for characterization of chiral molecules. However, the sensitivity of this method is inherently deficient because of the extremely weak measured CD signal of a chiral sample and often masked by the noise, and the sensitivity is inherently deficient. Thus, to overcome these practical limitations an efficient detection approach with adequate sensitivity is in high demand at the present time.

There are few existing techniques that can detect chiral drugs in small amounts up to a few milliliters. High-performance liquid chromatography, capillary electrochromatography, gas chromatography, and NMR spectroscopy based techniques are among them, but these methods take a long time to operate. Moreover, they are not compatible with real-time analysis and in-situ characterization of chiral drugs at low molecular concentration limits. Nanophotonic environments have the potential to significantly enhance the chiroptical signal at the resonance of nanostructures. This concept has been utilized in many advanced techniques like Plasmon-enhanced chiral detection [20, 21], ultrafast and nonlinear chiroptical spectroscopy techniques [22], and metasurface enhanced enantiomer-selective molecular sensing [23]. In practical applications, the detection limit is still a few milliliters, as the chiroptical response is intrinsically very weak. Traditional chiroptical interactions include both electric and magnetic dipole interactions, but the chiral-specific responses mostly rely on the weaker magnetic dipole contribu-

tions. Linear optical phenomena, e.g., transmission, reflection, and absorption, are primarily governed by electric dipole interactions. However, chiroptical effects like CD and ORD involve both electric and magnetic dipole transitions. Typically, the magnetic dipole contributions are much weaker compared to the electric dipole counterparts. As a result, the overall strength of linear chiroptical effects is usually smaller than that of conventional linear optical properties. The relatively weaker magnetic transition dipole moments in chiral molecules play major roles in limiting the sensitivity of traditional enantiomer discrimination techniques. The recent advancement in linear chiroptical sensing offers significant enhancement of CD and ORD signals. All-optical chiral spectroscopic techniques [24, 25, 26, 27] have been developed based on light-matter interaction, considering only electric dipole contribution. Several nonlinear chiroptical sensing techniques are developed to enhance sensitivity and specificity harnessing Second Harmonic Generation and Two-Photon Excited Fluorescence. Moreover, natural nonlinear optical activity is significantly evident as the optical harmonics exhibit high sensitivity to the asymmetries present in structural and molecular configurations [28]. Lower-order nonlinear processes are also employed to probe the structural and dynamical properties of chiral amino acids[29], achiral organic molecules [30], peptides [31], proteins [32], DNA [33] and other relevant biological systems at interfaces[34]. Furthermore, chiral recognition based on the interference [35] between sum frequency generation and third harmonic generation have also been developed. Currently developed ultrafast nonlinear chiroptical spectroscopic techniques [36] enable advanced methodologies that offer deeper insights on molecular chirality, including time-resolved chiral dynamics [37, 38], ultrafast imaging of chiral processes [39], ultrafast charge migration [40, 41], electronic ring currents [42], and photoelectron momentum distributions [43]. Despite notable technological advancements, achieving the detection sensitivity required for nanoliter volumes remains a challenging task in the characterization of chiral molecular mixtures.

1.1 Thesis aspects and objectives.

The goal of this thesis is to provide possible solutions to the long-standing challenge of inadequate sensitivity regarding the low molecular concentration of chiral drugs. Utilizing realistic chiral drugs, we propose novel chiroptical sensing techniques capable of measuring enantiomeric excess in nl-volume chiral mixtures. We have investigated the chiroptical responses of three chiral drugs supplied by Dompé Farmaceutici S.p.A., a pharmaceutical company. The first one is Reparixin, which has been adopted as a CXCR1/CXCR2 inhibitor [44] in a preliminary investigation to cure severe COVID-19 pneumonia-affected patients. Another important drug named Levodropropizine has been employed for the treatment of non-productive coughs (dry coughs) [45, 46]. The last one is Ladarixin which has the ability to prevent diabetes [47, 48]. All these chiral drugs are studied in solution. In the case of Reparixin, two examined systems are: (i) Reparixin dissolved in water and (ii) Reparixin dissolved in a mixture of water and acetonitrile with a 50:50 volume ratio. A mix solvent of ethanol and hexane with a 40:60 volume ratio has been employed as a solvent for Levodropropizine. Additionally, we have investigated chiroptical response of Ladarixin dissolved in water. The main aspects of this work include: (a) Firstly, developing a theoretical framework to investigate the quantum-molecular properties of chiral drug solutions. In order to do that, Molecular Dynamics (MD) simulation is adopted to study the behavior of the above-mentioned chiral molecules dissolved in a particular solvent. We then statistically sample the MD trajectories to account for the conformational fluctuations resulting from molecule-solvent interaction. Subsequently, the electronic and vibronic properties of each important conformation are evaluated using Time-Dependent Density Functional Theory (TDDFT). Finally, the quantum-molecular observables of the drug solution arising due to the interaction with external radiation are calculated using a quantum chemical approach.

(b) In the second part, we model radiation-molecule interaction. Starting from the first principles and perturbatively solving the density matrix evolution of the chiral drug solution, we calculate the induced electric and magnetic dipole moments. Since the molecules are randomly dispersed in the solution, we calculate the averages over molecular orientation and calculate the macroscopic polarization and magnetization. Then, by introducing the Bi-Anisotropic Constitutive Relations (BACRs), we calculate the linear response of each chiral drug solution. (c) Finally, we propose some novel methods to detect and quantify the enantiomeric imbalance in a chiral drug solutions. Based on the linear responses we have investigated CD spectroscopy of the chiral drug solutions enhanced by Surface-Plasmon Polariton (SPP)s at noble metal surfaces and Localized Surface Plasmon Resonance (LSPR)s in plasmonic nanostructures.

1.2 Outline.

This thesis mainly focuses on the theoretical modeling of radiation-chiral molecule interaction in nanophotonic environments. The thesis is organized as follows. This Chapter 1 presents the fundamental theoretical concepts and frameworks necessary for understanding light-matter interaction that will be utilized in the following chapters. After introducing the macroscopic Maxwell equations and the constitutive relations in Section 1.3, the basic concepts of light polarization and Stokes parameters are reviewed in section Section 1.4. A brief discussion on chiroptical activity in chiral media is presented in Section 1.5, covering phenomena like CD and ORD that hold central significance to the study of chiral molecules. Finally, Section 1.6 reviews plasmonic nanomaterials, specifically focusing on SPPs and LSPRs, which are used to enhance light-matter interactions in nanoscale.

In Chapter 2, we present the theoretical modeling of the spectroscopic properties of the chiral drugs. Introducing molecular interaction and classical MD sim-

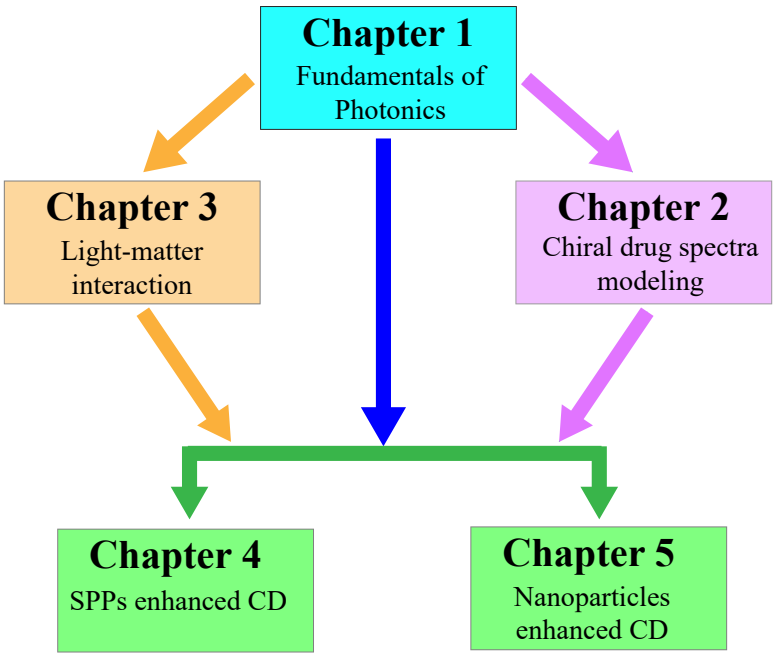


Figure 1.1: Schematic representation of thesis outline.

ulation techniques in Sections 2.1-2.3, the basic concepts behind electronic structure theory, including Hartee-Fock (HF) equations and Density Functional Theory (DFT), are reviewed in Section 2.4. Key features of advanced techniques like TDDFT and linear response theory in the weak perturbation regime are also discussed. Section 2.5 provides a description of a hybrid computational method based on the quantumQuantum Mechanics (QM)/Molecular Mechanics (MM) approach. In order to account for the solvent effects, the Perturbed Matrix Method (PMM) is explored in Section 2.6, which provides frameworks to evaluate the molecular observables of the chiral drug solutions. Section 2.7 provides the key concepts behind electronic absorption spectral modeling. Finally, the results are described in Section 2.8, including the details of the simulation method adopted to obtain electronic absorption spectra along with the ensemble averages of molecular observables.

Chapter 3 describes the theoretical modeling of the interaction of chiral molecules with light, which plays a central role in chiroptical sensing. In sections 3.1 and 3.2, we introduce the fundamental concepts necessary for developing a mathe-

matical framework. Section 3.3 describes the theory of the chiroptical interaction in the density matrix formalism. Upon excitation with external radiation, the field-induced dipole moments and orientational-averaged microscopic responses are evaluated through the Euler rotation matrix approach. Finally, the macroscopic response and BACRs of the chiral drug solution are determined. In section 3.4, we discuss the enantioselective properties of chiral molecules, highlighting the unique responses exhibited by opposite enantiomers. The theoretical foundation described in this Chapter is later utilized in subsequent chapters to develop chiral sensors of interest.

In Chapter 4, we utilize SPPs at noble metal interfaces to enhance the sensitivity of CD spectroscopy of chiral drug solutions. Section 4.2 reviews optical properties of metals, including dielectric susceptibility and plasma frequency. The propagation of SPPs at a single metal-dielectric interface in the linear regime is discussed in Section 4.3. We briefly analyze the experimental techniques to excite SPP in Section 4.4, highlighting prism coupling mechanisms that are employed in this study. Section 4.5 provides the description of the interaction of radiation with aqueous Reparixin, including electronic and vibrational structure and the bi-anisotropic response of Reparixin dissolved in water. The modeling of plasmon-enhanced CD spectroscopy adopting the Otto and Kretschmann coupling schemes is presented in 4.6, and the corresponding reflected polarization dynamics are investigated. The results depict the application of SPP to enhance weak Circular Dichroism Differential Absorption (CDDA) to probe enantiomeric imbalance in nl-volume chiral drug solutions. Finally, the plasmon-enhanced CDDA is assessed in Section 4.7, adopting different noble metals. The results emphasize the potential of SPPs in developing innovative chiral sensors capable of measuring enantiomeric excess in nl-volume chiral mixtures.

Chapter 5 describes the enhancement of Vibrational Circular Dichroism (VCD) of chiral drug solutions by incorporating plasmonic nanostructures. The theoreti-

cal framework required for modeling the scattering problem of achiral and chiral nanoshells is presented in Section 5.2. In addition, the Green function approach to describe wave interactions in chiral media is also discussed. Section 5.3 describes the dipolar excitation of the nanoshells in the electrostatic limit, focusing on the scattering problem under circular polarization. Subsequently, the modeling of absorption cross sections and the polarizability of the nanoshells embedding chiral samples are determined. Finally, in Section 5.4, we investigate the plasmon-enhanced VCD of chiral drug solutions based on Aluminum-Doped Zinc Oxide (AZO)-nanostructures supporting LSPRs. We demonstrate how LSPRs can significantly enhance the sensitivity of VCD measurements. The chapter concludes with the obtained results and detailed discussions on how we can retrieve enantiomeric imbalance in nl-volume chiral drug solutions adopting AZO-based plasmonic nanostructures. Thus, analogous to Chapter 4, we achieve significant enhancement of VCD signal, which opens a window of opportunity to design innovative chiral sensors compatible with real-time analysis and lab-on-a-chip integration schemes. A schematic map of the thesis outline is presented in Fig. 1.1 which depicts the connections between the chapters.

1.3 Fundamentals of electromagnetism: Macroscopic Maxwell's Equations in achiral media.

The propagation of light through matter can be characterized from the electric and magnetic field descriptions provided by the four fundamental laws of classical electromagnetism, known as macroscopic Maxwell's equations [49]

$$\nabla \cdot \mathbf{D} = \rho, \tag{1.1a}$$

$$\nabla \cdot \mathbf{B} = 0, \tag{1.1b}$$

$$\nabla \times \mathbf{E} = -\frac{\partial \mathbf{B}}{\partial t}, \tag{1.1c}$$

$$\nabla \times \mathbf{H} = \mathbf{J} + \frac{\partial \mathbf{D}}{\partial t}, \tag{1.1d}$$

where $\mathbf{E}$ and $\mathbf{H}$ refer to the electric and magnetic fields, respectively, ρ is the charge density, $\mathbf{J}$ is the current density. Furthermore, $\mathbf{D}$ indicates the electric displacement vector, and $\mathbf{B}$ is the magnetic induction. Note that in the above equations, we follow the SI unit system, which will be used throughout this work. Taking curl of Eq. (1.1d) and utilizing Eq. (1.1a), we get the continuity equation

$$\frac{\partial \rho}{\partial t} + \nabla \cdot \mathbf{J} = 0, \tag{1.2}$$

which ensures local charge conservation in a given volume. The constitutive relations are given by

$$\mathbf{D} = \epsilon_0 \mathbf{E} + \mathbf{P}, \tag{1.3a}$$

$$\mathbf{B} = \mu_0 \mathbf{H} + \mathbf{M}, \tag{1.3b}$$

where $\mathbf{P}$ is the induced electric polarization, $\mathbf{M}$ is the magnetization, and ϵ_0, μ_0 indicate the vacuum electric permittivity and magnetic permeability. For achi-

ral medium, within the linear-response approximation, the electric and magnetic responses of a homogeneous, isotropic medium can be expressed in terms of electric susceptibility χ_e and magnetic susceptibility χ_m. Consequently, we define the medium's electric permittivity $\epsilon = \epsilon_0(1 + \chi_e)$ and magnetic permeability $\mu = \mu_0(1 + \chi_m)$. However, material response is not instantaneous to the impinging light, and the delay can be captured by modeling the polarization and magnetization as follows

$$\mathbf{P}(\mathbf{r}, t) = \epsilon_0 \int_{-\infty}^{+\infty} dt' \chi_e(t - t')\mathbf{E}(\mathbf{r}, t), \tag{1.4a}$$

$$\mathbf{M}(\mathbf{r}, t) = \int_{-\infty}^{+\infty} dt' \chi_m(t - t')\mathbf{H}(\mathbf{r}, t), \tag{1.4b}$$

where $\chi_e(t - t')$ and $\chi_e(t - t')$ refer to the temporal response functions [50] of the medium, and we consider them position independent scalars in the homogeneous and isotropic assumptions. In addition, we assume spatially local response, meaning that the respective non-local ($\mathbf{r} \neq \mathbf{r}'$) contributions of $\mathbf{E}(\mathbf{r}, t)$ and $\mathbf{H}(\mathbf{r}, t)$ to the $\mathbf{P}(\mathbf{r}, t)$ and $\mathbf{M}(\mathbf{r}, t)$ are not accounted. Furthermore, utilizing causality, one gets $\chi_e(t-t') = 0, \chi_m(t-t') = 0$, for $\tau = t-t' < 0$. Defining the temporal Fourier integrals $\mathbf{F}(\tau) = \mathbf{E}(\tau), \mathbf{H}(\tau), \mathbf{P}(\tau), \mathbf{M}(\tau)$ as

$$\mathbf{F}(\tau) = \frac{1}{2\pi} \int_{-\infty}^{+\infty} d\omega \tilde{\mathbf{F}}(\omega) e^{-i\omega t}, \tag{1.5}$$

and using the convolution theorem [51], we obtain

$$\tilde{\mathbf{P}}(\mathbf{r}, \omega) = \epsilon_0 \chi_e(\omega) \tilde{\mathbf{E}}(\mathbf{r}, \omega), \tag{1.6a}$$

$$\tilde{\mathbf{M}}(\mathbf{r}, \omega) = \mu_0 \chi_m(\omega) \tilde{\mathbf{H}}(\mathbf{r}, \omega), \tag{1.6b}$$

where $\chi_e(\omega)$ and $\chi_m(\omega)$ are the Fourier Transform (FT) of $\chi_e(t-t')$ and $\chi_m(t-t')$, respectively. It's worth mentioning that the electric and magnetic fields are real

quantity in the time domain and hence they satisfy $\tilde{\mathbf{E}}(\mathbf{r},\omega) = \tilde{\mathbf{E}}^*(\mathbf{r},-\omega)$ and $\tilde{\mathbf{H}}(\mathbf{r},\omega) = \tilde{\mathbf{H}}^*(\mathbf{r},-\omega)$. Inserting Eq. (1.6) into Eq. (1.3) we obtain the constitutive relations

$$\tilde{\mathbf{D}}(\mathbf{r},\omega) = \epsilon_0\epsilon_{\mathrm{r}}(\omega)\tilde{\mathbf{E}}(\mathbf{r},\omega), \tag{1.7a}$$

$$\tilde{\mathbf{B}}(\mathbf{r},\omega) = \mu_0\mu_{\mathrm{r}}(\omega)\tilde{\mathbf{H}}(\mathbf{r},\omega),. \tag{1.7b}$$

where $\epsilon_{\mathrm{r}}(\omega) = 1+\chi_e(\omega)$ is the relative dielectric permittivity and $\mu_{\mathrm{r}}(\omega) = 1+\chi_m(\omega)$ is the relative magnetic permeability of the medium. For systems with interfaces between different materials, fields can be calculated by applying Boundary Conditions (BCs) that adjust the fields across the interface and ensure conformity of Maxwell's equations. By setting the continuity of tangential components of electric and magnetic fields and normal components of electric displacement and magnetic induction field, BCs are obtained directly from Maxwell's equation Eq. (1.1) as follows

$$\hat{\mathbf{n}} \times (\mathbf{E}_i - \mathbf{E}_j) = 0, \qquad \hat{\mathbf{n}} \times (\mathbf{H}_i - \mathbf{H}_j) = \mathbf{K}, \tag{1.8a}$$

$$\hat{\mathbf{n}} \cdot (\mathbf{D}_i - \mathbf{D}_j) = \sigma, \qquad \hat{\mathbf{n}} \cdot (\mathbf{B}_i - \mathbf{B}_j) = 0, \tag{1.8b}$$

where subscript i and j refer to the fields in lower and upper medium of the interface, receptively. Here, $\hat{\mathbf{n}}$ is the unit vector normal to the interface, $\mathbf{K}$ and σ indicate the surface current and charge densities at the interface, respectively. Lastly, for a medium with no charge and current sources i.e., $\rho = 0$ and $\mathbf{J} = 0$, the Maxwell's equation Eq. (1.1) provides the governing equation (wave equation) of electromagnetic wave propagation inside the medium. The wave equation can be expressed in the Fourier domain as the Helmholtz equation

$$\nabla^2\tilde{\mathbf{E}} + \frac{\omega^2}{c^2}n^2\tilde{\mathbf{E}} = 0, \tag{1.9}$$

where $c = 1/\sqrt{\mu_0\epsilon_0}$ is the speed of light and $n = \sqrt{\epsilon_r\mu_r}$ is known as the material's refractive index which determines the phase velocity $v = c/n$ of the field propagation in the medium.

1.4 Plane wave, polarization and Stokes parameters.

Plane waves are a special type of electromagnetic wave having fields that depend only on a single spatial coordinate. For example, a z-propagating plane wave contains uniform fields over every plane perpendicular to the z direction. Assuming a monochromatic (single frequency) plane wave solution

$$\mathbf{E}(\mathbf{r}, t) = \mathrm{Re}\left\{\tilde{\mathbf{E}} e^{i\mathbf{k}\cdot\mathbf{r} - i\omega t}\right\}, \tag{1.10}$$

where $\tilde{\mathbf{E}}$ is the complex field amplitude, $\mathbf{k}$ is the wave vector and ω is the angular frequency. By substituting Eq. (1.10) in Eq. (1.9), we derive the dispersion relation $k = \dfrac{n(\omega)}{c}\omega$ for the wave propagation in the medium. The orientation and pattern of the oscillating electric field determines the polarization state of an electromagnetic wave.

Fresnel first reported the fundamental concept of light polarization with the discovery of the transverse field vector of light (1821) and the circularly polarized light (1822). Polarization of light is the process of confining the electric field vector oscillations in a single plane. Light originated from ordinary sources usually possesses random, temporally incoherent polarization. Such an unpolarized light can be converted to specific polarization by passing it through a polarizer. Based on the orientation of the electric field oscillation, light polarization can be categorized into Linear Polarization (LP), Chiral Parameter (CP) and elliptical polarization. As the light propagates, the electric field of LP oscillates in a fixed plane that is perpendicular to the direction of propagation, while for CP and elliptical polarization, the electric field traces a circular and elliptical path,

respectively. Considering a z-propagating light with angular frequency ω and orthogonal electric field components $\tilde{E}_x$ and $\tilde{E}_y$ having relative phase difference ϕ, the electric field of the light can be described by

$$\mathbf{E}(\mathbf{r},t) = \mathrm{Re}\left\{\left[\tilde{E}_x e^{ikz}\hat{\mathbf{e}}_x + \tilde{E}_y e^{i(kz+\phi)}\hat{\mathbf{e}}_y\right] e^{-i\omega t}\right\}, \tag{1.11}$$

where k refers to the wave vector in the z-direction and the orthogonal field components are propagating in the x and y directions as defined by the corresponding respective unit vectors $\hat{\mathbf{e}}_x$ and $\hat{\mathbf{e}}_y$. For a monochromatic wave, the FT amplitude is delta-like and thus we rewrite the field in this way. Considering the relative phase difference $\phi = 0$ or multiple of $\pm 2\pi$, the electric field becomes

$$\mathbf{E}(\mathbf{r},t) = \mathrm{Re}\left\{\left[\left(\tilde{E}_x\hat{\mathbf{e}}_x + \tilde{E}_y\hat{\mathbf{e}}_y\right) e^{ikz}\right] e^{-i\omega t}\right\}, \tag{1.12}$$

which represents a linearly polarized light. When the magnitudes of orthogonal field components are equal, i.e., $\tilde{E}_x = \tilde{E}_y = \tilde{E}/\sqrt{2}$ and the relative phase difference $\phi = \pm\pi/2$, utilizing the identity $e^{i(kz\pm\frac{\pi}{2})} = \pm i e^{ikz}$, we obtain the total field

$$\mathbf{E}(\mathbf{r},t) = \mathrm{Re}\left\{\frac{\tilde{E}}{\sqrt{2}}\left[\left(\hat{\mathbf{e}}_x \pm i\hat{\mathbf{e}}_y\right)e^{ikz}\right] e^{-i\omega t}\right\}. \tag{1.13}$$

This expression describes a circularly polarized light, where the electric field rotates in the plane perpendicular to the direction of propagation. The orientation of circular motion is determined by the unit vector

$$\hat{\mathbf{n}}_\pm = \frac{1}{\sqrt{2}}\left(\hat{\mathbf{e}}_x \pm i\hat{\mathbf{e}}_y\right). \tag{1.14}$$

Specifically, if $\phi = +\frac{\pi}{2}$, the light exhibits Right Circular Polarization (RCP), while $\phi = -\frac{\pi}{2}$ corresponds to Left Circular Polarization (LCP). In turn, the electric field

of the RCP and LCP states can be expressed as

$$\mathbf{E}_+(\mathbf{r},t) = \mathrm{Re}\left\{\left[\tilde{E}e^{ikz}\hat{\mathbf{n}}_+\right]e^{-i\omega t}\right\}, \tag{1.15a}$$

$$\mathbf{E}_-(\mathbf{r},t) = \mathrm{Re}\left\{\left[\tilde{E}e^{ikz}\hat{\mathbf{n}}_-\right]e^{-i\omega t}\right\}, \tag{1.15b}$$

Note that these states are orthogonal to each other, leading to the basis sets for any arbitrary polarization state. For example, the superposition of the RCP and LCP states given by Eq. (1.15) provides

$$\begin{aligned}\mathbf{E}_+(\mathbf{r},t) + \mathbf{E}_-(\mathbf{r},t) &= \mathrm{Re}\left\{\left[\tilde{E}e^{ikz}\left(\hat{\mathbf{n}}_+ + \hat{\mathbf{n}}_-\right)\right]e^{-i\omega t}\right\}, \\ &= \mathrm{Re}\left\{\left[\sqrt{2}\tilde{E}e^{ikz}\hat{\mathbf{e}}_x\right]e^{-i\omega t}\right\}, \end{aligned} \tag{1.16a}$$

which describes a linearly polarized light [52]. Commonly, the polarization state of an electromagnetic radiation can be described in terms of a set of four parameters called Stokes parameters (S_0, S_1, S_2, and S_3) introduced by George Gabriel Stokes [53]. For the z-propagating monochromatic light given by Eq. (1.11), the Stokes parameters are given by

$$S_0 = |\tilde{E}_x|^2 + |\tilde{E}_y|^2, \tag{1.17a}$$

$$S_1 = |\tilde{E}_x|^2 - |\tilde{E}_y|^2, \tag{1.17b}$$

$$S_2 = 2\tilde{E}_x\tilde{E}_y^* \cos\phi, \tag{1.17c}$$

$$S_3 = 2\tilde{E}_x\tilde{E}_y^* \sin\phi. \tag{1.17d}$$

Here S_0 refers to the total intensity of light, and S_3 accounts for the ellipticity of the polarization. In addition, the power associated with two orthogonal components is determined by S_1 and S_2, which in turn represent the orientation of the

polarization ellipse. The four Stokes parameters are related by

$$S_0^2 \geq S_1^2 + S_2^2 + S_3^2. \tag{1.18}$$

Basically, the complex electric field vector of electromagnetic radiation can be realized in three-dimensional space using the Stokes parameters. However, S_0 is constant for lossless propagation, and hence the polarization state determined by S_1, S_2, and S_3 basis sets can be projected on a sphere of radius S_0. Conventionally, it has been accomplished by using Poincaré sphere, where one can visualize all the possible polarization states. Equator of the sphere describes LPs, poles indicate CPs, and other points on the surface correspond to elliptical polarizations.

1.5 Chiroptical activity in chiral media.

Arago (1811) and Biot (1812) first observed that there are some special mediums capable of rotating the polarization plane of a linearly polarized light. In fact, they found wavelength-dependent rotation of the polarization plane for polychromatic light. Drude(1902) first modeled these effects. According to him, the amount of rotation as a function of wavelength(λ) can be expressed as:

$$\phi(\lambda) = \sum_j \frac{a_j}{\lambda^2 - \lambda_j^2}, \tag{1.19}$$

where a_j is a constant related to electronic absorption at the wavelength λ_j. This new phenomena is termed as optical activity and the associated medium is called optically active medium. Eventually, the origin of such optical activities was recognized as the characteristic properties of chiral medium.

1.5.1 Bi-anisotropic media.

In the case of a simple linear isotropic medium, from the constitutive equations Eq. (1.4), we see that $\mathbf{D} \parallel \mathbf{E}$ and $\mathbf{B} \parallel \mathbf{H}$. However, in general cases, such isotropic assumptions are not valid. Moreover, $\mathbf{D}$ and $\mathbf{H}$ may possess dependencies on $\mathbf{E}$ and $\mathbf{B}$ when the medium acquires magnetoelectric coupling. A medium with anisotropy and non-zero magnetoelectric coupling is called a bi-anisotropic medium. In this work, we focus on an isotropic chiral medium where the constitutive relations can be written following different conventions, including Born's relations [54, 55], Post's relations [56], and Tellegen's relations [54, 57, 58]. Although different froms are equivalent, throughout this work we will use Tellegen's relations

$$\tilde{\mathbf{D}} = \epsilon_0 \epsilon_\mathrm{r} \tilde{\mathbf{E}} - \frac{1}{c} i\kappa \tilde{\mathbf{H}}, \tag{1.20a}$$

$$\tilde{\mathbf{B}} = \frac{1}{c} i\kappa \tilde{\mathbf{E}} + \mu_0 \mu_\mathrm{r} \tilde{\mathbf{H}}, \tag{1.20b}$$

where κ is called "*chirality parameter*" (also known as Pasteur parameter), which defines the degree of chirality and flips sign for opposite enantiomers. In addition, ϵ_r and μ_r are scalar quantities since the medium is isotropic. Essentially, for a racemic mixtures where opposite enantiomers exist in equal amounts, $\kappa = 0$. Note that in such a representation, the chirality parameter is a dimensionless quantity. Assuming monochromatic fields with time-harmonic dependence ($e^{-i\omega t}$), the source-free Maxwell's equations provide

$$\nabla \cdot \tilde{\mathbf{D}} = 0, \qquad \nabla \cdot \tilde{\mathbf{B}} = 0, \tag{1.21a}$$

$$\nabla \times \tilde{\mathbf{E}} = -i\omega \tilde{\mathbf{B}}, \qquad \nabla \times \tilde{\mathbf{H}} = i\omega \tilde{\mathbf{D}}, \tag{1.21b}$$

Utilizing Eq. (1.20) together with Eq. (1.21) and the vector identity $\nabla\times(\nabla\times\tilde{\mathbf{E}}) = \nabla\cdot(\nabla\cdot\tilde{\mathbf{E}}) - \nabla^2\tilde{\mathbf{E}}$, one gets

$$\nabla^2\tilde{\mathbf{E}} + (\epsilon_{\mathrm{r}}\mu_{\mathrm{r}} - \kappa^2)\frac{\omega^2}{c^2}\tilde{\mathbf{E}} + 2\kappa\frac{\omega}{c}\nabla\times\tilde{\mathbf{E}} = 0. \tag{1.22}$$

Without loss of generality, for an isotropic and homogeneous medium, we can assume a z-propagating monochromatic plane wave solution

$$\tilde{\mathbf{E}} = \left[\tilde{E}_x\hat{\mathbf{e}}_x + \tilde{E}_y\hat{\mathbf{e}}_y\right]e^{ikz}, \tag{1.23}$$

with wavevector k and and two orthogonal field amplitude $\tilde{E}_x$ and $\tilde{E}_y$ in the direction defined by respective unit vectors $\hat{\mathbf{e}}_x$ and $\hat{\mathbf{e}}_y$. Substituting Eq. (1.23) in Eq. (1.22), the two eigenwaves [59] in the isotropic chiral media are given by

$$\tilde{\mathbf{E}}_\pm = \left[\tilde{E}_x\hat{\mathbf{e}}_x \pm i\tilde{E}_y\hat{\mathbf{e}}_y\right]e^{ik_\pm z}, \tag{1.24}$$

where $k_\pm = \dfrac{\omega}{c}(\sqrt{\epsilon_{\mathrm{r}}\mu_{\mathrm{r}}} \pm \kappa)$ indicates the wavevector component in the z-direction of two eigenwaves. Note that when $\tilde{E}_x = \tilde{E}_y$, the two eigenmodes, see Eq. (1.24), represent the RCP and LCP waves associated with k_+ and k_-, respectively, that propagate with different phase velocities through the chiral media. Thus, chiral media offers different refractive indices [56, 59] $n_\pm = \sqrt{\epsilon_{\mathrm{r}}\mu_{\mathrm{r}}} \pm \kappa$ for RCP and LCP. Consequently, the respective phase velocities $v_+ = c/\mathrm{Re}[n_+]$ and $v_- = c/\mathrm{Re}[n_-]$ of RCP and LCP are also different in the chiral medium. It is worth mentioning that the $\mathrm{Re}[\kappa]$ is responsible for the rotatory power and $\mathrm{Im}[\kappa]$ causes CD in a chiral medium.

1.5.2 Optical rotatory dispersion.

The linearly polarized light can be expressed as the superposition of RCP and LCP light, as discussed in the previous section. When a linearly polarized light passes

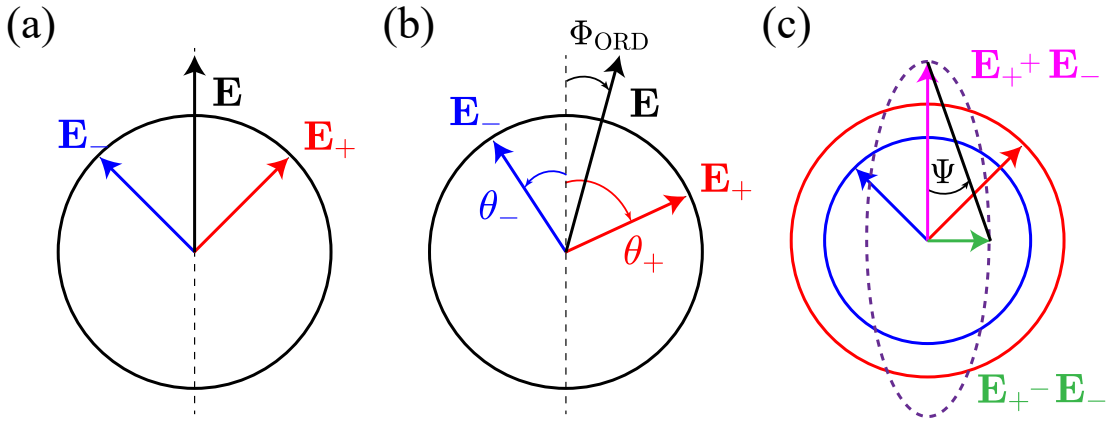


Figure 1.2: **(a)** Propagation of linearly polarized (**E**) light is decomposed into coherent right ($\mathbf{E}_+$) and left ($\mathbf{E}_-$) circularly polarized components within achiral medium. **(b)** Rotation (ϕ) of the electric field vector of the linearly polarized light while propagating through an optically active medium, resulting from the orientation of the right (θ_+) and left (θ_-) circularly polarized components at some point. **(c)** Two coherent right and left circularly polarized components with different amplitudes recombine to produce an elliptically polarized light with an ellipticity of Ψ within a chiral medium.

through an isotropic achiral medium the RCP and LCP components travel with equal velocities. Therefore, the relative phase difference between two components is zero and after recombination, they produce a linear polarized light parallel to the incident light. In this case the electric field vectors of RCP and LCP components are oriented at equal angles with respect to the direction of incident polarization as depicted in Fig. 1.2(a). Conversely, as we have seen in a chiral medium, the respective phase velocities v_+ and v_- of the RCP and LCP components

$$\mathbf{E}_+(\mathbf{r},t) = \mathrm{Re}\left\{\left[\tilde{E}e^{ik_+ z}\hat{\mathbf{n}}_+\right]e^{-i\omega t}\right\}, \tag{1.25a}$$

$$\mathbf{E}_-(\mathbf{r},t) = \mathrm{Re}\left\{\left[\tilde{E}e^{ik_- z}\hat{\mathbf{n}}_-\right]e^{-i\omega t}\right\}, \tag{1.25b}$$

are not same and hence leads to a phase difference between them throughout the propagation inside chiral media. As a result, the direction of the resultant field vector of two circularly polarized components at some point inside chiral medium differs from the direction of the incident linearly polarized light field,

see Fig. 1.2(b). Moreover, the amount of rotation is different for light with different wavelength. Such a wavelength dependent rotation of polarization plane of a linearly polarized light by optically active media is called Optical Rotatory Dispersion (ORD). Let's consider that, at a given position and time, the RCP and LCP components inside the active medium are oriented at angles θ_+ and θ_-, respectively, with respect to the direction of incident linearly polarized light. Therefore, the angle of rotation expressed in radians can be written as [60]

$$\Phi_{\mathrm{ORD}}(\lambda) = \frac{\theta_+ + \theta_-}{2} \tag{1.26}$$

Considering unit propagation length inside the active medium and writing the refractive index $n = n' + in''$ in terms of real n' and imaginary n'' parts, we obtain

$$\Phi_{\mathrm{ORD}}(\lambda) = \frac{\pi c}{\lambda}\left(\frac{1}{v_+} - \frac{1}{v_-}\right) = \frac{\omega}{2c}(n'_+ - n'_-), \tag{1.27}$$

where $\lambda = 2\pi c/\omega$ is the vacuum wavelength. Throughout the propagation, the orientation of the resultant vector of the RCP and LCP components inside the medium will rotate but it still remains linearly polarized. A similar kind of effect can be observed in birefringence, where orthogonal linear polarized light experiences different phase velocities. Thus, such a chiral counterpart of birefringence can be realized as circular birefringence of an optically active medium.

1.5.3 Circular dichroism.

When a medium is illuminated with light, some part of the light will be absorbed by the medium. The absorption depends on the imaginary part (also known as extinction coefficient) of the refractive index of the material. We have seen that the optically active medium exhibits different refractive indices for RCP and LCP light. As a consequence, these media absorb an unequal amount of RCP and

LCP, and therefore, the magnitude of the electric field components of RCP and LCP differs when light propagates through such medium. In turn, the coherent RCP and LCP components with different amplitudes recombine to produce an elliptically polarized light, as illustrated in Fig. 1.2(c). Circular Dichroism (CD) is the measure of this differential absorption. For an optically active medium, considering wavelength dependent RCP absorbance $A_+(\lambda)$ and LCP absorbance $A_-(\lambda)$, we define CDDA

$$\Delta A(\lambda) = A_+(\lambda) - A_-(\lambda). \tag{1.28}$$

From an experimental point of view, enantioselectivity is often measured in terms of the Kuhn's asymmetry factor [61]

$$g = 2\left[\frac{A_+(\lambda) - A_-(\lambda)}{A_+(\lambda) + A_-(\lambda)}\right]. \tag{1.29}$$

Furthermore, considering the medium's refractive index $n = n' + in''$, the Beer-Lambert law provides the intensity of light after traveling a distance d through the medium as

$$I(d) = I_0 e^{-2(\omega/c)n''d}, \tag{1.30}$$

where I_0 is the initial intensity of light. The above equation can be extended to measure CD in terms of the intensity differences of transmitted RCP and LCP components using

$$\Delta A(\lambda) = (1 - T_+) - (1 - T_-) = e^{-2(\omega/c)n''_- d} - e^{-2(\omega/c)n''_+ d}, \tag{1.31}$$

where T_+ and T_- are the transmission coefficients for RCP and LCP components. Additionally, the CD signal is often measured in terms of the ellipticity of generated elliptically polarized light. We can determine the ellipticity Ψ, see Fig. 1.2(c),

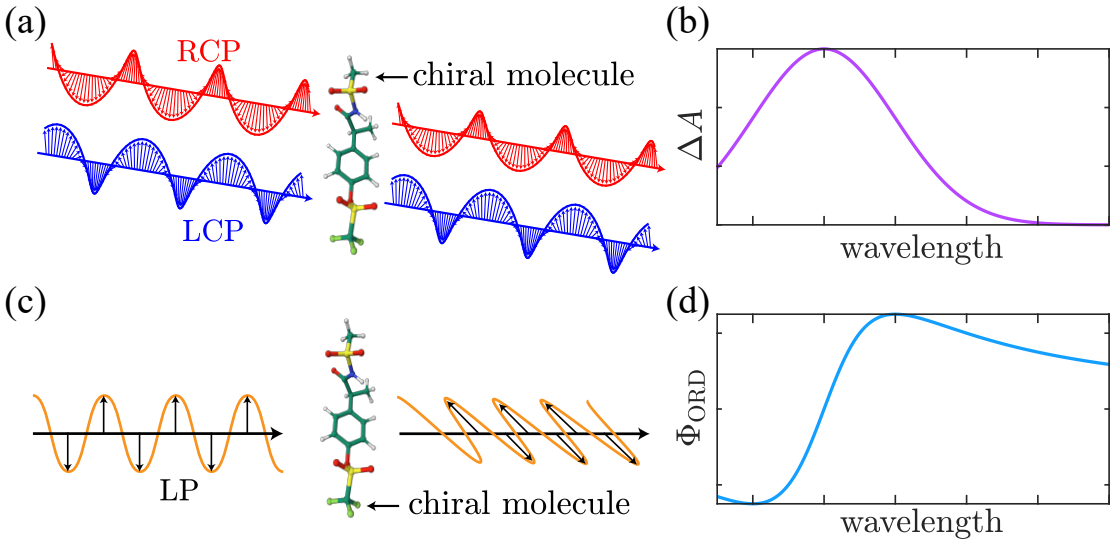


Figure 1.3: Schematic representation of **(a)** circular dichroism, illustrating differential absorption of Right Circular Polarization (RCP) and Left Circular Polarization (LCP) exhibited by a chiral medium, and **(c)** optical rotatory dispersion, illustrating rotation of polarization plane of Linear Polarization (LP), when it propagates through the chiral medium. Representative spectra, depicting wavelength-dependent **(b)** differential absorption ΔA of RCP and LCP, and **(d)** rotation Φ_{ORD} of the polarization plane of LP.

in terms of the major and minor axes of the ellipse as

$$\Psi = \arctan\left(\frac{E_+ - E_-}{E_+ + E_-}\right). \tag{1.32}$$

Note that $\Psi => 0$ for $E_+ > E_-$, corresponds to clockwise and $\Psi =< 0$ for $E_+ < E_-$, corresponds to counter clockwise rotation of the electric field within a fixed plane of the elliptically polarized light. Fig. 1.3 represents a schematic of the optical activities exhibited by a chiral molecule as an active medium. By applying Eq. (1.28), CD spectra can be obtained from the extinction spectra of RCP and LCP light at each wavelength as shown schematically in Fig. 1.3(a,b). Similarly, by comparing the transmitted polarization plane with the incident one, ORD spectra Fig. 1.3(c,d) can be obtained. In general, for an optically active medium, both the real and imaginary parts of the refractive index are different for RCP and LCP, which leads to the simultaneous optical rotation and circular dichroism.

Hence, fundamentally, the CD and ORD spectra carry equivalent information and connected through Kramers-Kronig transforms[62, 63].

1.6 Plasmonic nanomaterials.

Over time, the detection limit of molecular chiral sensing has been significantly improved utilizing engineered plasmonic nanomaterials. Recent advancements in fabrication techniques enable tailor-designing of micro/nanoscale structures, which dramatically boost the exploration of light-matter interaction at the nanoscale. Artificially designed plasmonic nanomaterials allow controlled manipulation of electromagnetic radiation over diverse frequency ranges. Among all the fascinating optical properties exhibited by plasmonic materials, locally enhanced fields have been utilized in a wide range of molecular sensing and spectroscopy applications. As a result, plasmonic nanomaterials find significant importance in developing nanophotonic devices, biochemical sensing, and surface-enhanced spectroscopy. In this section, we present an overview of relevant aspects of plasmonic nanomaterials, focusing on surface plasmon polaritons and localized surface plasmons.

1.6.1 Surface plasmon polariton.

By definition, SPP refers to an electromagnetic wave confined to the metal-dielectric interface that propagates along the surface while exponentially decaying in a perpendicular direction to the interface. In general, the response of a metal surface to an external electromagnetic radiation can be described in terms of plasma (free electron gas in metal) oscillations. Upon excitation with light, the collective oscillations of free electrons on the metal surface can be coupled with the incident photons to generate a couple state called plasmon polariton. However, special geometric configuration and material properties are needed to excite such surface modes. For a single metal-dielectric interface characterized by

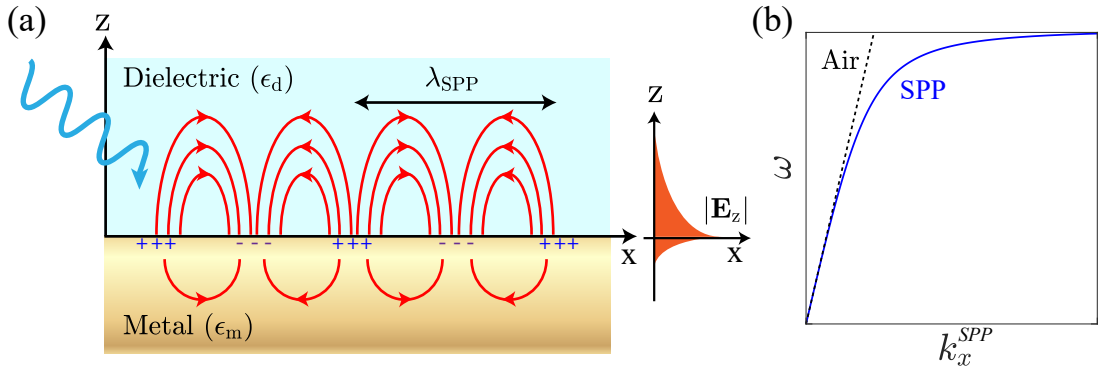


Figure 1.4: **(a)** Schematic illustration of Surface-Plasmon Polariton (SPP) with wavelength λ^{SPP} at the metal (permittivity ϵ_{m})-dielectric (permittivity ϵ_{d}) interface. The SPP propagates along the interface with wavevector k_x^{SPP} and possess exponentially decaying amplitude ($\mathbf{E}_z$) in the z-direction. **(b)** Representative SPP dispersion curve (blue curve) which lies to the right side of the light line (black dotted line) in air.

the permittivities of metal $\epsilon_{\mathrm{m}}(\omega)$ and dielectric $\epsilon_{\mathrm{d}}(\omega)$, such that $\mathrm{Re}[\epsilon_{\mathrm{m}}(\omega)] < 0$ and $\mathrm{Re}[\epsilon_{\mathrm{d}}(\omega)] > 0$, SPPs can be excited at the interface. Fig. 1.4(a) illustrates a cross section of the geometry. In this configuration, the dispersion relation of SPP propagating along the x direction can be written as [64]

$$k_x^{\mathrm{SPP}}(\omega) = \frac{\omega}{c}\sqrt{\frac{\epsilon_{\mathrm{m}}(\omega)\epsilon_{\mathrm{d}}(\omega)}{\epsilon_{\mathrm{m}}(\omega)+\epsilon_{\mathrm{d}}(\omega)}}, \tag{1.33}$$

where k_x^{SPP} is the wave vector of SPP, ω is the angular frequency and c is the light speed. Note that for every ω neglecting losses, SPP always possesses a larger wave vector than that of the light in free space $k_x^{\mathrm{SPP}} > k_{\mathrm{light}}$, where $k_{\mathrm{light}} = \omega/c$ and the SPP wavelength $\lambda_{\mathrm{SPP}} = 2\pi/k_x^{\mathrm{SPP}}$ is shorter than the wavelength of light in free space. Consequently, the SPP dispersion curve always lies on the right side of the light line, see Fig. 1.4(b), and hence the conservation of momentum does not allow SPPs excitation by directly impinging light from the same dielectric at the interface. Therefore, some special techniques are required to provide a radiation momentum kick. Commonly used experimental strategies, such as well-known Otto [65] and Kretschmann [66] geometry, utilize high-index prisms to

match the projection of the incident light wavevector with the SPP wave vector. Importantly, in these configurations, the SPP excitation strongly depends on the optical incidence angle, which is highly sensitive to the variation of the dielectric environment. In turn, by attaching the molecules to the metal surface, efficient molecular characterization is possible through the measurement of induced angular shift [67]. Furthermore, the sub-wavelength confinement [68] of SPPs and the locally enhanced field [69] offered by SPPs can be employed to achieve greater interaction between the light and nearby molecules [70]. Such unique features of SPPs will enable us to attain enhanced circular dichroism of chiral drug solutions (discussed in Chapter 4).

1.6.2 Localized surface plasmon.

Within the quasi-static approximation, an oscillating electromagnetic field can induce coherent oscillations of electron gas, provided the particle size is much smaller than the wavelength of impinging radiation. Fig. 1.5 represents the schematic illustration of the coherent oscillation of charges induced by an external radiation field. Because of the smaller size of the particle, the variations of the electromagnetic field can be assumed to be negligible over the particle, and hence, the entire electron gas uniformly responds to the driving field. When the frequency of such oscillating electron gas coincides with that of the impinging radiation, we can achieve the so-called Localized Surface Plasmon (LSP) resonances. Typically, LSPs are non-propagating excitations that can be coherently excited to achieve a maximum excitation efficiency at their resonance frequency, defined by the effective polarizability of the plasmonic nanoparticle. Importantly, the nanoparticles's geometry, material properties, and the surrounding medium strongly affect the LSP resonances. Considering a spherical metallic nanoparticle with permittivity $\epsilon_{\mathrm{m}}(\omega)$ and radius $R \ll \lambda$, where λ indicates the vacuum wavelength, surrounded by a dielectric background with permittivity $\epsilon_{\mathrm{b}}(\omega)$, the polarizability of the nanopar-

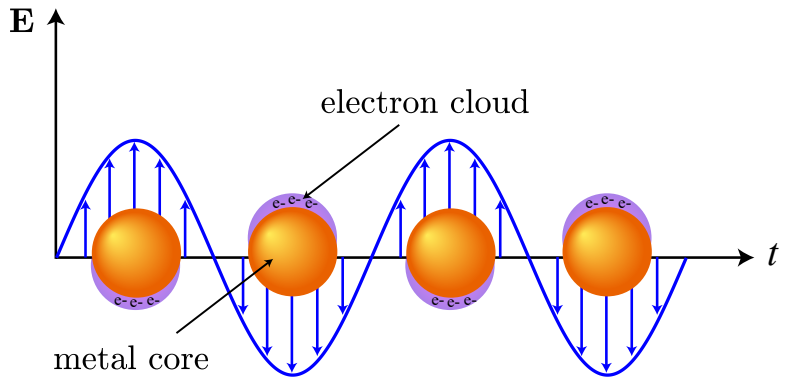


Figure 1.5: Schematic illustration of Localized Surface Plasmon (LSP) arising from coherent oscillation of charges induced by the external radiation $\mathbf{E}(t)$, in sub-wavelength metallic nanoparticles .

ticle can be written as [64]

$$\alpha(\omega) = 4\pi R^3 \frac{\epsilon_{\mathrm{b}}(\omega) - \epsilon_{\mathrm{m}}(\omega)}{\epsilon_{\mathrm{b}}(\omega) + 2\epsilon_{\mathrm{m}}(\omega)}. \tag{1.34}$$

As we can see, the condition $\epsilon_{\mathrm{b}}(\omega) = -2\epsilon_{\mathrm{m}}(\omega)$ corresponds to the maximum polarizability and hence the LSP resonance condition. However, in complex geometric configurations, obtaining an analytical expression for LSP resonance is not trivial. Nevertheless, the plasmonic nanoparticle will still exhibit resonant scattering at the LSP resonance. Like SPP, the LSP also provides strong near-field enhancement in the vicinity of plasmonic nanoparticles, and the resonance frequency is highly sensitive to the background dielectric environment. In turn, LSP holds potential applications in molecular sensing applications [71, 72, 73]. In Chapter 5, we present an enhanced chiroptical sensing approach utilizing LSP resonanaces of plasmonic nanoshell.

Chapter 2

Physical Chemistry Modeling of Spectroscopic Properties of Chiral Drug Solutions

In this chapter, we provide an overview of the theoretical framework utilized to evaluate the spectroscopic properties of the chiral drug solutions under study. We have adopted a combination of computational methods based on electronic structure approaches. We mainly focus on classical Molecular Dynamics (MD), DFT, and a hybrid QM/MM approach, in particular MD-PMM.

2.1 Introduction.

A simulation replicates the representative configurations of a macroscopic system with manageable numbers of constituent elements (atoms or molecules) to predict several properties of the system. Feasible computations enable us to predict structural and thermodynamical properties with high accuracy through simulation. It also provides a detailed understanding of how the atomic and molecular systems dynamically change their configurations over time. Molecular simulations generate thermodynamic data sets of important features of the system without performing any experiments. There are two common molecular modeling simulation techniques: the MD and the Monte Carlo methods. Here we will focus on molecular dynamics, which is based on the evaluation of the time-dependent behavior of a molecular system.

Molecular Dynamics analyzes movements of interacting atoms and molecules inside the system to trace the physical dynamics of the system. It is based on a deterministic method, meaning that the future state of the system can be determined from it's current state. Usually, the system is defined in terms of a bounded volume which is often called a simulation box. The box contains certain number of molecules and the behavior of such molecules are computed through the simulation. The equations of motion of the interacting particles of the system are computed by considering the force-fields and potentials. In each step of the simulation, the forces acting on the particles are calculated, combining them with current positions and velocities, thus enabling the determination of the subsequent state of the system. In turn, the simulated motion of the atoms and molecules generates a trajectory, providing the time evolution of dynamic variables.

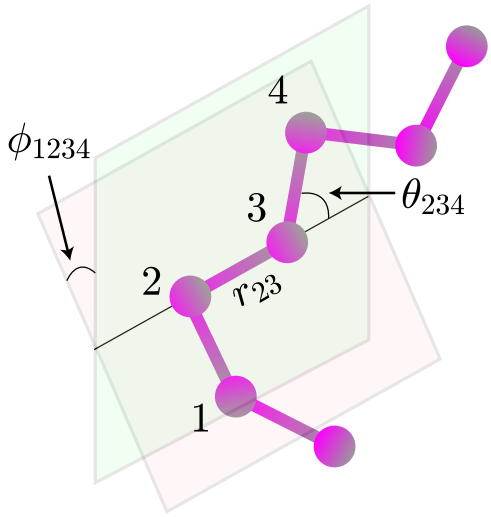


Figure 2.1: Geometrical illustration of bond length (r_{23}), bend angle (θ_{234}) and dihedral angle (ϕ_{1234}) in a simple chiral molecule.

2.2 Molecular Interactions.

In a solution, molecules interact both with solvent molecules and with one another. Broadly, there are two types of molecular interactions, bonded and non-bonded; each holds a significant role in determining the structural and functional properties of the molecules. Non-bonded molecules interact through electrostatic forces arising from the electric fields generated by electrons and protons in the molecules, leading to intermolecular forces. In contrast, intramolecular forces are originated from the constrained motion of bonded atoms within the molecule. Usually, the non-bonded interactions are assumed pair-additive and three-body(or higher order) interactions are neglected. Among the theoretical and experimental models of such interaction potentials in the literature [74, 75], the Coulomb potential and Lennard-Jones potential are most commonly used. The electrostatic interactions between charged (or partially charged) atoms can be described by the Coulomb interaction with the associated potential function

$$V_{ij}^{(\mathrm{C})}(r_{ij}) = \sum_{i,j} \frac{1}{4\pi\epsilon_0\epsilon_\mathrm{r}} \frac{q_i q_j}{r_{ij}}, \tag{2.1}$$

where q_i and q_j are the charges of i-th and j-th atoms, respectively, and they are separated by a distance r_{ij}. Here ϵ_0 and ϵ_r indicate the vacuum dielectric constant and relative dielectric constant of the medium, respectively. The Lennard-Jones Potential is another simple model to describe two-body interactions between non-bonded particles. Basically, it has two components: an attractive potential, which includes Van-der-Waals interaction between the atoms and molecules at intermediate distances, and a repulsive potential, which involves repulsion between the atoms and molecules at very close range. The widely used expression of the Lennard-Jones potential is given by

$$V_{ij}^{(\mathrm{LJ})}(r_{ij}) = \sum_{i,j} 4w_{ij} \left[\left(\frac{d_{ij}}{r_{ij}} \right)^{12} - \left(\frac{d_{ij}}{r_{ij}} \right)^{6} \right], \tag{2.2}$$

where the two parameters w_{ij} and d_{ij} are the depth of the potential well and the collision parameter related to the separation corresponding to the minimum energy, receptively.

Within a single molecule, atoms can not move independently since they are connected to each other through the bonds and oriented in certain bond angles. Fig. 2.1 illustrates a geometric representation of the bond length, bending angle and dihedral angle [1] in a simple molecule. The origin of the intramolecular bonding interactions can be described through (i) vibrations due to the bond stretching, see Fig. 2.2(a), (ii) bending vibrations of successive bonds in molecules with three or more atoms, see Fig. 2.2(b), (iii) internal rotation about a bond (also known as torsion) in molecules with 4 or more atoms, see Fig. 2.2(c). Typically, the potentials of these interactions are assumed to be harmonic, and we can express

[1] A dihedral angle represents the relative orientation of two planes constructed through four atoms in a molecule. It is also referred to as torsion angle.

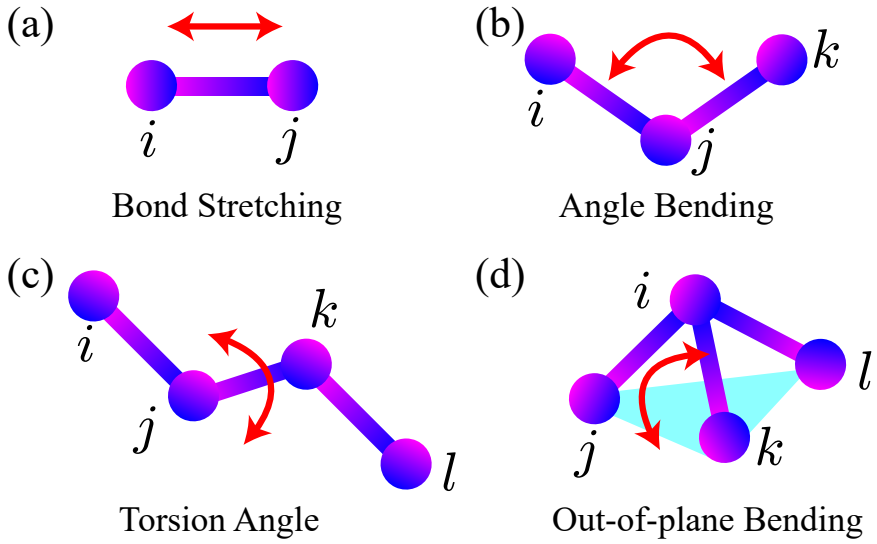


Figure 2.2: Schematic illustrations of **(a)** bond stretching, **(b)** angle bending, **(c)** torsion angle, and **(d)** out-of-plane bending.

these contributions as

$$V_{\text{bonds}}(r_{ij}) = \frac{1}{2}\sum_{\text{bonds}} k^{b}_{ij}(r_{ij} - r_{\text{eq}})^2, \tag{2.3a}$$

$$V_{\text{angles}}(\theta_{ijk}) = \frac{1}{2}\sum_{\text{angles}} k^{\theta}_{ijk}(\theta_{ijk} - \theta_{\text{eq}})^2, \tag{2.3b}$$

$$V_{\text{dihs}}(\phi_{ijkl}) = \frac{1}{2}\sum_{\text{dihedrals}}\sum_{n} k^{\phi,n}_{ijkl}[1 + \cos(n\phi_{ijkl} - \delta_n)], \tag{2.3c}$$

where r_{ij} is the bond separation between adjacent atom-pairs (i-th and j-th) and r_{eq} refers to the bond length at equilibrium condition. θ_{ijk} denotes the bend angle between successive bond vectors and θ_{eq} corresponds to the angle at equilibrium. ϕ_{ijkl} is the dihedral angle between ijk and jkl-planes, see Fig. 2.2(c). Usually, the potential contribution arising from the internal rotation is expanded in periodic functions with periodicity $n = 1, 2, ...$ and phase δ_n. Furthermore, k^{b}_{ij},k^{θ}_{ijk} and $k^{\phi,n}_{ijkl}$ are the corresponding force constants of the three above mentioned potentials.

2.3 Classical Molecular Dynamics.

The total wave function of a molecule can be approximated as a product of electronic and nuclear wave functions by utilizing the Born-Oppenheimer approximation [76] which allows decoupling of electronic and nuclear dynamics. Within the validity of this foundation, one gets [77]

$$\hat{\mathcal{H}}_{\text{tot}}\psi_{\text{tot}}(\mathbf{R},\mathbf{r}) = E_{\text{tot}}\psi_{\text{tot}}(\mathbf{R},\mathbf{r}), \tag{2.4a}$$

$$\hat{\mathcal{H}}_{\text{tot}} = \hat{\mathcal{H}}_{\text{el}} + \hat{\mathcal{H}}_{\text{N}}, \tag{2.4b}$$

$$\psi_{\text{tot}}(\mathbf{R},\mathbf{r}) \approx \psi_{\text{N}}(\mathbf{R})\psi_{\text{el}}(\mathbf{r},\mathbf{R}), \tag{2.4c}$$

$$\hat{\mathcal{H}}_{\text{el}}\psi_{\text{el}}(\mathbf{r},\mathbf{R}) = E_{\text{el}}(\mathbf{R})\psi_{\text{el}}(\mathbf{r},\mathbf{R}), \tag{2.4d}$$

$$\left[\hat{T}_{\text{N}} + E_{\text{el}}(\mathbf{R})\right]\psi_{\text{N}}(\mathbf{R}) = E_{\text{tot}}\psi_{\text{N}}(\mathbf{R}). \tag{2.4e}$$

In the above equations, ψ_{tot} is the total molecular wave function, $\mathbf{R}$ is the nuclear coordinates and $\mathbf{r}$ is the electronic coordinates. $\hat{\mathcal{H}}_{\text{tot}}$ and $\hat{\mathcal{H}}_{\text{el}}$ represent total molecular Hamiltonian and electronic Hamiltonian, with corresponding energies E_{tot} and E_{el}, respectively. $\psi_{\text{el}}(\mathbf{r},\mathbf{R})$ indicates the electronic wave function with parametric dependence on nuclear coordinates. $\psi_{\text{N}}(\mathbf{R})$ and $\hat{T}_{\text{N}}$ are the nuclear wave function and kinetic energy operator, respectively. Note that the relative masses of nuclei are very large compared to those of electrons, and hence the coupling between the velocities of nuclei and electrons can be neglected. In turn, the positions of nuclei can be assumed to be fixed from an electron standpoint.

In this framework, the nuclear motions can be realized on a potential energy surface, and classical Newton's law can explain these motions with good accuracy. Therefore, the solutions of electronic Schrödinger equations are capable of adequately explaining the time evolution of a molecular system. However, particularly for larger systems, quantum-mechanical simulations are computationally very expensive and inconvenient to do dynamics. On the other hand, classical

Molecular Dynamics can be an alternative tool for the ab initio calculations to describe the electronic energies with the force field combined with certain fitted parameters from experimental and higher-order computational data. These parameters are assigned in such a way that the computational models can precisely replicate real physical and chemical properties of the system. Accounting all the contributions, the total force field energy can be written as

$$E_{\text{tot}} = E_{\text{bonds}} + E_{\text{angles}} + E_{\text{dihs}} + E_{\text{VdW}} + E_{\text{elst}} + E_{\text{oop}}, \tag{2.5}$$

where the contributions to the energy function from bond stretching, angle bending, and torsional energy are denoted by E_{bonds}, E_{angles}, and E_{dihs}, respectively. In the previous section, we have discussed the bonded interactions. The non-bonded contributions E_{VdW} and E_{elst} correspond to the Van-der-Waals and electrostatic interactions, respectively. The Van-del-Waals interactions can be described in terms of the Lennard-Jones potential and the electrostatic interactions can be well-approximated by the Coulomb potential by considering the atoms as fixed point charges, as mentioned in previous section. Lastly, in case of four atoms, we have to include another contribution E_{oop} arising from out-of-plane bending. There are various methods to describe the out-of-plane bending angle. A straightforward approach is to include an improper dihedral angle as depicted in Fig. 2.2(d). Assuming a harmonic potential, we can write this contribution as

$$E_{\text{oop}}(\xi_{ijk}) = \frac{1}{2} \sum_{\text{improps}} k^{\xi}_{ijk}(\xi_{ijk} - \xi_{\text{eq}})^2 \tag{2.6}$$

where k^{ξ}_{ijk} is the force constant, ξ_{ijkl} is the improper dihedral angle and ξ_{eq} corresponds to the equilibrium condition. Thus, including all the contributions, the

total energy becomes

$$
\begin{aligned}
E_{\text{tot}} = & \frac{1}{2}\sum_{\text{bonds}} k^{b}_{ij}(r_{ij}-r_{\text{eq}})^2 + \frac{1}{2}\sum_{\text{angles}} k^{\theta}_{ijk}(\theta_{ijk}-\theta_{\text{eq}})^2 \\
& + \frac{1}{2}\sum_{\text{dihedrals}}\sum_{n} k^{\phi,n}_{ijkl}[1+\cos(n\phi_{ijkl}-\delta_n)] + \frac{1}{2}\sum_{\text{improps}} k^{\xi}_{ijk}(\xi_{ijk}-\xi_{\text{eq}})^2 \\
& + 4\sum_{i,j} w_{ij}\left[\left(\frac{d_{ij}}{r_{ij}}\right)^{12} - \left(\frac{d_{ij}}{r_{ij}}\right)^{6}\right] + \sum_{i,j}\frac{1}{4\pi\epsilon_0\epsilon_r}\frac{q_i q_j}{r_{ij}}.
\end{aligned}
\tag{2.7}
$$

Although this force field approach is computationally efficient, the system size still remains a limiting factor. In order to evaluate macroscopic properties, we introduce Periodic Boundary Conditions (PBCs), which surround the simulation box with translated replicas of itself. When an atom strikes on a boundary, PBCs effectively remove that atom, and it re-enters at the opposite boundary, maintaining the direction and velocity of the atom. Thus, the simulation domain essentially resembles the behavior of atoms in a bulk system. Such an approach raises the number of non-bonded interactions that need to be considered. This can be resolved by defining a cut-off radius for the Van-der-Waals interactions. Pair of atoms that are inside the cut-off region are considered as the neighbor list, and beyond which, pairwise interactions are not included in the computation. Conversely, to optimize the accuracy and computational efforts for long-range Coulomb interactions, we can adopt the Particle Mesh Ewald (PME) method [78], which calculates such interactions utilizing Fourier transformations.

Once the force field energy of an initial conformation of the molecule are provided, the temporal evolution of the system can be determined from the equation of motions obtained from Newton's second law. This is accomplished by solving these equations over a series of small time steps. A common numerical technique

is the Verlet algorithm

$$\mathbf{r}_{i+1} = 2\mathbf{r}_i - \mathbf{r}_{i-1} + \ddot{\mathbf{r}}_i(\Delta t)^2, \tag{2.8a}$$

$$\dot{\mathbf{r}}_i = \frac{1}{2\Delta t}\left(\mathbf{r}_{i+1} - \mathbf{r}_{i-1}\right), \tag{2.8b}$$

where $\mathbf{r}_i$ and Δt are the position at time t_i and the time step, respectively. Note that we truncate the Taylor expansion at third order, and the velocity can be approximately calculated from $\dot{\mathbf{r}}_i$. Since we are interested in thermodynamic macroscopic properties of the molecular system, we have to define the statistical ensemble as well. We performed the MD simulation in NVT ensembles, which corresponds to a fixed number of molecules inside the simulation box with constant volume. The macroscopic temperature is related to the kinetic energy and therefore to the velocities of constituent atoms in the system. The temperature of the system is maintained by rescaling the velocities through a thermostat which adjust the temperature (T) deviation form a reference temperature T_0 by multiplying a factor to the velocities. Berendsen et al. [79] proposed one such weak coupling method, where the multiplication factor is given by

$$f_T = \left[1 + \frac{\Delta t}{\tau_T}\left(\frac{T_0}{T} - 1\right)\right]^{1/2}, \tag{2.9}$$

where τ_T is called the coupling time constant which is responsible for the required time to reach the desired temperature. The outcome of the MD-simulation provide positions and velocities of all atoms at each step of the simulation. From this trajectory data, thermodynamic properties of the system can be evaluated through subsequent analysis.

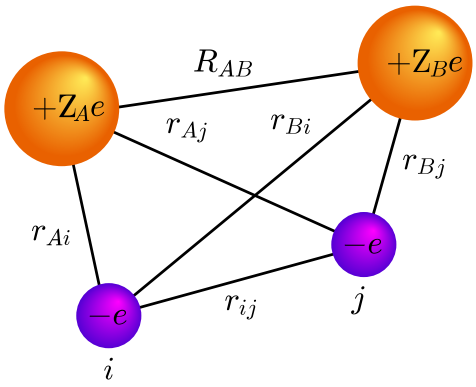


Figure 2.3: Schematic of a molecular system consisting two nuclei, labeled A and B and two electrons labeled i and j. Two nuclei, with charges $+Z_A$ and $+Z_B$ are separated by a distance R_{AB} and at a distances r_{Ai}, r_{Aj} and r_{Bi}, r_{Bj}, respectively, from the electrons. The electrons, each with charge $-e$ are separated from each other by a distance r_{ij}.

2.4 Electronic Structure Theory.

Classical MD is less complicated and less expensive to investigate the dynamics of a molecular system. However, the accurate descriptions of the electronic motion can be captured by employing Quantum Mechanical approach. To achieve that, we need to solve the time independent Schrödinger equation. Let's consider a molecular system consists of two nuclei, labeled A and B and two electrons labeled i and j, as depicted in Fig. 2.3. The nuclei, with charges $+Z_A$ and $+Z_B$ are separated by a distance R_{AB} and at a distances r_{Ai}, r_{Aj} and r_{Bi}, r_{Bj} from the electrons. The electrons, each with charge $-e$ are separated from each other by a distance r_{ij}. The total Hamiltonian of the system can be written as

$$\hat{\mathcal{H}} = \hat{T}_{\text{el}}(\mathbf{r}) + \hat{T}_{\text{N}}(\mathbf{R}) + \hat{V}_{\text{el,el}}(\mathbf{r}) + \hat{V}_{\text{el,N}}(\mathbf{r},\mathbf{R}) + \hat{V}_{\text{N,N}}(\mathbf{R}), \tag{2.10}$$

where the kinetic energy operators of nuclei and electrons are denoted by $\hat{T}_{\text{N}}$ and $\hat{T}_{\text{el}}$, respectively. The potential energy operators, $\hat{V}_{\text{el,N}}$, $\hat{V}_{\text{N,N}}$, and $\hat{V}_{\text{el,el}}$ correspond to the electrons-nuclei, nuclei-nuclei, and electrons-electrons electrostatic interac-

tion, respectively. Explicit expressions of these operators are given by

$$\hat{T}_{\mathrm{el}}(\mathbf{r}) = -\frac{\hbar^2}{2m_e}\sum_{i}^{\mathrm{elec}}\nabla_i^2, \tag{2.11a}$$

$$\hat{T}_{\mathrm{N}}(\mathbf{R}) = -\sum_{A}^{\mathrm{nuc}}\frac{\hbar^2}{2M_A}\nabla_A^2, \tag{2.11b}$$

$$\hat{V}_{\mathrm{el,el}}(\mathbf{r}) = \frac{1}{4\pi\epsilon_0}\sum_{i>j}^{\mathrm{elec}}\frac{e^2}{r_{ij}}, \tag{2.11c}$$

$$\hat{V}_{\mathrm{el,N}}(\mathbf{r},\mathbf{R}) = -\frac{1}{4\pi\epsilon_0}\sum_{A}^{\mathrm{nuc}}\sum_{i}^{\mathrm{elec}}\frac{Z_A e^2}{r_{Ai}}, \tag{2.11d}$$

$$\hat{V}_{\mathrm{N,N}}(\mathbf{R}) = \frac{1}{4\pi\epsilon_0}\sum_{A>B}^{\mathrm{nuc}}\frac{Z_A Z_B e^2}{R_{AB}}, \tag{2.11e}$$

where M and m indicate the masses of the nucleus and electron, respectively. In the Born-Oppenheimer approximation, the electronic Schrödinger equation, given by Eq. (2.4d) can describe the electronic motion using the Hamiltonian

$$\hat{\mathcal{H}}_{\mathrm{el}} = \hat{T}_{\mathrm{el}} + \hat{V}_{\mathrm{el,el}} + \hat{V}_{\mathrm{el,N}} + \hat{V}_{\mathrm{N,N}} \tag{2.12}$$

However, for many-electron systems, analytically solving the Schrödinger equation is nearly impossible and hence requires numerical methods and certain approximations.

2.4.1 Hartree-Fock Equations.

Computationally finding "correct" solutions to the many-body Schrödinger equation for larger systems is often unfeasible; instead, we try to obtain the "best" wave function. Thanks to the variational principle which provides a mechanism to calculate approximate solutions. According to this theorem, the energy associated with an approximate wave function will always be greater than or equal to the exact energy of the true wave function [77]. Therefore, the idea is to assume a trial wave function and minimize the expectation value of the Hamiltonian oper-

ator in each step of computation. For electrons, the trial wave function has to be antisymmetric since they are fermion and follow the Pauli exclusion principle. Typically, the wave function of an N-electrons system can be approximated by constructing the Slater determinants

$$\psi_{\mathrm{SD}}(1,2,\cdots,N)=\frac{1}{\sqrt{N!}}\begin{vmatrix}\psi_1(1) & \psi_2(1) & \cdots & \psi_N(1)\\ \psi_1(2) & \psi_2(2) & \cdots & \psi_N(2)\\ \vdots & \vdots & \ddots & \vdots\\ \psi_1(N) & \psi_2(N) & \cdots & \psi_N(N)\end{vmatrix}, \tag{2.13}$$

where single-electron wave functions are denoted by $\psi_i(j)$ and the factor $N!$ accounts for the normalization. In addition, the rows and columns of the determinant represent the electron label and spin-orbital, respectively. Utilizing the single Slater determinant, the total energy of the molecule can be obtained by employing the HF method

$$E_{\mathrm{HF}}=\sum_{i=1}^{N}h_i+\frac{1}{2}\sum_{i=1}^{N}\sum_{j=1}^{N}(J_{ij}+K_{ij})+V_{\mathrm{N,N}}, \tag{2.14}$$

where $\hat{h}_i=-\hbar^2/(2m_e)\nabla_i^2-1/(4\pi\epsilon_0)\sum_A^{\mathrm{nuc}}(Z_Ae^2/r_{Ai})$ is the one-electron operator. Furthermore, J_{ij} and K_{ij} refer to the two-particle terms accounting for the repulsive electron-electron Coulomb interaction energy and antisymmetric requirement of the electronic wave function. The explicit expression of the energy is given by

$$\begin{aligned}E_{\mathrm{HF}}=&\sum_{i=1}^{N}\langle\psi_i(1)|-\frac{\hbar^2}{2m_e}\nabla_i^2-\frac{1}{4\pi\epsilon_0}\sum_{A}^{\mathrm{nuc}}\frac{Z_Ae^2}{r_{Ai}}|\psi_i(1)\rangle\\&+\sum_{i=1}^{N}\sum_{j>1}^{N}\left[\langle\psi_i(1)\psi_j(2)|\frac{1}{r_{12}}\psi_i(1)\psi_j(2)\rangle+\langle\psi_i(1)\psi_j(2)|\frac{1}{r_{12}}\psi_j(1)\psi_i(2)\rangle\right]\\&+\sum_{A>B}^{\mathrm{nuc}}\frac{1}{4\pi\epsilon_0}\frac{Z_AZ_Be^2}{R_{AB}},\end{aligned} \tag{2.15}$$

where r_{12} and R_{AB} are the distances between two electrons and nuclei, respectively. The optimal solution of the system can be achieved from the solution of the set of HF equations

$$\hat{\mathcal{F}}_i \psi_i = \varepsilon_i \psi_i, \tag{2.16a}$$

$$\hat{\mathcal{F}}_i = \hat{h}_i + \sum_j^N (J_j - K_j), \tag{2.16b}$$

where the operator $\hat{\mathcal{F}}_i$ depends on spin orbital and generates a set of pseudo-eigenvalue equations that can be computed in successive iterations. ε_i is the associated energy of the spin-orbitals ψ_i that are usually expanded as a linear combination of the infinite basis set ϕ_ν as $\psi_i = \sum_\nu C_{i,\nu}\phi_\nu$, where $C_{i,\nu}$ denote coefficients of expansion. It is worth mentioning that such expansion must be truncated to obtain computationally feasible solutions. In summary, the HF method provides an approximate solution of the many-electron problem with a few essential simplifications: (a) Born-Oppenheimer approximations; (b) considering only non-relativistic effects; (c) determining energy eigenfunctions in terms of antisymmetric single-electron wave functions; (d) decomposing the solution into a linear combination of orthogonal basis functions; and (e) mean-field environment approximation.

2.4.2 Post-Hartee-Fock Methods.

In practice, the predicted energy by the HF method differs from the real lowest possible energy of the system even with a sufficiently large number of basis sets. To improve the accuracy of calculating the exact energy of the system, we first need to address the limitations of the HF method. The HF method captures electron-electron interactions in a mean-field approximation, which is an average effect. In order to obtain the exact energy of the system, we need to account for

the influence of repulsive interactions between electrons with opposite spin. The difference between the exact and predicted energy by the HF method is referred to as Electron Correlation (EC) energy [80, 81, 82]. As mentioned before, the HF method provides optimal single-determinant solution to determine the energy. However, adding more than the single-Slater determinant to the trial wave function can improve the accuracy. This is accomplished by writing the generic trial wave function

$$\psi_{\text{gen}} = a_0\psi_{\text{HF}} + \sum_i a_i\psi_i, \tag{2.17}$$

where ψ_{HF} is the HF wave function, a_0 denotes a normalization constant, and ψ_i is the Slater-determinant that can be determined self-consistently. Given a system with N electrons and M basis functions, we have $N/2$ occupied spin-orbitals and the $M - N/2$ unoccupied virtual spin-orbitals. Considering the excited states, a series of Slater determinants can be constructed by replacing occupied spin orbitals with unoccupied ones. Depending on how many occupied spin orbitals, such as one, two, three, etc., are replaced, the Slater determinant is labeled as singly, doubly, triply, etc., excited. Finally, we can incorporate these determinants into the trial wave function through electron correlation methods. However, the HF-method is not capable of accounting for the electron correlation, and therefore, we need to rely on alternative methods. Density Functional Theory (DFT) is one of the most popular approaches that can include EC in the computational methods.

2.4.3 Density Functional Theory.

The DFT approach becomes a matter of prime interest to the quantum-chemical calculations since the late 20th century [83, 84, 85]. Unlike HF-method which calculates the full wave function of a N-electron system, the central idea of DFT is to establish a relationship between the total energy of electrons and the density distribution of electrons. Earlier attempts at the Thomas-Fermi model turned

out to be poor in performance and the true potential of DFT was revealed by the findings of Hohenberg and Kohn [86]: the ground state energy and other properties can be uniquely determined by the electron density. Essentially, the goal shifted towards the calculation of electron density (function of only three spatial coordinates) instead of the wave function (depends on three spatial coordinates and one spin coordinate for each electron, i.e., 4N variables for an N-electron system). The second leading paper in the development of DFT, by Kohn and Sham [87], introduced a method for applying the Hohenberg and Kohn theorem to a chemical system. They reformulated the energy to include :

- the kinetic energy (analogous to the HF method) containing the non interacting term (T_{S}) and a correction term in the Exchange-Correlation (XC) term;
- the electron-nuclear interaction energy ($E_{\mathrm{el,N}}$);
- the electron-electron interaction energy containing the Coulomb interaction (J) and XC term (E_{XC}).

Thus, the geneal expression of the DFT energy [77] becomes

$$E_{\mathrm{DFT}}[\rho(\mathbf{r})] = T_{\mathrm{S}}[\rho(\mathbf{r})] + E_{\mathrm{el,N}}[\rho(\mathbf{r})] + J[\rho(\mathbf{r})] + E_{\mathrm{XC}}[\rho(\mathbf{r})], \tag{2.18}$$

where $\rho(\mathbf{r})$ indicates the electron density and

$$E_{\mathrm{XC}}[\rho(\mathbf{r})] = (T[\rho(\mathbf{r})] - T_{\mathrm{S}}[\rho(\mathbf{r})]) + (E_{\mathrm{el,el}}[\rho(\mathbf{r})] - J[\rho(\mathbf{r})])\,. \tag{2.19}$$

Note that, E_{XC} has two parts: (i) kinetic correlation energy (in the first parenthesis); (ii) potential correlation plus exchange energy (in the second parenthesis). Clearly, finding the XC term is crucial in determining the total energy function. The accuracy of DFT calculations through different approaches depends on the

choice of computing XC functionals. Jacob's Ladder [88] provides a framework to choose the most appropriate approximation method relative for specific purposes.

The simplest method is the Local Density Approximation (LDA), which considers uniform electron density all over the space, and the XC energy is divided into exchange ($E_{\mathrm{X}}^{\mathrm{LDA}}$) and correlation terms ($E_{\mathrm{C}}^{\mathrm{LDA}}$) as

$$E_{\mathrm{XC}}^{\mathrm{LDA}} = E_{\mathrm{X}}^{\mathrm{LDA}} + E_{\mathrm{C}}^{\mathrm{LDA}}. \tag{2.20}$$

For homogeneous electron gas model, the Dirac formula [77] provides a simple formula of exchange functional

$$E_{\mathrm{X}}^{\mathrm{LDA}}[\rho(\mathbf{r})] = C_{\mathrm{X}} \int \rho^{4/3}(\mathbf{r}) d\mathbf{r}, \tag{2.21}$$

where C_{X} is a constant. For the correlation functional, there are several expressions [89, 90, 91] based on fitting accurate quantum chemical calculation results. However, a few sophisticated approximations have been developed to improve accuracy. Generalized Gradient Approximation (GGA), which includes the dependence on the first derivative of density, meta-GGA (incorporates higher-order derivatives), hybrid-GGA (includes a portion of exact exchange energy from the HF method), and Møller-Plesset second-order perturbation theory (Double Hybrid Methods) are on the list. A popular hybrid functionals, B3LYP (Becke, three-parameter, Lee-Yang-Parr)[92, 93, 94] provides exchange-correlation functional as

$$E_{\mathrm{XC}}^{\mathrm{B3LYP}} = E_{\mathrm{XC}}^{\mathrm{LDA}} + a_0(E_{\mathrm{X}}^{\mathrm{HF}} - E_{\mathrm{X}}^{\mathrm{LDA}}) + a_x(E_{\mathrm{X}}^{\mathrm{GGA}} - E_{\mathrm{X}}^{\mathrm{LDA}}) + a_c(E_{\mathrm{C}}^{\mathrm{GGA}} - E_{\mathrm{C}}^{\mathrm{LDA}}), \tag{2.22}$$

where a_0, a_x and a_c are empirical fitting parameter [95]. $E_{\mathrm{X}}^{\mathrm{HF}}$ is the HF exact exchange functional. $E_{\mathrm{X}}^{\mathrm{GGA}}$ refers to the Becke 88 exchange functional[96] and $E_{\mathrm{C}}^{\mathrm{GGA}}$ is the correlation functional of Lee, Yang and Parr [97]. and $E_{\mathrm{C}}^{\mathrm{LDA}}$ refers to the LDA correlation functional of Vosko-Wilk-Nusair [90].

2.4.4 Time-Dependent Density Functional Theory.

The ground-state properties of electrons in the presence of time-independent potential are well explained by DFT based on the Hohenberg-Kohn theorem. However, to deal with time-dependent potential and excitation problems, we need to extend DFT, and the Runge-Gross theorem provides a formal foundation of Time-Dependent Density Functional Theory (TDDFT). In both time-dependent and time-independent cases, the Runge-Gross theorem [98] states that the one-to-one correspondence between the external potential of a quantum mechanical system and the electron density can be established for a given initial state. Considering a time-dependent external electric potential $\hat{V}_{\text{ext}}(\mathbf{r}, t)$, the time-dependent Schrödinger equation is given by [77]

$$i\frac{\partial}{\partial t}\psi_{\text{t}}(\mathbf{r}, t) = \hat{\mathcal{H}}(\mathbf{r}, t)\psi_{\text{t}}(\mathbf{r}, t), \tag{2.23a}$$

$$\hat{\mathcal{H}}(\mathbf{r}, t) = \hat{\mathcal{H}}_0(\mathbf{r}) + \hat{V}_{\text{ext}}(\mathbf{r}, t), \tag{2.23b}$$

where the time-dependent wave function $\psi_{\text{t}}(\mathbf{r}, t)$ can be written as a regular wave function $\Psi(\mathbf{r}, t)$ multiplied by a phase factor $e^{-i\omega t}$ [77]. $\hat{\mathcal{H}}_0(\mathbf{r})$ and $\hat{\mathcal{H}}(\mathbf{r}, t)$ are the time-independent and time-dependent Hamiltonian, respectively. Furthermore, $\hat{V}_{\text{ext}}(\mathbf{r}, t)$ denotes the external potential which is assumed to be activated at time t_0 and can be written as

$$\hat{V}_{\text{ext}}(\mathbf{r}, t) = \theta(t - t_0)\hat{V}_{\text{ext}}(\mathbf{r}, t), \tag{2.24}$$

where θ is the Heaviside step function defined as $\theta(t) = 0$ for $t < 0$ and $\theta(t) = 1$ for $t \geq 0$. The solution of the time-dependent Schrödinger equation can be expressed as

$$\psi(\mathbf{r}, t) = \hat{\mathcal{U}}(t, t_0)\psi(\mathbf{r}, t_0), \tag{2.25}$$

where $\hat{\mathcal{U}}(t,t_0) = \exp\left[-i\int_{t_0}^{t}\hat{\mathcal{H}}(\tau)d\tau\right]$ is the exponential time-evolution operator approximated as a sequence of time steps $\hat{\mathcal{U}}(t_0,\Delta t) \approx exp(-i\hat{\mathcal{H}}\Delta\tau)$, similar to the classical molecular dynamics. In the time-dependent case, the system is evolving with time and therefore, the energy of the system is also changing. Following a similar treatment to the variational principle for the time-independent case, the solution in the time-dependent case can be obtained from the stationary condition $\Delta S = 0$ for the action

$$S[\psi] = \int_{t_0}^{t}\langle\psi|\left(i\frac{\partial}{\partial t'} - \hat{\mathcal{H}}\right)|\psi\rangle dt'. \tag{2.26}$$

The time-dependent density can be determined from a set of orbitals (ϕ_i) of a non-interacting reference system. The wave function in such reference frame is a Slater determinant consisting Kohn-Sham orbitals that are evaluated by solving the time-dependent Kohn-Sham equations self-consistently [77]

$$i\frac{\partial}{\partial t}\phi_i(\mathbf{r},t) = (\hat{\mathcal{F}} + \hat{V}_{\text{ext}}(t))\phi_i(\mathbf{r},t), \tag{2.27a}$$

$$\rho(\mathbf{r},t) = \sum_{i=1}^{\mathrm{N}}\phi_i^2(\mathbf{r},t), \tag{2.27b}$$

where $\hat{\mathcal{F}}$ represents the Fock operator.

2.4.5 Linear response (Weak perturbation).

In general, time-dependent problems can be studied using TDDFT but for most practical applications, we consider weak perturbation to investigate linear response. In that regime, perturbation theory can be utilized instead of solving full time-dependent Schrödinger equation Eq. (2.27). In the dipole approximation, considering an oscillating field as the weak perturbation to the system, we can write

$$\hat{V}_{\text{ext}}(t) = \hat{\mu}F\cos(\omega t) \tag{2.28}$$

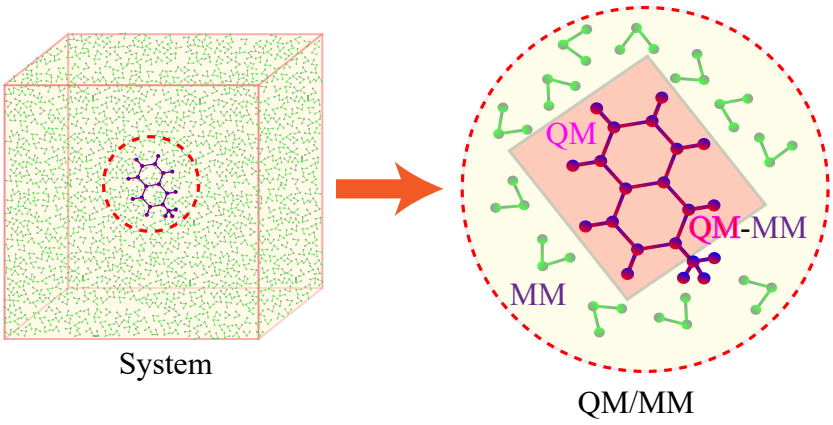


Figure 2.4: Schematic representation of hybrid Quantum Mechanics(QM)/Molecular Mechanics(MM) partitioning of a molecular system.

Here $\hat{\mu}$ is the dipole operator, ω and F are the frequency and strength of the field, respectively. The first-order response is obtained by solving eigenvalue problems leading to the calculations of excitation and de-excitation energies. The eigenvalue problem is expresses as follows

$$\begin{bmatrix} \mathbf{A} & \mathbf{B} \\ \mathbf{B}^* & \mathbf{A}^* \end{bmatrix} \begin{bmatrix} \mathbf{Y} \\ \mathbf{Z} \end{bmatrix} = \omega \begin{bmatrix} 1 & 0 \\ 0 & -1 \end{bmatrix} \begin{bmatrix} \mathbf{Y} \\ \mathbf{Z} \end{bmatrix}. \tag{2.29}$$

The real and imaginary parts of the first-order response are represented by the vector $(\mathbf{Y}, \mathbf{Z})$. The elements of matrix $\mathbf{A}$ correspond to orbital energy difference between an occupied (ij) and virtual $(i'j')$ orbitals together with electron-electron interaction differences on alternating orbital occupancy. The elements of matrix $\mathbf{B}$ correspond to interaction between different electronic transitions.

$$A_{ij}^{i'j'} = \delta_{ij}\delta_{i'j'}(\varepsilon_{i'} - \varepsilon_i) + \langle \phi_i \phi_j | \phi_{i'} \phi_{j'} \rangle - \langle \phi_i \phi_{i'} | \phi_j \phi_{j'} \rangle, \tag{2.30a}$$

$$B_{ij}^{i'j'} = \langle \phi_i \phi_j | \phi_{i'} \phi_{j'} \rangle - \langle \phi_i \phi_j | \phi_{j'} \phi_{i'} \rangle, \tag{2.30b}$$

where ε_i and $\varepsilon_{i'}$ correspond to the energies of the i-th and i'-th orbitals. The TDDFT formalism enables calculations of ground and excited state energies.

2.5 Quantum Mechanics/Molecular Mechanics.

The Quantum Mechanics (QM)/Molecular Mechanics (MM) [99, 100] method is a popular hybrid computational tool to study complex biochemical systems. MM is efficient to study large molecular systems through MD simulation based on empirical force fields. However, bond breaking/forming during a chemical reaction cannot be captured by such force fields due to their inherent limitations. On the other hand, QM provides accurate descriptions of electronic properties and chemical reactions. But, quantum chemical computation is very costly and typically limited to investigating relatively small systems. The combination of MM and QM fulfills demands for both speed and accuracy. Within the QM/MM method, the active region of interest is investigated through QM calculations, and the rest of the system is studied classically. This kind of strategy is illustrated in Fig. 2.4. This hybrid method can be implemented through a subtractive scheme [101, 102, 103] by dividing the problem into three parts that are performed independently. The partition can be done as follows:

- the entire system is examined through MM calculation;
- the QM region is examined through QM calculation;
- the QM region is examined through MM calculation.

In turn, the expression of total energy ($E_{\text{sub}}^{\text{QM/MM}}$) becomes

$$E_{\text{sub}}^{\text{QM/MM}}(\text{QM}+\text{MM}) = E^{\text{QM}}(\text{QM}) + E^{\text{MM}}(\text{QM}+\text{MM}) - E^{\text{MM}}(\text{MM}), \quad (2.31)$$

where the considered region of the system is put in the parenthesis and the superscript denotes the subsequent level of calculation. The subtractive scheme is simpler because of the absence of coupling terms, and therefore, MM and QM calculations can be performed without any complications.

Another QM/MM treatment is the additive scheme [104, 105], which provides detailed treatment of the interaction between QM and MM regions. The energy in that case is given by

$$E_{\text{add}}^{\text{QM/MM}}(\text{QM}+\text{MM}) = E^{\text{QM}}(\text{QM}) + E^{\text{MM}}(\text{MM}) + E^{\text{QM-MM}}(\text{QM}+\text{MM}), \tag{2.32a}$$

$$E^{\text{QM-MM}} = E_{\text{el}}^{\text{QM-MM}} + E_{\text{VdW}}^{\text{QM-MM}} + E_{\text{bond}}^{\text{QM-MM}}, \tag{2.32b}$$

with the coupling energy $E^{\text{QM-MM}}$ which includes electrostatic $E_{\text{el}}^{\text{QM-MM}}$, Van-der-Walls $E_{\text{VdW}}^{\text{QM-MM}}$ interactions energy between atoms in QM and MM region, and the bonded energy $E_{\text{bond}}^{\text{QM-MM}}$. The Van-der-Waals and bonded energy contributions can be determined by force fields, while electrostatic interactions are addressed through different approaches. One technique is to introduce electrostatic embedding in the QM calculation of QM region. The strategy is to assume the effect of fixed charges in MM region as perturbation to the total Hamiltonian of QM region. Meaning that, the polarization of the QM region driven by the electric field produced by the fixed charges in MM region is considered as perturbation. Therefore, the additional term that we have to add with the Hamiltonian in QM calculation is given by [105]

$$\hat{\mathcal{H}}_{\text{el}}^{\text{QM-MM}} = -\sum_{i}^{N}\sum_{J}^{M}\frac{q_J e}{|\mathbf{r}_i - \mathbf{R}_J|} + \sum_{A}^{L}\sum_{J}^{M}\frac{q_J Z_A}{|\mathbf{R}_A - \mathbf{R}_J|} \tag{2.33}$$

where the indices i, J, and A are summed over the total number of electrons (N) in QM , atoms (M) in MM , and nuclei (L) in QM, respectively. The charge of the J-th atom in MM, located at $\mathbf{R}_J$, is denoted by q_J. The charge of the A-th nucleus in QM, located at $\mathbf{R}_A$, is denoted by Z_A, and r_i refers to the position of i-th electron in QM. Such an approach is computationally efficient.

However, the mutual polarization between QM and MM is not accounted

for. To include this contribution, one can follow other schemes, like polarized-embedding, where fluctuating charges [106], Drude oscillators[107], point dipoles or multipoles [108, 109, 110] are considered instead of fixed point charges. In addition, it's difficult to define a QM-MM boundary when the QM and MM regions are connected through a covalent bond. One way to overcome this problem is to couple two regions with link atoms or to use frozen hybridized orbitals or boundary atoms [111].

2.6 Perturbed Matrix Method.

The hybrid QM/MM approach has been well adopted in the MD-Perturbed Matrix Method (PMM) [112, 113, 114, 115] for investigating molecular systems at an efficient computational cost. In the MD-PMM method, the MD simulation provides MM calculations, and the QM region is considered as the Quantum Center (QC), which is subjected to the perturbing environment of the MM region. In turn, the perturbed electronic wave functions of the system can be calculated by applying a small perturbing external field to the Hamiltonian. Considering the perturbation energy operator ($\hat{\mathcal{V}}$) accounted for the interaction between the QC and its surroundings, the electric Hamiltonian operator ($\hat{\mathcal{H}}$) of the QC can be constructed as:

$$\hat{\mathcal{H}} = \hat{\mathcal{H}}_0 + \hat{\mathcal{V}}, \tag{2.34}$$

where $\hat{\mathcal{H}}_0$ indicates the unperturbed electronic Hamiltonian operator of the QC. The time-independent Schrödinger equation describing the perturbed system is expressed in matrix notation as

$$\mathcal{H}c_j = \mathcal{U}_j c_j, \tag{2.35}$$

where $\mathcal{H}$ is the perturbed Hamiltonian matrix. c_j and $\mathcal{U}_j$ refer to the j-th eigenvector of $\mathcal{H}$ matrix and the corresponding Hamiltonian eigenvalue, respectively. We can express $\mathcal{H}$ and $\mathcal{U}_j$ in terms of the basis set of unperturbed eigenstates (Φ_n^0) of the unperturbed Hamiltonian matrix. Thus, we obtain

$$\Phi_j = \sum_n^{\infty} c_{j,n}^0 \Phi_n^0, \tag{2.36a}$$

$$[\mathcal{H}]_{n,n'} = \langle \Phi_n^0 | \hat{\mathcal{H}} | \Phi_{n'}^0 \rangle = \mathcal{U}_n^0 \delta_{n,n'} + \langle \Phi_n^0 | \hat{\mathcal{V}} | \Phi_{n'}^0 \rangle, \tag{2.36b}$$

where $c_{j,n}^0$ are the expansion coefficients, $\mathcal{U}_n^0$ are the eigenvalues of unperturbed Hamiltonian and $\delta_{n,n'}$ is the Kronecker delta. Note that the $\langle \Phi_n^0 | \hat{\mathcal{V}} | \Phi_{n'}^0 \rangle$ term arises because of the interaction between QC and the surrounding. Such interaction can be determined from the MD simulation trajectory. Moreover, to extract all the properties of the perturbed system, we need to diagonalize the $\mathcal{H}$ matrix. In turn, we can calculate the eigenvalues and corresponding eigenvectors of the perturbed Hamiltonian. Thus, we obtain all the properties of the system containing the QC surrounded by the environment.

The perturbation imposed on QC due to the environment can be equivalently thought of as a perturbation caused by an external field that is created by the charge density of the semiclassical atomic-molecular environment. Based on this approximation, we can write the perturbation energy operator as

$$\hat{\mathcal{V}} = \sum_i V(\mathbf{r}_i) q_i. \tag{2.37}$$

The summation over i accounts for all the particles of interest in QC, and V is the electric potential associated with the perturbing environment. In addition, the charge and coordinate of the i-th particle (in QC) are denoted by q_i and $\mathbf{r}_i$, respectively. Considering the center of mass of the QC as a reference position, we

can expand the perturbing electric potential

$$V(\mathbf{r}) = V(\mathbf{r}_0) - \mathbf{E}(\mathbf{r}_0)\cdot(\mathbf{r}-\mathbf{r}_0) - \frac{1}{2}\sum_{k=1}^{3}\sum_{k'=1}^{3}\left(\frac{\partial E_k}{\partial r_{k'}}\right)_{\mathbf{r}=\mathbf{r}_0}(r_k - r_{0,k})\,(r_{k'} - r_{0,k'}) + ..., \tag{2.38}$$

where the index k refers to the Cartesian components and $\mathbf{E} = -\partial V/\partial \mathbf{r}$ is the electric field. Finally, substituting Eq. (2.38) in Eq. (2.37) and inserting the perturbation energy operator $\hat{\mathcal{V}}$ in Eq. (2.36b), we get

$$[\mathcal{H}]_{n,n'} = \mathcal{U}_n^0\delta_{n,n'} + V(\mathbf{r}_0)q_T\delta_{n,n'} - \mathbf{E}(\mathbf{r}_0)\cdot\langle\Phi_n^0|\hat{\boldsymbol{\mu}}|\Phi_{n'}^0\rangle + \frac{1}{2}\mathrm{Tr}[\Theta\mathcal{Q}_{n,n'}] + ..., \tag{2.39}$$

where,

$$q_T = \sum_i q_i, \tag{2.40a}$$

$$\hat{\boldsymbol{\mu}} = \sum_i q_i(\mathbf{r}_i - \mathbf{r}_0), \tag{2.40b}$$

$$[\Theta]_{k,k'} = -\left(\frac{\partial E_k}{\partial r_{k'}}\right)_{\mathbf{r}=\mathbf{r}_0}, \tag{2.40c}$$

$$[\mathcal{Q}_{n,n'}] = \sum_i q_i\langle\Phi_n^0|\,(r_k - r_{0,k})\,(r_{k'} - r_{0,k'})\,|\Phi_{n'}^0\rangle. \tag{2.40d}$$

Note that one can consider dipole (up to the term incorporating the QC dipole operator $\hat{\boldsymbol{\mu}}$) and quadruple (up to the term incorporating the QC quadrupole matrices expressed in terms of eigenstates basis set $[\tilde{\mathcal{Q}}_{n,n'}]$ of unperturbed QC) contributions by including corresponding approximation of the perturbation operator. Therefore, in the dipole approximation, one gets[112, 113]

$$[\mathcal{H}]_{n,n'} \cong \mathcal{U}_n^0\delta_{n,n'} + V(\mathbf{r}_0)q_T\delta_{n,n'} - \mathbf{E}(\mathbf{r}_0)\cdot\langle\Phi_n^0|\hat{\boldsymbol{\mu}}|\Phi_{n'}^0\rangle, \tag{2.41}$$

while, in the quadrupole approximation, one gets[116]

$$[\mathcal{H}]_{n,n'} \cong \mathcal{U}_n^0 \delta_{n,n'} + V(\mathbf{r}_0) q_T \delta_{n,n'} - \mathbf{E}(\mathbf{r}_0) \cdot \langle \Phi_n^0 | \hat{\boldsymbol{\mu}} | \Phi_{n'}^0 \rangle + \frac{1}{2} \mathrm{Tr}[\Theta \mathcal{Q}_{n,n'}]. \tag{2.42}$$

Such an approximation based on QC expansion provides reasonable results for many systems[117, 118, 119]. However, for large and complex systems, further improvement in the accuracy demands incorporation of atomistic details [114] into the MD-PMM method.

2.6.1 Atom based expansion.

In the atom-based expansion, we further write the perturbing potential in terms of atomic regions (meaning an isolated spatial zone centered around each nucleus) in the proper QC space, $\mathcal{R}^3_{QC}$. Here, the proper QC space refers to the Cartesian subspace that includes all the QC nuclei and all the substantial spatial coordinates accessible to the QC electrons. With reasonable assumption that there is no significant electron density outside the atomic region, we can reformulate the potential as

$$V(\mathbf{r}_i) \cong \sum_N \Omega_N(\mathbf{r}) V(\mathbf{r}_i); \qquad \mathbf{r} \in \mathcal{R}^3_{QC}, \tag{2.43}$$

where the sum over N refers to all QC atoms and each Ω_N describes a step function (i.e., Ω_N= 0 on the outside and = 1 inside the N-th atomic region). Now, expanding the perturbing electric potential inside the range of each N-th atomic region centered on the respective atomic center $\mathbf{R}_N$ and substituting in Eq. (2.37), we obtain

$$\hat{\mathcal{V}} \cong \sum_N \sum_i \Omega_N(\mathbf{r}_i) \Big[V(\mathbf{R}_N) - E(\mathbf{R}_N) \cdot (\mathbf{r}_i - \mathbf{R}_N) + ... \Big] q_i \tag{2.44}$$

Thus, the perturbed matrix elements for a QC with non-zero atomic charges are then given by

$$[\mathcal{H}]_{n,n'} \cong \mathcal{U}_n^0 \delta_{n,n'} + \sum_N V(\mathbf{R}_N)\langle\Phi_n^0|\hat{q}_N|\Phi_{n'}^0\rangle - \sum_N \mathbf{E}(\mathbf{R}_N)\cdot\langle\Phi_n^0|\hat{\boldsymbol{\mu}}_N|\Phi_{n'}^0\rangle + \Delta\mathcal{V}\delta_{n,n'}, \tag{2.45}$$

where the atomic charge $\hat{q}_N$ and dipole $\hat{\boldsymbol{\mu}}_N$ operator of N-th atom are given by

$$\hat{q}_N = \sum_i \Omega_N(\mathbf{r}_i) q_i, \tag{2.46a}$$

$$\hat{\boldsymbol{\mu}}_N = \sum_i \Omega_N(\mathbf{r}_i) q_i (\mathbf{r}_i - \mathbf{R}_N). \tag{2.46b}$$

Note that, we consider terms up to dipole approximation in the Eq. (2.45) since the expansion was performed within each small atomic region. All the terms beyond the atomic dipolar ones are included in the nuclear position function $\Delta\mathcal{V}$. Furthermore, $\langle\Phi_n^0|\hat{q}_N|\Phi_{n'}^0\rangle$ refers to the n-th unperturbed electronic eigenstate atomic charges, and the electron density of such an unperturbed electronic eigenstate within each atomic region can be considered symmetric around the nucleus. Meaning that corresponding unperturbed atomic dipoles can be neglected, i.e., $\langle\Phi_n^0|\hat{\boldsymbol{\mu}}_N|\Phi_{n'}^0\rangle \cong 0$. In turn, the most widely followed Hamiltonian in the atom-based expansion is given by

$$[\mathcal{H}]_{n,n'} \cong \mathcal{U}_n^0 \delta_{n,n'} + \sum_N V(\mathbf{R}_N)\langle\Phi_n^0|\hat{q}_N|\Phi_{n'}^0\rangle. \tag{2.47}$$

Generally, in practical applications, various levels of theory [114] facilitated by the PMM framework can be employed. Here we mention four PMM implementations to calculate the Hamiltonian matrix:

- Considering QC as a reference, the expansion of the perturbation operator within the dipolar approximation as given by Eq. (2.41);

- Considering QC as a reference, the expansion of the perturbation operator within the quadrupole approximation as given by Eq. (2.42);

- Combination of the atom-based expansion of the perturbation operator to calculate diagonal elements of $\mathcal{H}$ and the QC-based expansion of the perturbation operator within dipole approximation to calculate off-diagonal elements of $\mathcal{H}$ in the following way

$$\begin{aligned}[\mathcal{H}]_{n,n'} \cong & \Big\{\mathcal{U}_n^0 + \sum_N V(\mathbf{R}_N)\langle\Phi_n^0|\hat{q}_N|\Phi_{n'}^0\rangle\Big\}\delta_{n,n'} \\ & - \mathbf{E}(\mathbf{R}_0)\cdot\langle\Phi_n^0|\hat{\boldsymbol{\mu}}|\Phi_{n'}^0\rangle(1-\delta_{n,n'});\end{aligned} \tag{2.48}$$

- Combination of the atom-based expansion of the perturbation operator to calculate diagonal elements of $\mathcal{H}$ and the QC-based expansion of the perturbation operator within quadrupole approximation to calculate off-diagonal elements of $\mathcal{H}$ in the following way

$$\begin{aligned}[\mathcal{H}]_{n,n'} \cong & \Big\{\mathcal{U}_n^0 + \sum_N V(\mathbf{R}_N)\langle\Phi_n^0|\hat{q}_N|\Phi_{n'}^0\rangle\Big\}\delta_{n,n'} \\ & + \Big\{ - \mathbf{E}(\mathbf{R}_0)\cdot\langle\Phi_n^0|\hat{\boldsymbol{\mu}}|\Phi_{n'}^0\rangle + \frac{1}{2}\mathrm{Tr}[\tilde{\Theta}\tilde{\mathcal{Q}}_{n,n'}]\Big\}(1-\delta_{n,n'}).\end{aligned} \tag{2.49}$$

In summary, employing the MD-PMM approach, the instantaneous perturbed quantum chemical observables of the QC can be obtained through the denationalization of the perturbed electronic Hamiltonian matrix at each MD frame, providing the trajectory of the perturbed eigenvalues and eigenvectors $\mathbf{c}_{j,n}(t)$ as described by Eq. (2.36a). For example, we can probe the spectral signal associated with the $i \to j$ transition by evaluating the corresponding perturbed electric ($\mathbf{d}_{i,j}$) and magnetic ($\mathbf{m}_{i,j}$) transition dipole moments. This is accomplished by applying the electric $\hat{\mathbf{d}}$ and magnetic $\hat{\mathbf{m}}$ dipole operator on the perturbed eigenvectors. In turn,

we get

$$d_{k,(i,j)} = \mathbf{c}_i^{*\mathrm{T}} \tilde{d}_k^0 \mathbf{c}_j \tag{2.50a}$$

$$[\tilde{d}_k^0]_{n,n'} = \langle \Phi_n^0 | \hat{\mathbf{d}}_k | \Phi_{n'}^0 \rangle \tag{2.50b}$$

$$m_{k,(i,j)} = \mathbf{c}_i^{*\mathrm{T}} \tilde{m}_k^0 \mathbf{c}_j \tag{2.50c}$$

$$[\tilde{m}_k^0]_{n,n'} = \langle \Phi_n^0 | \hat{\mathbf{m}}_k | \Phi_{n'}^0 \rangle \tag{2.50d}$$

where $[d_k^0]_{n,n'}$ and $[m_k^0]_{n,n'}$ matrices correspond to the electric and magnetic dipole operators, respectively, in the Φ_n^0 basis set (i.e., the unperturbed dipole moments). In addition, d_k^0 and m_k^0 are the k-th Cartesian component of electric and magnetic dipole moment matrices, respectively.

2.7 Modeling of absorption spectra.

In this section, we discuss the calculation of absorption spectra of the QC (embedded in an atomic-molecular environment) using the perturbed eigenvectors, eigenvalues, and instantaneous quantum observables that are obtained through the MD-PMM approach. Let's consider a perturbed excitation involving the m-th vibronic transition associated with the $0 \rightarrow i$ electronic excitation. Meaning that the vibronic transition occurs from the vibronic ground state ($\Phi_0\phi_{0,0}$) to the m-th vibrational eigenstate ($\Phi_i\phi_{i,m}$) of the i-th electronic excited state, where ϕ represents the vibrational eigenstates. In practice, we can reasonably consider a relevant vertical vibronic transition, and the statistical ensemble state distribution of the QC environment can be sampled by using a sufficiently large number of MD-trajectory frames. The general expression of the extinction coefficient describing

the complete vibronic spectral signal is given by [114]

$$\varepsilon^m_{0,i}(\nu) \cong \sum_{\nu^m_{\mathrm{Ref}}} \frac{\Gamma_{\mathrm{Abs}}(\nu^m_{\mathrm{Ref}}) n(\nu^m_{\mathrm{Ref}}) h\nu}{N_{\mathrm{frame}}} \frac{e^{-(\nu-\nu^m_{\mathrm{Ref}})^2/(2\sigma^2)}}{\sigma\sqrt{2\pi}}, \tag{2.51a}$$

$$\Gamma_{\mathrm{Abs}}(\nu^m_{\mathrm{Ref}}) = |\langle\phi^0_{0,0}|\phi^0_{i,m}\rangle|^2_{\nu^m_{\mathrm{Ref}}} \frac{|\boldsymbol{\mu}_{0,i}|^2_{\nu^m_{\mathrm{Ref}}}}{6\epsilon_0 c\hbar^2}, \tag{2.51b}$$

where c, ϵ_0, and h are the light speed, vacuum permittivity, and the Plank constant ($\hbar = h/2\pi$), respectively. The summation runs over the the frequency bins used to generate the spectrum and ν^m_{Ref} are the middle value of such bins, representing m-th vibronic transition frequencies. The total number of MD-trajectory frames is denoted by N and $n(\nu^m_{\mathrm{Ref}})$ refers to the number of MD frames associated with m-th vibronic transition frequency ν within the considered bin centered at ν^m_{Ref}. $|\boldsymbol{\mu}_{0,i}|^2_{\nu^m_{\mathrm{Ref}}}$ is the corresponding mean electronic vertical transition dipole square length obtained by averaging over the MD frames associated to the bin. $|\langle\phi^0_{0,0}|\phi^0_{j_i,m}\rangle|^2_{\nu^m_{\mathrm{Ref}}}$ is the square norm of the overlap of the unperturbed vibrational eigenstate obtained by averaging over the bin frames. $\phi^0_{0,0}$ and $\phi^0_{i,m}$ are the vibrational ground (of the unperturbed electronic groundstate which is virtually equivalent to the perturbed one) and m-th (of i-th unperturbed electronic eigenstate) eigenstates, respectively. The Gaussian distributions with the center at ν^m_{Ref} are introduced to approximate the broadening effects (beyond the homogeneous broadening) caused by the QC semiclassical vibrations that are not considered in PMM since they are typically negligible in electronic excitations. For simplicity, we can assume a constant variance (σ) for all the possible conformations and possibly estimate it from a set of unperturbed electronic excitation energies associated with unperturbed QC configurations characterized by MD sampling [114]. In the vertical vibronic transition approximation including unitary vibrational overlap, we obtain the extinction coefficient for $\Phi_0 \rightarrow \Phi_i$ electronic excitation (providing transition dipole $\langle\Phi_0|\hat{\boldsymbol{\mu}}||phi_i\rangle = \boldsymbol{\mu}_{0,i}$) from the general expression of complete vibronic spectrum

Eq. (2.51b)[117]. Thus, we get

$$\varepsilon_{0,i}(\nu) \cong \sum_{\nu_{\text{Ref}}} \frac{\Gamma_{\text{Abs}}(\nu_{\text{Ref}}) n(\nu_{\text{Ref}}) h\nu}{N_{\text{frame}}} \frac{e^{-(\nu-\nu_{\text{Ref}})^2/(2\sigma^2)}}{\sigma\sqrt{2\pi}}, \tag{2.52a}$$

$$\Gamma_{\text{Abs}}(\nu_{\text{Ref}}) = \frac{|\boldsymbol{\mu}_{0,i}|^2_{\nu_{\text{Ref}}}}{6\epsilon_0 c\hbar^2}. \tag{2.52b}$$

Now, the summation runs over the the frequency bins centered at ν_{Ref} (the reference frequency) and $n(\nu_{\text{Ref}})$ refers to the number of MD frames associated with electronic excitation frequency ν. $|\boldsymbol{\mu}_{0,i}|^2_{\nu_{\text{Ref}}}$ is the corresponding mean electronic vertical transition dipole square length obtained by averaging over the MD frames associated to the bin.

2.8 Electronic structure of chiral drugs: Computational details and results.

In this section, we present a brief description of the computational details for the calculations of quantum molecular observables (electric/magnetic transition dipole moments, ground and electronic excitation energies, and their corresponding static electric dipole moments) for each of the four systems involved in this work:

1. **Reparixin** dissolved in water,
2. **Reparixin** dissolved in a mixture of acetonitrile and water (with a 50:50 volume ratio),
3. **Levodropropizine** dissolved in a mixture of ethanol and hexane (with a 40:60 volume ratio),
4. **Ladarixin** dissolved in water.

The modeling of electronic spectral signals for all four chiral drug solutions is based on the above-mentioned MD-PMM method. For each system, we start

with MD simulation to explore extensive configurational space and carefully select relevant molecular geometry which we will refer to as "*conformation*" hereafter. Subsequently, we perform TDDFT to calculate the unperturbed eigenfunctions of the QC, and the perturbation effect of the solvent is incorporated in the MD-PMM through constrained-MD simulation (performed only accounting for the dynamics of the solvent while keeping the QC fixed for a particular conformation). Finally, the MD-PMM method provides the perturbed eigenvalues and eigenfunctions of the QC at each MD frame. The absorption spectra are then obtained by calculating the extinction coefficients at each frequency bin and reconstructing them through Gaussian smoothing. The ensemble averages of all quantum molecular observables (including the spectra) are calculated by incorporating the statistical weight of individual conformations. In Fig. 2.5, we present the schematic flowchart of the adopted computational technique, which is discussed in the subsequent sections.

2.8.1 MD-Simulation details.

STEP-1: First, we performed a MD simulation of the chiral drug solution with the free software GROMACS [120](version 5.1.2), widely used to design biochemical molecules e.g., proteins, lipids, and nucleic acids and non-biological systems like polymers. The topology of the molecules and the force parameters (Gromos force field, version G53a6) were collected from Automatic Topology Builder sites [121]. We built the simulation box by placing the specific chiral molecule (Reparixin/Levodropropizine/Ladarixin) at the center of a cubic box filled with the respective solvents. The simulations were carried out in an NVT ensemble (constant number of molecules, volume and temperature) and spanned for 10 ns, setting 1.0 fs time step to rectord the the trajectories. In order to replicate the same average pressure exerted by the solvent computed through MD simulations of the same number of solvent molecules excluding the solute (i.e., the chiral molecule) in the

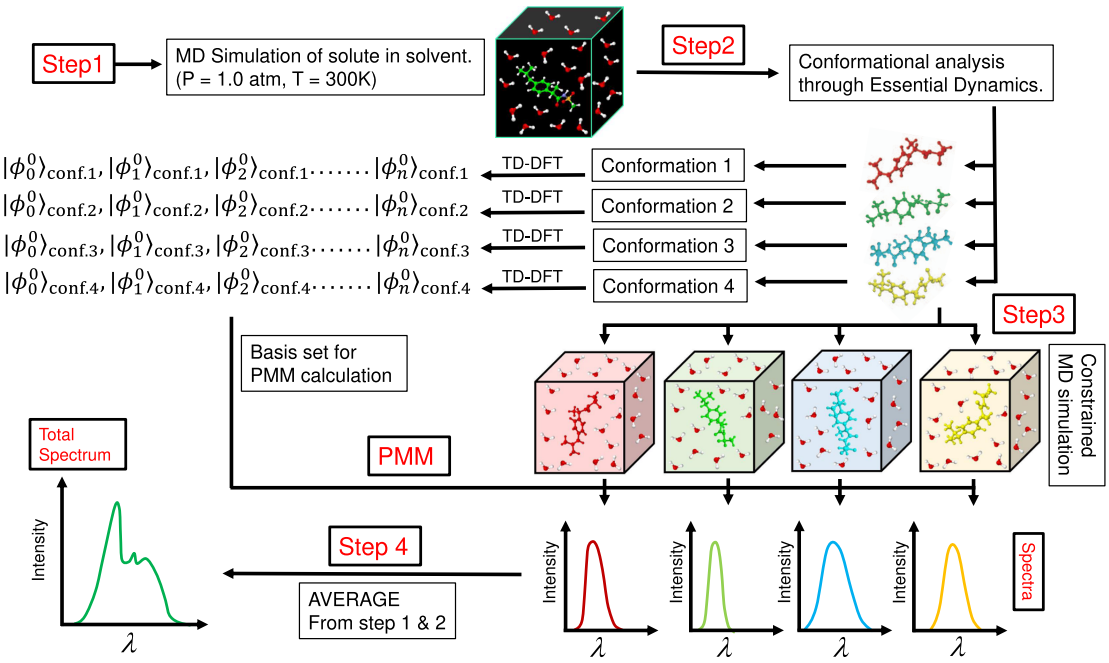


Figure 2.5: Schematic representation of the calculation of electronic spectra of chiral drug solutions. **Step 1**. Molecular Dynamics (MD) simulation of the chiral drug in specific solution. **Step 2**. (2a) Conformational analysis of the MD-trajectory through Essential Dynamics (ED) (see main text). (2b) Time-Dependent Density Functional Theory (TDDFT) calculation for each relevant conformation state selected in the ED, which provides the unperturbed basis set. **Step 3**. (3a) Constrained-MD simulation (keeping the solute frozen and allowing solvent dynamics) for each configuration states to evaluate the electric field experienced by the solute and exerted by the solvent. 3(b) Utilizing this electric field as perturbation together with the previously calculated unperturbed basis set, the Perturbed Matrix Method (PMM) (see main text) is applied to determine the instantaneous expectation value of quantum-molecular observables (e.g., electronic energy, electric dipoles, and electric or magnetic transition moments) at each MD-frame. **Step 4**. Finally, all the observables and the Ultraviolet (UV) spectrum of the entire system are calculated by incorporating the statistical probabilities of the respective conformations, assuming an ergodic behavior of the generated trajectories.

experimental environments (temperature, pressure, and density), we adjusted the density of the whole system and essentially the box size. The adjustment of the box size, and in turn, the density of the entire system, ensures the replication of the same average pressure calculated through MD simulations for the same number of solvent molecules (excluding the solute i.e., the chiral molecule) at their specific experimental conditions (temperature, pressure, and density). The tem-

perature was kept constant at 300 K by utilizing proper thermostat [79, 122] and all bond lengths were constrained by utilizing the LINCS algorithm [123]. For the long-range electrostatic interactions, the Particle mesh Ewald method (with 34 wave vectors in each dimension), a 4-th order cubic interpolation, 1.0 nm cut-off, and periodic boundary conditions were employed. After the end of each simulation, the molecule was re-centered in the middle of the simulation box by Using the trajectory to proceed with further analysis.

2.8.2 Essential Dynamics: analysis of MD trajectory.

STEP-2: In the given simulation conditions, the molecule undergoes conformational changes due to the rotations around bonds and other internal degrees of freedom, which play a significant role in the molecular functionalities, dynamics and interactions. The MD trajectory contains a series of snapshots (the coordinates of the system) over the simulation time, and to understand the most significant modes of motion within the conformational space, we need to analyze the trajectory. We analyzed the conformational repertoire spanned by the chiral molecules (Reparixin Levodropropizine and Ladarixin) by employing Essential Dynamics (ED) (also known as Principal Component Analysis)[124], a statistical analysis technique that effectively reduces the dimensionality of large data sets and recognizes the principal components of the modes. Typically, it is accomplished in three steps:

(i) The instantaneous geometry of the molecule at each MD simulation frame is fitted onto a reference structure to filter the internal motions from overall roto-translational motions by constructing a covariance matrix (of mass-weighted positional fluctuations over time)

$$C_{ij} = \langle \sqrt{M_{ii}} \left(x_i - \langle x_i \rangle\right) \sqrt{M_{jj}} \left(x_j - \langle x_j \rangle\right)^T \rangle \tag{2.53}$$

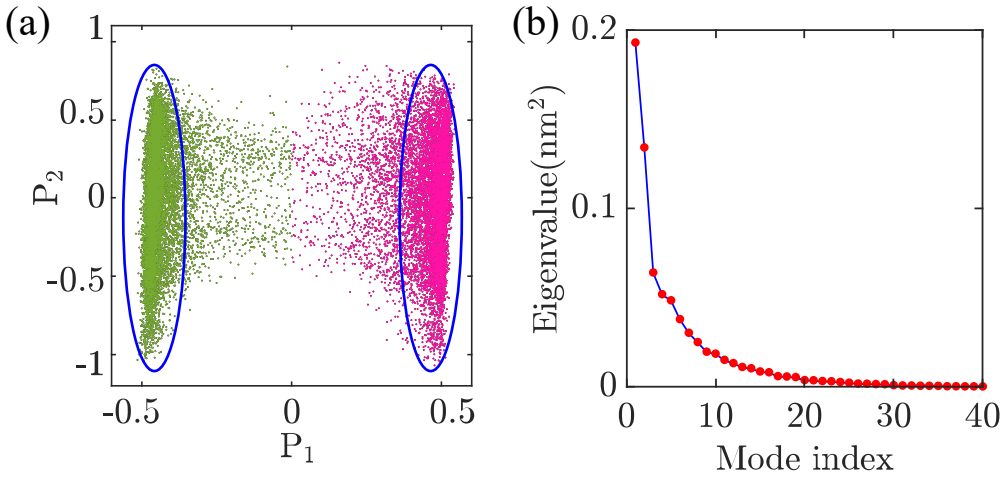


Figure 2.6: (**a**) Projection of the dynamics of chiral drug solution (specifically, pure R-Ladarixin dissolved in water) onto the first two principal components P_1 and P_2, indicating the co-existence of two statistically relevant conformation state basins. (**b**) Eigenvalues versus eigenvector index plot, calculated through Essential Dynamics (ED), where the most important modes of the dynamics are associated with the first two modes.

where the masses of atoms are included in the diagonal matrix M, x denotes the atomic coordinates, and $\langle\cdot\rangle$ represents the average value.

(ii) For a system of N atoms, the matrix C is a $3N \times 3N$ symmetric matrix, which is then diagonalized as

$$C = Q\Lambda Q^T \tag{2.54}$$

where Q is an orthogonal transformation matrix containing the eigenvectors (of C matrix) in the columns. These eigenvectors are also known as principal (or essential) modes. Λ is a diagonal matrix containing eigenvalues that represents the mean square fluctuations of principal components. The eigenvalues are sorted in order of decreasing value, and the first few eigenvectors represent the largest positional fluctuations [124] and, hence, the largest principal components that basically provide important collective motions of the molecule.

(iii) Finally, the trajectory, $\mathbf{x}(t)$ can be projected along the largest principal modes

$$\mathbf{P}(t) = Q^T\sqrt{M}\left(\mathbf{x}(t) - \langle\mathbf{x}\rangle\right), \tag{2.55}$$

with the largest eigenvalues **P** (typically 2 or 3). The molecular conformation states can be identified from the projection of molecular Cartesian coordinates onto the principal eigenvectors at each MD frame. Fig. 2.6 represents one such example of (**a**) the projections of position vectors of chiral drug solution (in particular, pure R-Ladarixin dissolved in water) onto the eigenvectors of the all-atom covariance matrix, indicating the co-existence of two distinct conformation state basins and (**b**) the most important modes calculated through ED. The molecular conformations associated with the most dense basins are then picked up for further calculations, and the density of each basis is used to calculate the relative free energies of different conformations.

2.8.3 Unperturbed quantum chemical calculations.

STEP-3: The quantum chemical calculations on the previously extracted geometries (sampled during ED) are then carried out to obtain unperturbed basis sets. This is accomplished through the DFT-based computations in Gaussian 09 [125] package. The computation involves the following steps:

(i) The extracted geometries (corresponding to each conformation) are first minimized in the gas phase using the hybrid B3LYP functional [92, 93, 94] along with the $6-31G^*$ basis set. During the minimization process, the internal coordinates associated with the molecule's essential eigenvectors (typically the torsion angles) were kept frozen in order to attain minimal errors in the subsequent calculations. The atomic charges of each molecule were also calculated by using the RESP procedure [126].

(ii) With the same functional, atomic basis set and package, we performed TDDFT calculations (in linear response approximation) on the optimized structures to obtain the unperturbed ground and first six excited states of each model of the molecule. The obtained unperturbed quantum observables (ground and excited energy states, static electric dipole moments associated with the energy

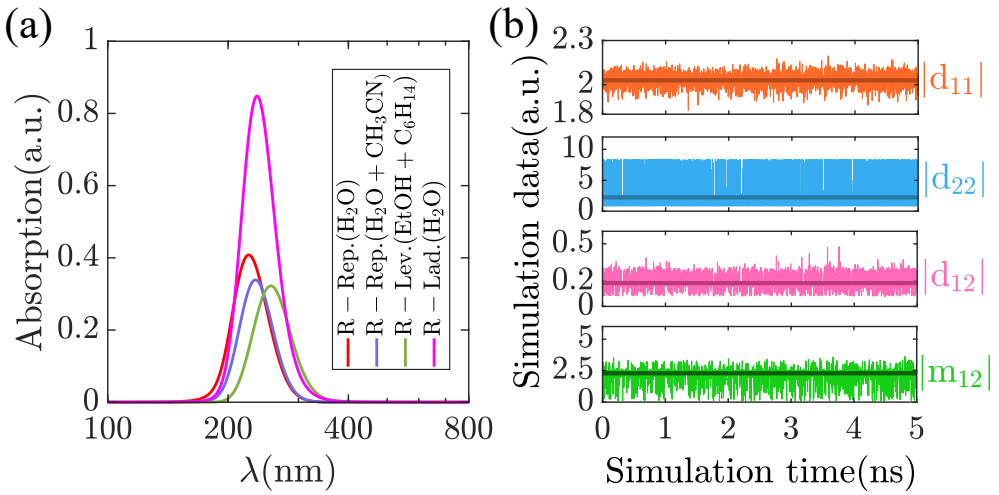


Figure 2.7: (**a**) UV-absorption spectra of the four systems involved in this work: pure R-Reparixin dissolved in water (H_2O), pure R-Reparixin dissolved in a mixed solvent of (H_2O) and acetonitrile (CH_3CN), pure R-Levodropropizine dissolved in a mixed solvent of ethanol (EtOH) and hexene (C_6H_{14}), and pure R-Ladarixin dissolved in (H_2O). (**b**) Temporal dynamics of the modulus of electric dipole moment of ground ($\mathbf{d}_{11}$) and first excited ($\mathbf{d}_{11}$) state, transition electric ($\mathbf{d}_{12}$) and magnetic ($\mathbf{m}_{12}$) dipole moments for the transition from ground to first excited state in case of R-Reparixin dissolved in water.

states, and electric/magnetic transition dipole moments) are later utilized during the PMM calculations.

2.8.4 Absorption spectra and ensemble averages of molecular observables.

STEP-4: Treating the solvent effect as perturbation and considering the chiral molecule as QC, the perturbed molecular quantum observables are determined through the MD-PMM approach. To do that, we first carried out constrained-MD simulations for each model with the chiral molecule frozen in a particular conformation (selected in ED) and allowing the solvent molecules to move freely. The instantaneous electric field generated by the solvent molecules and exerted on the QC is then evaluated at each MD frame. Utilizing the electric field as perturbation, the Hamiltonian matrix of the perturbed system is constructed in the previously calculated basis set in the DFT-based calculations on unperturbed

QC. Diagonalization of the perturbed Hamiltonian provides the instantaneous eigenvalue (electronic energies, electric dipoles, transition electric/magnetic moments) and the corresponding eigenvectors. We compute the electronic absorption spectra (including absorption maxima and spectral width) using the trajectories of the eigenvalues and eigenvectors of each conformation. In addition, the averaged molecular observables, such as electric/magnetic dipoles and absorption spectra, are determined by incorporating the statistical weight of each conformation as obtained from the basin probabilities during principal component analysis. It is worth mentioning that, in the ergodic assumption, the quantum molecular observables calculated as time averages over the MD simulation time scale are considered equivalent to ensemble averages. Basically, the behavior of a system at a microscopic level can be linked to its macroscopic observables through such an assumption. Provided that the time evolution of a dynamical system covers all its possible microstates, the time averages and ensemble averages of an observable are then linked in a consistent manner. Mathematically, one can write

$$\langle Q \rangle_{\text{time}} = \lim_{T \to \infty} (1/T) \int_0^T Q(T) dt \approx \langle Q \rangle_{\text{ensem}}, \tag{2.56}$$

where Q is the observable Q and T denotes time.

In Fig. 2.7, we present (**a**) the UV-absorption spectrum of the four systems studied in this work, and (**b**) the temporal dynamics of static electric dipole moment and the transition electric/magnetic dipole moments for one representative system, calculated through the sequence of the above-mentioned steps. Such computational method has been employed to determine each quantum molecular observables for each of the four systems. However, to highlight the methodology, results for one representative system are illustrated here. In the subsequent chapters, we will discuss the relevant observables of interest required for specific analysis.

2.9 Concluding remarks.

This chapter provides a comprehensive overview of the computational framework utilized to model four molecular systems of interest. Starting from the fundamental concepts, we present theoretical understanding of the simulation methods and calculation of the molecular observables of the systems through classical and quantum approaches. We discuss different techniques, including HF methods, post-HF methods, DFT and TDDFT, that enable the computation of quantum molecular observables relevant in the system we studied in this work. Furthermore, focusing on hybrid QM/MM approaches, we discuss efficient quantum chemical calculation for large and complex systems. Particularly, considering solvent perturbation, the MD-PMM approach offers reasonable accuracy in the calculation of electronic energies, electric dipoles and electric/magnetic transition dipole moments of molecular solutions. Consequently, these observables are incorporated in the modeling of the absorption spectra of the system. Finally, we implement this method in the investigation of the electronic structure of the chiral drug solutions and briefly describe the key computational aspects employed in the simulations. The quantum molecular observables and the absorption spectra calculated through the adopted method are later utilized in the subsequent works that we discussed in the next chapters.

Chapter 3

Chiroptical Light-Matter Interactions

In this chapter, we present the theoretical modeling of the interaction of light with chiral molecules, starting from the first principles. We develop a semi-classical approach to investigate chiroptical light-matter interaction considering the electromagnetic field classically (following macroscopic Maxwell's equations) and treating the chiral molecules quantum mechanically (density-matrix formalism). Such a semi-classical theoretical approach enables us to interpret the linear response of the system (dilute chiral drug solution) upon excitation by external electromagnetic fields, leading to the development of novel chiroptical sensing concepts.

3.1 Introduction.

The material response to external electromagnetic radiation depends on how the constituent particles interact with the external electromagnetic field. Fundamentally, every material can be interpreted as an assembly of atoms, each consisting of a certain number of charged particles such as electrons and protons. The electronic structure of the material primarily governs the outcomes of light-matter interaction. In addition, the outcomes of the light-matter interaction rely on how intense the light is, as well as the resonance between the impinging light wave and the natural oscillations of constituent elements of the material. Additionally, the intensity of the impinging light and the resonance between the light wave and the natural oscillations of constituent elements of the material highly influence the outcomes as well. Therefore, to investigate the material response, explicit understanding of how an atomic-molecular system interacts with electromagnetic radiation is required. In general, a material has many degrees of freedom, involving a large number of dynamical equations that are often impossible to solve at once. However, certain reasonable simplifications enable us to deal with large and complex systems. Here, we focus on the weak coupling regime, considering the electric field as an assembly of quasi monochromatic wave trains, each containing frequency elements that are narrowly confined around a carrier frequency. In this way, we can consider only those degrees of freedom that resonate directly or indirectly with the fields, hence contributing to the overall sustainable responses over time. Such a treatment significantly reduces the number of governing equations. However, we still need to account for the rest of the degrees of freedom that are weakly coupled to the mode of concern in a non-resonating fashion, since they are plenty in numbers and can accumulate to a collective effect. One way to do that is to consider a damping term (also called homogeneous broadening), which includes outflow of the energy from a particular excitation to the heat bath composed of

remaining degrees of freedom. In the case of direct resonances, we see that the electronic transitions of molecules involve ultraviolet and visible frequencies, the vibrational modes of molecules lead to Infrared (IR) frequencies, and the rotational modes lie in the far IR-microwave domain of the electromagnetic spectrum. On the other hand, the indirect resonances can excite low frequency mode through two-photon processes like Raman scattering and Brillouin scattering [127].

In most realistic phenomena, the atoms inside a molecular system attain a steady state condition when the excitation and relaxation rates are equal. To describe the time evolution of an atomic-molecular system interacting with light, we need a distribution of the wave functions instead of representing the system with a single wave function. Solving Schrödinger equations for pure quantum states is not applicable in this case; rather, the time evolution of a system needs to be described in terms of a *density operator*, which involves a statistical mixture of quantum states. In this chapter, we present a theoretical modeling of light-chiral drug solution interaction in the density-matrix formalism from the first principles. Our calculations focus on the dipole transitions that are assumed to be homogeneously broadened. In addition, the non-radiative recombination to the ground state is included by utilizing the Lindblad operator, accounting for the interaction of a single atomic-molecular system with the thermal bath.

3.2 Fundamental concepts.

In this section, we present an overview of the fundamental mathematical framework required for the subsequent analysis of the chiroptical light-matter interaction. We introduce the density matrix and its temporal evolution to model the dynamics of a system upon excitation by external electromagnetic radiation. These mathematical descriptions provide essential equations for the calculation of the macroscopic response of chiral drug solutions.

3.2.1 Density operator: definition and temporal evolution.

For an atomic-molecular system, the wave function formalism alone is not capable of capturing the broadening of atomic resonances arising from collisional effects. In turn, it does not provide adequate information regarding the width of resonances required to determine the bandwidth of laser frequency. Moreover, the wave function approach is often insufficient to precisely define a quantum state of the system, particularly for the cases that include decoherence and mixed states. Therefore, alternative formalism, such as the density matrix approach, needs to be addressed in order to model these systems [128, 129]. The statistical state of a quantum system can be described by the density operator

$$\hat{\rho} = \sum_j p_j |\psi_j\rangle\langle\psi_j|, \tag{3.1}$$

where $|\psi_j\rangle$ represents a set of orthonormal quantum states and p_j is the corresponding probability of the system to be in the state $|\psi_j\rangle$. The density operator representation includes both pure states and mixed states depending on p_j values. A mixed quantum state possesses multiple non-zero p_j, which indicates a statistical mixture of different quantum states. On the other hand, when the system is in a pure quantum state $|\psi_i\rangle$, all the elements of the ensemble can be described by the same state with the probability $p_j = \delta_{ji}$, where δ_{ji} is the Kronecker delta, and hence, the density operator becomes

$$\hat{\rho} = |\psi_i\rangle\langle\psi_i|. \tag{3.2}$$

Now, expanding $|\psi_i\rangle$ on a basis of a complete orthonormal set $\{|n\rangle\}$, one gets

$$|\psi_i\rangle = \sum_n C_n^i |n\rangle = \sum_n |n\rangle\langle n|\psi_i\rangle, \tag{3.3}$$

where the projection of $|\psi_i\rangle$ onto the basis vector $|n\rangle$ is defined by

$$\langle n|\psi_i\rangle = C_n^i. \tag{3.4}$$

It is worth mentioning that the indices n and m run over all of the possible energy eigenstates of the system. Utilizing the closure relation $\sum_n |n\rangle\langle n| = I$ and substituting Eq. (3.4) and Eq. (3.3) in the density operator expression Eq. (3.1), we get

$$\begin{aligned}\hat{\rho} &= \sum_j p_j \sum_{n,m} |n\rangle\langle n|\psi_j\rangle\langle\psi_j|m\rangle\langle m| \\ &= \sum_j p_j \sum_{n,m} C_n^j {C_m^j}^* |n\rangle\langle m|. \\ &= \sum_{n,m} \rho_{n,m}|n\rangle\langle m| \end{aligned} \tag{3.5}$$

In the above representation, the matrix elements of the density operator are given by

$$\rho_{n,m} = \langle n|\hat{\rho}|m\rangle = \sum_j p_j C_n^j {C_m^j}^* \tag{3.6}$$

Note that the matrix elements satisfy the relation $\langle n|\hat{\rho}|m\rangle^* = \langle m|\hat{\rho}|n\rangle$, which means $\hat{\rho}$ is a Hermitian operator, leading to real eigenvalues. Physically, the diagonal elements $\langle n|\hat{\rho}|n\rangle$ correspond to the probability of the system being in the energy eigenstate $|n\rangle$ and the off-diagonal elements $\langle n|\hat{\rho}|m\rangle (n \neq m)$ interpret "coherence"[1] between $|n\rangle$ and $|n\rangle$ [129]. In such a representation, the expectation value of a physical observable $\hat{A}$ can be determined from

$$\langle \hat{A} \rangle = \mathrm{Tr}[\hat{\rho}\hat{A}], \tag{3.7}$$

where the trace operation for a matrix M is defined as $\mathrm{Tr}[\hat{M}] = \sum_n M_{n,n}$.

[1] i.e., the state of the system can be described as a coherent superposition of the associated energy eigenstate

To investigate the time evolution of a quantum system, one can follow different "representations" of the time dependence of operators and quantum state vectors associated with the system. In the Schrödinger representation, the wavefunction (or state vector) contains the time dependence, while the operators that determine the dynamical variables are time-independent. Conversely, in the Heisenberg representation, the operators encode explicit time dependency, while the state vectors are independent of time. In the density matrix formalism, a commonly followed method, particularly in perturbative interactions, the total Hamiltonian of the system is written as the sum of the time-independent unperturbed Hamiltonian $\hat{\mathcal{H}}_0$ of the system in the absence of external influence and a time-dependent part $\hat{\mathcal{V}}_{\text{int}}(t)$ accounting for the coupling interactions [130] between the system and the external influences. Thus, we write the total Hamiltonian

$$\hat{\mathcal{H}}(t) = \hat{\mathcal{H}}_0 + \hat{\mathcal{V}}_{\text{int}}(t). \tag{3.8}$$

The time-dependent density operator is defined as

$$\begin{aligned} \hat{\rho}(t) &= \sum_j p_j |\psi_j(t)\rangle\langle\psi_j(t)| \\ &= \hat{U}(t, t_0)\hat{\rho}(t_0)\hat{U}^\dagger(t, t_0), \end{aligned} \tag{3.9}$$

where $\hat{U}(t, t_0) = \exp(-i\hat{\mathcal{H}}(t - t_0)/\hbar)$ is the time evolution operator representing the evolution of the density operator from an initial time t_0 to a later time t. The time derivative of the time-dependent density operator provides [128]

$$\frac{d\hat{\rho}(t)}{dt} = \frac{1}{i\hbar}\left[\hat{\mathcal{H}}(t), \hat{\rho}(t)\right]. \tag{3.10}$$

The above equation represents the quantum mechanical analog to the classical

Liouville equation[2]. Writing the density operator in terms of the matrix element as discussed in Eq. (3.6), the temporal evolution of the density operator is given by

$$\begin{aligned}\frac{d\rho_{m,n}(t)}{dt} &= \frac{1}{i\hbar}\langle m|\left[\hat{\mathcal{H}}(t),\hat{\rho}(t)\right]|n\rangle \\ &= \frac{1}{i\hbar}\langle m|\left[\hat{\mathcal{H}}_0+\hat{\mathcal{V}}_{\text{int}}(t),\hat{\rho}(t)\right]|n\rangle \\ &= \frac{1}{i\hbar}(E_n-E_m)\langle m|\hat{\rho}(t)|n\rangle+\frac{1}{i\hbar}\langle m|\left[\hat{\mathcal{V}}_{\text{int}}(t),\hat{\rho}(t)\right]|n\rangle,\end{aligned} \tag{3.11}$$

where E_n and E_m are the unperturbed energy eigenvalues corresponding to the respective states $|n\rangle$ and $|m\rangle$. In general, for many-body interactions, the density matrix accounts for the total system. However, in what follows, we focus on single electron transitions and adopt the single particle density matrix, where other degrees of freedom are traced out and produce non-radiative recombination.

3.2.2 Lindblad operator.

An absolutely isolated real physical system is elusive; indeed, for a realistic system, we need to include the interaction of the system with its surroundings. In turn, the energy dissipates into the surroundings, leading to the decoherence. The situation is similar to the energy exchange between a system and a thermal reservoir. In the framework of the semi-classical density matrix approach, including such interactions, the temporal dynamics of the density matrix of an open quantum system can be described in terms of the Lindblad master equation [131]

$$\frac{d\hat{\rho}}{dt} = \frac{1}{i\hbar}\left[\hat{\mathcal{H}},\hat{\rho}\right]+\hat{\mathcal{L}}(\hat{\rho}), \tag{3.12a}$$

$$\hat{\mathcal{L}}(\hat{\rho}) = \sum_j \frac{\gamma_j}{2}\left[2\hat{L}_j\hat{\rho}\hat{L}_j^\dagger-\left\{\hat{L}_j^\dagger\hat{L}_j,\hat{\rho}\right\}\right], \tag{3.12b}$$

[2]For a classical system, the temporal evolution of the corresponding phase space distribution function $f(\mathbf{r},\mathbf{P},t)$, where $\mathbf{r}$ and $\mathbf{p}$ denote the position and momentum coordinates, respectively, is governed by the classical *Liouville equation* $\dot{f}=\{H,f\}$, where H is the system's Hamiltonian and $\{.,.\}$ indicates Poisson bracket.

where $\hat{\mathcal{L}}(\hat{\rho})$ is called the Lindblad superoperator, $\hat{L}_j$ refers to the jump operator which includes the dissipative part of the dynamics, $\{\cdot,\cdot\}$ denotes anticommutator, and $\gamma_j \geq 0$ represents damping rate associated with transition. Note that, putting $\gamma_j = 0$ in the Eq. (3.12) recovers Eq. (3.10) which describes unitary dynamics. Considering a system with N discrete energy levels, the density matrix operator can be written as $\hat{\rho} = \sum_{n,m=1}^{N} |n\rangle\langle m|$, see Eq. (3.5), and accounting decay or transition from state $|n\rangle$ to the ground state $|1\rangle$ through $\hat{L} = |1\rangle\langle n|$, Eq. (3.12b) provides

$$\hat{\mathcal{L}}(\hat{\rho}) = \sum_{n=2}^{N} \frac{\gamma_n}{2} \left[2\rho_{n,n}|1\rangle\langle 1| - |n\rangle\langle n|\hat{\rho} - \hat{\rho}|n\rangle\langle n|\right], \tag{3.13}$$

where we used the identity $\left\{\hat{a}, \hat{b}\right\} = \hat{a}\hat{b} + \hat{b}\hat{a}$ and γ_n corresponds to the decay rate from $|n\rangle$ to $|1\rangle$.

3.3 Multilevel chiroptical interaction.

We consider a chiral sample, in particular chiral drug solution, with N discrete energy levels so that the system can be described with the unperturbed Hamiltonian

$$\hat{\mathcal{H}}_0 = \sum_{n=1}^{N} \hbar\omega_n |n\rangle\langle n|, \tag{3.14}$$

where $\hbar\omega_n$ represents the energy eigenvalue associated with the eigenstate $|n\rangle$. In the dipole approximation, we further assume the system is excited by quasi monochromatic radiation consisting of electric and magnetic induction field components as follows

$$\mathbf{E}(t) = \mathrm{Re}\left[\tilde{\mathbf{E}}_0 e^{-i\omega t}\right], \tag{3.15a}$$

$$\mathbf{B}(t) = \mathrm{Re}\left[\tilde{\mathbf{B}}_0 e^{-i\omega t}\right], \tag{3.15b}$$

where ω is the angular frequency of the external radiation with carrier wavelength $\lambda = 2\pi c/\omega$ in vacuum and the fields exhibit time-harmonic dependence. Upon excitation by external radiation driving the molecule, the total Hamiltonian of the system is given by

$$\hat{\mathcal{H}}(t) = \sum_{n=1}^{N} \hbar\omega_n |n\rangle\langle n| - \mathbf{E}(t) \cdot \hat{\mathbf{d}} - \mathbf{B}(t) \cdot \hat{\mathbf{m}}, \tag{3.16}$$

where $\hat{\mathbf{d}}$ and $\hat{\mathbf{m}}$ are single electron electric and magnetic dipole operators, respectively. Note that the total Hamiltonian contains both internal molecular energy and the dipolar contribution from the light-matter interaction. In the set of radiation unperturbed energy states, we define $\hat{\mathbf{d}}$ and $\hat{\mathbf{m}}$ operators in the the dyadic representation as

$$\hat{\mathbf{d}} = \sum_{n,m=1}^{N} \mathbf{d}_{n,m} |n\rangle\langle m|, \tag{3.17a}$$

$$\hat{\mathbf{m}} = \sum_{n,m=1}^{N} \mathbf{m}_{n,m} |n\rangle\langle m|. \tag{3.17b}$$

In the above equations, the matrix element $\mathbf{d}_{n,m}$ represents the transition electric dipole moment between the states $|n\rangle$ and $|m\rangle$ for $m \neq n$ and static electric dipole moment of the state $|n\rangle$ for $m = n$. Similarly, $\mathbf{m}_{n,m}$ represents the transition magnetic dipole moment between the states $|n\rangle$ and $|m\rangle$ for $m \neq n$ and static magnetic dipole moment of the state $|n\rangle$ for $m = n$. It is worth mentioning that, the considered chiral drugs in the present study, are non magnetic and hence $\mathbf{m}_{n,n} = 0$ for all n. The system can be described by the time dependent density matrix

$$\hat{\rho}(t) = \sum_{n,m=1}^{N} \rho_{n,m} |n\rangle\langle m|, \tag{3.18}$$

and thus the temporal dynamics of the system is governed by the density matrix equation

$$\begin{aligned}\frac{d\hat{\rho}(t)}{dt} &= \frac{1}{i\hbar}\Big[\hat{\mathcal{H}}(t),\hat{\rho}(t)\Big] + \hat{\mathcal{L}}(\hat{\rho}) \\ &= \frac{1}{i\hbar}\Big[\hat{\mathcal{H}}(t),\hat{\rho}(t)\Big] + \sum_{n=2}^{N}\frac{\gamma_n}{2}\Big[2\rho_{n,n}|1\rangle\langle 1| - |n\rangle\langle n|\hat{\rho} - \hat{\rho}|n\rangle\langle n|\Big],\end{aligned} \tag{3.19}$$

where the non-radiative recombination to the ground state is included through the Lindblad operator as given by Eq. (3.13). Since the interactions with the driving fields are included in $\hat{\mathcal{H}}(t)$, Eq. (3.19) describes how the system evolves in time as a result of these interactions. In turn, the density matrix equations provide

$$\begin{aligned}\dot{\rho}_{i,j} &= -i\left(\omega_i - \omega_j\right)\rho_{i,j} \\ &+ \frac{1}{i\hbar}\sum_{n=1}^{N}\Big\{\rho_{i,n}\Big[\mathbf{E}(t)\cdot\mathbf{d}_{n,j} + \mathbf{B}(t)\cdot\mathbf{m}_{n,j}\Big] - \rho_{n,j}\Big[\mathbf{E}(t)\cdot\mathbf{d}_{i,n} + \mathbf{B}(t)\cdot\mathbf{m}_{i,n}\Big]\Big\} \\ &+ \Big\{\sum_{n=2}^{N}\gamma_n\rho_{n,n}\Big\}\delta_{i,1}\delta_{j,1} - \frac{\gamma_i}{2}\rho_{i,j}\left(1-\delta_{i,1}\right) - \frac{\gamma_j}{2}\rho_{i,j}\left(1-\delta_{j,1}\right),\end{aligned} \tag{3.20}$$

where we introduce the indices i and j to refer to the quantum states that the system can go through when it interacts with external perturbations. In addition, δ_{ij} is the Kronecker delta defined as $\delta_{ij} = 1$ if $i = j$, and 0 if $i \neq j$. Explicitly, for the diagonal elements, we get

$$\dot{\rho}_{1,1} = \frac{2}{\hbar}\sum_{n=2}^{N}\mathrm{Im}\Big\{\rho_{1,n}\Big[\mathbf{E}(t)\cdot\mathbf{d}_{n,1} + \mathbf{B}(t)\cdot\mathbf{m}_{n,1}\Big]\Big\} + \sum_{n=2}^{N}\gamma_n\rho_{n,n}, \tag{3.21}$$

$$\dot{\rho}_{i,i}^{(i\neq 1)} = -\frac{2}{\hbar}\mathrm{Im}\Big\{\rho_{1,i}\Big[\mathbf{E}(t)\cdot\mathbf{d}_{i,1} + \mathbf{B}(t)\cdot\mathbf{m}_{i,1}\Big]\Big\} - \gamma_i\rho_{i,i}. \tag{3.22}$$

For the off-diagonal elements, we get

$$\dot{\rho}_{1,i}^{(i\neq 1)} = \left[i\left(\omega_i - \omega_1\right) - \frac{\gamma_i}{2}\right]\rho_{1,i} - \frac{i}{\hbar}\sum_{\substack{n=2\\ n\neq i}}^{N}\rho_{1,n}\left[\mathbf{E}(t)\cdot\mathbf{d}_{n,i} + \mathbf{B}(t)\cdot\mathbf{m}_{n,i}\right] + \frac{i}{\hbar}\left\{\begin{array}{l}\left[\mathbf{E}(t)\cdot\mathbf{d}_{1,i} + \mathbf{B}(t)\cdot\mathbf{m}_{1,i}\right]\left(\rho_{i,i} - \rho_{1,1}\right)\\ + \left[\mathbf{E}(t)\cdot\left(\mathbf{d}_{1,1} - \mathbf{d}_{i,i}\right) + \mathbf{B}(t)\cdot\left(\mathbf{m}_{1,1} - \mathbf{m}_{i,i}\right)\right]\rho_{1,i}\end{array}\right\}. \tag{3.23}$$

In most of the problems of physical interest, analytically solving the density matrix equation Eq. (3.20) is not trivial. Therefore, we attempt to find the solution in terms of a perturbation expansion, which can be accomplished by introducing a parameter $0 < a < 1$ and considering $|\mathbf{E}(t)|, |\mathbf{B}(t)| \propto a$ in Eq. (3.20). Essentially, the parameter a represents the perturbation strength, and for a real physical situation, it is taken as $a = 1$. This expansion allow us to find a solution of the form

$$\rho_{i,j}(t) = \rho_{i,j}^{(0)}(t) + a\rho_{i,j}^{(1)}(t) + ..., \tag{3.24}$$

which must satisfy Eq. (3.20) for any value of a to be a solution. To fulfill this requirement, the individual coefficient of power a must satisfy Eq. (3.20). Thus, the multiple scale expansions up to first order provide

$$\rho_{1,i}^{(i\neq 1)} \simeq \rho_{1i}^{(1)}, \tag{3.25a}$$

$$\rho_{1,1} \simeq 1, \tag{3.25b}$$

$$\rho_{i,i} \simeq 0, \tag{3.25c}$$

where we are neglecting thermal excitation of excited states at equilibrium. Such an expansion enables the calculation of linear (at first order) response of the system upon excitation by external radiation.

Linear response in the density matrix formalism.

The linear response of the system is governed by the contributions $\propto \rho^{(1)}$ in Eq. (3.25). Thus, by solving the density matrix equations at the first order, we obtain

$$\begin{aligned}\rho_{1i}^{(1)}(t) &= -\frac{i\left(\mathbf{d}_{1,i}\cdot\tilde{\mathbf{E}}_0^* + \mathbf{m}_{1,i}\cdot\tilde{\mathbf{B}}_0^*\right)}{\hbar\left\{\gamma_i + 2i\Big[\omega - (\omega_i-\omega_1)\Big]\right\}}e^{i\omega t} - \frac{i\left(\mathbf{d}_{1,i}\cdot\tilde{\mathbf{E}}_0 + \mathbf{m}_{1,i}\cdot\tilde{\mathbf{B}}_0\right)}{\hbar\left\{\gamma_i - 2i\Big[\omega + (\omega_i-\omega_1)\Big]\right\}}e^{-i\omega t}, \\ &= \mathrm{P}_{1i}^{(+\omega)}e^{i\omega t} + \mathrm{P}_{1i}^{(-\omega)}e^{-i\omega t}, \end{aligned} \tag{3.26}$$

which describes the oscillatory nature of the system's dynamics (at first order) under the perturbation, which in this case is an external periodic electromagnetic field. $\mathrm{P}_{1i}^{(\pm\omega)}$ indicates the amplitude corresponding to the oscillation at $\pm\omega$. Note that the respective amplitudes depend on the energy differences between the excited and ground states, as well as the damping rates of the transitions.

3.3.1 Induced dipole moments.

The expectation value of any physical observable can be calculated directly from the density matrix elements, and the temporal evolution of the observable can be determined from the evolution of the density matrix [128]. We calculate the expectation values of induced electric $\mathbf{d}(t)$ and magnetic $\mathbf{d}(t)$ dipole moment operators according to the Eq. (3.7). In turn, we write

$$\mathbf{d}(t) = \mathrm{Tr}\left[\hat{\mathbf{d}}\hat{\rho}\right] = \rho_{1,1}\mathbf{d}_{1,1} + \sum_{i=2}^{N}\rho_{i,i}\mathbf{d}_{i,i} + 2\sum_{i=2}^{N}\mathrm{Re}\left[\rho_{i,1}\mathbf{d}_{1,i}\right], \tag{3.27a}$$

$$\mathbf{m}(t) = \mathrm{Tr}\left[\hat{\mathbf{m}}\hat{\rho}\right] = \rho_{1,1}\mathbf{m}_{1,1} + \sum_{i=2}^{N}\rho_{i,i}\mathbf{m}_{i,i} + 2\sum_{i=2}^{N}\mathrm{Re}\left[\rho_{i,1}\mathbf{m}_{1,i}\right]. \tag{3.27b}$$

We simplify the above equation by substituting the density matrix elements derived in the previous section. This is accomplished by inserting Eq. (3.26) in

Eq. (3.25). Consequently, we obtain the explicit expressions for the induced dipole moments

$$\mathbf{d}(t) = \mathbf{d}_{1,1} + \sum_{i=2}^{N} \mathrm{Re}\left\{\left[2\mathbf{d}_{1,i}\left(\mathrm{P}_{1i}^{(+\omega)}\right)^{*} + 2\mathbf{d}_{i,1}\mathrm{P}_{1i}^{(-\omega)}\right]e^{-i\omega t}\right\}, \tag{3.28a}$$

$$\mathbf{m}(t) = \mathbf{m}_{1,1} + \sum_{i=2}^{N} \mathrm{Re}\left\{\left[2\mathbf{m}_{1,i}\left(\mathrm{P}_{1i}^{(+\omega)}\right)^{*} + 2\mathbf{m}_{i,1}\mathrm{P}_{1i}^{(-\omega)}\right]e^{-i\omega t}\right\}. \tag{3.28b}$$

At the microscopic level, typically molecules in a solution are randomly oriented, meaning that the induced dipoles are not aligned in any specific orientation. To calculate the overall response of the system, it is necessary to determine the orientational average of these dipoles. As a consequence, all the observable quantities of the system are obtained as isotropic (i.e., that they are identical in all directions) quantities.

3.3.2 Averaging over molecular orientation.

Generally, the calculation of macroscopic properties of a bulk system based on molecular microscopic parameters involves summing over the contributions of all molecules to the overall response. Finally, division by the total number of molecules provides the macroscopic response on a single-molecule basis. Alternatively, we can calculate the average of the particular observable over all possible orientations of a single molecule, assuming random molecular fluctuations are not involved in the measurement [132, 133]. Considering the laboratory coordinate system (X, Y, Z) and the molecular coordinate system (x, y, z), the orientation of the molecule in the laboratory frame can be described in terms of the Euler angles $\phi, \theta,$ and χ, see Fig. 3.1, where these angles represent how the molecular axes rotate with respect to the laboratory frame. Using the Euler angles that describe

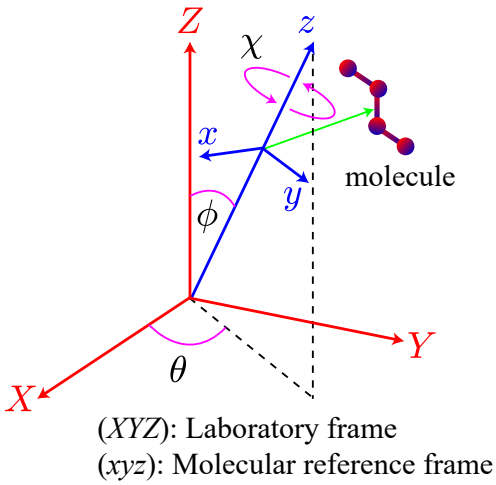


Figure 3.1: Schematic of the laboratory (XYZ) and molecular (xyz) coordinate systems that are related by the Euler angles ϕ, θ, and χ.

the relative rotation between two frames, we define the direction cosine matrix

$$\hat{R}(\phi,\theta,\chi) = \begin{bmatrix} \cos\phi\cos\theta\cos\chi - \sin\phi\sin\chi & -\cos\phi\cos\theta\sin\chi - \sin\phi\cos\chi & \cos\phi\sin\theta \\ \sin\phi\cos\theta\cos\chi + \cos\phi\sin\chi & -\sin\phi\cos\theta\sin\chi + \cos\phi\cos\chi & \sin\phi\sin\theta \\ -\sin\theta\cos\chi & \sin\theta\sin\chi & \cos\theta \end{bmatrix}.$$

The rotation of any vector quantity $\mathcal{A}(\phi,\theta,\chi)$ describing a microscopic molecular observable can be determined in the laboratory frame by utilizing the direction cosine matrix as

$$\mathcal{A}(\alpha,\beta,\gamma) = \hat{R}(\phi,\theta,\chi)\mathcal{A} \tag{3.29}$$

Subsequently, the rotational average of such quantity for an isotropic molecular system on a single-molecule basis can obtained by averaging over all orientations. The average of $\mathcal{A}$ is given by

$$\langle\mathcal{A}\rangle_{\phi,\theta,\chi} = \frac{1}{8\pi^2}\int_0^{2\pi} d\phi \int_0^{\pi} d\theta \int_0^{2\pi} d\chi \mathcal{A}(\phi,\theta,\chi)\sin\theta, \tag{3.30}$$

where the $\sin\theta$ factor in the integration accounts for the Haar-measure [132, 133].

3.3.3 Microscopic response.

We calculate the average induced dipole moments by rotating individual dipole elements first and then taking the orientational average over all directions. Upon molecular rotation, the diagonal and off diagonal electric/magnetic dipole elements rotate according to

$$\begin{cases} \mathbf{D}_{1,i}(\alpha,\beta,\gamma) = \hat{R}(\phi,\theta,\chi)\mathbf{d}_{1,i} \\ \mathbf{D}_{n,i}(\alpha,\beta,\gamma) = \hat{R}(\phi,\theta,\chi)\mathbf{d}_{n,i} \\ \mathbf{D}_{i,i}(\alpha,\beta,\gamma) = \hat{R}(\phi,\theta,\chi)\mathbf{d}_{i,i} \end{cases} \qquad \begin{cases} \mathbf{M}_{1,i}(\alpha,\beta,\gamma) = \hat{R}(\phi,\theta,\chi)\mathbf{m}_{1,i} \\ \mathbf{M}_{n,i}(\alpha,\beta,\gamma) = \hat{R}(\phi,\theta,\chi)\mathbf{m}_{n,i} \\ \mathbf{M}_{i,i}(\alpha,\beta,\gamma) = \hat{R}(\phi,\theta,\chi)\mathbf{m}_{i,i} \end{cases} . \tag{3.31}$$

Now, following Eq. (3.30), the average induced electric and magnetic dipole moments are calculated as

$$\langle \mathbf{d}(t) \rangle_{\phi,\theta,\chi} = \frac{1}{8\pi^2} \int_0^{2\pi} d\phi \int_0^{\pi} d\theta \int_0^{2\pi} d\chi \sin\theta \mathbf{D}(t), \tag{3.32a}$$

$$\langle \mathbf{m}(t) \rangle_{\phi,\theta,\chi} = \frac{1}{8\pi^2} \int_0^{2\pi} d\phi \int_0^{\pi} d\theta \int_0^{2\pi} d\chi \sin\theta \mathbf{M}(t), \tag{3.32b}$$

Further simplifications lead to the final expressions

$$\langle \mathbf{d}(t) \rangle = \mathrm{Re}\left\{ \left[\mathrm{A}_{\mathrm{d,E}} \tilde{\mathbf{E}}_0 + \mathrm{A}_{\mathrm{d,B}} \tilde{\mathbf{B}}_0 \right] e^{-i\omega t} \right\}, \tag{3.33a}$$

$$\langle \mathbf{m}(t) \rangle = \mathrm{Re}\left\{ \left[\mathrm{A}_{\mathrm{m,B}} \tilde{\mathbf{B}}_0 + \mathrm{A}_{\mathrm{m,E}} \tilde{\mathbf{E}}_0 \right] e^{-i\omega t} \right\}, \tag{3.33b}$$

where the parameters $\mathrm{A_{d,E}}$ and $\mathrm{A_{m,B}}$ represent the isotropic linear electric and magnetic polarizabilities, respectively, while $\mathrm{A_{d,B}}$ and $\mathrm{A_{m,E}}$ denote the isotropic linear mixing polarizabilities. The dependencies of the linear polarizabilities on

the microscopic system parameters are explicitly given by

$$\mathrm{A_{d,E}} = \sum_{n=2}^{N} \frac{|\mathbf{d}_{1,n}|^2}{3\hbar} \left\{ \frac{1}{[\,\omega + (\omega_n - \omega_1) + i\gamma_n/2]} - \frac{1}{[\,\omega - (\omega_n - \omega_1) + i\gamma_n/2]} \right\}, \tag{3.34a}$$

$$\mathrm{A_{d,B}} = \sum_{n=2}^{N} \frac{(\mathbf{d}_{1,n} \cdot \mathbf{m}_{1,n})}{3\hbar} \left\{ \frac{1}{[\,\omega + (\omega_n - \omega_1) + i\gamma_n/2]} + \frac{1}{[\,\omega - (\omega_n - \omega_1) + i\gamma_n/2]} \right\}, \tag{3.34b}$$

$$\mathrm{A_{m,B}} = \sum_{n=2}^{N} \frac{|\mathbf{m}_{1,n}|^2}{3\hbar} \left\{ \frac{1}{[\,\omega + (\omega_n - \omega_1) + i\gamma_n/2]} - \frac{1}{[\,\omega - (\omega_n - \omega_1) + i\gamma_n/2]} \right\}, \tag{3.34c}$$

$$\mathrm{A_{m,E}} = \sum_{n=2}^{N} \frac{2\,(\mathbf{d}_{1,n} \cdot \mathbf{m}_{1,n})}{3\hbar} \left\{ \frac{-2[\,\omega + (\omega_n - \omega_1) + i\gamma_n}{4[\,\omega + (\omega_n - \omega_1)]\, + \gamma_n^2} + \frac{-2[\,\omega - (\omega_n - \omega_1) + i\gamma_n}{4[\,\omega - (\omega_n - \omega_1)]\, + \gamma_n^2} \right\}. \tag{3.34d}$$

Note that Eq. (3.34d) can be simplified to obtain $\mathrm{A_{m,E}} = -\mathrm{A_{d,B}}$. It is worth mentioning that the electric dipole moments are polar vectors, while the magnetic dipole moments are axial vectors. Their scalar and vector products hold important significance that reflects in the enantioselective properties of the chiral molecules. We will discuss how these products behave for different enantiomers in the subsequent section of this chapter.

3.3.4 Macroscopic response.

In the limit of low molecular density (i.e., for dilute isotropic chiral solution), the macroscopic polarization and magnetization fields are obtained by multiplying the orientation-averaged induced electric/magnetic dipole moments with the molecular number density of chiral molecules. Let's consider the molecular number density as $n_{\mathrm{mol}} = n_{\mathrm{mol}}^{(\mathrm{R})} + n_{\mathrm{mol}}^{(\mathrm{S})}$, where $n_{\mathrm{mol}}^{(\mathrm{R})}$ and $n_{\mathrm{mol}}^{(\mathrm{S})}$ indicate the molecular number

densities of the R and S enantiomers of the chiral molecule. In turn, we write

$$\mathbf{P}(\mathbf{r},t) = n_{\mathrm{mol}}\langle \mathbf{d}(t)\rangle, \tag{3.35a}$$

$$\mathbf{M}(\mathbf{r},t) = n_{\mathrm{mol}}\langle \mathbf{m}(t)\rangle, \tag{3.35b}$$

where $\mathbf{P}(\mathbf{r},t)$ and $\mathbf{M}(\mathbf{r},t)$ are the macroscopic polarization and magnetization fields, respectively, of the system. Now, substituting Eq. (3.33) in the Eq. (3.35), we obtain

$$\mathbf{P}(\mathbf{r},t) = \left\{ \epsilon_0 \mathrm{Re}\left\{ \left[\frac{n_{\mathrm{mol}}\mathrm{A}_{\mathrm{d,E}}}{\epsilon_0}\tilde{\mathbf{E}}_0 + \frac{n_{\mathrm{mol}}\mathrm{A}_{\mathrm{d,B}}}{\epsilon_0}\tilde{\mathbf{B}}_0 \right] e^{-i\omega t} \right\}, \tag{3.36a}$$

$$\mathbf{M}(\mathbf{r},t) = \left\{ \mathrm{Re}\left\{ \left[n_{\mathrm{mol}}\mathrm{A}_{\mathrm{m,E}}\tilde{\mathbf{E}}_0 + n_{\mathrm{mol}}\mathrm{A}_{\mathrm{m,B}}\tilde{\mathbf{B}}_0 \right] e^{-i\omega t} \right\}, \tag{3.36b}$$

Such polarization and magnetization fields produce the microscopic charges and current densities

$$\rho_{\mathrm{P}}(\mathbf{r},t) = -\nabla\cdot\mathbf{P}(\mathbf{r},t), \tag{3.37a}$$

$$\rho_{\mathrm{M}}(\mathbf{r},t) = 0, \tag{3.37b}$$

$$\mathbf{J}_{\mathrm{P}}(\mathbf{r},t) = \partial_t\mathbf{P}(\mathbf{r},t), \tag{3.37c}$$

$$\mathbf{J}_{\mathrm{M}}(\mathbf{r},t) = \nabla\times\mathbf{M}(\mathbf{r},t), \tag{3.37d}$$

where $\rho_{\mathrm{P}}(\mathbf{r},t)$ and $\rho_{\mathrm{M}}(\mathbf{r},t)$ are the polarization and magnetization charge density respectively, while $\mathbf{J}_{\mathrm{P}}(\mathbf{r},t)$ and $\mathbf{J}_{\mathrm{M}}(\mathbf{r},t)$ are the polarization and magnetization current density, respectively. Incorporating these source terms, we can determine the microscopic Maxwell equations for monochromatic fields $\mathbf{E}(\mathbf{r},t) = \mathrm{Re}[\tilde{\mathbf{E}}_0^{(\omega)}e^{-i\omega t}]$

and $\mathbf{B}(\mathbf{r},t) = \mathrm{Re}[\tilde{\mathbf{B}}_0^{(\omega)} e^{-i\omega t}]$ with angular frequency ω, as follows

$$\begin{cases} \nabla \cdot \tilde{\mathbf{E}}_0^{(\omega)}(\mathbf{r}) = \dfrac{1}{\epsilon_0 \epsilon_{\mathrm{sol}}(\omega)} \rho_{\mathrm{P}}^{(\omega)}(\mathbf{r}), \\ \nabla \cdot \tilde{\mathbf{B}}_0^{(\omega)}(\mathbf{r}) = 0, \\ \nabla \times \tilde{\mathbf{E}}_0^{(\omega)}(\mathbf{r}) = i\omega \tilde{\mathbf{B}}_0^{(\omega)}(\mathbf{r}), \\ \nabla \times \tilde{\mathbf{B}}_0^{(\omega)}(\mathbf{r}) = \mu_0 \mathbf{J}_{\mathrm{P}}^{(\omega)}(\mathbf{r}) + \mu_0 \mathbf{J}_{\mathrm{M}}^{(\omega)}(\mathbf{r}) - \dfrac{i\omega}{c^2} \epsilon_{\mathrm{sol}}(\omega) \tilde{\mathbf{E}}_0^{(\omega)}(\mathbf{r}), \end{cases} \tag{3.38a}$$

where ϵ_{sol} is the relative electric permittivity of the chiral solution containing low molecular number density of the solute (i.e., chiral molecules). Such dilute chiral solution can be treated as an effective medium, and the macroscopic response of the whole system (chiral molecules dissolved in a solvent) can be determined from the weighted average effect of the contributions of solute and solvent. By introducing the constitutive relations, the microscopic Maxwell equations can be recast into the macroscopic formulation

$$\begin{cases} \nabla \cdot \tilde{\mathbf{D}}_0^{(\omega)}(\mathbf{r}) = 0, \\ \nabla \cdot \tilde{\mathbf{B}}_0^{(\omega)}(\mathbf{r}) = 0, \\ \nabla \times \tilde{\mathbf{E}}_0^{(\omega)}(\mathbf{r}) = i\omega \tilde{\mathbf{B}}_0^{(\omega)}(\mathbf{r}), \\ \nabla \times \tilde{\mathbf{H}}_0^{(\omega)}(\mathbf{r}) = -i\omega \tilde{\mathbf{D}}_0^{(\omega)}(\mathbf{r}), \end{cases} \tag{3.39}$$

where $\mathbf{D}(\mathbf{r},t) = \mathrm{Re}[\tilde{\mathbf{D}}_0^{(\omega)} e^{-i\omega t}]$ and $\mathbf{H}(\mathbf{r},t) = \mathrm{Re}[\tilde{\mathbf{H}}_0^{(\omega)} e^{-i\omega t}]$.

3.3.5 Constitutive relations.

Including ω frequency contribution, the constitutive equations for the fields with angular frequency ω are given by

$$\tilde{\mathbf{D}}_0^{(\omega)}(\mathbf{r}) = \epsilon_0 \left[\epsilon_{\mathrm{r}}(\omega) \tilde{\mathbf{E}}_0^{(\omega)}(\mathbf{r}) - i\mu_0 c \kappa(\omega) \tilde{\mathbf{H}}_0^{(\omega)}(\mathbf{r}) \right], \tag{3.40a}$$

$$\tilde{\mathbf{B}}_0^{(\omega)}(\mathbf{r}) = \mu_0 \left[\frac{1}{\mu_0 c} i\kappa(\omega) \tilde{\mathbf{E}}_0^{(\omega)}(\mathbf{r}) + \mu_{\mathrm{r}}(\omega) \tilde{\mathbf{H}}_0^{(\omega)}(\mathbf{r}) \right], \tag{3.40b}$$

where we have introduced three parameters

$$\epsilon_{\rm r}(\omega) = \epsilon_{\rm sol}(\omega) + \frac{1}{\epsilon_0} n_{\rm mol} {\rm A}_{\rm d,E} + \frac{\mu_0 n_{\rm mol}^2 {\rm A}_{\rm m,E} {\rm A}_{\rm d,B}}{\epsilon_0 (1 - \mu_0 n_{\rm mol} {\rm A}_{\rm m,B})}, \tag{3.41a}$$

$$\kappa(\omega) = \frac{i n_{mol} {\rm A}_{\rm d,B}}{\epsilon_0 c (1 - \mu_0 n_{\rm mol} {\rm A}_{\rm m,B})}, \tag{3.41b}$$

$$\mu_{\rm r}(\omega) = \frac{1}{(1 - \mu_0 n_{\rm mol} {\rm A}_{\rm m,B})}, \tag{3.41c}$$

that determine the effective linear response of the chiral drug solution in the form of the well-known BACRs Eq. (1.20). Here, $\epsilon_{\rm r}(\omega)$ is the relative dielectric permittivity, $\kappa(\omega)$ is the chiral parameter, and $\mu_{\rm r}(\omega)$ is the relative magnetic permeability of the medium.

3.4 Enantioselective properties.

Two enantiomers of a chiral molecule are nonsuperimposible mirror images of each other. In this section we discuss how the electric/magnetic dipole moments differ for two enantiomers of the chiral molecule, leading to the different physical properties. Considering an unit vector $\hat{\mathbf{n}}$ perpendicular to the plane where the reflection symmetry is broken, we define a reflection operator $\hat{\mathcal{R}}_{\hat{n}} = 1 - 2\hat{\mathbf{n}}\hat{\mathbf{n}}\cdot$ by the plane. When we switch from R to S-enatiomer, the electric dipole moment ($\mathbf{d}$) which is a polar vector and the magnetic dipole moment ($\mathbf{m}$) which is an axial vector undergoes a reflection as illustrated in Fig. 3.2. Upon reflection, a polar vector ($\mathbf{p}$) and an axial vector ($\mathbf{a}$) transforms according to

$$\mathbf{p}({\rm R}) = \hat{\mathcal{R}}_{\hat{n}} \mathbf{p}({\rm S}) = [1 - 2\hat{\mathbf{n}}\hat{\mathbf{n}}\cdot]\, \mathbf{p}({\rm S}) = \mathbf{p}({\rm S}) - 2[\mathbf{p}({\rm S}) \cdot \hat{\mathbf{n}}]\hat{\mathbf{n}}, \tag{3.42a}$$

$$\mathbf{a}({\rm R}) = -\hat{\mathcal{R}}_{\hat{n}} \mathbf{a}({\rm S}) = -\,[1 - 2\hat{\mathbf{n}}\hat{\mathbf{n}}\cdot]\, \mathbf{a}({\rm S}) = -\mathbf{a}({\rm S}) + 2[\mathbf{a}({\rm S}) \cdot \hat{\mathbf{n}}]\hat{\mathbf{n}}. \tag{3.42b}$$

Note that the modulus of such vectors are unaffected by the type of the enantiomers ($|\mathbf{p}({\rm R})| = |\mathbf{p}({\rm S})|$ and $|\mathbf{a}({\rm R})| = |\mathbf{a}({\rm S})|$). Now, utilizing the reflection oper-

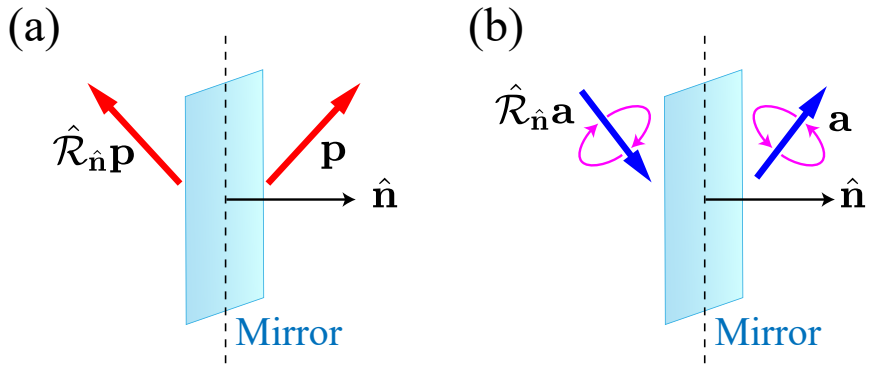


Figure 3.2: Illustration of how (**a**) a polar vector $\mathbf{p}$ and (**b**) an axial vector $\mathbf{a}$ transform under a reflection operation. The reflection operator is defined as $\hat{\mathcal{R}}_{\hat{\mathbf{n}}} = 1 - 2\hat{\mathbf{n}}\hat{\mathbf{n}}\cdot$, where $\hat{\mathbf{n}}$ denote the unit normal to the mirror plane.

ator, we determine the dependence of the linear polarizabilities as follows

$$\mathrm{A}_{\mathrm{d,E}}(\mathrm{R}) \propto |\mathbf{p}(\mathrm{R})|^2 \propto |\mathbf{p}(\mathrm{S})|^2 = \mathrm{A}_{\mathrm{d,E}}(\mathrm{S}), \tag{3.43a}$$

$$\mathrm{A}_{\mathrm{d,B}}(\mathrm{R}) \propto \mathbf{p}(\mathrm{R}) \cdot \mathbf{a}(\mathrm{R}) \propto -\mathbf{p}(\mathrm{S}) \cdot \mathbf{a}(\mathrm{S}) = -\mathrm{A}_{\mathrm{d,B}}(\mathrm{S}), \tag{3.43b}$$

$$\mathrm{A}_{\mathrm{m,B}}(\mathrm{R}) \propto |\mathbf{a}(\mathrm{R})|^2 \propto |\mathbf{a}(\mathrm{S})|^2 = \mathrm{A}_{\mathrm{m,B}}(\mathrm{S}), \tag{3.43c}$$

$$\mathrm{A}_{\mathrm{m,E}}(\mathrm{R}) \propto \mathbf{p}(\mathrm{R}) \cdot \mathbf{a}(\mathrm{R}) \propto -\mathbf{p}(\mathrm{S}) \cdot \mathbf{a}(\mathrm{S}) = -\mathrm{A}_{\mathrm{m,E}}(\mathrm{S}). \tag{3.43d}$$

3.5 Concluding remarks.

In this chapter we present the modeling of radiation-matter interaction through density matrix equations in the electric/magnetic dipole approximation. We solve these density matrix equations perturbatively in order to derive expectation values of the induced electric/magnetic dipole moments produced by the external radiation. Finally, owing to the random molecular orientation, we average the induced electric/magnetic dipole moments over arbitrary rotations via the Euler rotation matrix approach and calculate the macroscopic polarization and magnetization fields of the effective medium. In turn, we obtain the bi-anisotropic constitutive relation that contains all the physical effects that will be described in the next chapters. In the following chapters, we will utilize such constitutive relations in

order to shed light on the dynamics provided by chiral molecules interacting with external electromagnetic radiation.

Chapter 4

Enhancement of Circular Dichroism Spectroscopy by Surface Plasmon Polaritons

In this Chapter, we examine the potential of Surface-Plasmon Polariton (SPP) at noble metal interfaces to enhance the sensitivity of chiroptical sensing techniques applicable for nanoliter volume dilute chiral drug solutions. We investigate plasmonic excitation in both Otto and Kretschmann configurations, enabling enhanced Circular Dichroism Differential Absorption (CDDA). Owing to the substantial near-field and subwavelength localization of SPPs, highly sensitive chiroptical activities can be achieved by placing minimal amounts of drug solutions close to the metal surfaces. Implementing a realistic dilute chiral drug solution, in particular Reparixin dissolved in water with concentrations ≤ 5 mg/ml and nanoliter volume, we attain enhanced CDDA by a factor $\simeq 20$. Such a finding can lead to novel chiroptical sensors to trace the enantiomeric imbalance in nanoliter volume pharmaceutical chiral solutions.

4.1 Introduction.

Existing technologies at the current time for the measurement of enantiomeric imbalance of chiral mixtures, which include gas chromatography [134], nuclear magnetic resonance [135], and high-performance liquid chromatography [136], provide sophisticated instruments for drug safety. These techniques operate with macroscopic drug volumes, which, in turn, are not compatible for real-time analysis or intriguing lab-on-a-chip integration schemes. Recent advancements in designing photonic devices have opened a window to prevail over such limitations. However, the evolution of technology in this domain is restricted by intrinsic weak chiroptical interactions in chiral drug solutions. The necessary volume limit for sensing through, for instance, polarimetry [137] or electronic/vibrational Circular Dichroism (CD) [138, 139] lies in the order of ml volume. In literature, numerous strategies have been developed to boost the chiroptical interaction in order to push below the detection volume limit. Ultrafast and nonlinear spectroscopic techniques [37, 38, 39, 36] based on synthetic chiral light and pronounced electric-dipole transitions have been employed for precise chiral characterization. In addition, the interaction between chiral molecules and superchiral fields [140, 141] offered by nanophotonic structures or metasurfaces [142, 143, 144] has been explored to serve this purpose. In practice, the application of superchiral fields to design innovative chiral sensing methods remains as a challenging task since the majority of experimental sensing methods adopt chiral nanoplasmonic substrates. In these cases, the chiral sample is positioned in the vicinity of nanostructures to access the intense near-field. As a result, the observed CD signal is compromised by the chiroptical response of these nanostructures, which serve as significant background noise, suppressing the weak chiroptical signal of the sample itself [145]. Notably, in the case of chiral drug solutions, the chiroptical responses are modulated over time due to the deformation of chiral drugs caused by the conformational fluctuations

of the molecules interacting with the solvent at finite temperature. Nanostructures supporting both electric and magnetic resonances provide enhanced CD due to the simultaneous amplification of electric and magnetic fields [146]. Although these schemes hold potential for single-molecule chiral discrimination, their application to extended drug solutions is challenging. This is because enhancement of CD occurs solely at specific hot spots where electric and magnetic field lines are strong, parallel, and $\pi/2$ shifted [145, 146]. In a complementary context, metal-based nanophotonic structures facilitate plasmon-enhanced CD spectroscopy [147], which has been anticipated for isolated molecules [20], while it has been primarily employed for the characterization of chiral nanoparticles [148, 149, 150]. Our investigation predicts that CD differential absorption of dilute drug solutions with nl volume can be enhanced by a factor $\simeq 20$ through the excitation of SPPs at the interface between a noble metal and the chiral sample. For this study, we specifically examine an isotropic assembly of Reparixin solvated in water. The molecular number density of the dilute drug solution is taken to be approximately $n_{\mathrm{mol}} = n_{\mathrm{mol}}^{(\mathrm{R})} + n_{\mathrm{mol}}^{(\mathrm{S})} \approx 10^{-2}\mathrm{nm}^{-3}$, where $n_{\mathrm{mol}}^{(\mathrm{R,S})}$ denote number densities of the respective R and S enantiomers of Reparixin, which corresponds to a concentration of 5 mg/ml. In order to ensure momentum matching requirements for SPPs excitation, a radiation momentum kick can be provided to the SPPs through attenuated total reflection in well known Otto [65] or Kretschmann [66] or configurations or adopting grating coupling [151, 152]. However, the implementation of grating coupling substantially alters the SPP dispersion; hence, we utilize silica prism coupling in this work.

Upon right/left circular polarization excitation, we find that CDDA $\Delta A = A_{\mathrm{R}} - A_{\mathrm{L}} \propto \Delta n_{\mathrm{mol}}$, where $\Delta n_{\mathrm{mol}} = n_{\mathrm{mol}}^{(\mathrm{S})} - n_{\mathrm{mol}}^{(\mathrm{R})}$ indicates the density of enantiomeric excess. Therefore, we can recover Δn_{mol} from CDDA measurements. Additionally, we observe that adopting silver as a metal substrate in the Otto configuration, the highest plasmon-induced CDDA enhancement factor (f_{CDDA}) $\simeq 20$ can be

obtained, whereas other noble metals like copper and gold produce a lower f_{CDDA}. For the calculation of macroscopic optical parameters of isotropic solutions of aqueous Reparixin, we adopt the theoretical/computational approach as described in the previous chapters. The plasmon-enhanced CDDA ΔA is assessed through classical electrodynamics calculations, considering (i) the Otto and Kretschmann SPP coupling schemes employing silica prisms, (ii) the macroscopic bi-anisotropic response of the chiral sample, and (iii) the dielectric response of noble metals. Our findings of adequate plasmon-enhanced CDDA using nl volume isotropic chiral drug solutions pave the way to potential innovative applications for integrated chiroptical sensing schemes.

4.2 Optical properties of metals.

Substantial research in the last century [153] covers the study of the optical properties of metals. The characteristics of the metal response at optical frequencies in the presence of electromagnetic fields are available in standard solid state physics books [154]. Here we discuss a brief review of metal behaviors in the context of optics. While doing so, we restrict our analysis solely to classical electrodynamics without involving quantum mechanical descriptions. Conversely to semiconductors, for metals the valence band is fully filled and the conduction band is partially filled. In turn, the free electron density in the conduction bands is quite high inside metals, accounted by a continuum of states in the conduction band [155]. As a consequence, meta optics arises from intraband transitions of electron occupying the conduction band and interband transitions of valence electrons.

Well-established observations confirm that in the electrostatic regime, metals are opaque and possess high reflectance in the microwave to far-Infrared (IR) electromagnetic frequency range. The ohmic dissipation is not efficient in this regime because of the negligible amount of electromagnetic field penetration. Conversely,

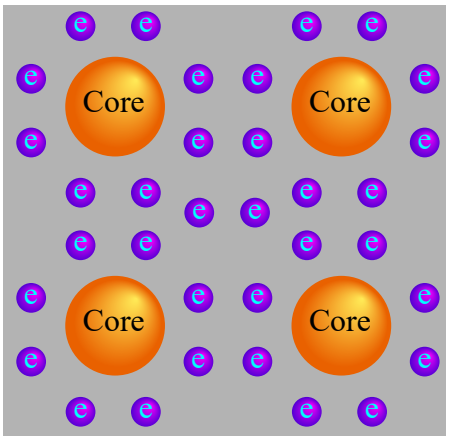


Figure 4.1: Illustration of free electron gas model indicating electrons e are oscillating on a background of stationary lattice of positively charged ion cores.

in the visible frequency range, the field penetrates significantly, and therefore the dissipation increases. For the higher frequencies, in the ultraviolet metals are nearly transparent.

We can derive the dielectric constants $\epsilon(\omega)$ of a metal in the plasma approximation [156], which considers metals to be composed of free electrons having minimal interaction with the fixed positive ion cores, similar to a gas, as illustrated in Fig. 4.1. Experimental results based on reflection techniques provide precise values of $\epsilon(\omega)$ for noble metals [157, 158]. When an optical field propagates through the medium, electrons oscillate in response to the field and collide with each other. Let's consider the electrons with effective mass m [155] undergoing field-induced damped oscillatory motion with characteristic collision frequency $\gamma = 1/\tau$, where τ is the relaxation time. In the non-relativistic regime, neglecting the Lorentz force on the electron charge in the non-relativistic regime [159], we can describe the equation of motion of a generic electron by the Newton equation

$$m\ddot{\mathbf{r}}(t) + m\gamma\dot{\mathbf{r}}(t) = -e\mathbf{E}(t), \tag{4.1}$$

where e, $\mathbf{r}(t)$ and $\mathbf{E}(t)$ indicate the electronic charge, position at time t and the electric field that propagates through the medium, respectively. Considering a

monochromatic plane wave, the time dependence is harmonic and the electric field is then given by $\mathbf{E}(t) = \mathrm{Re}[\tilde{\mathbf{E}}_0 e^{-i\omega t}]$, where ω is the angular frequency. By assuming the position $\mathbf{r}(t) = \mathrm{Re}[\tilde{\mathbf{r}}_0 e^{-i\omega t}]$, the solution of Eq. (4.1) provides

$$\mathbf{r}(t) = \frac{e\tilde{\mathbf{E}}_0 e^{-i\omega t}}{\mathrm{Re}[m(\omega^2 + i\gamma\omega)]}. \tag{4.2}$$

The displacements of the electrons induce a macroscopic polarization $\mathbf{P}(t) = -Ne\mathbf{r}(t)$, where N refers to the free electron density in the medium. Consequently, the electric displacement vector $\mathbf{D}$ becomes

$$\mathbf{D}(t) = \epsilon_0 \mathrm{Re}\left\{\left[1 - \frac{\omega_\mathrm{p}^2}{\omega^2 + i\gamma\omega}\right]\tilde{\mathbf{E}}_0 e^{-i\omega t}\right\}, \tag{4.3}$$

where $\omega_p = \sqrt{Ne^2/\epsilon_0 m}$ is known as the plasma frequency. In metals, the typical plasma frequency value of free electron gas lies in the ultraviolet range, e.g., in the case of silver, $\omega_\mathrm{p} \approx 1.45 \times 10^{16}$ rad/sec, corresponding to $\lambda_\mathrm{p} \approx 130$ nm. Thus, the dielectric constant of the medium is given by

$$\epsilon(\omega) = 1 - \frac{\omega_\mathrm{p}^2}{\omega^2 + i\gamma\omega}. \tag{4.4}$$

The condition $\omega = \omega_\mathrm{p}$ leads to the excitation of longitudinal collective oscillation of the electrons, usually called volume plasmons [155]. In addition, if one neglects the damping, i.e., $\gamma = 0$ for $\omega = \omega_\mathrm{p}$, Eq. (4.3) provides $\mathbf{D} = 0$, meaning that the electric field $\mathbf{E}$ is unable to induce a magnetic response in the medium. As a result, transverse oscillations are suppressed and the magnetic field is vanishing since $\nabla \times \tilde{\mathbf{B}} = -(i\omega/c^2)\tilde{\mathbf{D}} = 0$; that's why these collective oscillations are called electrostatic modes. Within this basic framework, for the frequency less than the plasma frequency $\omega < \omega_\mathrm{p}$, metals are opaque. For frequencies higher than the plasma frequency $\omega > \omega_\mathrm{p}$, metals are transparent and allow plane waves $\mathbf{E}(\mathbf{r}, t) = \mathrm{Re}[\tilde{\mathbf{E}}_0 e^{i\mathbf{k}\cdot\mathbf{r} - i\omega t}]$ propagation. Maxwell equations Eq. (1.1c) and Eq. (1.1d)

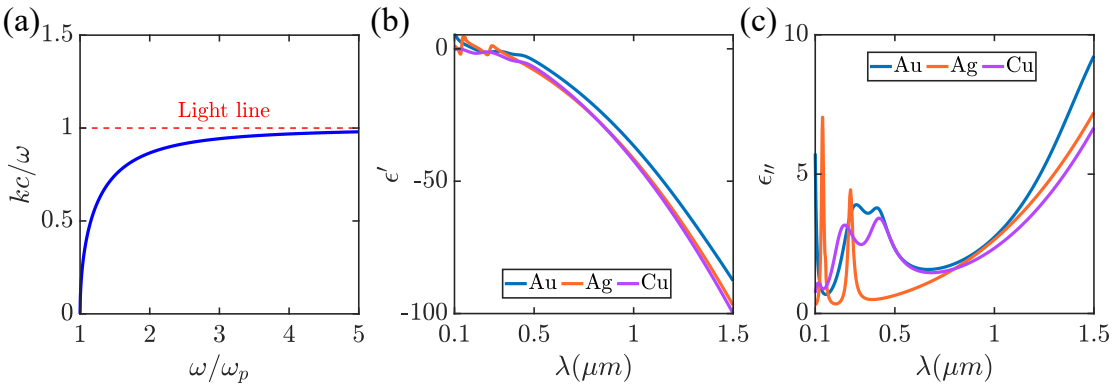


Figure 4.2: (**a**) Dispersion of plane-wave propagating in the metal bulk. (**b**) Real and (**c**) imaginary parts of dielectric constants of gold, silver and copper.

then provide the dispersion relation

$$\omega^2 = \omega_{\mathrm{p}}^2 + k^2 c^2, \tag{4.5}$$

where $c = 1/\sqrt{\epsilon_0 \mu_0}$ is the light speed in vacuum. Note that the wave number k is purely imaginary for $\omega < \omega_{\mathrm{p}}$ and the plane waves do not propagate through the metal, while for $\omega \geq \omega_{\mathrm{p}}$ the transverse plane waves propagate (neglecting loss), and the corresponding dispersion relation is shown in Fig. 4.2(a). When $\omega \gg \omega_{\mathrm{p}}$ the plane wave dispersion approaches the light line $\omega = ck$, which represents the dispersion of light in vacuum. However, to take into account interband transitions, we need to go beyond such plasma treatment and consider the weighted combination of multiple oscillators contributions to the dielectric constant

$$\epsilon(\omega) = \epsilon_\infty + \sum_{m=0}^{N} \frac{f_m \omega_{\mathrm{p}}^2}{\omega_m^2 - \omega^2 + i\gamma_m \omega}, \tag{4.6}$$

where ϵ_∞ is the dielectric constants of the background ion cores, ω_m and γ_m are the resonance angular frequency and damping coefficient of the m-th interband resonance, respectively, and f_m is the corresponding weighted strength. The dielectric constants obtained from this model are illustrated in Fig. 4.2(b,c) for gold, silver and copper. Note that the magnitude of the real part $\epsilon'(\omega)$ alters by two

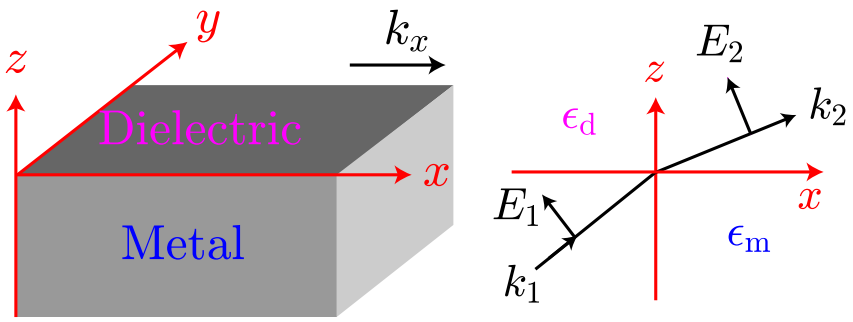


Figure 4.3: Schematic for the Surface-Plasmon Polariton (SPP) propagation at a single metal-dielectric interface with geometric representation of quantities required for obtaining propagation in x-direction. The dielectric constants of metal and dielectric media are indicated by ϵ_m and ϵ_d, respectively.

orders, see Fig. 4.2(b), and the imaginary part $\epsilon''(\omega)$ has peaks at the interband transitions, see Fig. 4.2(c), in the wavelength range $\lambda = 100$ nm $- 1.5$ μm. All the above mentioned parameters for these metals can be determined by fitting the experimental data [158].

4.3 SPPs at a single interface.

Surface-Plasmon Polariton (SPP)s propagate along the metal-dielectric interface and are evanescently confined into the direction perpendicular to the interface. As the distance increases both inside the metal and the dielectric, the amplitude of SPP decays exponentially. The coupled oscillatory state of photon and material excitations corresponding to plasma oscillations in metals, is termed plasmon polariton. Here we derive linear plasmonic modes at a single metal-dielectric interface by considering the system as illustrated in Fig. 4.3. We assume the metal - with complex dielectric constant $\epsilon_m(\omega)$ and the dielectric - with real dielectric constant $\epsilon_d(\omega)$, are separated by the $z = 0$ plane. Our goal is to find a solution to the Maxwell equation for a propagating wave that travels in the x-direction along the interface and evanescently decays in the z-direction. We further assume the polarization of the wave lies in the $x - z$ plane since the SPP modes are Transverse Magnetic (TM)-polarized waves [160]. Now, we write the electric field

of the monochromatic light inside metal ($\mathbf{E}_\mathrm{m}$) and dielectric ($\mathbf{E}_\mathrm{d}$) as follows

$$\mathbf{E}_\mathrm{m}(\mathbf{r},t) = \mathrm{Re}\left\{[\tilde{E}_{\mathrm{m},x}\hat{\mathbf{e}}_x + \tilde{E}_{\mathrm{m},z}\hat{\mathbf{e}}_z]e^{i(k_x x-\omega t)}e^{ik_{\mathrm{m},z}z}\right\} \qquad \text{for} \quad z<0, \tag{4.7a}$$

$$\mathbf{E}_\mathrm{d}(\mathbf{r},t) = \mathrm{Re}\left\{[\tilde{E}_{\mathrm{d},x}\hat{\mathbf{e}}_x + \tilde{E}_{\mathrm{d},z}\hat{\mathbf{e}}_z]e^{i(k_x x-\omega t)}e^{ik_{\mathrm{d},z}z}\right\} \qquad \text{for} \quad z>0, \tag{4.7b}$$

where $\tilde{E}_{\mathrm{m},x}$, $\tilde{E}_{\mathrm{m},z}$, $\tilde{E}_{\mathrm{d},x}$ and $\tilde{E}_{\mathrm{d},z}$ are the field amplitudes. Note that the propagation constants of both waves are the same (k_x) in the x-direction, while in the z-direction they are set to be spatially dependent so that $k_{\mathrm{m},z}$ and $k_{\mathrm{d},z}$ can have imaginary components to find a localized solution near the interface $z=0$. For a monochromatic plane wave, Maxwell equations provide $\nabla\cdot\mathbf{D}=0$ meaning that $\mathbf{k}\cdot\mathbf{D}=0$. Thus utilizing the constitutive relation $\tilde{\mathbf{D}}=\epsilon_j\tilde{\mathbf{E}}$, where $j=\mathrm{d},\mathrm{m}$ refer to the metal and dielectric region, we get

$$k_x\tilde{E}_{\mathrm{m},x} + k_{\mathrm{m},z}\tilde{E}_{\mathrm{m},z} = 0, \tag{4.8a}$$

$$k_x\tilde{E}_{\mathrm{d},x} + k_{\mathrm{d},z}\tilde{E}_{\mathrm{d},z} = 0. \tag{4.8b}$$

The boundary conditions for the continuity of the $\mathbf{E}$ components along the interface and the $\mathbf{D}$ components normal to the interface provide

$$\tilde{E}_{\mathrm{m},x} - \tilde{E}_{\mathrm{d},x} = 0, \tag{4.9a}$$

$$\epsilon_\mathrm{m}(\omega)\tilde{E}_{\mathrm{m},x} - \epsilon_\mathrm{d}(\omega)\tilde{E}_{\mathrm{d},x} = 0. \tag{4.9b}$$

Eq. (4.8) and Eq. (4.9) form a set of four homogeneous equations with four unknowns, leading to the characteristic equation for non-vanishing solutions. Thus, by equating the determinant of the matrix of coefficients to zero, we have

$$k_x\left[\epsilon_\mathrm{m}(\omega)k_{\mathrm{d},z} - \epsilon_\mathrm{d}(\omega)k_{\mathrm{m},z}\right] = 0. \tag{4.10}$$

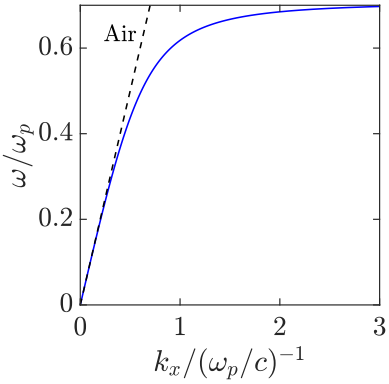


Figure 4.4: SPP dispersion relation at an interface between ideal metal (neglecting damping) and air.

However, the first solution $k_x = 0$ of Eq. (4.10) does not describe a propagating excitation along the interface, while the other solution

$$\epsilon_{\mathrm{m}}(\omega)k_{\mathrm{d},z} - \epsilon_{\mathrm{d}}(\omega)k_{\mathrm{m},z} = 0, \tag{4.11}$$

corresponds to a wave that travels along the interface. Moreover, the corresponding electromagnetic waves must satisfy the Helmholtz equation $\nabla^2\tilde{\mathbf{E}} - (\omega^2/c^2)\epsilon(\omega)\tilde{\mathbf{E}} = 0$. Thus, by inserting the fields given by Eq. (4.7) into the Helmholtz equation, one reaches

$$k_x^2 + k_{\mathrm{m},z}^2 = \epsilon_{\mathrm{m}}(\omega)\omega^2/c^2, \tag{4.12a}$$

$$k_x^2 + k_{\mathrm{d},z}^2 = \epsilon_{\mathrm{d}}(\omega)\omega^2/c^2. \tag{4.12b}$$

In turn, we obtain the dispersion relation of SPP modes, which is given by

$$k_x = \frac{\omega}{c}\sqrt{\frac{\epsilon_{\mathrm{m}}(\omega)\epsilon_{\mathrm{d}}(\omega)}{\epsilon_{\mathrm{m}}(\omega) + \epsilon_{\mathrm{d}}(\omega)}}. \tag{4.13}$$

It is worth mentioning that this expression is generally valid for both complex and real $\epsilon_{\mathrm{m}}(\omega)$, which refers to metals without or with attenuation. Fig. 4.4 illustrates the plot of the real value of propagation constant given by Eq. (4.13),

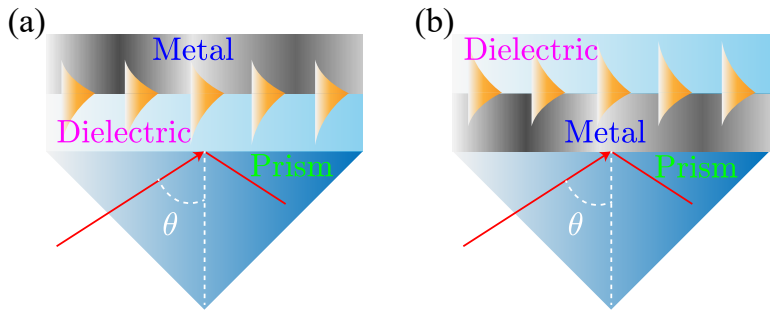


Figure 4.5: Excitation of SPPs using prism coupling in the (**a**) Otto and (**b**) Kretschmann configurations.

at an interface between air ($\epsilon_{\mathrm{d}}(\omega) = 1$) and generic Drude metal (neglecting the damping γ) with $\epsilon_{\mathrm{m}}(\omega) = 1 - \omega_{\mathrm{p}}^2/\omega^2$. In this plot, we rescaled the angular frequency ω to the plasma frequency ω_p. The blue curve refers to the SPP dispersion, and the light line $k_0 = \omega/c$ is indicated by the dashed black line. Often, for a traveling wave, the complex parameter $\beta = k_x$ is termed the propagation constant, which corresponds to the component of the wavevector in the direction of propagation. The excitation of SPP modes involves the portion of the dispersion curve on the right side of the light line since SPPs are bound to the surface.

4.4 SPP excitation.

As described above, the intrinsic bound nature of SPPs results in a larger wave vector of SPP than that of the light in the dielectric, $\beta_{\mathrm{SPP}} > \beta_{\mathrm{light}}$ at every given ω. Physically, the strong coupling between surface charge and light is responsible for such increased momentum of SPP. As a consequence, the SPP dispersion curve lies on the right side of the light line in the dielectric, and therefore, it is not possible to excite SPPs by directly impinging an electromagnetic plane wave on the metal from the dielectric medium. To overcome this limitation, we need to employ special phase-matching techniques to match the wavevector of incident light that propagates in the bulk dielectric with the wavevector of SPP mode on the

single interface. Methods like prism or grating coupling can be adopted to fulfill such a phase matching requirement. Other methods, like end-fire coupling [161] involving spatial-mode matching rather than phase matching, can also be used for SPP excitation. However, the grating coupling technique for SPP excitation modifies significantly the SPP dispersion[151, 152], and hence we focus on prism coupling. We present a brief review of the relevant aspects of prism coupling in the following section.

4.4.1 Prism coupling.

The simplest phase-matching condition to excite SPPs can be attained through a coupling scheme based on Attenuated Total Internal Reflection (ATR). The two commonly used experimental arrangements, Kretschmann and Otto configurations based on ATR, are illustrated in Fig. 4.5(a,b). Such methods consist of a three-layer system: a thin metal film and two different dielectrics with different dielectric constants. In the Kretschmann configuration, the metal layer is placed on top of a glass prism with a higher dielectric constant $\epsilon_{\mathrm{p}}(\omega) > \epsilon_{\mathrm{d}}(\omega)$ than that of the dielectric placed on the opposite side of the metal layer. In this geometry, the impinging electromagnetic wave from the prism side gets reflected back by the metal layer. However, some part of the light evanescently penetrates the metal layer in the form of an evanescent wave [162]. At optical frequencies, for a sufficiently thin ($\approx$ 100 nm) metal film, the tails of such evanescent waves couple with the SPPs at the other metal-dielectric interface. In Fig. 4.6, the single metal-dielectric SPP dispersions are depicted for metal-air (blue curve) and metal-prism (red curve) interfaces. The dielectric constant of the prism is assumed to be $\epsilon_{\mathrm{p}}(\omega) = 2.25$ and the dielectric constant of metal (neglecting damping) is modeled through the Drude model, as discussed above. The light dispersions in the air (black) and bulk prism (red) are indicated by dashed lines. The black circle indicates the intersection of the light line in prism and the metal-air SPP

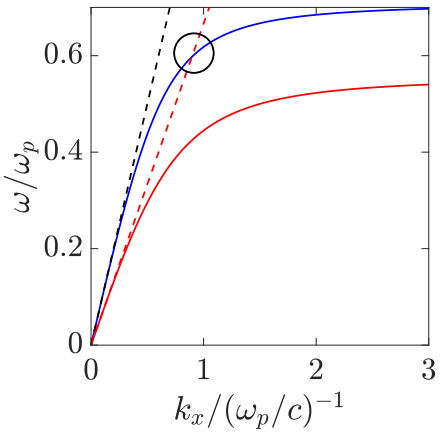


Figure 4.6: SPP dispersion curve in case of metal-air (blue) and metal-prism (red) interfaces.

dispersion, enabling the SPP excitation. In contrast, the excitation of SPP mode at the interface between metal and prism is not allowed, as the SPP dispersion line in this case stays outside the prism light cone. The phase matching condition for an incident angle θ is achieved via

$$\beta = k_0\sqrt{\epsilon_{\mathrm{p}}}\sin\theta. \tag{4.14}$$

In this configuration, the maximum angular frequency ω_{max} that allows the phase matching condition corresponds to $\theta = \pi/2$. For lower frequencies $\omega < \omega_{\mathrm{max}}$, the resonance condition for SPP excitation can be attained by tuning the angle of incidence. Experimentally, the occurrence of SPP excitation is obtained from the reflectivity measurement at every incident angle. The reflectivity drastically drops at a particular angle when the phase-matching condition for SPP excitation is satisfied [163]. The detailed calculations of reflectivity as a function of incident angle can be done by utilizing the Fresnel theory for multilayer structures [49].

In the Otto configuration, a thin dielectric layer with dielectric constant $\epsilon_{\mathrm{d}}(\omega)$ is sandwiched in between metal and a prism with dielectric constant $\epsilon_{\mathrm{p}}(\omega)$ such that $\epsilon_{\mathrm{p}}(\omega) > \epsilon_{\mathrm{d}}(\omega)$. The electromagnetic wave travels trough the prism and impinges on the prism-dielectric interface experiencing total internal reflection for incident

angles larger than the critical angle of total internal reflection [50]. When the thickness of the dielectric layer is comparable to the optical wavelength, the evanescent wave penetrates the metal and excites the SPPs at the metal-dielectric interface. The phase matching condition for the coupling of SPP modes $\beta = k_0\sqrt{\epsilon_p(\omega)}\sin\theta$ can also be achieved in this method, as mentioned above. The SPP excitation corresponds to the dip of the reflectivity-incident angle curve like the Kretschmann configuration. However, broad and shifted SPP resonance is observed for very small thicknesses of dielectric layer compared to the wavelength. The origin of such an effect is the SPP radiation damping [163] involving coupling between SPP modes and prism radiative modes. Conversely, very large thicknesses of dielectric layer produce inefficient SPP excitation. Thus, Otto configuration is less favored than Kretschmann configuration unless direct contact with metal is unwanted.

Moreover, the excited SPPs emerging from the phase-matching condition in the prism coupling techniques are inherently leaky waves, meaning that the impinging light from the prism couples with the SPP mode and the other way around. In turn, along with inherent metal absorption, the leakage of radiation into the prism is also involved in the effective loss. Hence, apart from the coupling to SPP modes, the destructive interference caused by the leakage of SPP modes also affects the incident angle-dependent reflectivity curve.

4.5 Interaction of radiation with Reparixin in water.

The functionality and behavior of a molecule dissolved in a solution depends on several factors, like its interaction with the solvent, and the temperature and pressure of the environment, influencing molecular dynamics. As a result, the molecules adopt different molecular geometries ("conformations") through the rearrangement of atoms and bonds. Such molecular conformational changes are ensured by the energy landscape and internal degrees of freedom of the molecule.

Therefore, to study the interaction of and external radiation with the molecule in solution, the evaluation of quantum molecular observables (e.g., electric and magnetic moments, ground state energy, electronic and vibrational excitation energies) is necessary. However, this is a challenging task because the molecule possesses a large number of configurations inside the solvent that essentially demand the determination of averaged quantum expectation values of the molecular observables on on a statistical-mechanical basis.

We adopted a combination of computational approaches for the evaluation of the quantum molecular observables of the solvated drug, i.e., aqueous Reparixin. The detailed theoretical descriptions and computational aspects adopted for the evaluation of the observables of interests are described in Chapter 2. We illustrate the complete scheme in Fig. 2.5, leading to the calculation of electric/magnetic transition dipoles, electronic and vibrational excitation energies of aqueous Reparixin. All these molecular observables are evaluated assuming electronic wavefunction within the Born-Oppenheimer approximation. Such wavefunctions, along with the associated expectation values of physical observables, strongly rely on the molecular conformations. In principle, this is applicable for a molecule in solution where the (supra) molecular wavefunction and the associated observables should be evaluated for all the molecule-solvent conformations sampled along the conformational space at a given temperature and pressure. This is practically challenging and hence required diverse theoretical-computational approaches as previously reported.

4.5.1 Electronic and vibrational structure of Reparixin in water.

The key features of the evaluation of relevant quantum-molecular observables are illustrated in Fig. 4.7. The electric/magnetic transition dipole moments and the associated UV/Vibrational absorption spectra of solvated Reparixin in water are

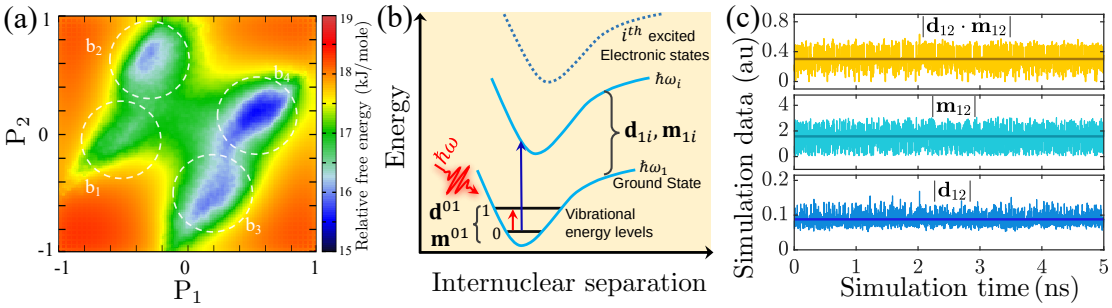


Figure 4.7: (**a**) Relative free-energy of the Reparixin pure S enanatiomer (dissolved in water) at $T = 298$ K, calculated through MD simulations followed by Essential Dynamics analysis (see Chapter 2 for details). White dotted circles confirm the coexistence of four distinct, statistically relevant conformation state basins b_k, where $k = 1 - 4$. P_1 and P_2 are the projections of the solvated Reparixin position vectors (obtained through the MD simulation sampling) onto the eigenvectors of the covariance matrix constructed from the all-atom mass-weighted positional fluctuations (see Chapter 2 for additional details). (**b**) Schematic of Reparixin vibronic dynamics driven by a laser field within the electric/magnetic dipole approximation. (**b**) Temporal evolution of electronic transition dipole moduli $|\mathbf{d}_{12}|$, $|\mathbf{m}_{12}|$ and modulus of the chiral projection $|\mathbf{d}_{12} \cdot \mathbf{m}_{12}|$ (in atomic units) of single Reparixin molecule in b_1 conformation state at each temporal MD frame (expressed in nanoseconds) obtained through MD-PMM method (see Chapter 2 for more details). We used a MD simulation box with ≈ 3 nm lateral size and ≈ 27 nm^3 volume, and this is not related to the thickness of the chiral sample used in this study.

calculated as ensemble averages. From the MD simulation and ED analysis, we find that in water, Reparixin exists in four high probability conformation states that are representative of the free-energy basins b_k, where $k = 1 - 4$, depicted in Fig. 4.7(a) for Reparixin S enantiomer. We emphasize that, owing to selection rules, we consider only two vibrational states that are responsible for resonant interaction with external radiation in the Mid-Infrared (MIR). These vibrational states are labeled by the index $\nu = 0, 1$ with corresponding vibrational energy $\hbar\omega_\nu$ independent over the Reparixin conformation state k. Moreover, we found that the nature of the vibrational mode coincides for all conformation states, which ensures that $\hbar\omega_\nu$ is barely affected by the molecular conformational state. Hereafter, we label the two enantiomers of Reparixin with the index $a = \mathrm{R}, \mathrm{S}$, and the radiation-unperturbed vibronic structure of each enantiomer is approximated

by independent electronic/vibrational Hamiltonians $\hat{\mathcal{H}}_0^{\mathrm{el,vib}}(k,a)$ as follows

$$\hat{\mathcal{H}}_0^{\mathrm{el}}(k,a) = \sum_{i=1}^{5} \hbar\omega_i(k)|i(k,a)\rangle\langle i(k,a)|, \tag{4.15a}$$

$$\hat{\mathcal{H}}_0^{\mathrm{vib}}(k,a) = \sum_{\nu=0,1} (\nu+1/2)\hbar\omega_\nu|\nu(a)\rangle\langle\nu(a)|, \tag{4.15b}$$

where $\hbar\omega_i(k)$ and $\hbar\omega_\nu(\nu+1/2)$ are the respective electronic and vibrational energy eigenvalues with respective eigenstates $|i(k,a)\rangle$ and $|\nu(a)\rangle$. We emphasize that, for flexible solvated molecules (e.g., Reparixin), the UV spectrum is primarily shaped by the chromophore and solvent conformational transitions, while the vibronic transitions possess negligible effect on the UV spectral shape. Thus, the fine structure in the electronic transitions are not observed because of the spectral broadening produced by the semi-classical molecular vibrations and solvent perturbations. In addition, we only consider those electronic states, in this case $i = 1-5$, that produce resonant electronic absorption peaks in the UV. Fig. 4.7(b) represents the considered vibronic structure of Reparixin corresponding to a generic molecular conformation state. Thus, the fine structure in the electronic transitions is not observed because of the spectral broadening produced by the semi-classical molecular vibrations and solvent perturbations. Adopting the density matrix formalism, we model the interaction of the molecule with external radiation within the electric/magnetic dipole approximation (presented in detail in Chapter 3).

It's worth mentioning that, particularly in Reparixin, there are two electrons with opposite spin in the ground state. As a result, the static magnetic dipole moments vanish for every electronic eigenstate (within the Born-Openheimer approximation), while the static electric dipole moments have finite values. In addition, the vibrational[1] transition magnetic dipole moments are calculated beyond

[1]The vibrational calculations in this work were conducted by Matteo Venturi [164]. I would like to express my gratitude to him and appreciate his contribution in this work.

the Born-Oppenheimer approximation. As we have seen in Chapter 3, the scalar product of the transition electric and magnetic dipole moments flips sign upon switching opposite enantiomeric forms. We call this pseudoscalar a *chiral projection*, which consists of a scalar product of a polar and axial vector. Fig. 4.7(c) shows the temporal evolution of electric $|\mathbf{d}_{12}|$ and magnetic $|\mathbf{d}_{12}|$ dipole moments moduli associated with the electronic transition from electronic ground ($i = 0$) to first ($i = 1$) excited state and the modulus of the chiral projection $|\mathbf{d}_{12} \cdot \mathbf{m}_{12}|$ subjected to the electronic contributions in case of pure S Reparixin enantiomer in conformation state $k = 1$. These time-dependent quantities are calculated through the MD-PMM method as discussed in Chapter 2. Within the ergodic assumption, the time averages of these quantum molecular observables (computed over the MD-frame $\simeq$ ns timescale) are incorporated as ensemble averages ($\langle \mathbf{d}_{12} \rangle$, $\langle \mathbf{m}_{12} \rangle$, and $\langle \mathbf{d}_{12} \cdot \mathbf{m}_{12} \rangle$) in our quantum-mechanical treatment for macroscopic bi-anisotropic response.

4.5.2 Macroscopic bi-anisotropic response of Reparixin in water.

The governing equations of radiation-induced electron/vibrational dynamics of the chiral sample (aqueous Reparixin in this case) for every enantiomeric form a and conformation state k are assessed through density matrix equations as discussed in the Chapter 3. We perturbatively solve the density matrix equations at first-order for the density matrix $\hat{\rho}_{k,a}^{\mathrm{el,vib}}(\mathbf{r}, t)$. For all the Reparixin conformation states subjected to each enantiomeric form a, the expectation values of the induced dipole moments are expressed in terms of ensemble average. By plugging in the individual relative statistical weights of the conformation states, the expectation values are given by

$$\mathbf{o}_a^{\mathrm{el,vib}} = \sum_{k=1}^{4} p(k) \mathrm{Tr} \left[\hat{\rho}_{k,a}^{\mathrm{el,vib}} \hat{\mathbf{o}}_a^{\mathrm{el,vib}}(k, a) \right], \tag{4.16}$$

where $\mathbf{o} = \mathbf{d}, \mathbf{m}$ indicates the respective induced electric/ magnetic dipole moments and $p(k) = 0.25$. Since the molecules are randomly oriented inside a solution, the induced electric $\mathbf{d}_a$ and magnetic $\mathbf{m}_a$ dipole moments are averaged over arbitrary rotations using the Euler rotation matrix approach, as described in Chapter 3. In turn, we obtain the wavelength-dependent linear isotropic electric, magnetic, and mixing polarizabilities of every Reparixin enantiomer. These polarizabilities are explicitly given by

$$\alpha^{(a)}_{\mathrm{e,b,m}}(\omega) = \mathcal{C}^{(vib)}_{\mathrm{e,b,m}}(a)\mathcal{F}^{\mathrm{vib}}(\omega) + \sum_{k=1}^{4} p(k) \sum_{j=2}^{5} \mathcal{C}^{(el)}_{j,\mathrm{e,b,m}}(k,a)\mathcal{F}^{\mathrm{el}}_{j,k}(\omega), \tag{4.17}$$

where

$$\mathcal{C}^{(\mathrm{vib,el})}_{\mathrm{e}} = \frac{1}{3\hbar}\langle|\mathcal{D}^{(\mathrm{vib,el})}_{\mathrm{e}}|^2\rangle, \tag{4.18a}$$

$$\mathcal{C}^{(\mathrm{vib,el})}_{\mathrm{b}} = \frac{1}{3\hbar}\langle|\mathcal{M}^{(\mathrm{vib,el})}_{\mathrm{e}}|^2\rangle, \tag{4.18b}$$

$$\mathcal{C}^{(\mathrm{vib,el})}_{\mathrm{m}} = \frac{i}{3\hbar}\langle \mathrm{Im}\left[\mathcal{D}^{(\mathrm{vib,el})}_{\mathrm{e}} \cdot \mathcal{M}^{(\mathrm{vib,el})}_{\mathrm{e}}\right]\rangle, \tag{4.18c}$$

$$\mathcal{F}^{\mathrm{vib}}(\omega) = \sum_{\sigma=\pm1} \frac{\sigma}{\omega + \sigma\langle\omega_\nu\rangle + i\gamma/2}, \tag{4.18d}$$

$$\mathcal{F}^{\mathrm{el}}_{j,k}(\omega) = \sum_{\sigma=\pm1} \frac{\sigma}{\omega + \sigma\langle\omega_j(k) - \omega_1(k)\rangle + i\gamma^{\mathrm{el}}_j(k)/2}. \tag{4.18e}$$

In the above expressions, $\langle(...)\rangle$ indicates the ensemble average and $\mathcal{D}^{\mathrm{vib}} = \mathbf{d}^{01}, \mathcal{D}^{\mathrm{el}}_j = \mathbf{d}^{1j}, \mathcal{M}^{\mathrm{vib}} = \mathbf{m}^{01}, \mathcal{M}^{\mathrm{el}} = \mathbf{m}^{1j}$. Furthermore, $\gamma_\nu = 0.012\ \mathrm{fs}^{-1}$ is the relaxation rate of the vibrational transition $\nu = 0 \rightarrow 1$ of only Reparixin at $\lambda = 5.69\ \mu m$ (with corresponding energy $\hbar\omega_\nu = 0.218$ eV). The calculated values of vibrational electric/magnetic transition dipole moments are given by $\sqrt{\langle|\mathbf{d}^{01}|^2\rangle}/d_0 = 0.105$, $\sqrt{\langle|\mathbf{m}^{01}|^2\rangle}/m_0 = 0.398$, and $\mathrm{Im}\left[\mathbf{d}^{01}(S) \cdot \mathbf{m}^{01}(S)\right]/m_0 d_0 = 0.007$, where $d_0 = |e|a_0$, $a_0 = \hbar/m_e c\alpha$ is the Bohr radius, $m_0 = e\hbar/2m_e$ is the Bohr magneton, α refers to the fine-structure constant, e is the electron charge and m represents the electron

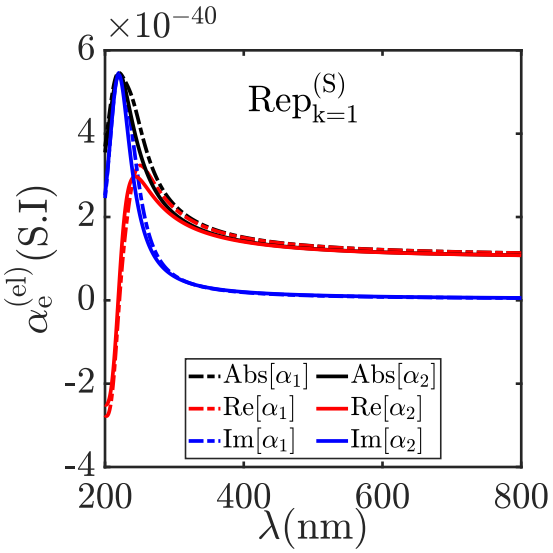


Figure 4.8: Electronic polarizability as a function of the vacuum wavelength λ. The full curves represent the results obtained through the expression given by Eq. (4.17) while the dashed curves refer to the results obtained through the MD-PMM method, considering averaged microscopic polarizability over temporal evolution. Note that the well-matched results validate the evaluation of microscopic polarizability by utilizing the individually averaged transition dipoles and corresponding energies.

mass. The calculated values of electronic relaxation rates $\gamma_j^{(e)}$ (computed from the bandwidth of the UV absorption spectra) together with the ensemble averages of electronic transition energies, electronic/magnetic transition dipole moduli, and the chiral projections are reported in the Table 4.1. To check the consistency of the results based on our ergodic assumptions, we evaluate the full microscopic polarizabilities averaged over time and compare them with the results obtained by considering individually averaged electric/magnetic transition dipole moduli, chiral projections and transition energies. The results are consistent and reported in Fig. 4.8. In the low molecular density limit, the bi-anisotropic macroscopic response of aqueous Reparixin is accounted by the bi-anisotropic constitutive re-

		$j=2$	$j=3$	$j=4$	$j=5$
	$\hbar[\omega_j(1)-\omega_1(1)]$ (eV)	5.20	5.35	5.79	6.55
	$\hbar\gamma_j^{(e)}(1)$ (eV)	1.02	1.02	1.18	1.80
k = 1	$\lvert\mathbf{d}_{1j}(1,\mathrm{S})\rvert/d_0$	0.09	0.17	0.34	0.88
	$\lvert\mathbf{m}_{1j}(1,\mathrm{S})\rvert/m_0$	3.49	5.02	5.04	7.57
	$\mathrm{Im}[\mathbf{d}_{1j}(1,\mathrm{S})\cdot\mathbf{m}_{1j}(1,\mathrm{S})]/d_0m_0$	0.21	-0.23	1.12	6.24
	$\hbar[\omega_j(2)-\omega_1(2)]$ (eV)	4.99	5.23	5.56	6.1
	$\hbar\gamma_j^{(e)}(2)$ (eV)	1.04	1.02	1.10	1.38
k = 2	$\lvert\mathbf{d}_{1j}(2,\mathrm{S})\rvert/d_0$	0.56	0.56	0.56	0.56
	$\lvert\mathbf{m}_{1j}(2,\mathrm{S})\rvert/m_0$	4.44	2.38	6.30	7.07
	$\mathrm{Im}[\mathbf{d}_{1j}(2,\mathrm{S})\cdot\mathbf{m}_{1j}(2,\mathrm{S})]/d_0m_0$	2.07	1.11	-2.83	3.34
	$\hbar[\omega_j(3)-\omega_1(3)]$ (eV)	5.01	5.44	5.62	6.38
	$\hbar\gamma_j^{(e)}(3)$ (eV)	1.04	1.12	1.24	1.76
k = 3	$\lvert\mathbf{d}_{1j}(3,\mathrm{S})\rvert/d_0$	0.72	0.47	0.54	0.47
	$\lvert\mathbf{m}_{1j}(3,\mathrm{S})\rvert/m_0$	4.63	3.35	5.66	7.24
	$\mathrm{Im}[\mathbf{d}_{1j}(3,\mathrm{S})\cdot\mathbf{m}_{1j}(3,\mathrm{S})]/d_0m_0$	-2.51	-0.84	-2.11	3.18
	$\hbar[\omega_j(4)-\omega_1(4)]$ (eV)	5.08	5.33	5.73	5.98
	$\hbar\gamma_j^{(e)}(4)$ (eV)	1.10	1.18	1.30	1.62
k = 4	$\lvert\mathbf{d}_{1j}(4,\mathrm{S})\rvert/d_0$	0.66	0.43	0.23	0.30
	$\lvert\mathbf{m}_{1j}(4,\mathrm{S})\rvert/m_0$	3.64	3.61	5.71	7.81
	$\mathrm{Im}[\mathbf{d}_{1j}(4,\mathrm{S})\cdot\mathbf{m}_{1j}(4,\mathrm{S})]/d_0m_0$	2.17	1.14	1.03	-2.02

Table 4.1: Calculated values of time averaged electric/magnetic transition dipole moments, energies, and relaxation rates associated with the electronic transitions $1\to j$, contributing to the UV absorption spectrum of aqueous S-Reparixin enantiomer for every state basin b_k, where $k=1-4$. The chiroptical response of opposite enantiomeric form is assessed by flipping the sign of chiral projections $(\mathbf{d}_{1j}(k,\mathrm{R})\cdot\mathbf{m}_{1j}(k,\mathrm{R})=-\mathbf{d}_{1j}(k,\mathrm{S})\cdot\mathbf{m}_{1j}(k,\mathrm{S})$. We rescaled the electric/magnetic dipole module to $d_0=|e|a_0$ and $m_0=|e|\hbar/2m_e$, with Bohr radius $a_0=\hbar/m_ec\alpha$, where α is the fine-structure constant, e, and m_e refers to the electron charge and mass.

lations

$$\mathbf{D}(\mathbf{r},t)=\epsilon_0\mathrm{Re}\left\{\left[\epsilon_\mathrm{r}(\lambda)\tilde{\mathbf{E}}_0(\mathbf{r})-i\mu_0c\kappa(\lambda)\tilde{\mathbf{H}}_0(\mathbf{r})\right]e^{-i\omega t}\right\}, \tag{4.19a}$$

$$\mathbf{B}(\mathbf{r},t)=\mu_0\mathrm{Re}\left\{\left[\frac{1}{\mu_0c}i\kappa(\lambda)\tilde{\mathbf{E}}_0(\mathbf{r})+\mu_\mathrm{r}(\lambda)\tilde{\mathbf{H}}_0(\mathbf{r})\right]e^{-i\omega t}\right\}, \tag{4.19b}$$

where $\mathbf{D}(\mathbf{r},t)=\mathrm{Re}[\tilde{\mathbf{D}}(\mathbf{r})e^{-i\omega t}]$ denote the electric displacement vector, $\mathbf{B}(\mathbf{r},t)=\mathrm{Re}[\tilde{\mathbf{B}}(\mathbf{r})e^{-i\omega t}]$ is the magnetic induction field, $\mathbf{E}(\mathbf{r},t)=\mathrm{Re}[\tilde{\mathbf{E}}(\mathbf{r})e^{-i\omega t}]$, and $\mathbf{H}(\mathbf{r},t)=$

$\mathrm{Re}[\tilde{\mathbf{H}}(\mathbf{r})e^{-i\omega t}]$ refer to the electric and magnetic fields, respectively. Furthermore, the chiral sample is characterized by the relative dielectric permittivity $\epsilon_{\mathrm{r}}(\lambda)$, relative dielectric permeability $\mu_{\mathrm{r}}(\lambda)$ and chiral parameter $\kappa(\lambda)$, explicitly given by

$$\epsilon_{\mathrm{r}}(\lambda) = \epsilon_{\mathrm{H_2O}}(\lambda) + n_{\mathrm{mol}}\alpha_{\mathrm{e}}(\lambda)/\epsilon_0, \tag{4.20a}$$

$$\mu_{\mathrm{r}}(\lambda) = 1 + \mu_0 n_{\mathrm{mol}}\alpha_{\mathrm{b}}(\lambda), \tag{4.20b}$$

$$\kappa(\lambda) = i\sum_{a=\mathrm{R,S}} n_{\mathrm{mol}}^{(a)}\alpha_m^{(a)}(\lambda)/\epsilon_0 c. \tag{4.20c}$$

Note that $\epsilon_{\mathrm{r}}(\lambda) = \epsilon_{\mathrm{H_2O}}(\lambda) + \Delta\epsilon_{\mathrm{r}}(\lambda)$ includes both the dielectric permittivity $\epsilon_{\mathrm{H_2O}}$ of the solvent, water in this case, and the correction $\Delta\epsilon_{\mathrm{r}}(\lambda)$ produced by Reparixin. Most importantly, the mixing polarizability flips sign in case of opposite enantiomers, i.e., $\alpha_{\mathrm{m}}^{(\mathrm{R})} = -\alpha_{\mathrm{m}}^{(\mathrm{S})}$. In turn, the chiral parameter is directly proportional to imbalance in enantiomeric number density: $\Delta n_{\mathrm{mol}} = n_{\mathrm{mol}}^{(\mathrm{S})} - n_{\mathrm{mol}}^{(\mathrm{R})}$. Thus, for a racemic mixture with $n_{\mathrm{mol}}^{(\mathrm{R})} = n_{\mathrm{mol}}^{(\mathrm{S})}$, the optical activity is not observed.

Fig. 4.9 illustrates the dependence of $\Delta\epsilon_{\mathrm{r}}$, μ_{r}, and κ of pure S-Reparixin solvated in water (i.e., $n_{\mathrm{mol}}^{(\mathrm{R})} = 0$ and $n_{\mathrm{mol}} = n_{\mathrm{mol}}^{(\mathrm{S})}$) over the vacuum wavelength λ of impinging radiation and the molecular number density n_{mol}. Both the resonant electronic ($\lambda \simeq 250\mathrm{nm}$) and vibrational ($\lambda \simeq 6\mu\mathrm{m}$) transition tails contribute to the chiroptical response of Reparixin. Note that, the dilute number density $10^{-3}\mathrm{nm}^{-3} < n_{\mathrm{mol}} < 10^{-1}\mathrm{nm}^{-3}$, see Figs. 4.9(a-d), of Reparixin leads to the minute contribution of $\mathrm{Re}\left[\epsilon_{\mathrm{r}}(\lambda)\right]$ to the refractive index dispersion: $n(\lambda) = \mathrm{Re}\left[\sqrt{\epsilon_{\mathrm{r}}(\lambda)}\right]$ which is dominated by the water refractive index. The imaginary part of ϵ_{r} leads to the extinction coefficient $k_{\mathrm{ext}}(\lambda) = \mathrm{Im}\left[\sqrt{\epsilon_{\mathrm{r}}(\lambda)}\right]$ which is chirally insensitive and also dominated by the water absorption; see Figs. 4.9(a-d). The chirally insensitive relative magnetic permeability μ_{r} originates from the magnetic response of Reparixin and produces very small corrections to the absorption and dispersion of the chiral mixture; see Figs. 4.9(b-e). Lastly, we show the behavior of the

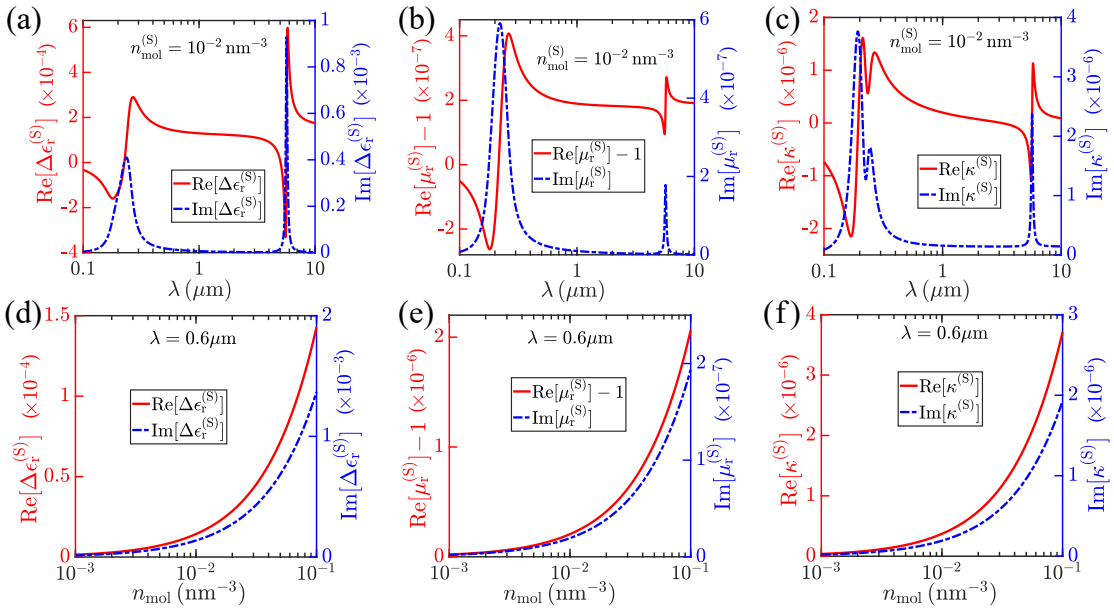


Figure 4.9: Dependencies on $(\mathbf{a}-\mathbf{c})$ vacuum wavelength λ and $(\mathbf{d}-\mathbf{f})$ molecular number density $n_{\rm mol}$ are shown for $(\mathbf{a},\mathbf{d})$ relative dielectric constant correction $\Delta\epsilon_{\rm r}$, $(\mathbf{b},\mathbf{e})$ relative magnetic permeability correction $\mu_{\rm r}-1$ and $(\mathbf{c},\mathbf{f})$ chiral parameter κ. These results obtained for aqueous solution of pure S Reparixin enantiomer at $(\mathbf{a}-\mathbf{c})$ fixed $n_{\rm mol}=10^{-2}{\rm nm}^{-3}$ and $(\mathbf{d}-\mathbf{e})$ fixed $\lambda=0.6\ \mu$m.

complex dimensionless chiral parameter κ as a function of vacuum wavelength λ in Fig. 4.9(c) and molecular number density $n_{\rm mol}$ in Fig. 4.9(e). Observe that the chiral parameter possesses a maximum value at the electronic/vibrational resonance of Reparixin. Importantly, the real and imaginary parts of $\kappa(\lambda)$ govern the rotatory power ($\propto {\rm Re}\,[\kappa(\lambda)]$) and circular dichroism ($\propto {\rm Im}\,[\kappa(\lambda)]$), respectively.

4.6 Plasmon enhanced CD spectroscopy.

In this section, we investigate the potential of SPPs at a planer interface between noble metal and the chiral sample for surface-enhanced chiroptical sensing of dilute drug solutions. Here we focus on an isotropic assembly of Reparixin with dilute molecular density ($n_{\rm mol}=n_{\rm mol}^{\rm (R)}+n_{\rm mol}^{\rm (S)}\simeq 10^{-2}\ {\rm nm}^{-3}$) solvated in water. The confinement of SPPs in the subwavelength region can be utilized to generate large near-field intensities of plasmonic excitations. In turn, the chiroptical

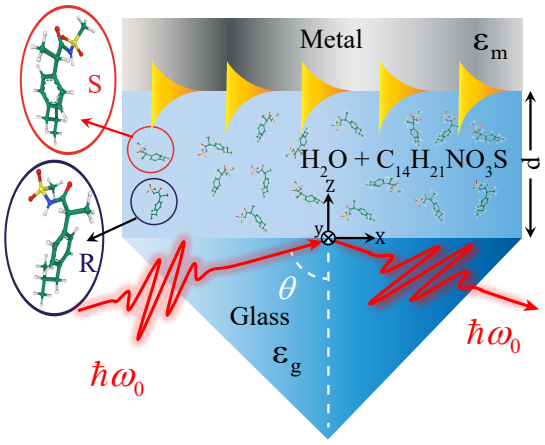


Figure 4.10: Schematic illustration of plasmon-enhanced CD in the Otto coupling scheme with the considered chiral sample consisting of a solution of S and R enantiomers of Reparixin dissolved in water. The thickness of the chiral sample is d, and the molecular density is n_{mol}.

sensitivity can be enhanced through such excitations. In the previous section, we discussed the greater momentum of SPPs than the radiation momentum in a vacuum. Therefore, it is necessary to provide a radiation momentum kick for the excitation of SPPs. Here, we rely on SPPs excitation through prism coupling in the Otto and Kretschmann configurations and investigate the CDDA of the chiral sample upon right/left circularly polarization excitation. In the following sections, we present the evaluation of plasmon-enhanced CDDA by adopting the classical electrodynamics calculations.

4.6.1 Otto coupling scheme.

We illustrate the considered Otto coupling scheme in Fig. 4.10, where the chiral sample is placed at $0 < z < d$ and embedded in between a silica prism and a noble metal substrate. The metal substrate with dielectric constant $\epsilon_{\text{m}}(\lambda)$ is placed at $z > d$ and the chiral drug solution (aqueous Reparixin) with thickness d (100 nm $< d <$ 1 μm) is characterized by the bi-anisotropic response given by Eq. (4.19). We consider a monochromatic impinging radiation with vacuum wavelength λ and arbitrary polarization given by the superposition of right ($s =$

+1) and left ($s = -1$) circularly polarized components. Assuming an incident angle θ of the impinging radiation at the interface between chiral sample and a BK7 silica prism (with relative dielectric permittivity $\epsilon_{\rm g}(\lambda)$ [165]), the electric and magnetic fields of the impinging radiation are expressed as

$$\mathbf{E}_0(\mathbf{r},t) = \sum_{s=\pm1} \mathrm{Re}\Big\{ \left[E_{0,s}^{(\mathrm{o})} \hat{\mathbf{e}}_s^{(0)}(\theta) e^{ik_x x + ik_{\rm g} z} \right] e^{-i\omega t} \Big\}, \tag{4.21a}$$

$$\mathbf{H}_0(\mathbf{r},t) = \sum_{s=\pm1} \mathrm{Re}\Big\{ \frac{s}{i\mu_0 c}\sqrt{\epsilon_{\rm g}} \left[E_{0,s}^{(\mathrm{o})} \hat{\mathbf{e}}_s^{(0)}(\theta) e^{ik_x x + ik_{\rm g} z} \right] e^{-i\omega t} \Big\}, \tag{4.21b}$$

where the unit vectors $\hat{\mathbf{e}}_s^{(0)}(\theta)$ of the right/left circular components are given by

$$\hat{\mathbf{e}}_s^{(0)}(\theta) = \frac{1}{\sqrt{2}}(\cos\theta \hat{\mathbf{e}}_x + is\hat{\mathbf{e}}_y - \sin\theta\hat{\mathbf{e}}_z), \tag{4.22}$$

and the superscript 'o' indicates the considered Otto coupling configuration, $\omega = 2\pi c/\lambda$ is the angular frequency, $k_0 = \omega/c$ is the vacuum wavenumber, and $E_{0,\pm1}^{(\mathrm{o})}$ are the projections of the vectorial field amplitude of the impinging radiation over $\hat{\mathbf{e}}_{\pm1}^{(0)}$. The x-component of the conserved impinging $\mathbf{k}$-vector is indicated by $k_x = k_0\sqrt{\epsilon_g}\sin\theta$ and $k_{\rm g} = \sqrt{k_0^2\epsilon_{\rm g} - k_x^2}$. Analogously, for the reflected fields we get

$$\mathbf{E}_{\rm R}(\mathbf{r},t) = \sum_{s=\pm1} \mathrm{Re}\Big\{ \left[E_{\mathrm{R},s}^{(\mathrm{o})} \hat{\mathbf{e}}_s^{(\mathrm{R})}(\theta) e^{ik_x x - ik_{\rm g} z} \right] e^{-i\omega t} \Big\}, \tag{4.23a}$$

$$\mathbf{H}_{\rm R}(\mathbf{r},t) = \sum_{s=\pm1} \mathrm{Re}\Big\{ \frac{s}{i\mu_0 c}\sqrt{\epsilon_{\rm g}} \left[E_{\mathrm{R},s}^{(\mathrm{o})} \hat{\mathbf{e}}_s^{(\mathrm{R})}(\theta) e^{ik_x x - ik_{\rm g} z} \right] e^{-i\omega t} \Big\}, \tag{4.23b}$$

where $E_{\mathrm{R},\pm1}^{(\mathrm{o})}$ are the projections of the reflected field amplitude over the reflected circular polarization unit vectors

$$\hat{\mathbf{e}}_s^{(\mathrm{R})}(\theta) = \frac{1}{\sqrt{2}}(-\cos\theta \hat{\mathbf{e}}_x + is\hat{\mathbf{e}}_y - \sin\theta\hat{\mathbf{e}}_z). \tag{4.24}$$

The impinging electromagnetic wave interacts with the chiral solution in the region $0 < z < d$. Since circularly polarized waves are the eigenfunctions of the Maxwell

equations, the forward ($\sigma = +1$) and backward ($\sigma = -1$) wave within the chiral medium are solutions of

$$\nabla \cdot \tilde{\mathbf{D}}_{\mathrm{in},\sigma} = 0, \tag{4.25a}$$

$$\nabla \cdot \tilde{\mathbf{B}}_{\mathrm{in},\sigma} = 0, \tag{4.25b}$$

$$\nabla \times \tilde{\mathbf{E}}_{\mathrm{in},\sigma} = i\omega \tilde{\mathbf{B}}_{\mathrm{in},\sigma}, \tag{4.25c}$$

$$\nabla \times \tilde{\mathbf{H}}_{\mathrm{in},\sigma} = -i\omega \tilde{\mathbf{D}}_{\mathrm{in},\sigma}, \tag{4.25d}$$

where

$$\tilde{\mathbf{D}}_{\mathrm{in},\sigma} = \epsilon_0 \left[\epsilon_{\mathrm{r}}(\lambda) \tilde{\mathbf{E}}_{\mathrm{in},\sigma} - i\mu_0 c\kappa(\lambda) \tilde{\mathbf{H}}_{\mathrm{in},\sigma} \right], \tag{4.26a}$$

$$\tilde{\mathbf{B}}_{\mathrm{in},\sigma} = \mu_0 \left[\frac{i\kappa(\lambda)}{\mu_0 c} \tilde{\mathbf{E}}_{\mathrm{in},\sigma} + \mu_{\mathrm{r}}(\lambda) \tilde{\mathbf{H}}_{\mathrm{in},\sigma} \right]. \tag{4.26b}$$

The subscript 'in' refers to the fields inside the chiral solution. The general monochromatic solutions are obtained in the form

$$\mathbf{E}_{\mathrm{in},\sigma=\pm1} = \sum_{s=\pm1} \mathrm{Re}\Big\{ \left[E^{(\mathrm{o})}_{\sigma,s} \mathbf{n}^{\sigma}_{s} e^{ik_x x + i\sigma\beta_s z} \right] e^{-i\omega t} \Big\}, \tag{4.27a}$$

$$\mathbf{H}_{\mathrm{in},\sigma=\pm1} = \sum_{s=\pm1} \mathrm{Re}\Big\{ \frac{s}{i\mu_0 c} \sqrt{\frac{\epsilon_{\mathrm{r}}}{\mu_{\mathrm{r}}}} \left[E^{(\mathrm{o})}_{\sigma,s} \mathbf{n}^{\sigma}_{s} e^{ik_x x + i\sigma\beta_s z} \right] e^{-i\omega t} \Big\}, \tag{4.27b}$$

where

$$\beta_s = \sqrt{k_0^2(\kappa - s\sqrt{\epsilon_{\mathrm{r}}\mu_{\mathrm{r}}})^2 - k_x^2}, \tag{4.28a}$$

$$\mathbf{n}^{\sigma=\pm1}_{s} = \sigma \hat{\mathbf{e}}_x - \frac{k_0}{\beta_s} i \left[\kappa - s\sqrt{\epsilon_{\mathrm{r}}\mu_{\mathrm{r}}} \right] \hat{\mathbf{e}}_y - \frac{k_x}{\beta_s} \hat{\mathbf{e}}_z. \tag{4.28b}$$

Note that the optical activity in the chiral solution is caused by the z-component of polarization-dependent wavenumber β_s . Within the metal substrate ($z > d$)

the fields are obtained as the superposition

$$\mathbf{E}_{\mathrm{T}}(\mathbf{r},t)=\sum_{s=\pm1}\mathrm{Re}\Big\{\Big[E^{(\mathrm{o})}_{\mathrm{T},s}\hat{\mathbf{e}}^{(\mathrm{T})}_{s}(\theta)e^{ik_x x+ik_{\mathrm{m}}z}\Big]\,e^{-i\omega t}\Big\}, \tag{4.29a}$$

$$\mathbf{H}_{\mathrm{T}}(\mathbf{r},t)=\sum_{s=\pm1}\mathrm{Re}\Big\{\frac{s}{i\mu_0 c}\sqrt{\epsilon_{\mathrm{m}}}\Big[E^{(\mathrm{o})}_{\mathrm{T},s}\hat{\mathbf{e}}^{(\mathrm{T})}_{s}(\theta)e^{ik_x x+ik_{\mathrm{m}}z}\Big]\,e^{-i\omega t}\Big\}, \tag{4.29b}$$

where $k_{\mathrm{m}}=\sqrt{k_0^2\epsilon_{\mathrm{m}}-k_x^2}$ and $E^{(\mathrm{o})}_{\mathrm{T},\pm1}$ are the projection of transmitted field amplitudes over

$$\hat{\mathbf{e}}^{(\mathrm{T})}_{s}(\theta)=\frac{1}{\sqrt{2}}\Big[\sqrt{1-(\epsilon_{\mathrm{g}}/\epsilon_{\mathrm{m}})\sin^2\theta}\hat{\mathbf{e}}_x+is\hat{\mathbf{e}}_y-\sqrt{\epsilon_{\mathrm{g}}/\epsilon_{\mathrm{m}}}\sin\theta\hat{\mathbf{e}}_z\Big]. \tag{4.30}$$

Thus, in the considered Otto configuration, the electric/magnetic fields, displacement vector and magnetic induction field over all space are provided by

$$\begin{aligned}\mathbf{E}_{\mathrm{o}}(\mathbf{r},t)=\sum_{s=\pm1}\mathrm{Re}\Big\{\Big[&\tilde{\mathbf{E}}^{(\mathrm{o},s)}_{<}(\mathbf{r})\Theta(-z)+\tilde{\mathbf{E}}^{(\mathrm{o},s)}_{\mathrm{in}}(\mathbf{r})\Theta_{\mathrm{in}}(z)\\&+\tilde{\mathbf{E}}^{(\mathrm{o},s)}_{>}(\mathbf{r})\Theta(z-d)\Big]\,e^{-i\omega t}\Big\},\end{aligned} \tag{4.31a}$$

$$\begin{aligned}\mathbf{H}_{\mathrm{o}}(\mathbf{r},t)=\sum_{s=\pm1}\mathrm{Re}\Big\{\frac{s}{i\mu_0 c}\Big[&\sqrt{\epsilon_{\mathrm{g}}}\tilde{\mathbf{E}}^{(\mathrm{o},s)}_{<}(\mathbf{r})\Theta(-z)+\sqrt{\epsilon_{\mathrm{r}}/\mu_{\mathrm{r}}}\tilde{\mathbf{E}}^{(\mathrm{o},s)}_{\mathrm{in}}(\mathbf{r})\Theta_{\mathrm{in}}(z)\\&+\sqrt{\epsilon_{\mathrm{m}}}\tilde{\mathbf{E}}^{(\mathrm{o},s)}_{>}(\mathbf{r})\Theta(z-d)\Big]\,e^{-i\omega t}\Big\},\end{aligned} \tag{4.31b}$$

$$\begin{aligned}\mathbf{D}_{\mathrm{o}}(\mathbf{r},t)=\sum_{s=\pm1}\mathrm{Re}\Big\{\epsilon_0\Big[&\epsilon_{\mathrm{g}}\tilde{\mathbf{E}}^{(\mathrm{o},s)}_{<}(\mathbf{r})\Theta(-z)+\Big(\epsilon_{\mathrm{r}}-s\kappa\sqrt{\epsilon_{\mathrm{r}}/\mu_{\mathrm{r}}}\Big)\,\tilde{\mathbf{E}}^{(\mathrm{o},s)}_{\mathrm{in}}(\mathbf{r})\Theta_{\mathrm{in}}(z)\\&+\epsilon_{\mathrm{m}}\tilde{\mathbf{E}}^{(\mathrm{o},s)}_{>}(\mathbf{r})\Theta(z-d)\Big]\,e^{-i\omega t}\Big\},\end{aligned} \tag{4.31c}$$

$$\begin{aligned}\mathbf{B}_{\mathrm{o}}(\mathbf{r},t)=\sum_{s=\pm1}\mathrm{Re}\Big\{\frac{1}{c}\Big[&-is\sqrt{\epsilon_{\mathrm{g}}}\tilde{\mathbf{E}}^{(\mathrm{o},s)}_{<}(\mathbf{r})\Theta(-z)+i\left(\kappa-s\sqrt{\epsilon_{\mathrm{r}}\mu_{\mathrm{r}}}\right)\tilde{\mathbf{E}}^{(\mathrm{o},s)}_{\mathrm{in}}(\mathbf{r})\Theta_{\mathrm{in}}(z)\\&-is\sqrt{\epsilon_{\mathrm{m}}}\tilde{\mathbf{E}}^{(\mathrm{o},s)}_{>}(\mathbf{r})\Theta(z-d)\Big]\,e^{-i\omega t}\Big\},\end{aligned} \tag{4.31d}$$

where $\Theta(z)$ is the Heaviside step function, $\Theta_{\text{in}}(z) = \Theta(z) - \Theta(z-d)$ and

$$\tilde{\mathbf{E}}_{<}^{(\text{o},s)} = \left[E_{0,s}^{(\text{o})}\hat{\mathbf{e}}_s^{(0)}e^{ik_g z} + E_{\text{R},s}^{(\text{o})}\hat{\mathbf{e}}_s^{(\text{R})}e^{-ik_g z}\right]e^{ik_x x}, \tag{4.32a}$$

$$\tilde{\mathbf{E}}_{\text{in}}^{(\text{o},s)}(\mathbf{r}) = \sum_{\sigma=\pm 1} E_{\sigma,s}^{(\text{o})}\mathbf{n}_s^{\sigma}e^{ik_x x + i\sigma\beta_s z}, \tag{4.32b}$$

$$\tilde{\mathbf{E}}_{>}^{(\text{o},s)}(\mathbf{r}) = E_{\text{T},s}^{(\text{o})}\hat{\mathbf{e}}_s^{(\text{T})}e^{ik_x x + i\beta_s z}. \tag{4.32c}$$

Boundary Conditions (BCs) for the continuity of (I) the normal component of the displacement vector and magnetic induction field and (II) the tangential component of electric and magnetic fields at the interfaces ($z = 0$ and $z = d$) provide

$$\mathbf{D}_{\text{o}}(x,y,0^-,t)\cdot\hat{e}_z = \mathbf{D}_{\text{o}}(x,y,0^+,t)\cdot\hat{e}_z, \tag{4.33a}$$

$$\hat{e}_z \times \left[\mathbf{E}_{\text{o}}(x,y,0^+,t) - \mathbf{E}_{\text{o}}(x,y,0^-,t)\right] = 0, \tag{4.33b}$$

$$\mathbf{D}_{\text{o}}(x,y,d^-,t)\cdot\hat{e}_z = \mathbf{D}_{\text{o}}(x,y,d^+,t)\cdot\hat{e}_z, \tag{4.33c}$$

$$\hat{e}_z \times \left[\mathbf{E}_{\text{o}}(x,y,d^+,t) - \mathbf{E}_{\text{o}}(x,y,d^-,t)\right] = 0, \tag{4.33d}$$

$$\mathbf{B}_{\text{o}}(x,y,0^-,t)\cdot\hat{e}_z = \mathbf{B}_{\text{o}}(x,y,0^+,t)\cdot\hat{e}_z, \tag{4.33e}$$

$$\hat{e}_z \times \left[\mathbf{H}_{\text{o}}(x,y,0^+,t) - \mathbf{H}_{\text{o}}(x,y,0^-,t)\right] = 0, \tag{4.33f}$$

$$\mathbf{B}_{\text{o}}(x,y,d^-,t)\cdot\hat{e}_z = \mathbf{B}_{\text{o}}(x,y,d^+,t)\cdot\hat{e}_z, \tag{4.33g}$$

$$\hat{e}_z \times \left[\mathbf{H}_{\text{o}}(x,y,d^+,t) - \mathbf{H}_{\text{o}}(x,y,d^-,t)\right] = 0. \tag{4.33h}$$

Now plugging the fields from Eq. (4.31) into the BCs Eq. (4.33), we obtain the following system of algebraic equations

$$\sum_{s=\pm1}\Big[E^{(\mathrm{o})}_{0,s}+E^{(\mathrm{o})}_{\mathrm{R},s}\Big]=\sqrt{2}\sum_{s=\pm1}\frac{k_0}{\beta_s\sqrt{\epsilon_\mathrm{g}}}\Big(\epsilon_\mathrm{r}-\kappa s\sqrt{\frac{\epsilon_\mathrm{r}}{\mu_\mathrm{r}}}\Big)\Big[E^{(\mathrm{o})}_{+,s}+E^{(\mathrm{o})}_{-,s}\Big], \tag{4.34a}$$

$$\sum_{s=\pm1}\Big[E^{(\mathrm{o})}_{0,s}-E^{(\mathrm{o})}_{\mathrm{R},s}\Big]=\sqrt{2}\sum_{s=\pm1}\frac{k_0\sqrt{\epsilon_\mathrm{g}}}{k_\mathrm{g}}\Big[E^{(\mathrm{o})}_{+,s}-E^{(\mathrm{o})}_{-,s}\Big], \tag{4.34b}$$

$$\sum_{s=\pm1}s\Big[E^{(\mathrm{o})}_{0,s}+E^{(\mathrm{o})}_{\mathrm{R},s}\Big]=\sqrt{2}\sum_{s=\pm1}\frac{k_0}{\beta_s}\Big(-\kappa+s\sqrt{\epsilon_\mathrm{r}\mu_\mathrm{r}}\Big)\Big[E^{(\mathrm{o})}_{+,s}+E^{(\mathrm{o})}_{-,s}\Big], \tag{4.34c}$$

$$\sum_{s=\pm1}s\Big[E^{(\mathrm{o})}_{0,s}-E^{(\mathrm{o})}_{\mathrm{R},s}\Big]=\sqrt{2}\sum_{s=\pm1}\frac{k_0}{k_\mathrm{g}}s\sqrt{\frac{\epsilon_\mathrm{r}}{\mu_\mathrm{r}}}\Big[E^{(\mathrm{o})}_{+,s}-E^{(\mathrm{o})}_{-,s}\Big], \tag{4.34d}$$

$$\sqrt{2}\sum_{s=\pm1}\frac{k_0}{\beta_s}\left(-\kappa+s\sqrt{\epsilon_\mathrm{r}\mu_\mathrm{r}}\right)\Big[E^{(0)}_{+,s}e^{i\beta_s d}+E^{(0)}_{-,s}e^{-i\beta_s d}\Big]=\sum_{s=\pm1}sE^{(0)}_{\mathrm{T},s}e^{ik_\mathrm{m}d}, \tag{4.34e}$$

$$\sqrt{2}\frac{k_0}{k_\mathrm{m}}\sum_{s=\pm1}s\sqrt{\frac{\epsilon_\mathrm{r}}{\mu_\mathrm{r}}}\Big[E^{(\mathrm{o})}_{+,s}e^{i\beta_s d}-E^{(\mathrm{o})}_{-,s}e^{-i\beta_s d}\Big]=\sum_{s=\pm1}sE^{(\mathrm{o})}_{\mathrm{T},s}e^{ik_\mathrm{m}d}, \tag{4.34f}$$

$$\sqrt{2}\sum_{s=\pm1}\frac{k_0}{\beta_s\sqrt{\epsilon_\mathrm{m}}}\Big(\epsilon_\mathrm{r}-\kappa s\sqrt{\frac{\epsilon_\mathrm{r}}{\mu_\mathrm{r}}}\Big)\Big[E^{(\mathrm{o})}_{+,s}e^{i\beta_s d}+E^{(\mathrm{o})}_{-,s}e^{-i\beta_s d}\Big]=\sum_{s=\pm1}E^{(\mathrm{o})}_{\mathrm{T},s}e^{ik_\mathrm{m}d}, \tag{4.34g}$$

$$\sqrt{2}\sum_{s=\pm1}\frac{k_0\sqrt{\epsilon_\mathrm{m}}}{k_\mathrm{m}}\Big[E^{(\mathrm{o})}_{+,s}e^{i\beta_s d}-E^{(\mathrm{o})}_{-,s}e^{-i\beta_s d}\Big]=\sum_{s=\pm1}\psi_{\mathrm{T},s}e^{ik_\mathrm{m}d}. \tag{4.34h}$$

Thus, the boundary conditions lead to an 8×8 inhomogeneous system of algebraic equations which can be rewritten in the matrix form

$$\begin{bmatrix}
-1 & -1 & -g^{(1)}_{+} & -g^{(1)}_{+} & -g^{(1)}_{-} & -g^{(1)}_{-} & 0 & 0\\
1 & 1 & g^{(2)}_{+} & g^{(2)}_{-} & g^{(2)}_{+} & g^{(2)}_{-} & 0 & 0\\
-1 & 1 & -c^{(1)}_{+} & -c^{(1)}_{+} & -c^{(1)}_{-} & -c^{(1)}_{-} & 0 & 0\\
1 & -1 & c^{(2)}_{+} & c^{(2)}_{-} & c^{(2)}_{-} & c^{(2)}_{+} & 0 & 0\\
0 & 0 & r^{(1)}_{+,+} & r^{(1)}_{+,-} & r^{(1)}_{-,+} & r^{(1)}_{-,-} & \tau_- & \tau_+\\
0 & 0 & r^{(2)}_{+,+} & -r^{(2)}_{-,+} & -r^{(2)}_{+,-} & r^{(2)}_{-,-} & \tau_- & \tau_+\\
0 & 0 & t^{(1)}_{+,-,+} & t^{(1)}_{+,-,-} & t^{(1)}_{-,+,+} & t^{(1)}_{-,+,-} & \tau_- & \tau_-\\
0 & 0 & t^{(2)}_{+,+,+} & t^{(2)}_{-,+,-} & t^{(2)}_{+,-,+} & t^{(2)}_{-,-,-} & \tau_- & \tau_-
\end{bmatrix}\cdot\begin{bmatrix}E^{(\mathrm{o})}_{\mathrm{R},+}\\E^{(\mathrm{o})}_{\mathrm{R},-}\\E^{(\mathrm{o})}_{+,+}\\E^{(\mathrm{o})}_{-,+}\\E^{(\mathrm{o})}_{+,-}\\E^{(\mathrm{o})}_{-,-}\\E^{(\mathrm{o})}_{\mathrm{T},+}\\E^{(\mathrm{o})}_{\mathrm{T},-}\end{bmatrix}=\hat{S}\cdot\begin{bmatrix}E^{(\mathrm{o})}_{\mathrm{R},+}\\E^{(\mathrm{o})}_{\mathrm{R},-}\\E^{(\mathrm{o})}_{+,+}\\E^{(\mathrm{o})}_{-,+}\\E^{(\mathrm{o})}_{+,-}\\E^{(\mathrm{o})}_{-,-}\\E^{(\mathrm{o})}_{\mathrm{T},+}\\E^{(\mathrm{o})}_{\mathrm{T},-}\end{bmatrix}=\begin{bmatrix}E^{(\mathrm{o})}_{0,+}+E^{(\mathrm{o})}_{0,-}\\E^{(\mathrm{o})}_{0,+}+E^{(\mathrm{o})}_{0,-}\\E^{(\mathrm{o})}_{0,+}-E^{(\mathrm{o})}_{0,-}\\E^{(\mathrm{o})}_{0,+}-E^{(\mathrm{o})}_{0,-}\\0\\0\\0\\0\end{bmatrix}, \tag{4.35}$$

where $\tau_\pm = \pm e^{ik_\mathrm{m}d}$ and

$$g_\pm^{(1)} = -\frac{\sqrt{2}k_0}{\beta_\pm\sqrt{\epsilon_\mathrm{g}}}\Big(\epsilon_\mathrm{r} \mp \kappa\sqrt{\epsilon_\mathrm{r}\mu_\mathrm{r}}\Big), \tag{4.36a}$$

$$g_\pm^{(2)} = \pm k_0\sqrt{2\epsilon_\mathrm{g}}/k_\mathrm{g}, \tag{4.36b}$$

$$c_\pm^{(1)} = \sqrt{2}k_0\Big(\kappa \mp \sqrt{\epsilon_\mathrm{r}\mu_\mathrm{r}}\Big)/\beta_\pm, \tag{4.36c}$$

$$c_\pm^{(2)} = \pm k_0\sqrt{2\epsilon_\mathrm{r}/\mu_\mathrm{r}}/k_\mathrm{g}, \tag{4.36d}$$

$$r_{\sigma,s}^{(1)} = \frac{k_0\sqrt{2}}{\beta_\sigma}\Big(-\kappa + \sigma\sqrt{\epsilon_\mathrm{r}\mu_\mathrm{r}}\Big)e^{is\beta_\sigma d}, \tag{4.36e}$$

$$r_{s,\sigma}^{(2)} = k_0\sqrt{2\epsilon_\mathrm{r}/\mu_\mathrm{r}}e^{is\beta_\sigma d}/k_\mathrm{m}, \tag{4.36f}$$

$$t_{s,\sigma,p}^{(1)} = \frac{k_0\sqrt{2}}{\beta_s\sqrt{\epsilon_\mathrm{m}}}\Big(\epsilon_\mathrm{r} + \sigma\kappa\sqrt{\frac{\epsilon_\mathrm{r}}{\mu_\mathrm{r}}}\Big)e^{ip\beta_s d}, \tag{4.36g}$$

$$t_{s,\sigma,p}^{(2)} = sk_0\sqrt{2\epsilon_\mathrm{m}}e^{ip\beta_\sigma d}/k_\mathrm{m}. \tag{4.36h}$$

In turn, the s-dependent forward ($\sigma = +1$) and backward ($\sigma = -1$) amplitudes within the chiral medium $E_{\sigma,s}^{(o)}$, the reflected ($E_{\mathrm{R},s}^{(\mathrm{o})}$) and transmitted ($E_{\mathrm{T},s}^{(\mathrm{o})}$) field amplitudes can be determined from

$$\begin{bmatrix} E_{\mathrm{R},+}^{(\mathrm{o})} \\ E_{\mathrm{R},-}^{(\mathrm{o})} \\ E_{+,+}^{(\mathrm{o})} \\ E_{-,+}^{(\mathrm{o})} \\ E_{+,-}^{(\mathrm{o})} \\ E_{-,-}^{(\mathrm{o})} \\ E_{\mathrm{T},+}^{(\mathrm{o})} \\ E_{\mathrm{T},-}^{(\mathrm{o})} \end{bmatrix} = \hat{S}^{-1} \begin{bmatrix} E_{0,+}^{(\mathrm{o})} + E_{0,-}^{(\mathrm{o})} \\ E_{0,+}^{(\mathrm{o})} + E_{0,-}^{(\mathrm{o})} \\ E_{0,+}^{(\mathrm{o})} - E_{0,-}^{(\mathrm{o})} \\ E_{0,+}^{(\mathrm{o})} - E_{0,-}^{(\mathrm{o})} \\ 0 \\ 0 \\ 0 \\ 0 \end{bmatrix} \tag{4.37}$$

Now, for any impinging field components ($E_{0,\pm1}^{(\mathrm{o})}$), we obtain $E_{\mathrm{R},\pm1}^{(\mathrm{o})}$ and $E_{\mathrm{T},\pm1}^{(\mathrm{o})}$ by numerically inverting $\hat{S}$. Note that, in a racemic mixture of the drug solution, $n_\mathrm{mol}^{(\mathrm{S})} = n_\mathrm{mol}^{(\mathrm{R})}$, and essentially the chiral parameter of the mixture vanishes $\kappa(\lambda) = 0$. In that case, we can split the electromagnetic excitation of the system into

independent TM and Transverse Electric (TE) components. On the other hand, non-racemic mixtures where $n_{\text{mol}}^{(\text{S})} \neq n_{\text{mol}}^{(\text{R})}$ generate mixed polarization dynamics due to the chirality of Reparixin enantiomers. In such a case, the absorption of radiation by the system can be determined by subtracting the power carried by the reflected and transmitted waves from the total incident power. To do that, we calculate the perpendicular power density[2] averaged over a single cycle (for $z < 0$ and $z > d$), which is given by

$$\begin{aligned}\int_{-\infty}^{\infty} dx \langle \mathbf{S}_{\text{o}}(\mathbf{r},t)\cdot\hat{\mathbf{e}}_z\rangle_{\text{T}} &= \frac{1}{2}\int_{-\infty}^{\infty} dx \text{Re}\left[\mathbf{E}_{\text{o}}(\mathbf{r},t)\times\mathbf{H}_{\text{o}}^{*}(\mathbf{r},t)\right]\cdot\hat{\mathbf{e}}_z \\ &= \begin{cases} \dfrac{1}{2}\displaystyle\sum_{s=\pm1}\left[|E_{0,s}^{(\text{o})}|^2 - |E_{\text{R},s}^{(\text{o})}|^2\right]\frac{1}{\mu_0 c k_0}\text{Re}\left[k_{\text{g}}\right], & z<0, \\ 0, & z >> d, \end{cases}\end{aligned}$$

where $\mathbf{S}$ is the Poynting vector. In turn, the absorbance of the system in the Otto coupling scheme upon excitation with right ($s=+1, E_{0,-}^{(\text{o})}$) and left ($s=-1, E_{0,+}^{(\text{o})}$) circularly polarized radiation is given by

$$A_s^{(\text{o})}(\theta,\lambda) = 1 - \frac{\displaystyle\sum_{\sigma=\pm1}|E_{\text{R},\sigma}^{(\text{o})}|^2}{|E_{0,s}^{(\text{o})}|^2}. \tag{4.38}$$

We emphasize that, in the considered Otto coupling scheme, the transmitted intensity vanishes due to the absorption as we assumed $z >> d$, meaning that the metal/chiral sample is infinitely extended. However, in practice, the metal/chiral sample possesses finite physical dimensions regarding experimental realizations. In that case, the absorbance can be determined from $A = 1 - I_{\text{R}}/I_0 - I_{\text{T}}/I_0$, where $I_{0,\text{R,T}}$ represent the impinging intensity (I_0) and measure reflected (I_{R}) and transmitted (I_{R}) intensities, respectively. Once the absorption of RCP and

[2]The portion of energy flow that passes through the surface projection over the direction of wave propagation.

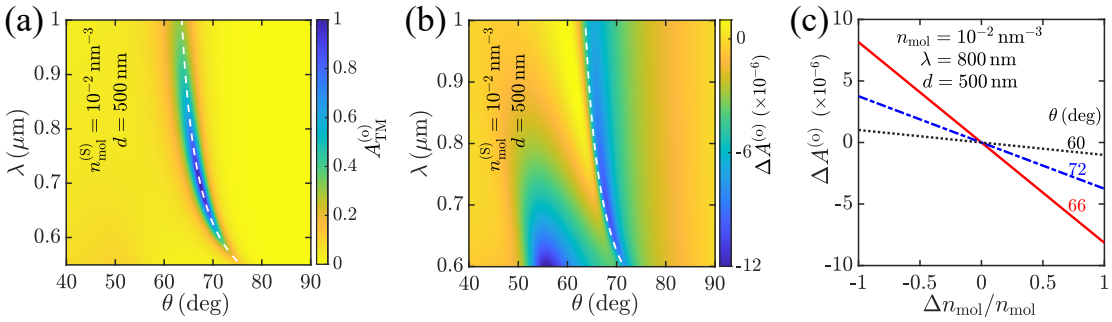


Figure 4.11: Dependence of (**a**) TM absorbance $A_{\rm TM}^{(\rm o)}(\theta,\lambda)$, under TM linear polarization excitation, and (**b**) CDDA, $\Delta A^{(\rm o)}(\theta,\lambda) = A_{\rm R}(\theta,\lambda) - A_{\rm L}(\theta,\lambda)$ under circular polarization excitation, over the vacuum wavelength λ and the incidence angle θ of the incoming radiation in the Otto coupling scheme, as depicted in Fig. 4.10. These plots are obtained for pure aqueous S Reparixin enantiomer with corresponding number density imbalance $\Delta n_{\rm mol} = n_{\rm mol}^{(\rm S)} - n_{\rm mol}^{(\rm R)} = n_{\rm mol}$. (**c**) Dependence of CDDA over the enantiomeric excess number density defined by $\Delta n_{\rm mol} = n_{\rm mol}^{(\rm S)} - n_{\rm mol}^{(\rm R)}$ for several θ and fixed $\lambda = 800$ nm. All these results are calculated using a silver substrate (associated dielectric constant $\epsilon_{\rm m}$[166]), $d = 500$ nm thick chiral sample with fixed number density $n_{\rm mol} = 10^{-2}$ nm^{-3}.

LCP is known, the measurement of CDDA is straightforward and is given by $\Delta A^{(\rm o)}(\theta,\lambda) = A_{+}^{(\rm o)} - A_{-}^{(\rm o)}$, where $A_{+}^{(\rm o)}$ and $A_{+}^{(\rm o)}$ are the absorbance of the system upon RCP and LCP excitation, respectively. Additionally, for TM impinging polarization, the impinging field amplitude is given by $E_{0,+}^{(\rm o)} = E_{0,-}^{(\rm o)} = E_0$. In turn, the TM absorbance is provided by

$$A_{\rm TM}^{(\rm o)}(\theta,\lambda) = 1 - \frac{\sum\limits_{\sigma=\pm 1} |E_{{\rm R},\sigma}^{(\rm o)}|^2}{|E_0|^2}. \tag{4.39}$$

Fig. 4.11(a) illustrates the dependence of TM absorbance $A_{\rm TM}^{(\rm o)}$ over λ and θ in the Otto coupling scheme using silver as a metal substrate, while Fig. 4.11(b) illustrates the dependence of CDDA, $\Delta A^{(\rm o)}$, over λ and θ for $d = 500$ nm and $n_{\rm mol}^{(\rm S)} = 10^{-2}$ nm^{-3}. Note that the maximum $A_{\rm TM}^{(\rm o)}$ is observed at the SPP excitation curve featured by

$$\theta_{\rm SPP}(\lambda) \simeq \arcsin\left\{ {\rm Re}\sqrt{\frac{\epsilon_{\rm r}(\lambda)\epsilon_{\rm m}(\lambda)}{\epsilon_{\rm g}(\lambda)[\epsilon_{\rm r}(\lambda)+\epsilon_{\rm m}(\lambda)]}} \right\}. \tag{4.40}$$

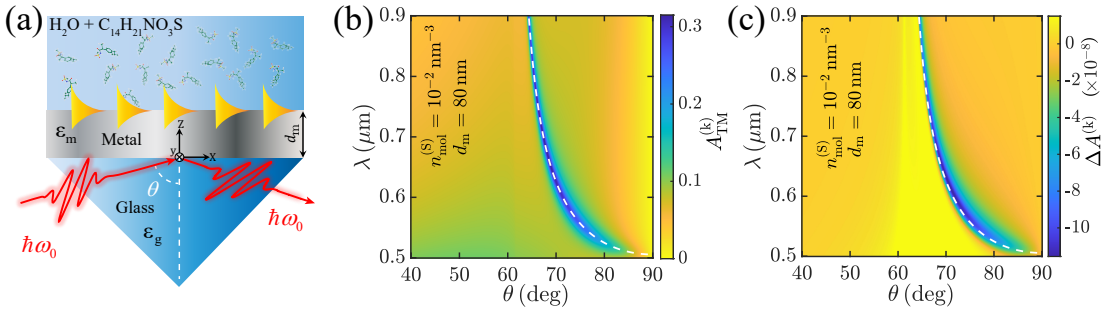


Figure 4.12: (**a**) Schematic illustration of plasmon-enhanced CD in the Kretschmann coupling scheme with the considered chiral sample consisting of a solution of S and R enantiomers of Reparixin dissolved in water. The thickness of the metal is $d_m = 80$ nm and the molecular density of chiral sample is n_{mol}. Dependence of (**b**) TM absorbance $A_{TM}^{(k)}(\theta, \lambda)$, under TM linear polarization excitation, and (**c**) CDDA, $\Delta A^{(k)}(\theta, \lambda) = A_R(\theta, \lambda) - A_L(\theta, \lambda)$ under circular polarization excitation, over the vacuum wavelength λ and the incidence angle θ of the incoming radiation in the Kretschmann coupling scheme. These plots are obtained for pure aqueous S Reparixin enantiomer with corresponding number density $\Delta n_{mol} = n_{mol}^{(S)} - n_{mol}^{(R)}$ and using a silver substrate with associated dielectric constant ϵ_m[166].

The white dashed lines in Fig. 4.11(a,b) represent the SPP excitation curve. Importantly, the CDDA is enhanced at the SPP dispersion curve because of SPP resonant absorption. On top of this, for right/left circular polarization excitation, we observe a Fabry-Perot resonance at 600 nm $< \lambda <$ 800 nm and $50° < \theta < 60°$. The CDDA is enhanced by a factor $f \simeq 10$ due to such Fabry-Perot resonance. Fig. 4.11(c) illustrates the dependence of $\Delta A^{(o)}$ in Otto coupling scheme over enantimeric excess $\Delta n_{mol}/n_{mol}$ for several distinct incidence angles at fixed wavelength $\lambda = 800$ nm considering $d = 500$ nm and $n_{mol} = 10^{-2}$ nm^{-3}. Note that in a recamic mixture ($\Delta n_{mol} = 0$), the CDDA $\Delta A^{(o)}$ vanishes and alters sign for opposite enantiomers. In turn, the enantiomeric imbalance can be retrieved by measuring the CDDA of the chiral mixture.

4.6.2 Kretschmann coupling scheme.

Fig. 4.12 (a) illustrates the considered Kretschmann coupling scheme, where the metal substrate (of thickness d_m) is sandwiched between the silica prism and the

chiral drug solution, i.e., aqueous Reparixin. This way the metal is located at $0 < z < d_{\mathrm{m}}$ and the chiral drug solution is placed at $z > d_{\mathrm{m}}$. We consider the monochromatic radiation with vacuum wavelength λ and arbitrary polarization given by the superposition of right ($s = +1$) and left ($s = -1$) circularly polarized components, similar to Otto configuration, impinging from the BK7 silica prism, where the electric and magnetic fields of the impinging radiation are given by

$$\mathbf{E}_0(\mathbf{r},t) = \sum_{s=\pm 1} \mathrm{Re}\Big\{ \Big[E^{(\mathrm{k})}_{0,s} \hat{\mathbf{e}}^{(0)}_s(\theta) e^{ik_x x + ik_{\mathrm{g}} z} \Big] e^{-i\omega t} \Big\}, \tag{4.41a}$$

$$\mathbf{H}_0(\mathbf{r},t) = \sum_{s=\pm 1} \mathrm{Re}\Big\{ \frac{s}{i\mu_0 c} \sqrt{\epsilon_{\mathrm{g}}} \Big[E^{(\mathrm{k})}_{0,s} \hat{\mathbf{e}}^{(0)}_s(\theta) e^{ik_x x + ik_{\mathrm{g}} z} \Big] e^{-i\omega t} \Big\}, \tag{4.41b}$$

the superscript 'k' indicates the considered Kretschmann coupling configuration, and the unit vectors $\hat{\mathbf{e}}^{(0)}_s(\theta)$ are given by Eq. (4.22). Again, the reflected fields in this case are given by

$$\mathbf{E}_{\mathrm{R}}(\mathbf{r},t) = \sum_{s=\pm 1} \mathrm{Re}\Big\{ \Big[E^{(\mathrm{k})}_{\mathrm{R},s} \hat{\mathbf{e}}^{(\mathrm{R})}_s(\theta) e^{ik_x x - ik_{\mathrm{g}} z} \Big] e^{-i\omega t} \Big\}, \tag{4.42a}$$

$$\mathbf{H}_{\mathrm{R}}(\mathbf{r},t) = \sum_{s=\pm 1} \mathrm{Re}\Big\{ \frac{s}{i\mu_0 c} \sqrt{\epsilon_{\mathrm{g}}} \Big[E^{(\mathrm{k})}_{\mathrm{R},s} \hat{\mathbf{e}}^{(\mathrm{R})}_s(\theta) e^{ik_x x - ik_{\mathrm{g}} z} \Big] e^{-i\omega t} \Big\}, \tag{4.42b}$$

where the unit vectors $\hat{\mathbf{e}}^{(\mathrm{R})}_s(\theta)$ are given by Eq. (4.24). Now, in this configuration, the chiral drug solution is located at $z > d_{\mathrm{m}}$, and the forward wave within the chiral sample is the solution of the Maxwell equations

$$\nabla \cdot \tilde{\mathbf{D}}_{z>d_{\mathrm{m}}} = 0, \tag{4.43a}$$

$$\nabla \cdot \tilde{\mathbf{B}}_{z>d_{\mathrm{m}}} = 0, \tag{4.43b}$$

$$\nabla \times \tilde{\mathbf{E}}_{z>d_{\mathrm{m}}} = i\omega \tilde{\mathbf{B}}_{z>d_{\mathrm{m}}}, \tag{4.43c}$$

$$\nabla \times \tilde{\mathbf{H}}_{z>d_{\mathrm{m}}} = -i\omega \tilde{\mathbf{D}}_{z>d_{\mathrm{m}}}, \tag{4.43d}$$

where

$$\tilde{\mathbf{D}}_{z>d_\mathrm{m}} = \epsilon_0 \left[\epsilon_\mathrm{r}(\lambda)\tilde{\mathbf{E}}_{z>d_\mathrm{m}} - i\mu_0 c\kappa(\lambda)\tilde{\mathbf{H}}_{z>d_\mathrm{m}}\right], \tag{4.44a}$$

$$\tilde{\mathbf{B}}_{z>d_\mathrm{m}} = \mu_0 \left[\frac{i\kappa(\lambda)}{\mu_0 c}\tilde{\mathbf{E}}_{z>d_\mathrm{m}} + \mu_\mathrm{r}(\lambda)\tilde{\mathbf{H}}_{z>d}\right]. \tag{4.44b}$$

We obtain the general monochromatic solution

$$\mathbf{E}_{z>d_\mathrm{m}} = \sum_{s=\pm 1} \mathrm{Re}\Big\{ \left[E^{(\mathrm{k})}_{\mathrm{T},s}\mathbf{n}^{(z>d_\mathrm{m})}_s e^{ik_x x + i\beta_s z}\right] e^{-i\omega t}\Big\}, \tag{4.45a}$$

$$\mathbf{H}_{z>d_\mathrm{m}} = \sum_{s=\pm 1} \mathrm{Re}\Big\{ \frac{s}{i\mu_0 c}\sqrt{\frac{\epsilon_\mathrm{r}}{\mu_\mathrm{r}}}\left[E^{(\mathrm{k})}_{\mathrm{T},s}\mathbf{n}^{(z>d_\mathrm{m})}_s e^{ik_x x + i\beta_s z}\right] e^{-i\omega t}\Big\}, \tag{4.45b}$$

where β_s is given by Eq. (4.29) and

$$\mathbf{n}^{(z>d_\mathrm{m})}_s = \hat{\mathbf{e}}_x - \frac{k_0}{\beta_s} i\left[\kappa - s\sqrt{\epsilon_\mathrm{r}\mu_\mathrm{r}}\right]\hat{\mathbf{e}}_y - \frac{k_x}{\beta_s}\hat{\mathbf{e}}_z. \tag{4.46}$$

The forward ($\sigma = +1$) and backward ($\sigma = -1$) fields within the metal are obtained as

$$\mathbf{E}_{\mathrm{in},\sigma=\pm 1} = \sum_{s=\pm 1} \mathrm{Re}\Big\{ \left[E^{(\mathrm{k})}_{\sigma,s}\mathbf{n}^{\sigma}_s e^{ik_x x + i\sigma k_\mathrm{m} z}\right] e^{-i\omega t}\Big\}, \tag{4.47a}$$

$$\mathbf{H}_{\mathrm{in},\sigma=\pm 1} = \sum_{s=\pm 1} \mathrm{Re}\Big\{ \frac{s}{i\mu_0 c}\sqrt{\epsilon_\mathrm{m}}\left[E^{(\mathrm{k})}_{\sigma,s}\mathbf{n}^{\sigma}_s e^{ik_x x + i\sigma k_\mathrm{m} z}\right] e^{-i\omega t}\Big\}, \tag{4.47b}$$

where

$$\mathbf{n}^{\sigma=\pm 1}_s = \frac{1}{\sqrt{2}}\Big[\sigma\sqrt{1 - (\epsilon_\mathrm{g}/\epsilon_\mathrm{m})\sin^2\theta}\hat{\mathbf{e}}_x + is\hat{\mathbf{e}}_y - \sqrt{\epsilon_\mathrm{g}/\epsilon_\mathrm{m}}\sin\theta\hat{\mathbf{e}}_z\Big]. \tag{4.48}$$

In turn, in the considered Kretschmann configuration, the electric/magnetic fields, displacement vector and magnetic induction field over all space are provided by

$$\mathbf{E}_{\mathrm{k}}(\mathbf{r},t) = \sum_{s=\pm1} \mathrm{Re}\left\{\left[\tilde{\mathbf{E}}_{<}^{(\mathrm{k},s)}(\mathbf{r})\Theta(-z) + \tilde{\mathbf{E}}_{\mathrm{in}}^{(\mathrm{k},s)}(\mathbf{r})\Theta_{\mathrm{in}}(z) + \tilde{\mathbf{E}}_{>}^{(\mathrm{k},s)}(\mathbf{r})\Theta(z-d_{\mathrm{m}})\right] e^{-i\omega t}\right\}, \tag{4.49a}$$

$$\mathbf{H}_{\mathrm{k}}(\mathbf{r},t) = \sum_{s=\pm1} \mathrm{Re}\left\{\frac{s}{i\mu_0 c}\left[\sqrt{\epsilon_{\mathrm{g}}}\tilde{\mathbf{E}}_{<}^{(\mathrm{k},s)}(\mathbf{r})\Theta(-z) + \sqrt{\epsilon_{\mathrm{m}}}\tilde{\mathbf{E}}_{\mathrm{in}}^{(\mathrm{k},s)}(\mathbf{r})\Theta_{\mathrm{in}}(z) + \sqrt{\epsilon_{\mathrm{r}}/\mu_{\mathrm{r}}}\tilde{\mathbf{E}}_{>}^{(\mathrm{k},s)}(\mathbf{r})\Theta(z-d_{\mathrm{m}})\right] e^{-i\omega t}\right\}, \tag{4.49b}$$

$$\mathbf{D}_{\mathrm{k}}(\mathbf{r},t) = \sum_{s=\pm1} \mathrm{Re}\left\{\epsilon_0\left[\epsilon_{\mathrm{g}}\tilde{\mathbf{E}}_{<}^{(\mathrm{k},s)}(\mathbf{r})\Theta(-z) + \epsilon_{\mathrm{m}}\tilde{\mathbf{E}}_{\mathrm{in}}^{(\mathrm{k},s)}(\mathbf{r})\Theta_{\mathrm{in}}(z) + \left(\epsilon_{\mathrm{r}} - s\kappa\sqrt{\epsilon_{\mathrm{r}}/\mu_{\mathrm{r}}}\right)\tilde{\mathbf{E}}_{>}^{(\mathrm{k},s)}(\mathbf{r})\Theta(z-d_{\mathrm{m}})\right] e^{-i\omega t}\right\}, \tag{4.49c}$$

$$\mathbf{B}_{\mathrm{k}}(\mathbf{r},t) = \sum_{s=\pm1} \mathrm{Re}\left\{\frac{1}{c}\left[-is\sqrt{\epsilon_{\mathrm{g}}}\tilde{\mathbf{E}}_{<}^{(\mathrm{k},s)}(\mathbf{r})\Theta(-z) - is\sqrt{\epsilon_{\mathrm{m}}}\tilde{\mathbf{E}}_{\mathrm{in}}^{(\mathrm{k},s)}(\mathbf{r})\Theta_{\mathrm{in}}(z) + i\left(\kappa - s\sqrt{\epsilon_{\mathrm{r}}\mu_{\mathrm{r}}}\right)\tilde{\mathbf{E}}_{>}^{(\mathrm{k},s)}(\mathbf{r})\Theta(z-d_{\mathrm{m}})\right] e^{-i\omega t}\right\}, \tag{4.49d}$$

where $\Theta(z)$ is the Heaviside step function, $\Theta_{\mathrm{in}}(z) = \Theta(z) - \Theta(z-d_{\mathrm{m}})$ and

$$\tilde{\mathbf{E}}_{<}^{(\mathrm{k},s)} = \left[E_{0,s}^{(\mathrm{k})}\hat{\mathbf{e}}_s^{(0)}e^{ik_g z} + E_{\mathrm{R},s}^{(\mathrm{k})}\hat{\mathbf{e}}_s^{(\mathrm{R})}e^{-ik_g z}\right]e^{ik_x x}, \tag{4.50a}$$

$$\tilde{\mathbf{E}}_{\mathrm{in}}^{(\mathrm{k},s)}(\mathbf{r}) = \sum_{\sigma=\pm1} E_{\sigma,s}^{(\mathrm{k})}\mathbf{n}_s^{\sigma}e^{ik_x x + i\sigma k_{\mathrm{m}} z}, \tag{4.50b}$$

$$\tilde{\mathbf{E}}_{>}^{(\mathrm{k},s)}(\mathbf{r}) = E_{\mathrm{T},s}^{(\mathrm{k})}\hat{\mathbf{n}}^{(z>d_{\mathrm{m}})}e^{ik_x x + i\beta_s z}. \tag{4.50c}$$

Again, BCs for the continuity of the (I) normal component of displacement vector and magnetic induction field and (II) tangent component of electric and magnetic

fields at the interfaces ($z = 0$ and $z = d_{\mathrm{m}}$) provide

$$\mathbf{D}_{\mathrm{k}}(x, y, 0^-, t) \cdot \hat{e}_z = \mathbf{D}_{\mathrm{k}}(x, y, 0^+, t) \cdot \hat{e}_z, \tag{4.51a}$$

$$\hat{e}_z \times \left[\mathbf{E}_{\mathrm{k}}(x, y, 0^+, t) - \mathbf{E}_{\mathrm{k}}(x, y, 0^-, t)\right] = 0, \tag{4.51b}$$

$$\mathbf{D}_{\mathrm{k}}(x, y, d_{\mathrm{m}}^-, t) \cdot \hat{e}_z = \mathbf{D}_{\mathrm{k}}(x, y, d_{\mathrm{m}}^+, t) \cdot \hat{e}_z, \tag{4.51c}$$

$$\hat{e}_z \times \left[\mathbf{E}_{\mathrm{k}}(x, y, d_{\mathrm{m}}^+, t) - \mathbf{E}_{\mathrm{k}}(x, y, d_{\mathrm{m}}^-, t)\right] = 0, \tag{4.51d}$$

$$\mathbf{B}_{\mathrm{k}}(x, y, 0^-, t) \cdot \hat{e}_z = \mathbf{B}_{\mathrm{k}}(x, y, 0^+, t) \cdot \hat{e}_z, \tag{4.51e}$$

$$\hat{e}_z \times \left[\mathbf{H}_{\mathrm{k}}(x, y, 0^+, t) - \mathbf{H}_{\mathrm{k}}(x, y, 0^-, t)\right] = 0, \tag{4.51f}$$

$$\mathbf{B}_{\mathrm{k}}(x, y, d_{\mathrm{m}}^-, t) \cdot \hat{e}_z = \mathbf{B}_{\mathrm{k}}(x, y, d_{\mathrm{m}}^+, t) \cdot \hat{e}_z, \tag{4.51g}$$

$$\hat{e}_z \times \left[\mathbf{H}_{\mathrm{k}}(x, y, d_{\mathrm{m}}^+, t) - \mathbf{H}_{\mathrm{k}}(x, y, d_{\mathrm{m}}^-, t)\right] = 0. \tag{4.51h}$$

Then, plugging the fields in Eq. (4.49) into the BCs Eq. (4.51), we obtain the following system of algebraic equations

$$\sqrt{\epsilon_{\mathrm{g}}} \sum_{s=\pm1} \left[E_{0,s}^{(\mathrm{k})} + E_{\mathrm{R},s}^{(\mathrm{k})}\right] = \sqrt{\epsilon_{\mathrm{m}}} \sum_{s=\pm1} \left[E_{+,s}^{(\mathrm{k})} + E_{-,s}^{(\mathrm{k})}\right], \tag{4.52a}$$

$$\frac{k_{\mathrm{g}}}{\sqrt{\epsilon_{\mathrm{g}}}} \sum_{s=\pm1} \left[E_{0,s}^{(\mathrm{k})} - E_{\mathrm{R},s}^{(\mathrm{k})}\right] = \frac{k_{\mathrm{m}}}{\sqrt{\epsilon_{\mathrm{m}}}} \sum_{s=\pm1} \left[E_{+,s}^{(\mathrm{k})} - E_{-,s}^{(\mathrm{k})}\right], \tag{4.52b}$$

$$\sum_{s=\pm1} s \left[E_{0,s}^{(\mathrm{k})} + E_{\mathrm{R},s}^{(\mathrm{k})}\right] = \sum_{s=\pm1} s \left[E_{+,s}^{(\mathrm{k})} + E_{-,s}^{(\mathrm{k})}\right], \tag{4.52c}$$

$$\sum_{s=\pm1} s k_{\mathrm{g}} \left[E_{0,s}^{(\mathrm{k})} - E_{\mathrm{R},s}^{(\mathrm{k})}\right] = \sum_{s=\pm1} s k_{\mathrm{m}} \left[E_{+,s}^{(\mathrm{k})} - E_{-,s}^{(\mathrm{k})}\right], \tag{4.52d}$$

$$\sqrt{\frac{\epsilon_{\mathrm{m}}}{2}} \sum_{s=\pm1} \left[E_{+,s}^{(\mathrm{k})} e^{ik_{\mathrm{m}}d_{\mathrm{m}}} + E_{-,s}^{(\mathrm{k})} e^{-ik_{\mathrm{m}}d_{\mathrm{m}}}\right] = \sum_{s=\pm1} \frac{k_0}{\beta_s} \left(\epsilon_{\mathrm{r}} - s\kappa \sqrt{\frac{\epsilon_{\mathrm{r}}}{\mu_{\mathrm{r}}}}\right) E_{\mathrm{T},s}^{(\mathrm{k})} e^{i\beta_s d_{\mathrm{m}}}, \tag{4.52e}$$

$$\frac{k_{\mathrm{m}}}{k_0\sqrt{2\epsilon_{\mathrm{m}}}} \sum_{s=\pm1} \left[E_{+,s}^{(\mathrm{k})} e^{ik_{\mathrm{m}}d_{\mathrm{m}}} - E_{-,s}^{(\mathrm{k})} e^{-ik_{\mathrm{m}}d_{\mathrm{m}}}\right] = \sum_{s=\pm1} E_{\mathrm{T},s}^{(\mathrm{k})} e^{i\beta_s d_{\mathrm{m}}}, \tag{4.52f}$$

$$\frac{1}{\sqrt{2}} \sum_{s=\pm1} s \left[E_{+,s}^{(\mathrm{k})} e^{ik_{\mathrm{m}}d_{\mathrm{m}}} + E_{-,s}^{(\mathrm{k})} e^{-ik_{\mathrm{m}}d_{\mathrm{m}}}\right] = -\sum_{s=\pm1} \frac{k_0}{\beta_s} \left(\kappa - s\sqrt{\epsilon_{\mathrm{r}}\mu_{\mathrm{r}}}\right) E_{\mathrm{T},s}^{(\mathrm{k})} e^{i\beta_s d_{\mathrm{m}}}, \tag{4.52g}$$

$$\frac{k_{\mathrm{m}}}{k_0\sqrt{2}} \sum_{s=\pm1} s \left[E_{+,s}^{(\mathrm{k})} e^{ik_{\mathrm{m}}d_{\mathrm{m}}} - E_{-,s}^{(\mathrm{k})} e^{-ik_{\mathrm{m}}d_{\mathrm{m}}}\right] = \sum_{s=\pm1} s \sqrt{\frac{\epsilon_{\mathrm{r}}}{\mu_{\mathrm{r}}}} E_{\mathrm{T},s}^{(\mathrm{k})} e^{i\beta_s d_{\mathrm{m}}}. \tag{4.52h}$$

Such BCs lead to an 8×8 inhomogeneous system of algebraic equations, rewritten in matrix form as

$$\begin{bmatrix} -1 & -1 & n_{\rm q} & n_{\rm q} & n_{\rm q} & n_{\rm q} & 0 & 0 \\ 1 & 1 & m_{\rm q} & -m_{\rm q} & m_{\rm q} & -m_{\rm q} & 0 & 0 \\ 1 & -1 & -1 & -1 & 1 & 1 & 0 & 0 \\ -1 & 1 & -v^{(1)} & v^{(1)} & v^{(1)} & -v^{(1)} & 0 & 0 \\ 0 & 0 & v_+^{(2)} & v_-^{(2)} & v_+^{(2)} & v_-^{(2)} & v_+^{(3)} & v_-^{(3)} \\ 0 & 0 & v_+^{(4)} & -v_-^{(4)} & v_+^{(4)} & -v_-^{(4)} & v_+^{(5)} & v_-^{(5)} \\ 0 & 0 & v_+^{(5)} & -v_-^{(6)} & -v_+^{(6)} & v_-^{(6)} & v_+^{(7)} & v_-^{(7)} \\ 0 & 0 & \sqrt{\epsilon_{\rm m}}v_+^{(4)} & \sqrt{\epsilon_{\rm m}}v_+^{(4)} & \sqrt{\epsilon_{\rm m}}v_+^{(4)} & \sqrt{\epsilon_{\rm m}}v_-^{(4)} & v_+^{(8)} & v_-^{(8)} \end{bmatrix} \cdot \begin{bmatrix} E_{\rm R,+}^{(\rm k)} \\ E_{\rm R,-}^{(\rm k)} \\ E_{+,+}^{(\rm k)} \\ E_{-,+}^{(\rm k)} \\ E_{+,-}^{(\rm k)} \\ E_{-,-}^{(\rm k)} \\ E_{\rm T,+}^{(\rm k)} \\ E_{\rm T,-}^{(\rm k)} \end{bmatrix} = \hat{S} \cdot \begin{bmatrix} E_{\rm R,+}^{(\rm k)} \\ E_{\rm R,-}^{(\rm k)} \\ E_{+,+}^{(\rm k)} \\ E_{-,+}^{(\rm k)} \\ E_{+,-}^{(\rm k)} \\ E_{-,-}^{(\rm k)} \\ E_{\rm T,+}^{(\rm k)} \\ E_{\rm T,-}^{(\rm k)} \end{bmatrix} = \begin{bmatrix} E_{0,+}^{(\rm k)} + E_{0,-}^{(\rm k)} \\ E_{0,+}^{(\rm k)} + E_{0,-}^{(\rm k)} \\ E_{0,-}^{(\rm k)} - E_{0,+}^{(\rm k)} \\ E_{0,-}^{(\rm k)} - E_{0,+}^{(\rm k)} \\ 0 \\ 0 \\ 0 \\ 0 \end{bmatrix} \tag{4.53}$$

where $n_{\rm q}\sqrt{\epsilon_{\rm m}/\epsilon_{\rm g}}, m_{\rm q} = \sqrt{1-(\epsilon_{\rm g}/\epsilon_{\rm m})\sin^2\theta}/\cos\theta$ and

$$v^{(1)} = \sqrt{\epsilon_{\rm m} - \epsilon_{\rm g}\sin^2\theta}/\sqrt{\epsilon_{\rm g}}\cos\theta, \tag{4.54a}$$

$$v_\pm^{(2)} = \sqrt{\epsilon_{\rm m}/2}e^{ik_{\rm m}d_{\rm m}}, \tag{4.54b}$$

$$v_\pm^{(3)} = -(k_0/\beta_\pm)(\epsilon_{\rm r} \mp \kappa\sqrt{\epsilon_{\rm r}/\mu_{\rm r}}e^{i\beta_\pm d_{\rm m}}), \tag{4.54c}$$

$$v_\pm^{(4)} = \sqrt{[1-(\epsilon_{\rm g}/\epsilon_{\rm m})\sin^2\theta]/2}e^{\pm ik_{\rm m}d_{\rm m}}, \tag{4.54d}$$

$$v_\pm^{(5)} = -e^{i\beta_\pm d_{\rm m}}, \tag{4.54e}$$

$$v_\pm^{(6)} = (1/\sqrt{2})e^{\pm ik_{\rm m}d_{\rm m}}, \tag{4.54f}$$

$$v_\pm^{(7)} = (k_0/\beta_\pm)(\kappa \mp \sqrt{\epsilon_{\rm r}\mu_{\rm r}})e^{i\beta_\pm d_{\rm m}}, \tag{4.54g}$$

$$v_\pm^{(8)} = \mp\sqrt{\epsilon_{\rm m}/\mu_{\rm m}}e^{i\beta_\pm d_{\rm m}}. \tag{4.54h}$$

By numerically inverting $\hat{S}$, we obtain $E_{\rm R,\pm1}^{(\rm k)}$ and $E_{\rm T,\pm1}^{(\rm k)}$ for a given impinging field component $E_{0,\pm1}^{(\rm k)}$. In turn, the absorbance of the system in the Kretschmann coupling scheme upon excitation with right ($s=+1, E_{0,-}^{(\rm k)}$) and left ($s=-1, E_{0,+}^{(\rm k)}$) circularly polarized radiation is given by

$$A_s^{(\rm k)}(\theta,\lambda) = 1 - \frac{\sum_{\sigma=\pm1}|E_{\rm R,\sigma}^{(\rm k)}|^2}{|E_{0,s}^{(\rm k)}|^2}. \tag{4.55}$$

Consequently, the Kretschman CDDA can be evaluated from $\Delta A^{(\mathrm{k})}(\theta,\lambda) = A_{+}^{(\mathrm{k})} - A_{-}^{(\mathrm{k})}$. Again, by setting TM impinging polarization ($E_{0,+}^{(\mathrm{k})} = E_{0,-}^{(\mathrm{k})} = E_0$), we can calculate the TM-absorbance: $A_{\mathrm{TM}}^{(\mathrm{k})} = 1 - \sum_{\sigma=\pm1} |E_{\mathrm{R},\sigma}^{(\mathrm{k})}|^2/|E_0|^2$. The dependencies of $A_{\mathrm{TM}}^{(\mathrm{k})}$ and $\Delta A^{(\mathrm{k})}$ over λ, θ are shown in Fig. 4.12 (b, c), respectively, considering a $d_{\mathrm{m}} = 80$ nm thick silver thin film. As observed in the Otto coupling scheme, the maximum Kretschman TM absorbance and CDDA are also attained at the SPP excitation curve $\theta_{\mathrm{SPP}}(\lambda)$, marked by the white dashed lines in Fig. 4.12(b,c). Note that, in contrast to the Otto coupling scheme, the excitation of Fabry-Perot resonances does not occur in the Kretschman coupling scheme due to the presence of intermediate metallic film. Moreover, thanks to the sub-wavelength metallic thickness ($d_{\mathrm{m}} \ll \lambda$), we observe a CDDA peak at $\theta = 61^{\circ}$ arising due to the polarization-dependent total internal reflection between glass and solvated Reparixin. The origin of such a phenomenon is the evanescent wave propagating through the thin metal film, allowing effective evanescent coupling between glass and solvated Reparixin. In addition, the Kretschmann CDDA is smaller than the Otto CDDA by two orders of magnitude when calculated for an equivalent chiral sample, i.e., identical n_{mol} and Δn_{mol}.

4.6.3 Reflected polarization dynamics.

Understanding the polarization dynamics of the system provides deeper insights on the interaction between SPPs, impinging electromagnetic radiation and the chiral drug solution. Also, it helps to analyze the response of the system to different parameters that can influence the light-matter interaction and, in turn, the designing of plasmonic sensors. Usually, the radiation polarization can be fully understood through the four Stokes parameters: S_0, S_1, S_2, S_3. In Otto configuration, the reflected radiation polarization is assessed by

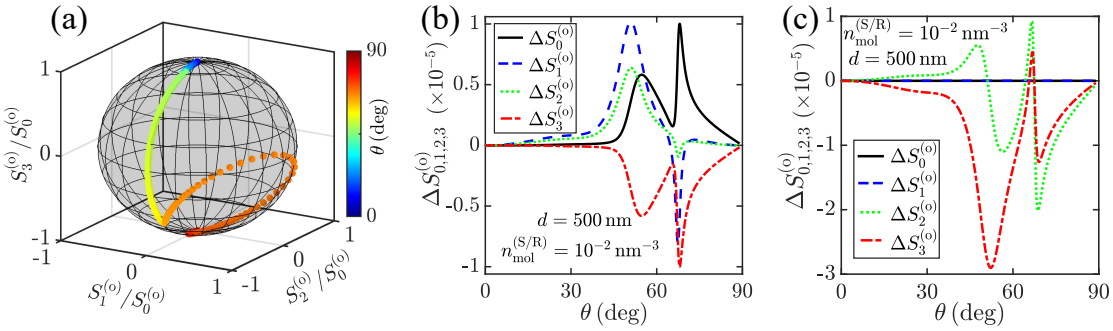


Figure 4.13: Reflected polarization dynamics in the Otto configuration at a vacuum wavelength of $\lambda = 700$ nm, associated with a silver substrate characterized by its dielectric constant $\epsilon_{\rm m}(\lambda)$, together with aqueous Reparixin with a thickness of $d = 500$ nm and a total molecular number density of $n_{\rm mol} = 10^{-2}$ nm^{-3}. (**a**) Stokes parameters evolution in the Poincaré sphere as a function of incidence angle θ upon right-circular impinging polarization for pure S enantiomer of Reparixin dissolved in water with enantiomeric number density excess $\Delta n_{\rm mol} = n_{\rm mol}^{\rm (S)} - n_{\rm mol}^{\rm (R)}$. Variation of the Stokes parameter, calculated between pure S and pure R enantiomers of Reparixin dissolved in water, under excitation with (**b**) right circular and (**c**) TM polarization.

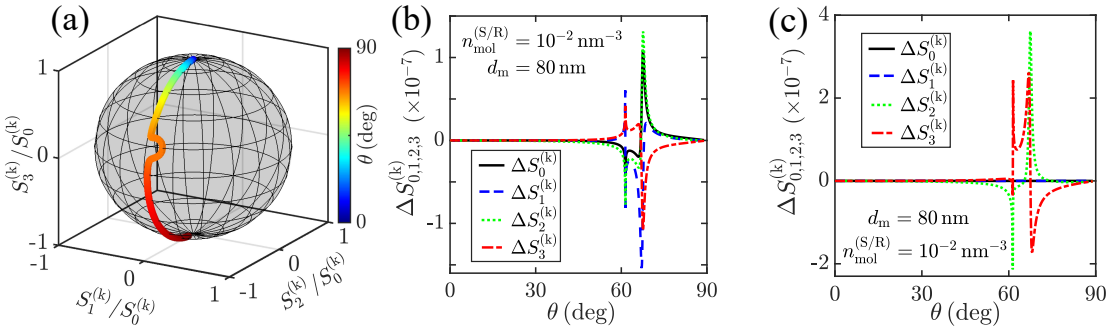


Figure 4.14: Reflected polarization dynamics in the Krteschmann configuration at a vacuum wavelength of $\lambda = 700$ nm, associated with a silver substrate with a thickness of $d_{\rm m} = 80$ nm characterized by its dielectric constant $\epsilon_{\rm m}$[166], together with aqueous Reparixin with total molecular number density of $n_{\rm mol} = 10^{-2}$ nm^{-3}. (**a**) Stokes parameters evolution in the Poincaré sphere as a function of incidence angle θ upon right-circular impinging polarization for pure S enantiomer of Reparixin dissolved in water with enantiomeric number density excess $\Delta n_{\rm mol} = n_{\rm mol}^{\rm (S)} - n_{\rm mol}^{\rm (R)}$. Variation of the Stokes parameter, calculated between pure S and pure R enantiomers of Reparixin dissolved in water, under excitation with (**b**) right circular and (**c**) TM polarization.

$$S_0^{\rm (o)} = |E_{\rm R,+}^{\rm (o)}|^2 + |E_{\rm R,-}^{\rm (o)}|^2, \tag{4.56a}$$

$$S_1^{\rm (o)} = 2{\rm Re}\left[E_{\rm R,+}^{\rm (o)} E_{\rm R,-}^{\rm (o)*}\right], \tag{4.56b}$$

$$S_2^{\rm (o)} = -2{\rm Im}\left[E_{\rm R,+}^{\rm (o)} E_{\rm R,-}^{\rm (o)*}\right], \tag{4.56c}$$

$$S_3^{\rm (o)} = |E_{\rm R,+}^{\rm (o)}|^2 - |E_{\rm R,-}^{\rm (o)}|^2. \tag{4.56d}$$

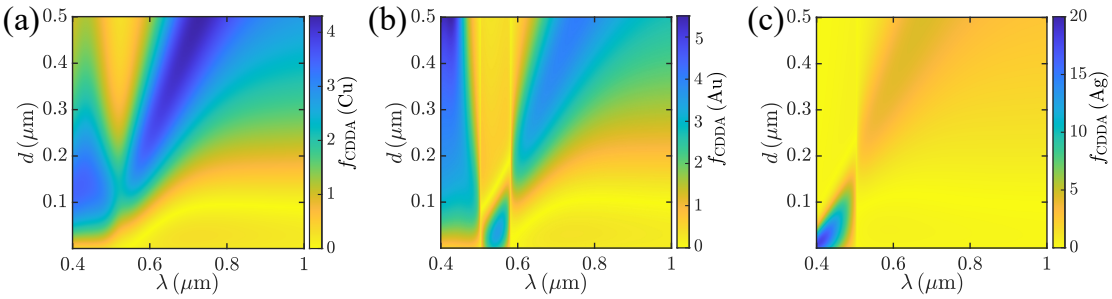


Figure 4.15: Enhancement factor to assess plasmon induced CDDA in the Otto coupling, defined as $f_{\mathrm{CDDA}}(\lambda) = \max|\Delta A^{(\mathrm{o,k})}|/A_{\mathrm{bulk}}|$ adopting (**a**) copper, (**b**) gold and (**c**) silver as metal substrate. The dielectric constants $\epsilon_{\mathrm{m}}(\lambda)$ of the considered noble metals are taken from [166] and other physical parameters coincide with the ones adopted in Fig. 4.11(a).

Fig 4.13 (a-c) depict the dependence of the Stokes parameters over the incident angle θ calculated at $\lambda = 700$ nm for silver substrate and $d = 500$ nm thick chiral medium specified with $\Delta n_{\mathrm{mol}} = n_{\mathrm{mol}} = 10^{-2}$ nm^{-3}. Note that, for both circular, see Fig 4.13 (b), and TM, see Fig 4.13 (c), polarization, the modulation is maximized at the specific angle $\theta_{\mathrm{SPP}} \simeq 70°$ where the SPP excitation occurs. In addition, the Fabry-Perot resonance of solvated Reparixin enhances the polarization dynamics at $\theta \simeq 50°$. However, such a phenomenon is not observed in the Kretschmann coupling scheme. In Fig 4.14(a-c), we report the Kretschmann Stokes parameters

$$S_0^{(\mathrm{k})} = |E_{\mathrm{R},+}^{(\mathrm{k})}|^2 + |E_{\mathrm{R},-}^{(\mathrm{k})}|^2, \tag{4.57a}$$

$$S_1^{(\mathrm{k})} = 2\mathrm{Re}\left[E_{\mathrm{R},+}^{(\mathrm{k})} E_{\mathrm{R},-}^{(\mathrm{k})*}\right], \tag{4.57b}$$

$$S_2^{(\mathrm{k})} = -2\mathrm{Im}\left[E_{\mathrm{R},+}^{(\mathrm{k})} E_{\mathrm{R},-}^{(\mathrm{k})*}\right], \tag{4.57c}$$

$$S_3^{(\mathrm{k})} = |E_{\mathrm{R},+}^{(\mathrm{k})}|^2 - |E_{\mathrm{R},-}^{(\mathrm{k})}|^2, \tag{4.57d}$$

dependencies over the incident angle θ, calculated at $\lambda = 700$ nm by adopting $d_{\mathrm{m}} = 80$ nm silver thin film and a chiral medium specified with $\Delta n_{\mathrm{mol}} = 10^{-2}$ nm^{-3}.

4.7 Results and discussions.

The plasmon-induced CDDA enhancement is assessed by defining the factor

$$f_{\mathrm{CDDA}}(\lambda) = \max \left| \frac{\Delta A^{(\mathrm{o,k})}(\theta, \lambda)}{\Delta A_{\mathrm{bulk}}(\lambda)} \right|, \tag{4.58}$$

where $\Delta A_{\mathrm{bulk}}(\lambda) = e^{-2\mathrm{Im}\beta_{-}^{(\mathrm{b})}} - e^{-2\mathrm{Im}\beta_{+}^{(\mathrm{b})}}$ indicates the absorbance of an aqueous Reparixin layer when there is no nanophotonic structure, and $\beta_{\pm}^{(\mathrm{b})} = k_0 \left(\sqrt{\epsilon_{\mathrm{r}}\mu_{\mathrm{r}}} \mp \kappa\right)$. We report the results in Fig. 4.15(a-c). The dependence of CDDA enhancement for (a) copper, (b) gold, and (c) silver interfaces over vacuum wavelength λ is shown in the Otto coupling scheme. For silver, we attain the maximum plasmon-induced CDDA enhancement $f_{\mathrm{CDDA}} \simeq 20$ (see Fig. 4.15(c)) at $\lambda \simeq 400$ nm in Otto configuration. In addition, gold and copper offer CDDA enhancement factors $f_{\mathrm{CDDA}} \simeq 5$ for wavelength $\lambda > 500$ nm. It is worth mentioning that, adopting a metal substrate with dimensions around 1×1 mm^2, the interaction volume of the chiroptical effects is $\mathrm{V_{int}} \lesssim 1$ nl, and the chiroptical signal (CDDA $\approx 10^{-6}$) can be easily measured by employing lock-in amplifiers. We emphasize that, with the considered low molecular number density $n_{\mathrm{mol}} \simeq 10^{-2}$ nm^{-3}, plasmon enhanced CD spectroscopy is sensitive enough to detect and distinguish $\lesssim 10^{13}$ R, S enantiomers in the considered $\mathrm{V_{int}}$ and therefore, leading to a viable platform for efficient chiroptical sensing. Additionally, the dissymetry factor can be evaluated by dividing the CDDA with the average absorbance of right and left circularly polarized impinging radiation. However, we observe that the nanostructure is not capable of affecting the dissymmetry factor even though the SPP excitation enhances the CDDA. In fact, the SPPs excitation offers enhanced local electric field, supporting higher averaged absorbance as well as the higher CDDA. As a result, the dissymmetry factor remains intact in such a CD spectroscopic method. In the literature, there are several superchirality approaches capable of enhancing

the dissymmetry factor, which are in turn distinct from our considered approach.. All in all, the most important aspect of such a CDDA enhancement technique is to reduce the volume of the drug solution for analysis.

4.8 Concluding remarks.

In this Chapter, we demonstrate the potential of SPPs at an interface between noble metals and a chiral sample for plasmonic enhancement of CD spectroscopy. In our investigation, we consider a realistic chiral drug solution, Reparixin dissolved in water, that has been utilized in clinical research for the treatment of community-acquired pneumonia, focusing on COVID-19 and acute respiratory distress syndrome. The microscopic observables of Reparixin are evaluated adopting a computational method based on MD simulations, TDDFT and PMM calculations. Such a combination of computational methods provides time-averaged permanent and transition electric/magnetic dipole moments of the drug solution. We calculate the macroscopic optical parameters of the isotropic assembly of the chiral drugs by perturbatively solving the density matrix equations. Finally, the plasmon-enhanced CDDA of the chiral mixture is demonstrated through analytical calculations. Thanks to SPPs, we are able to attain a CDDA enhancement of the order $f_{\mathrm{CDDA}} \simeq 20$ of sub-nl volume drug solutions. Our findings provide insights on the development of an innovative integrated framework for the chiroptical sensing of minimal amounts of drug solutions.

Chapter 5

Enhanced Vibrational Circular Dichroism of Plasmonic Nanostructures Embedding Chiral Drugs

In this chapter, we investigate the Mid-Infrared (MIR) chiroptical response of plasmonic nanostructures based on AZO and layers of an aqueous solution of Ladarixin, a chiral pharmaceutical currently under clinical trial for the treatment of type 1 diabetes. We explore the possibilities offered by LSPR for the enhancement of VCD of the considered chiral drug solution. Focusing on diverse plasmonic nanoshell geometries, we find that LSPRs provide an amplification factor of Vibrational Circular Dichroism Differential Absorption (VCDDA) cross section ranging from $\simeq 3$ to $\simeq 20$ thanks to near-field intensity enhancement produced by LSPRs. Our results indicate that nanoshell LSPRs are promising for probing molecular chirality at the nanoscale.

5.1 Introduction.

Chiral sensing based on chiroptical spectroscopic techniques is capable of providing a rapid response and precise detection limits [133, 167]. Circular Dichroism (CD) and Optical Rotatory Dispersion (ORD) measurements are the most popular approaches enabling estimation of optical activities in the transparent and absorbing regimes, respectively, at UV-vis and near-IR wavelengths. However, in this wavelength range, the detected molecular CD signal lacks extensive details on the molecular chemical structures, essentially because of their limited selectivity [12]. In turn, CD-based methods at these wavelengths are incapable of discriminating different types of chiral molecules present in a chiral mixture. Conversely, in the MIR region, the vibrational characteristics [168] of molecules can capture structural information and offer detailed insights through distinct absorption patterns arising from chemical bonds and functional groups—known as IR fingerprints [169, 170, 171]. Hence, a growing interest has been shifted towards VCD [138] to probe the chiral properties of molecules in the MIR wavelength range. Importantly, VCD-based optical sensing techniques offer the advantage of real-time analysis capabilities and potential lab-on-a-chip integration, and currently they are able to assess the enantiomeric excess of dilute chiral drug solutions with ml volume. Light manipulation in the subwavelength range using MIR nanophotonics facilitates surface-enhanced absorption in the IR, which leads to molecular sensing applications [168, 172, 173] through advanced technologies including metamaterials [174, 175, 176, 177], nanomaterials [178], photonic crystals [179, 180, 181, 182] and waveguide sensors [183]. Moreover, as discussed in the previous chapter, nanophotonics can amplify the chiroptical sensitivity to reduced sample volumes by nanodevices. To attain such a plasmon-mediated sensitivity enhancement over VCD, it is necessary to employ materials displaying surface plasmon resonance in the MIR part of the spectrum, e.g., graphene [184, 185], oxides

or nitrides [186, 187, 188, 189]. Employing chiral plasmonic structures, plasmon-enhanced VCD [190, 191, 192, 193, 194] has been investigated in the MIR regime. Possibilities offered by such materials for nanophotonics-enabled chiral sensing of drugs are hitherto unexplored.

Here, we investigate precisely the potential of AZO for plasmon-enhanced VCD of chiral drugs. In particular, we focus on two distinct AZO-based spherical nanoshell geometries, see Figs. 5.2(a,b), embedding nanometer-sized molecular layers of solvated Ladarixin, a dual allosteric inhibitor of CXCL8 (IL-8) receptors, CXCR1 and CXCR2, currently in phase 2 and 3 trials for the treatment of diabetes [47, 48]. We calculate the bi-anisotropic optical constants of such a chiral drug solution by the methods described in Chapter 2. Furthermore, we model LSPRs of such chiral nanostructures by an electrostatic approach that we validate by Electromagnetic Wave Frequency Domain (EWFD) calculations through commercial software [195]. Because the VCDDA cross-section $\Delta\sigma_{\rm abs} = \sigma_{\rm R} - \sigma_{\rm L}$ by right/left circular polarization excitation is proportional to the enantiomeric excess density $\Delta n_{\rm mol} = n_{\rm mol}^{\rm (S)} - n_{\rm mol}^{\rm (R)}$, by measuring VCDDA one can retrieve $\Delta n_{\rm mol}$. We observe a plasmon-induced VCDDA enhancement factor $f_{\rm VCD}$ ranging from $\simeq 3$ to $\simeq 20$, indicating that AZO-based plasmonic devices are promising for ultrasensitive probing of molecular chirality at the nanoscale.

5.2 Theoretical framework.

Let's consider a chiral dielectric spherical nanostructure with inner radius R and shell thickness h placed at $\mathbf{r} = 0$, where $\mathbf{r}$ represents the position vector of a reference frame located at the center of the sphere. Fig. 5.1 illustrates the considered nanostructure, indicating three regions: region 1, nanosphere core; region 2, spherical nanoshell; and region 3, background. We assume a monochromatic plane wave with vacuum wavelength λ impinging on such structure, with electric

field

$$\mathbf{E}(\mathbf{r},t) = \mathrm{Re}\left[\tilde{\mathbf{E}}_0(\mathbf{r})e^{-i\omega t}\right], \tag{5.1}$$

where $\tilde{\mathbf{E}}_0(\mathbf{r})$ is the electric field amplitude, $\omega = 2\pi c/\lambda$ is the angular frequency, and c is the light speed in vacuum. We further assume that the radius of the nanostructure is much smaller than the vacuum wavelength of the impinging radiation : $(R+h) \ll \lambda$. In such a limit, the problem reduces to the quasi-static limit where the external field is uniform over the nanostructure and the induced polarization charges follow adiabatically the external field over time. The linear electromagnetic response of such nanostructure is estimated through bi-anisotropic constitutive relations connecting the electric displacement vector $\mathbf{D}(\mathbf{r},t) = \mathrm{Re}[\tilde{\mathbf{D}}_0(\mathbf{r})e^{-i\omega t}]$ and the induction magnetic field $\mathbf{B}(\mathbf{r},t) = \mathrm{Re}[\tilde{\mathbf{B}}_0(\mathbf{r})e^{-i\omega t}]$ to the electric field $\mathbf{E}(\mathbf{r},t) = \mathrm{Re}[\tilde{\mathbf{E}}_0(\mathbf{r})e^{-i\omega t}]$ and the magnetic field $\mathbf{H}(\mathbf{r},t) = \mathrm{Re}[\tilde{\mathbf{H}}_0(\mathbf{r})e^{-i\omega t}]$. Explicitly, such bi-anisotropic constitutive relations (BACRs) are given by

$$\tilde{\mathbf{D}}_0(\mathbf{r}) = \epsilon_0\epsilon_\mathrm{t}(r,\lambda)\tilde{\mathbf{E}}_0(\mathbf{r}) - \frac{i}{c}\kappa_\mathrm{t}(r,\lambda)\tilde{\mathbf{H}}_0(\mathbf{r}), \tag{5.2a}$$

$$\tilde{\mathbf{B}}_0(\mathbf{r}) = \frac{i}{c}i\kappa_\mathrm{t}(r,\lambda)\tilde{\mathbf{E}}_0(\mathbf{r}) + \mu_0\mu_\mathrm{t}(r,\lambda)\tilde{\mathbf{H}}_0(\mathbf{r}), \tag{5.2b}$$

connecting the monochromatic complex vector fields via position and wavelength dependent effective optical profiles

$$\epsilon_\mathrm{t}(r,\lambda) = \sum_{l=1}^{3}\epsilon_l(\lambda)\Theta_l(r), \tag{5.3a}$$

$$\mu_\mathrm{t}(r,\lambda) = \sum_{l=1}^{3}\mu_l(\lambda)\Theta_l(r), \tag{5.3b}$$

$$\kappa_\mathrm{t}(r,\lambda) = \sum_{l=1}^{3}\kappa_l(\lambda)\Theta_l(r), \tag{5.3c}$$

where the media 1 (core), 2 (shell) and 3 (background) are characterized by their relative dielectric permittivities $\epsilon_{1,2,3}(\lambda)$, relative magnetic permeabilities $\mu_{1,2,3}(\lambda)$,

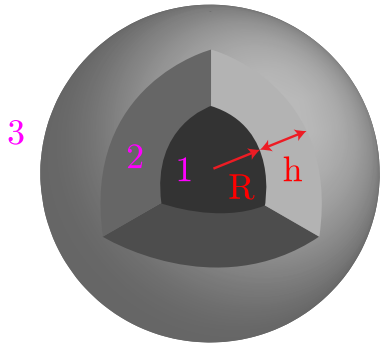


Figure 5.1: Schematic of a spherical structure with an inner radius R and thickness h having three regions: region 1 (core), region 2 (shell) and region 3 (background).

and chiral parameters: $\kappa_{1,2,3}(\lambda)$. $\Theta_1(r) = \Theta(R-r)$, $\Theta_2(r) = \Theta(R+h-r) - \Theta_1(r)$, $\Theta_3(r) = \Theta(r-R-h)$, and $\Theta(x)$ denote the Heaviside step function.

5.2.1 Achiral nanoshell.

In the achiral case, neglecting the chiral parameters ($\kappa_{1,2,3} = 0$), Eq. (5.2) reduces to the standard constitutive relations

$$\tilde{\mathbf{D}}_0(\mathbf{r}) = \epsilon_0\epsilon_1(r,\lambda)\tilde{\mathbf{E}}_0(\mathbf{r}), \tag{5.4a}$$

$$\tilde{\mathbf{B}}_0(\mathbf{r}) = \mu_0\mu_1(r,\lambda)\tilde{\mathbf{H}}_0(\mathbf{r}). \tag{5.4b}$$

Since there are no free charges and currents inside the nanostructure, the Maxwell equations provide

$$\nabla \cdot \tilde{\mathbf{E}}_0 = 0, \tag{5.5a}$$

$$\nabla \cdot \tilde{\mathbf{B}}_0 = 0, \tag{5.5b}$$

$$\nabla \times \tilde{\mathbf{E}}_0 = i\omega\tilde{\mathbf{B}}_0, \tag{5.5c}$$

$$\nabla \times \tilde{\mathbf{B}}_0 = -i\omega\tilde{\mathbf{D}}_0. \tag{5.5d}$$

In the electrostatic limit, Eq. (5.5c) becomes $\nabla \times \tilde{\mathbf{E}}_0 = 0$, suggesting that the electric field is irrotational and can be expressed as a gradient of the electric

potential (i.e., $\tilde{\mathbf{E}}_0 = -\nabla V$). Thus, the electrostatic solution within the nanoshell can be obtained by solving the Laplace equations

$$\nabla^2 V_{1,2,3} = 0 \tag{5.6}$$

in all regions. The solution of Eq. (5.6) can be written as

$$V_1 = A\hat{\mathbf{n}} \cdot \mathbf{r}, \tag{5.7a}$$

$$V_2 = B\hat{\mathbf{n}} \cdot \mathbf{r} + C\frac{\hat{\mathbf{n}} \cdot \mathbf{r}}{r^3}, \tag{5.7b}$$

$$V_3 = -E_0\hat{\mathbf{n}} \cdot \mathbf{r} + D\frac{\hat{\mathbf{n}} \cdot \mathbf{r}}{r^3}. \tag{5.7c}$$

In the above equation, we express $\tilde{\mathbf{E}}_0 = E_0\hat{\mathbf{n}}$, where $\hat{\mathbf{n}}$ is the impinging wave polarization unit vector and $\mathbf{r}$ is normal to the nanostructure surface, such that $\hat{\mathbf{n}} \cdot \mathbf{r} = r\cos\theta$ and A, B, C and D are unknown coefficients that can be determined from the boundary conditions. Note that the additional dipole terms due to the polarization of the dielectrics are included in the potential. In order to determine the coefficients explicitly, we impose the boundary conditions for the continuity of electric potential and its normal derivatives at the interface between two adjacent regions as follows

$$V_1(R) = V_2(R), \tag{5.8a}$$

$$V_2(R+h) = V_3(R+h), \tag{5.8b}$$

$$\epsilon_1 \frac{dV_1}{dr}\Big|_{r=R} = \epsilon_2 \frac{dV_2}{dr}\Big|_{r=R}, \tag{5.8c}$$

$$\epsilon_2 \frac{dV_2}{dr}\Big|_{r=R+h} = \epsilon_3 \frac{dV_3}{dr}\Big|_{r=R+h}. \tag{5.8d}$$

Inserting Eq. (5.7) in the Eq. (5.8), upon simplification, we obtain the potential in all three media as follows

$$V_1(r) = \frac{9\epsilon_3\epsilon_2}{[2f(\epsilon_1-\epsilon_2)(\epsilon_3-\epsilon_2)-(2\epsilon_2+\epsilon_1)(2\epsilon_3+\epsilon_2)]}\tilde{\mathbf{E}}_0\cdot\mathbf{r}, \tag{5.9a}$$

$$V_2(r) = \frac{3\epsilon_3(2\epsilon_2+\epsilon_1)}{[2f(\epsilon_1-\epsilon_2)(\epsilon_3-\epsilon_2)-(2\epsilon_2+\epsilon_1)(2\epsilon_3+\epsilon_2)]}\tilde{\mathbf{E}}_0\cdot\mathbf{r} - \frac{3\epsilon_3(\epsilon_1-\epsilon_2)}{\frac{1}{R^3}[2f(\epsilon_1-\epsilon_2)(\epsilon_3-\epsilon_2)-(2\epsilon_2+\epsilon_1)(2\epsilon_3+\epsilon_2)]}\frac{\tilde{\mathbf{E}}_0\cdot\mathbf{r}}{r^3}, \tag{5.9b}$$

$$V_3(r) = -\tilde{\mathbf{E}}_0\cdot\mathbf{r} + \frac{[f(\epsilon_2-\epsilon_1)(\epsilon_3-2\epsilon_2)+(2\epsilon_2+\epsilon_1)(2\epsilon_3-\epsilon_2)]}{[2f(\epsilon_1-\epsilon_2)(\epsilon_3-\epsilon_2)-(2\epsilon_2+\epsilon_1)(2\epsilon_3+\epsilon_2)]}(R+h)^3\frac{\tilde{\mathbf{E}}_0\cdot\mathbf{r}}{r^3}, \tag{5.9c}$$

where $f = R^3/(R+h)^3$. For an isotropic medium, we can write the induced dipole moment as $\mathbf{p} = \alpha_{\rm ns}\tilde{\mathbf{E}}_0$, where $\alpha_{\rm ns}$ is the polarizability of the nanoshell. Such a dipole generates an electric potential outside the nanoshell, which is given by

$$V_{\rm dip}(r) = \frac{1}{4\pi\epsilon_0\epsilon_3}\frac{\mathbf{p}\cdot\mathbf{r}}{r^3}. \tag{5.10}$$

Thus, by inspection, the polarizability of the nanoshell can be readily obtained from Eq. (5.9c) as [196]

$$\alpha_{\rm ns} = \alpha_0\frac{(\epsilon_2-\epsilon_3)(\epsilon_1+2\epsilon_2)+f(\epsilon_1-\epsilon_2)(\epsilon_3+2\epsilon_2)}{(\epsilon_2+2\epsilon_3)(\epsilon_1+2\epsilon_2)+2f(\epsilon_2-\epsilon_3)(\epsilon_1-\epsilon_2)}, \tag{5.11}$$

where $\alpha_0 = 3\epsilon_0\epsilon_3\tau_>$, $\tau_> = (4/3)\pi(R+h)^3$, and $\tau_< = (4/3)\pi R^3$. Note that by setting $h = 0$ in Eq. (5.11) one recovers the polarizability of an achiral sphere $\alpha_{\rm s} = (4/3)\pi R^3\epsilon_0\epsilon_3(3\epsilon_1-\epsilon_3)/(\epsilon_1+2\epsilon_3)$ of radius R.

5.2.2 Chiral naoshell.

In this section, we present the field calculation for the scattering problem of nanoshell including chiral media. The bi-anisotropic constitutive relations in a

chiral dielectric medium are mentioned above in Eq. (5.2). In the quasi-static approximation, considering the same configuration of the nanoshell, see Fig. 5.2, for generic isotropic chiral media and utilizing Eq. (5.2), Eq. (1.1) provides

$$\nabla \cdot \left[\epsilon_0\epsilon_1\mathbf{E} - \frac{i\kappa_1}{c}\mathbf{H}\right] = \rho, \tag{5.12a}$$

$$\nabla \cdot \left[\mu_0\mu_1\mathbf{H} + \frac{i\kappa_1}{c}\mathbf{E}\right] = 0, \tag{5.12b}$$

$$\nabla \times \mathbf{E} = -\frac{i\kappa_1}{c}\frac{\partial \mathbf{E}}{\partial t} - \mu_0\mu_1\frac{\partial \mathbf{H}}{\partial t}, \tag{5.12c}$$

$$\nabla \times \mathbf{H} = \mathbf{J} + \epsilon_0\epsilon_1\frac{\partial \mathbf{E}}{\partial t} - \frac{i\kappa_1}{c}\frac{\partial \mathbf{H}}{\partial t}, \tag{5.12d}$$

where ρ is the charge and $\mathbf{J}$ is the current density. Upon simplification, from the Eq. (5.12a) and Eq. (5.12b), one gets

$$\nabla \cdot \mathbf{E} = \frac{\mu_1\rho}{\epsilon_0\left(\mu_1\epsilon_1 - \kappa_1^2\right)}, \tag{5.13a}$$

$$\nabla \cdot \mathbf{H} = -i\kappa_1 c\frac{\rho}{\left(\mu_1\epsilon_1 - \kappa_1^2\right)}. \tag{5.13b}$$

Utilizing the vector identity $\nabla \times \nabla \times \mathbf{A} = \nabla(\nabla \cdot \mathbf{A}) - \nabla^2\mathbf{A}$ for a vector field $\mathbf{A}$ and taking curl of the Eq. (5.12c), we reach to

$$\nabla^2\mathbf{E} - \frac{1}{c^2}\left(\epsilon_1\mu_1 + \kappa_1^2\right)\frac{\partial^2 \mathbf{E}}{\partial t^2} + 2\frac{i\kappa_1}{c}\mu_1\mu_0\frac{\partial^2 \mathbf{H}}{\partial t^2} = \frac{\mu_1}{\epsilon_0\left(\mu_1\epsilon_1 - \kappa_1^2\right)}\nabla\rho + \mu_0\mu_1\frac{\partial \mathbf{J}}{\partial t}. \tag{5.14}$$

Following the same procedure for the magnetic field, Eq. (5.12d) provides

$$\nabla^2\mathbf{H} - \frac{1}{c^2}\left(\epsilon_1\mu_1 + \kappa_1^2\right)\frac{\partial^2 \mathbf{H}}{\partial t^2} - 2\frac{i\kappa_1}{c}\epsilon_0\epsilon_1\frac{\partial^2 \mathbf{E}}{\partial t^2} = -\frac{i\kappa_1 c}{\left(\mu_1\epsilon_1 - \kappa_1^2\right)}\nabla\rho - \nabla \times \mathbf{J} + \frac{i\kappa_1}{c}\frac{\partial \mathbf{J}}{\partial t}. \tag{5.15}$$

Note that, in the presence of a chiral dielectric medium, the wave equations are coupled, and by setting the chiral parameter, $\kappa = 0$, one can obtain the uncoupled wave equations for an achiral medium.

5.2.3 Green function for coupled wave equations in chiral media.

In order to find the solution for the electric and magnetic fields in Eqs. (5.14),(5.15), we adopt the Green function approach [49] to solve the inhomogeneous coupled wave equations in the chiral media. Let us consider, $G_{\mathrm{E}}(\mathbf{r},\mathbf{r}',t)$ and $G_{\mathrm{H}}(\mathbf{r},\mathbf{r}',t)$ Green functions of the fields $\mathbf{E}(\mathbf{r},t)$ and $\mathbf{H}(\mathbf{r},t)$, respectively. By definition, $G_{\mathrm{E}}(\mathbf{r},\mathbf{r}',t)$ and $G_{\mathrm{H}}(\mathbf{r},\mathbf{r}',t)$ are the solutions of the wave equations Eq. (5.14) (5.15), respectively, with a point-like source term described by the three-dimensional Dirac delta function $\delta^{(3)}(\mathbf{r}-\mathbf{r}')$ located at $\mathbf{r}=\mathbf{r}'$. In the absence of charges ($\rho=0$ and $\mathbf{J}=0$), the wave equations become

$$\nabla^2\mathbf{E}-\frac{1}{c^2}\left(\epsilon_1\mu_1+\kappa_1^2\right)\frac{\partial^2\mathbf{E}}{\partial t^2}+2\frac{i\kappa_1}{c}\mu_1\mu_0\frac{\partial^2\mathbf{H}}{\partial t^2}=0, \tag{5.16a}$$

$$\nabla^2\mathbf{H}-\frac{1}{c^2}\left(\epsilon_1\mu_1+\kappa_1^2\right)\frac{\partial^2\mathbf{H}}{\partial t^2}-2\frac{i\kappa_1}{c}\epsilon_0\epsilon_1\frac{\partial^2\mathbf{E}}{\partial t^2}=0. \tag{5.16b}$$

Without loss of generality, we can simplify the problem by looking for the solutions for individual field components (E_x,E_y,E_z) and (H_x,H_y,H_z), which allow us to seek the solution for a single field component E_j and H_j, where $j=x,y,z$. Furthermore, we define the distance between the source and the observation point as $\mathrm{R}=|\mathbf{r}-\mathbf{r}'|$ and rewrite Eq. (5.16) in spherical polar coordinates. In turn, we obtain

$$\frac{1}{R}\frac{\partial^2}{\partial R^2}\left(RE_j\right)-\frac{\epsilon_1\mu_1+\kappa_1^2}{c^2}\frac{\partial^2E_j}{\partial t^2}+\frac{2i\kappa_1\mu_0\mu_1}{c}\frac{\partial^2H_j}{\partial R^2}=0, \tag{5.17a}$$

$$\frac{1}{R}\frac{\partial^2}{\partial R^2}\left(RH_j\right)-\frac{\epsilon_1\mu_1+\kappa_1^2}{c^2}\frac{\partial^2H_j}{\partial t^2}-\frac{2i\kappa_1\epsilon_0\epsilon_1}{c}\frac{\partial^2E_j}{\partial R^2}=0. \tag{5.17b}$$

To eliminate the time derivatives of the field amplitudes in Eq. (5.17), we take the Ansatz

$$E_j = \mathrm{Re}\left[E_{0j}e^{-i\omega t}\right], \tag{5.18a}$$

$$H_j = \mathrm{Re}\left[H_{0j}e^{-i\omega t}\right]. \tag{5.18b}$$

Substituting Eq. (5.18) into Eq. (5.17) and rearranging, we get

$$\frac{\partial^2}{\partial R^2}\left(RE_{0j}\right) + \frac{(\epsilon_1\mu_1 + \kappa_1^2)\omega^2}{c^2}(RE_{0j}) - \frac{2i\kappa_1\mu_1\omega^2}{c^2}(\mu_0 cRH_{0j}) = 0, \tag{5.19a}$$

$$\frac{\partial^2}{\partial R^2}\left(\mu_0 cRH_{0j}\right) + \frac{(\epsilon_1\mu_1 + \kappa_1^2)\omega^2}{c^2}(\mu_0 cRH_{0j}) + \frac{2i\kappa_1\epsilon_1\omega^2}{c^2}(RE_{0j}) = 0. \tag{5.19b}$$

In order to eliminate the space derivatives, we further take the second Ansatz

$$RE_{0j} = Ae^{i\beta R}, \tag{5.20a}$$

$$\mu_0 cRH_{0j} = Be^{i\beta R}, \tag{5.20b}$$

where $\beta = \sqrt{(\epsilon_1\mu_1 + \kappa_1^2)\omega^2/c^2}$ represents the dispersion relation inside the chiral medium, and A and B are two unknown coefficients. Now, accounting for the field propagation in forward and backward directions, we rewrite the Eq. (5.20) as

$$RE_{0j} = Ae^{i\beta_+ R} + Ce^{i\beta_- R}, \tag{5.21a}$$

$$\mu_0 cRH_{0j} = Be^{i\beta_+ R} + De^{i\beta_- R}, \tag{5.21b}$$

where $\beta_\pm = \pm\dfrac{\omega}{c}[\sqrt{\epsilon_1\mu_1} \pm \kappa_1]$, and C and D are other two unknown coefficients. Substituting Eq. (5.21) in the Eq. (5.19), we get rid of two coefficients: $A =$

$-i\sqrt{\mu_1/\epsilon_1}B$ and $C = i\sqrt{\mu_1/\epsilon_1}D$. Thus, we are left with

$$RE_{0j} = -i\sqrt{\frac{\mu_1}{\epsilon_1}}\left[Be^{i\beta_+ R} - De^{i\beta_- R}\right], \tag{5.22a}$$

$$\mu_0 cRH_{0j} = Be^{i\beta_+ R} + De^{i\beta_- R}. \tag{5.22b}$$

We determine B and D utilizing the fact that each point on a wavefront can be considered as a source of secondary wavefronts that propagate in all directions (Huygens' Principle), allowing us to write

$$\nabla^2 E_{0j} = \delta^{(3)}(\mathbf{R}), \tag{5.23a}$$

$$\nabla^2 \mu_0 cH_{0j} = \delta^{(3)}(\mathbf{R}). \tag{5.23b}$$

Integration of Eq. (5.23) over all space provides

$$\int_{\text{all space}} \nabla^2 E_{0j} d\tau = \int_{\text{all space}} \delta^{(3)}(\mathbf{R}) d\tau = 1, \tag{5.24a}$$

$$\int_{\text{all space}} \nabla^2 \mu_0 cH_{0j} d\tau = \int_{\text{all space}} \delta^{(3)}(\mathbf{R}) d\tau = 1, \tag{5.24b}$$

where $d\tau$ denotes the volume element in three-dimensional space, and we have used the property that the integral of the Dirac delta function over the entire space equals 1. Finally, by utilizing Eq. (5.23), we calculate the explicit expression of all the unknown coefficients

$$A = \frac{1}{8\pi R}\left(1 - i\sqrt{\frac{\mu_1}{\epsilon_1}}\right), \tag{5.25a}$$

$$B = \frac{1}{8\pi R}\left(1 + i\sqrt{\frac{\epsilon_1}{\mu_1}}\right), \tag{5.25b}$$

$$C = \frac{1}{8\pi R}\left(1 + i\sqrt{\frac{\mu_1}{\epsilon_1}}\right), \tag{5.25c}$$

$$D = \frac{1}{8\pi R}\left(1 - i\sqrt{\frac{\epsilon_1}{\mu_1}}\right). \tag{5.25d}$$

Thus, the solutions of the homogeneous wave equation in Eqs. (5.16) can be determined using the coefficients given by Eq. (5.25). Since the Green functions also satisfy the homogeneous wave equations, we can write the expressions of the Green function for the fields $\mathbf{E}(\mathbf{r},t)$ and $\mathbf{H}(\mathbf{r},t)$ as follows

$$G_{\mathrm{E}}(|\mathbf{r}-\mathbf{r}'|,t) = \frac{1}{8\pi}\frac{e^{-i\omega t}}{|\mathbf{r}-\mathbf{r}'|}\left[\left(1-i\sqrt{\frac{\mu_1}{\epsilon_1}}\right)e^{i\beta_+|\mathbf{r}-\mathbf{r}'|}+\left(1+i\sqrt{\frac{\mu_1}{\epsilon_1}}\right)e^{i\beta_-|\mathbf{r}-\mathbf{r}'|}\right], \tag{5.26a}$$

$$\begin{aligned} G_{\mathrm{H}}(|\mathbf{r}-\mathbf{r}'|,t) &= \frac{1}{8\pi}\frac{e^{-i\omega t}}{|\mathbf{r}-\mathbf{r}'|}\left[\left(1+i\sqrt{\frac{\epsilon_1}{\mu_1}}\right)e^{i\beta_+|\mathbf{r}-\mathbf{r}'|}+\left(1-i\sqrt{\frac{\epsilon_1}{\mu_1}}\right)e^{i\beta_-|\mathbf{r}-\mathbf{r}'|}\right], \\ &= \frac{i}{8\pi}\sqrt{\frac{\epsilon_1}{\mu_1}}\frac{e^{-i\omega t}}{|\mathbf{r}-\mathbf{r}'|}\left[\left(1-i\sqrt{\frac{\mu_1}{\epsilon_1}}\right)e^{i\beta_+|\mathbf{r}-\mathbf{r}'|}-\left(1+i\sqrt{\frac{\mu_1}{\epsilon_1}}\right)e^{i\beta_-|\mathbf{r}-\mathbf{r}'|}\right]. \end{aligned} \tag{5.26b}$$

In turn, we evaluate the fields generated by the source term from the integrals

$$\mathbf{E}(\mathbf{r},t) = \mathrm{Re}\left[\int_\tau G_{\mathrm{E}}(|\mathbf{r}-\mathbf{r}'|,t)q_1(\mathbf{r}')d^3\mathbf{r}'\right], \tag{5.27a}$$

$$\mathbf{H}(\mathbf{r},t) = \mathrm{Re}\left[\int_\tau G_{\mathrm{H}}(|\mathbf{r}-\mathbf{r}'|,t)q_2(\mathbf{r}')d^3\mathbf{r}'\right], \tag{5.27b}$$

where $q_1(\mathbf{r}')$ and $q_2(\mathbf{r}')$ indicate the source terms given by

$$q_1(\mathbf{r}') = \frac{\mu_1}{\epsilon_0(\mu_1\epsilon_1-\kappa_1^2)}\nabla_{\mathbf{r}'}\rho(\mathbf{r}')+\mu_0\mu_1\frac{\partial\mathbf{J}(\mathbf{r}')}{\partial t}, \tag{5.28a}$$

$$q_2(\mathbf{r}') = -\frac{i\kappa_1 c}{(\mu_1\epsilon_1-\kappa_1^2)}\nabla_{\mathbf{r}'}\rho(\mathbf{r}')-\nabla_{\mathbf{r}'}\times\mathbf{J}(\mathbf{r}')+\frac{i\kappa_1}{c}\frac{\partial\mathbf{J}(\mathbf{r}')}{\partial t}. \tag{5.28b}$$

Setting the charge and current density as $\rho(\mathbf{r},t) = \mathrm{Re}\,[\rho_0(\mathbf{r})e^{-i\omega t}]$ and $\mathbf{J}(\mathbf{r},t) = \mathrm{Re}\,[\mathbf{J}_0(\mathbf{r})e^{-i\omega t}]$, respectively, one can show that $\nabla_{\mathbf{r}}\rho_0(\mathbf{r}) = -\nabla_{\mathbf{r}'}\rho_0(\mathbf{r}')$ and $\nabla_{\mathbf{r}}\times$

$\mathbf{J}_0(\mathbf{r}) = -\nabla_{\mathbf{r}'} \times \mathbf{J}_0(\mathbf{r}')$. Consequently, Eq. (5.27) becomes

$$\mathbf{E}(\mathbf{r},t) = \mathrm{Re}\left\{\int_\tau G_{\mathrm{E}}(|\mathbf{r}-\mathbf{r}'|,t)\left[-\frac{\mu_1}{\epsilon_0(\mu_1\epsilon_1-\kappa_1^2)}\nabla_{\mathbf{r}'}\rho_0(\mathbf{r}') - i\omega\mu_0\mu_1\mathbf{J}_0(\mathbf{r}')\right]d^3\mathbf{r}'\right\}, \tag{5.29a}$$

$$\mathbf{H}(\mathbf{r},t) = \mathrm{Re}\left\{\int_\tau G_{\mathrm{H}}(|\mathbf{r}-\mathbf{r}'|,t)\left[\begin{array}{l}\dfrac{i\kappa_1 c}{(\mu_1\epsilon_1-\kappa_1^2)}\nabla_{\mathbf{r}'}\rho_0(\mathbf{r}') + \nabla_{\mathbf{r}'}\times\mathbf{J}_0(\mathbf{r}') \\ + \dfrac{\kappa_1\omega}{c}\mathbf{J}_0(\mathbf{r}')\end{array}\right]d^3\mathbf{r}'\right\}. \tag{5.29b}$$

5.3 Dipolar excitation in electrostatic limit.

We investigate the scattering problem of the nanoshell considering point-like electric $\mathbf{d}(\mathbf{r},t) = \mathrm{Re}[\mathbf{d}_0 e^{-i\omega t}]$ and magnetic $\mathbf{m}(\mathbf{r},t) = \mathrm{Re}[\mathbf{m}_0 e^{-i\omega t}]$ oscillating dipoles and neglecting multipole terms. In such treatment, the polarization charges are strongly localised around the microscopic electric dipoles, whereas the temporal variation of electric dipole moments and the spatial variation of the magnetic dipole moments generate the current density. Thus, in the electric/magnetic dipolar excitation limit, we can express the associated charge and current density as

$$\rho_0(\mathbf{r}) = -\mathbf{d}_0 \cdot \nabla\delta(\mathbf{r}), \tag{5.30a}$$

$$\mathbf{J}_0(\mathbf{r}) = -i\omega\mathbf{d}_0\delta(\mathbf{r}) + \nabla\delta(\mathbf{r}) \times \mathbf{m}_0. \tag{5.30b}$$

In addition, for convenience, we express the Green function in terms of two auxiliary functions as

$$G_{\mathrm{E}}(r,t) = \frac{1}{8\pi} g_{\mathrm{E}}(r) e^{-i\omega t}, \tag{5.31a}$$

$$G_{\mathrm{H}}(r,t) = \frac{1}{8\pi} g_{\mathrm{H}}(r) e^{-i\omega t}. \tag{5.31b}$$

Finally, by substituting the charge and current density, see Eq. (5.30), in the Eq. (5.29) and using Eq. (5.31), we obtain the electric and magnetic field

$$\mathbf{E}(\mathbf{r},t) = \mathrm{Re}\left\{\frac{1}{8\pi}\left[\begin{array}{l}\dfrac{\mu_1}{\epsilon_0(\mu_1\epsilon_1-\kappa_1^2)}[\mathbf{d}_0\cdot\nabla_{\mathbf{r}}][\nabla_{\mathbf{r}}g_{\mathrm{E}}(r)] \\ +\omega^2\mu_0\mu_1\mathbf{d}_0 g_{\mathrm{E}}(r) + i\omega\mu_0\mu_1[\nabla_{\mathbf{r}}g_{\mathrm{E}}(r)]\times\mathbf{m}_0\end{array}\right]e^{-i\omega t}\right\}, \quad (5.32a)$$

$$\mathbf{H}(\mathbf{r},t) = \mathrm{Re}\left\{\frac{1}{8\pi}\left[\begin{array}{l}\dfrac{\kappa_1 c}{(\mu_1\epsilon_1-\kappa_1^2)}\sqrt{\dfrac{\epsilon_1}{\mu_1}}[\mathbf{d}_0\cdot\nabla_{\mathbf{r}}][\nabla_{\mathbf{r}}g_{\mathrm{H}}(r)] - \kappa_1\dfrac{\omega^2}{c}\sqrt{\dfrac{\epsilon_1}{\mu_1}}\mathbf{d}_0 g_{\mathrm{H}}(r) \\ -\omega\sqrt{\dfrac{\epsilon_1}{\mu_1}}[\mathbf{d}_0\times\nabla_{\mathbf{r}}g_{\mathrm{H}}(r)] - i\sqrt{\dfrac{\epsilon_1}{\mu_1}}\mathbf{m}_0\nabla_{\mathbf{r}}^2 g_{\mathrm{H}}(r) \\ -i\sqrt{\dfrac{\epsilon_1}{\mu_1}}\nabla_{\mathbf{r}}[\mathbf{m}_0\cdot\nabla_{\mathbf{r}}g_{\mathrm{H}}(r)] + i\kappa_1\dfrac{\omega}{c}\sqrt{\dfrac{\epsilon_1}{\mu_1}}[\mathbf{m}_0\times\nabla_{\mathbf{r}}g_{\mathrm{H}}(r)]\end{array}\right]e^{-i\omega t}\right\}. \quad (5.32b)$$

In the electrostatic limit, meaning that $(R+h)\ll\lambda$, the fields generated by the electric/magnetic dipoles can be determined by limiting $\omega\to 0$ in the Eq. (5.32). In turn, we obtain

$$\mathbf{E}(\mathbf{r},t) = \mathrm{Re}\left\{\left[\frac{[3(\mathbf{d}_0\cdot\hat{\mathbf{e}}_r)\hat{\mathbf{e}}_r-\mathbf{d}_0]}{4\pi\epsilon_0\epsilon_1 r^3}\right]e^{-i\omega t}\right\}, \quad (5.33a)$$

$$\mathbf{H}(\mathbf{r},t) = \mathrm{Re}\left\{\left[\frac{[3(\mathbf{m}_0\cdot\hat{\mathbf{e}}_r)\hat{\mathbf{e}}_r-\mathbf{m}_0]}{4\pi r^3} - i\kappa_1 c\frac{[3(\mathbf{d}_0\cdot\hat{\mathbf{e}}_r)\hat{\mathbf{e}}_r-\mathbf{d}_0]}{4\pi\mu_1\epsilon_1 r^3}\right]e^{-i\omega t}\right\}, \quad (5.33b)$$

where $\hat{\mathbf{e}}_r = \mathbf{r}/r$ is the radial unit vector. Note that in the presence of chiral media ($\kappa\neq 0$), the magnetic field has a contribution from the electric dipoles.

5.3.1 Scattering of nanoshell upon circular polarization excitation.

In the previous sections, we present the calculations of electric and magnetic fields inside both chiral and achiral media when exposed to monochromatic radiation in the electrostatic approximation. Utilizing those fields, here we investigate the scattering problem of the nanoshell upon circular polarization excitation. Moreover, we analyze the problem considering generic constituent media of the nanostructure so that depending on the configuration case, we can choose a particular medium

of interest. In order to do that we consider an impinging circularly polarized plane wave with wave-vector $\mathbf{k}_0$ and vectorial amplitude $\tilde{\mathbf{A}}_0$ such that $\mathbf{k}_0 \cdot \tilde{\mathbf{A}}_0 = 0$. Owing to the spherical symmetry, without any loss of generality, for the circularly polarized plane wave we set

$$\mathbf{k}_0 = k_0 \hat{\mathbf{e}}_z, \tag{5.34a}$$

$$\tilde{\mathbf{A}}_0 = \frac{A_0}{\sqrt{2}}(\hat{\mathbf{e}}_x + is\hat{\mathbf{e}}_y), \tag{5.34b}$$

where $s = \pm 1$ accounts for the right ($s = +1$) and left ($s = -1$) circularly polarized wave. In such assumption, the scattering problem can be solved by multipole expansion truncated to electric/magnetic dipole terms, obtaining the electrostatic/magnetostatic solutions

$$\tilde{\mathbf{E}}_0(\mathbf{r}) = \left[\alpha_1\Theta_1(r) + \alpha_2\Theta_2(r) + e^{i\mathbf{k}_0\cdot\mathbf{r}}\Theta_3(r)\right]\tilde{\mathbf{A}}_0 + \left[\gamma_2\Theta_2(r) + \gamma_3\Theta_3(r)\right]\tilde{\mathbf{F}}(\mathbf{r}), \tag{5.35a}$$

$$\begin{aligned}\tilde{\mathbf{H}}_0(\mathbf{r}) = &\left[\beta_1\Theta_1(r) + \beta_2\Theta_2(r) - is\sqrt{\epsilon_3/\mu_3}e^{i\mathbf{k}_0\cdot\mathbf{r}}\Theta_3(r)\right]\tilde{\mathbf{A}}_0/(\mu_0 c) \\ &+ \left[(\delta_2 - i\kappa_2\gamma_2/\mu_2)\Theta_2(r) + (\delta_3 - i\kappa_3\gamma_3/\mu_3)\Theta_3(r)\right]\tilde{\mathbf{F}}(\mathbf{r})/(\mu_0 c),\end{aligned} \tag{5.35b}$$

where $\tilde{\mathbf{F}}(\mathbf{r}) = 3(\tilde{\mathbf{A}}_0 \cdot \hat{\mathbf{e}}_r)\hat{\mathbf{e}}_r - \tilde{\mathbf{A}}_0]R^3/(4\pi r^3)$ and $\alpha_{1,2}, \beta_{1,2}, \gamma_{1,2}$, and $\delta_{1,2}$ are field amplitudes yet to be determined. The associated position-dependent displacement vectors and induction magnetic fields can be obtained from Eq. (5.2). Finally, we apply the BCs for the continuity of tangential components of $\tilde{\mathbf{E}}(\mathbf{r})$ and $\tilde{\mathbf{H}}(\mathbf{r})$ and the normal components of $\tilde{\mathbf{D}}(\mathbf{r})$ and $\tilde{\mathbf{B}}(\mathbf{r})$ at the interfaces $\mathbf{r} = R\hat{\mathbf{e}}_r$ and $\mathbf{r} = (R + h)\hat{\mathbf{e}}_r$. Thus, for the considered nanoshell with inner radius R and shell

thickness h, we set

$$\tilde{\mathbf{D}}_1(R)\cdot\hat{\mathbf{e}}_r=\tilde{\mathbf{D}}_2(R)\cdot\hat{\mathbf{e}}_r, \tag{5.36a}$$

$$\tilde{\mathbf{E}}_1(R)\times\hat{\mathbf{e}}_r=\tilde{\mathbf{E}}_2(R)\times\hat{\mathbf{e}}_r, \tag{5.36b}$$

$$\tilde{\mathbf{B}}_1(R)\cdot\hat{\mathbf{e}}_r=\tilde{\mathbf{B}}_2(R)\cdot\hat{\mathbf{e}}_r, \tag{5.36c}$$

$$\tilde{\mathbf{H}}_1(R)\times\hat{\mathbf{e}}_r=\tilde{\mathbf{H}}_2(R)\times\hat{\mathbf{e}}_r, \tag{5.36d}$$

$$\tilde{\mathbf{D}}_2(R+h)\cdot\hat{\mathbf{e}}_r=\tilde{\mathbf{D}}_3(R+h)\cdot\hat{\mathbf{e}}_r, \tag{5.36e}$$

$$\tilde{\mathbf{E}}_2(R+h)\times\hat{\mathbf{e}}_r=\tilde{\mathbf{E}}_3(R+h)\times\hat{\mathbf{e}}_r, \tag{5.36f}$$

$$\tilde{\mathbf{B}}_2(R+h)\cdot\hat{\mathbf{e}}_r=\tilde{\mathbf{B}}_3(R+h)\cdot\hat{\mathbf{e}}_r, \tag{5.36g}$$

$$\tilde{\mathbf{H}}_2(R+h)\times\hat{\mathbf{e}}_r=\tilde{\mathbf{H}}_3(R+h)\times\hat{\mathbf{e}}_r. \tag{5.36h}$$

Inserting Eq. (5.35) into the Boundary Conditions (BCs) Eq. (5.36), we obtain an 8×8 inhomogeneous algebraic system of equations (reduced from 12×8 thanks to redundancy of Maxwell's equations, manifesting also in BCs), which we numerically solve to determine 8 unknown field amplitudes. Thus, the scattering amplitudes are evaluated by numerically solving the system of equations written in the matrix form

$$\begin{bmatrix}
\epsilon_1 & -i\kappa_1 & -\epsilon_2 & i\kappa_2 & -\epsilon_2/2\pi & i\kappa_2/2\pi & 0 & 0\\
1 & 0 & -1 & 0 & 1/4\pi & 0 & 0 & 0\\
i\kappa_1 & \mu_1 & -i\kappa_2 & -\mu_2 & 0 & -\mu_2/2\pi & 0 & 0\\
0 & 1 & 0 & -1 & -i\kappa_2/4\pi\mu_2 & 1/4\pi & 0 & 0\\
0 & 0 & \epsilon_2 & -i\kappa_2 & \epsilon_2 q/2\pi & -i\kappa_2 f/2\pi & -\epsilon_3 f/2\pi & i\kappa_3 f/2\pi\\
0 & 0 & 1 & 0 & -f/4\pi & 0 & f/4\pi & 0\\
0 & 0 & i\kappa_2 & \mu_2 & 0 & \mu_2 f/2\pi & 0 & -\mu_3 f/2\pi\\
0 & 0 & 0 & 1 & i\kappa_2 f/4\pi & -f/4\pi & -i\kappa_3 f/4\pi & f/4\pi
\end{bmatrix}
\begin{bmatrix}\alpha_1\\ \beta_1\\ \alpha_2\\ \beta_2\\ \gamma_2\\ \delta_2\\ \gamma_3\\ \delta_3\end{bmatrix}
=
\begin{bmatrix}0\\ 0\\ 0\\ 0\\ w_1\\ 1\\ w_2\\ w_3\end{bmatrix}, \tag{5.37}$$

where $w_1=\epsilon_3-\kappa_3 s\sqrt{\epsilon_3/\mu_3}$, $w_2=i\kappa_3-is\sqrt{\mu_3\epsilon_3}$, and $w_3=-is\sqrt{\epsilon_3/\mu_3}$.

5.3.2 Power dissipation and absorption cross section.

Upon interaction with electromagnetic radiation, energy exchange occurs between the particles inside the matter and the radiation. As a consequence, the light-matter interaction involves different processes like absorption, emission, transmission, and scattering of light. However, all such processes maintain the energy conservation. Therefore, to calculate the dissipated power within the nanostructure, we start with the Poynting theorem

$$\nabla \cdot \mathbf{S} + \frac{du}{dt} = -\mathbf{J} \cdot \mathbf{E}, \tag{5.38}$$

where $\mathbf{J}$ is the current density, $\mathbf{S} = \mathbf{E} \times \mathbf{H}$ is the Poynting vector which represents the rate of electromagnetic energy flow per unit area and $u = (1/2)(\mathbf{E} \cdot \mathbf{D} + \mathbf{B} \cdot \mathbf{H})$ is the electromagnetic energy density. Here we focus on the absorption of electromagnetic radiation by the nanostructure, leading to the evaluation of energy dissipation rate

$$\frac{dU}{dt} = \left\langle \int_{\tau} \left[-\mathbf{J}(\mathbf{r}, t) \cdot \mathbf{E}(\mathbf{r}, t) + \mathbf{J}_{\text{far}}(\mathbf{r}, t) \cdot \mathbf{E}_{\text{far}}(\mathbf{r}, t) \Theta_3 \right] d\tau \right\rangle_T , \tag{5.39}$$

where $\mathbf{J}_{\text{far}}$ and $\mathbf{E}_{\text{far}}$ refer to the far field induced current density and the far field, respectively, and $\langle ... \rangle_T$ indicates the average over single cycle, where $T = 2\pi/\omega$ is the period of the cycle. Note that the far field contribution is excluded since we are interested in the absorbed power inside the nanostructure. Furthermore, the induced current density is related to the induced polarization thorough

$$\mathbf{J}(\mathbf{r}, t) = \partial_t \mathbf{P}(\mathbf{r}, t) = \text{Re}\left\{ -i\omega \left[\mathbf{D} - \epsilon_{\mathbf{0}} \mathbf{E} \right] e^{-i\omega t} \right\}. \tag{5.40}$$

Now, splitting the integral in Eq. (5.39) in different regions in space, we rewrite Eq. (5.39) as

$$\frac{dU}{dt} = \left\langle \int_{\tau_1} \left[-\mathbf{J}_1(\mathbf{r},t)\cdot\mathbf{E}_1(\mathbf{r},t)\right] d\tau \right\rangle_T + \left\langle \int_{\tau_2} \left[-\mathbf{J}_2(\mathbf{r},t)\cdot\mathbf{E}_2(\mathbf{r},t)\right] d\tau \right\rangle_T + \left\langle \int_{\tau_3} \left[-\mathbf{J}_3(\mathbf{r},t)\cdot\mathbf{E}_3(\mathbf{r},t)\right] d\tau \right\rangle_T + \left\langle \int_{\tau_3} \left[\mathbf{J}_{\text{far}}(\mathbf{r},t)\cdot\mathbf{E}_{\text{far}}(\mathbf{r},t)\right] d\tau \right\rangle_T , \tag{5.41}$$

where $\mathbf{E}_{1,2,3}$ and $\mathbf{J}_{1,2,3}$ are the respective electric fields and induced current densities in the region $1, 2$ and 3. For the quasi monochromatic field excitation, carrying out the averages in Eq. (5.41), we get

$$\frac{dU}{dt} = -\frac{1}{2}\text{Re}\left\{ \int_{\tau_1} \mathbf{J}_1^*\cdot\mathbf{E}_1 d\tau + \int_{\tau_2} \mathbf{J}_2^*\cdot\mathbf{E}_2 d\tau + \int_{\tau_3} \mathbf{J}_3^*\cdot\mathbf{E}_3 d\tau - \int_{\tau_3} \mathbf{J}_{\text{far}}^*\cdot\mathbf{E}_{\text{far}} d\tau \right\}. \tag{5.42}$$

Consequently, the absorption cross section is assessed by

$$\sigma_{\text{abs}} = -\frac{1}{I_0}\frac{dU}{dt}, \tag{5.43}$$

where $I_0 = (1/2)\epsilon_0 c\text{Re}[\sqrt{\epsilon_3/\mu_3}]|\tilde{\mathbf{A}}_0|^2$ is the intensity of the impinging radiation. Inserting the electric fields for different regions as given by Eq. (5.35a) and the current densities according to Eq. (5.40) in the Eq. (5.42), we obtain the absorption cross section of the nanoshell from Eq. (5.43), which is explicitly given by

$$\begin{aligned}\sigma_{\text{abs}} = &-\frac{\omega}{c\text{Re}\left[\sqrt{\epsilon_3/\mu_3}\right]}\left\{\frac{4}{3}\pi R^3 \text{Im}\left[\alpha_1\left[(\epsilon_1^*-1)\alpha_1^* + i\kappa_1^*\beta_1^*\right]\right]\right. \\ &+ \text{Im}\left\{\frac{4}{3}\pi\left[(R+h)^3 - R^3\right]\alpha_2\left[(\epsilon_2^*-1)\alpha_2^* + i\kappa_2^*\beta_2^*\right] + \right. \\ &+ \frac{R^6}{6\pi}\left[\frac{1}{R^3} - \frac{1}{(R+h)^3}\right]\gamma_2\left[(\epsilon_2^*-1)\gamma_2^* + i\kappa_2^*\delta_2^*\right]\Big\} + \\ &\left. + \frac{R^6}{6\pi}\left[\frac{1}{R^3} - \frac{1}{(R+h)^3}\right]\text{Im}\left\{\gamma_3\left[(\epsilon_3^*-1)\gamma_3^* + i\kappa_3^*\delta_3^*\right]\right\}\right\}\end{aligned} \tag{5.44}$$

where the amplitudes $\alpha_{1,2}, \beta_{1,2}, \gamma_{2,3}$, and $\delta_{2,3}$ are determined through the numerical inversion of 8×8 matrix, as mentioned in the previous section.

5.3.3 Polarizability of nanoshell surrounding chiral media

The electric polarizability $\alpha_{\mathrm{e}}^{\mathrm{ns}}$ of the nanoshell relating the electric dipole moment $\mathbf{d}_0$ and the external electric field is given by $\mathbf{d}_0 = \alpha_{\mathrm{e}}^{\mathrm{ns}}\mathbf{E}_0$. Furthermore, the dipole generates an electric field

$$\mathbf{E}_{\mathrm{dip}}(\mathbf{r}) = \frac{1}{4\pi\epsilon_0\epsilon_3 r^3}\left[3(\mathbf{d}_0 \cdot \hat{\mathbf{e}}_r)\hat{\mathbf{e}}_r - \mathbf{d}_0\right]. \tag{5.45}$$

The electric field in the medium 3 is the sum of the external field and the field generated by the dipole. Thus, utilizing Eq. (5.45), we get the nanoshell electric polarizability

$$\alpha_{\mathrm{e}}^{\mathrm{ns}} = \epsilon_0\epsilon_3\gamma_3 R^3. \tag{5.46}$$

Similarly, the magnetic polarizability $\alpha_{\mathrm{m}}^{\mathrm{ns}}$ of the nanoshell relating the magnetic dipole moment and the external magnetic field provides $\mathbf{m}_0 = \alpha_{\mathrm{m}}^{\mathrm{ns}}\mathbf{H}_0$. The magnetic field produced by the magnetic dipole is given by

$$\mathbf{H}_{\mathrm{dip}}(\mathbf{r}) = \frac{1}{4\pi r^3}\left[3(\mathbf{m}_0 \cdot \hat{\mathbf{e}}_r)\hat{\mathbf{e}}_r - \mathbf{m}_0\right]. \tag{5.47}$$

Again, utilizing equation Eq. (5.47), we get the magnetic polarizability

$$\alpha_{\mathrm{m}}^{\mathrm{ns}} = is\delta_3 R^3\sqrt{\frac{\mu_3}{\epsilon_3}}. \tag{5.48}$$

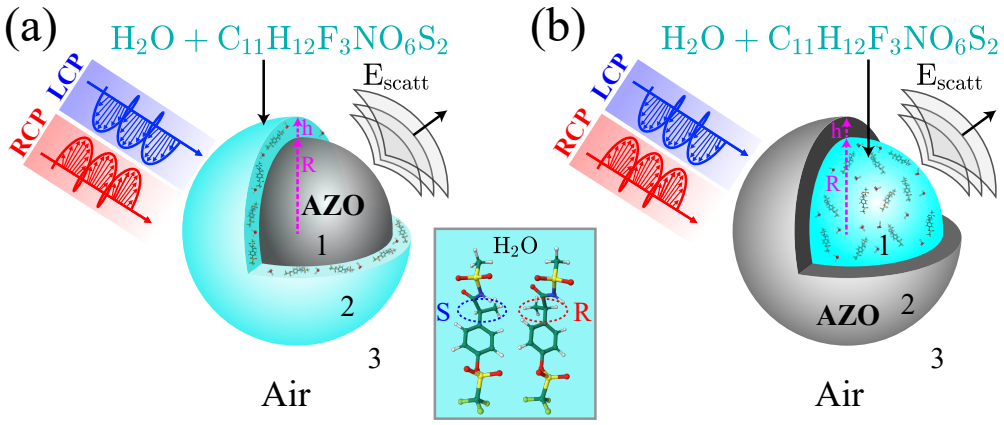


Figure 5.2: Schematic of (**a**) Aluminum-Doped Zinc Oxide (AZO) nanosphere with radius R surrounded by a layer of aqueous Ladarixin with thickness h immersed in air. (**b**) AZO-based nanoshell with inner/outer radii R and $R+h$, respectively, immersed in air and embedding aqueous Ladarixin at its core.

5.4 Plasmon-enhanced VCD of chiral drug solutions.

Fig. 5.2(a,b) illustrates the considered AZO-based nanostructures embedding chiral drugs, in particular, aqueous Ladarixin ($H_2O + C_{11}H_{12}F_3No_6S_2$). We investigate two configurations: (a) AZO nanosphere surrounded by a nanolayer of aqueous Ladarixin, and (b) spherical nanoshell of AZO surrounded by air, and the core is embedded with aqueous Ladarixin. In both cases, the radius of the inner and outer spheres are R and $R+h$, respectively. The linear electromagnetic response of such nanostructures upon circularly polarized excitation is accomplished by setting the optical parameters in Eq. (5.3) for three regions. These parameters are given by

$$
\begin{aligned}
(\mathbf{a}) \quad & \epsilon_1(\lambda) = \epsilon_{\mathrm{AZO}}(\lambda), \quad \epsilon_2(\lambda) = \epsilon_{\mathrm{cs}}(\lambda), \quad \epsilon_3(\lambda) = 1, \\
& \mu_1(\lambda) = \mu_3(\lambda) = 1, \quad \mu_2(\lambda) = \mu_{\mathrm{cs}}(\lambda), \\
& \kappa_1(\lambda) = \kappa_3(\lambda) = 0, \quad \kappa_2(\lambda) = \kappa_{\mathrm{cs}}(\lambda), \\
(\mathbf{b}) \quad & \epsilon_1(\lambda) = \epsilon_{\mathrm{cs}}(\lambda), \quad \epsilon_2(\lambda) = \epsilon_{\mathrm{AZO}}(\lambda), \quad \epsilon_3(\lambda) = 1, \\
& \mu_1(\lambda) = \mu_{\mathrm{cs}}(\lambda), \quad \mu_2(\lambda) = \mu_3(\lambda) = 1, \\
& \kappa_1(\lambda) = \kappa_{\mathrm{cs}}(\lambda), \quad \kappa_2(\lambda) = \kappa_3(\lambda) = 0,
\end{aligned}
$$

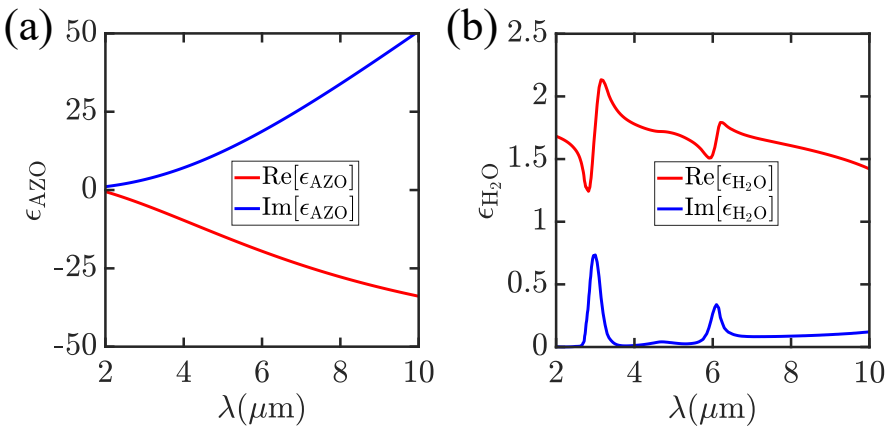


Figure 5.3: Vacuum wavelength (λ) dependence of the real (red curves) and imaginary (blue curves) parts of (**a**) the RDP $\epsilon_{AZO}(\lambda)$ of AZO [197] and (**b**) the RDP $\epsilon_{H_2O}(\lambda)$ of water [198].

where $\epsilon_{AZO}(\lambda)$ denotes the complex relative dielectric permittivity of AZO [197], and $\epsilon_{cs}(\lambda)$, $\mu_{cs}(\lambda)$, and $\kappa_{cs}(\lambda)$ represent the Relative Dielectric Permittivity (RDP), Relative Magnetic Permeability (RMP) and the Chiral Parameter (CP), respectively, of the considered Chiral Sample (CS), which is aqueous Ladarixin. Fig. 5.3 represents the vacuum wavelength dependency of (a) $\epsilon_{AZO}(\lambda)$ and (b) water RDP $\epsilon_{H_2O}(\lambda)$ [198]. The calculation of the Bi-Anisotropic Constitutive Relations (BACRs) effective optical constants of the CS is performed through a previously mentioned (in Chapter 2 and 3). In Fig. 5.4(a), we illustrate a schematic diagram of the Ladarixin vibronic structure along with the relevant electronic/vibrational transitions upon excitation by laser field in the electric/magnetic dipole approximation. From such analysis, we observe that aqueous Ladarixin contains two high-probability conformational states related to the free-energy basin minima in the case of the Ladarixin R enantiomer, depicted in Fig. 5.4(b). The temporal dynamics of electric transition dipole moment ($\mathbf{d}_{12}$) and magnetic transition dipole moment ($\mathbf{m}_{12}$) associated with the electronic transition from the ground to the first excited state are illustrated in Fig. 5.4(c). In addition, the temporal evolution of the pseudoscalar chiral projection ($\mathbf{d}_{12} \cdot \mathbf{m}_{12}$), which is chirally sensitive, is also shown. It is worth mentioning that, in the case of flexible aqueous Ladarixin,

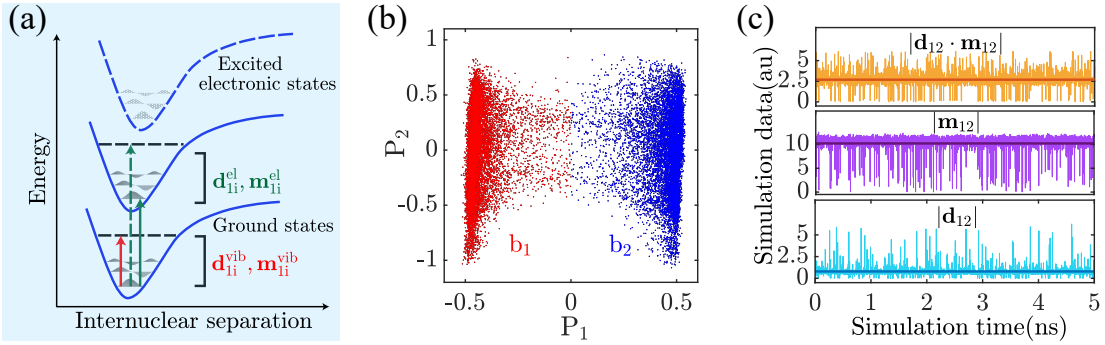


Figure 5.4: (**a**) Schematic diagram of the Ladarixin vibronic structure along with the relevant electronic/vibrational transitions upon excitation by laser field in the electric/magnetic dipole approximation. (**b**) Conformational basins obtained by projecting the MD trajectory onto the first two eigenvectors of the covariance matrix constructed from all-atom mass-weighted positional fluctuation for the pure R-enantiomer of Ladarixin dissolved in water at temperature $T = 298$ K. In equilibrium, there exist two distinct conformational state basins that are denoted as b_{k}, where $\mathrm{k} = 1, 2$. (**c**) Temporal evolution of moduli of the electric ($|\mathbf{d}_{12}|$)/magnetic ($|\mathbf{m}_{12}|$) transition dipole moment and the chiral projection ($|\mathbf{d}_{12} \cdot \mathbf{m}_{12}|$) obtained from PMM calculations at each MD simulation frame (written in terms of nanoseconds) in case of a single Ladarixin molecule in the b_1 conformation state.

vibronic transitions have no impact on the UV spectral shape, which is mainly dominated by chromophore-solvent conformational transitions. Moreover, we only account for two vibrational states responsible for resonant MIR response, and the corresponding vibrational energies and transition dipole moments are observed as independent over the Ladarixin conformational state since the vibrational modes in the two highly probable conformational states coincide. The macroscopic polarization and magnetization fields of the effective Ladarixin-water medium are calculated to obtain the BACRs given by Eq. (5.3).

In the section 5.2, we discussed the theoretical modeling of the absorption cross section of the nanoshells consisting of generic (both chiral and achiral) media within the electrostatic approach. Adopting such an approach we model the MIR plasmonic nanoshell VCD by incorporating BACRs optical constants $\epsilon(\lambda), \mu(\lambda)$, and $\kappa(\lambda)$ of chiral media (aqueous Ladarixin) along with the optical constants of AZO, upon circularly polarized excitation. Finally, we compared the results from

the semi-analytical approach with the EWFD calculations obtained through the commercial software [195].

5.5 Results and discussions.

The BACRs optical constants of aqueous Ladarixin, calculated from radiation-matter interaction modeling, are illustrated in Fig. 5.5 indicating the vacuum wavelength (λ) dependence of (a) $\Delta\epsilon_{\rm cs}(\lambda) = \epsilon_{\rm cs}(\lambda) - \epsilon_{\rm H_2O}(\lambda)$, (b) $\mu_{\rm cs}(\lambda) - 1$, and (c) $\kappa_{\rm cs}(\lambda)$ for fixed molecular number density $n_{\rm mol}^{\rm (R)} = n_{\rm mol} = 10^{-2}$ nm^{-3} of pure R-Ladarixin. The molecular number density $n_{\rm mol}^{\rm (R)} = n_{\rm mol}$ dependence of (d) $\Delta\epsilon_{\rm cs}(\lambda)$, (e) $\mu_{\rm cs}(\lambda) - 1$, and (f) $\kappa_{\rm cs}(\lambda)$ at fixed $\lambda = 5.4$ μm are shown for pure R-Ladarixin dissolved in water. Observe that the chiroptical response of Ladarixin has both electronic contributions arising from resonant electronic transition at $\lambda \simeq 236$ nm and vibrational contribution arising from resonant vibrational transition at $\lambda \simeq 5.4$ μm. Because of the considered dilute number densities (10^{-3} nm$^{-3} < n_{\rm mol} < 10^{-3}$ nm^{-2}) of Ladarixin molecule, the real part of water RDP $\epsilon_{\rm H_2O}(\lambda)$ dominates over the real part of $\epsilon_{\rm cs}(\lambda)$. In addition, water shows efficient absorption in the MIR range (see Im$[\epsilon_{\rm H_2O}]$ in Fig. 5.3(b)) and therefore dominates over the imaginary part of $\epsilon_{\rm cs}(\lambda)$. The relative permeability $\mu_{\rm cs}$ originates only from the magnetic response of Ladarixin. However, $\mu_{\rm cs}(\lambda)$ is chirally insensitive and possesses minor correction to the refractive index of the chiral sample as depicted in Fig. 5.5(b,e). At the vibrational resonance ($\lambda \simeq 5.4$ μm), Ladarixin exhibits VCD caused by Im$[\kappa_{\rm cs}(\lambda)]$, which is the prime concern of this present study.

Plasmon-enhanced VCDDA produced by the nanostructure is estimated from the absorption cross-section given by Eq. (5.44). Fig. 5.6 illustrates the results for vacuum wavelength λ dependent absorption cross section $\sigma_{\rm abs}(\lambda) = \sigma_{\rm abs}^{s=+1}(\lambda)$ of (a) type-1 and (b) type-2 configuration. In both cases, the nanoshell thickness is fixed at $h = 20$ nm for several inner radii $R = 100, 200, 300$ nm and the impinging field

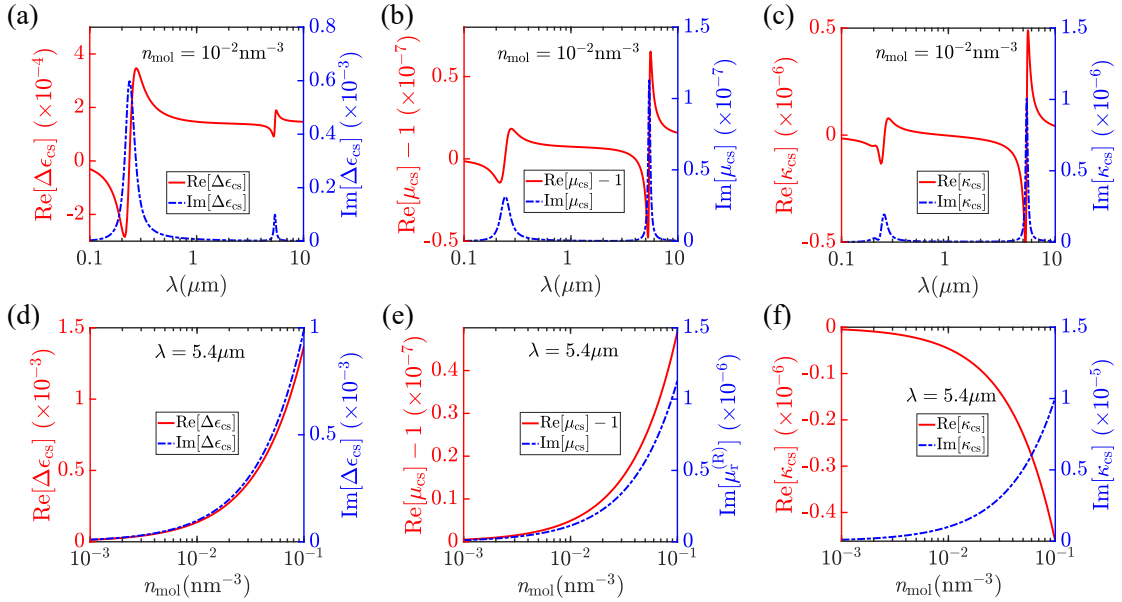


Figure 5.5: $(\mathbf{a},\mathbf{d})$ RDP correction $\Delta\epsilon_{\rm r}$, $(\mathbf{b},\mathbf{e})$ RMP correction $\Delta\mu_{\rm r}-1$, $(\mathbf{c},\mathbf{f})$ CP κ as a function of $(\mathbf{a}-\mathbf{c})$ the vacuum wavelength λ at fixed molecular number density $n_{\rm mol} = 10^{-2}$ nm^{-3}, and $(\mathbf{d}-\mathbf{f})$ $n_{\rm mol}$ at fixed $\lambda = 5.4$ μm in case of pure R-Ladarixin dissolved in water.

is taken as right circularly polarized. The full lines indicate the results obtained from our semi-analytical approach, and the dashed lines indicate the results evaluated from the EWFD calculation [195]. Note that the semi-analytical approach in the electrostatic/magnetostatic approximation shows good agreement with the EWFD calculations for radius $R \leq 100$ nm of the nanostructures in case of Type-1, see Fig. 5.6(a), and Type-2, see Fig. 5.6(b). However, the results deviate for larger radii where retardation effects are noticeable. In case of Type-1 configuration, ${\rm Re}[\epsilon_{\rm AZO}(\lambda_{\rm LSPR}^{\rm W-AZO}) + 2\epsilon_{\rm cs}(\lambda_{\rm LSPR}^{\rm W-AZO})] = 0$ leads to the maximum absorption cross-section (marked by black cycles in Fig. 5.6(a)) at $\lambda_{\rm LSPR}^{\rm W-AZO} \simeq 2.3$ μm, which is the water-AZO LSPR wavelength. In contrast, for Type-2 configuration, the maximum absorption cross-section (marked by black cycles in Fig. 5.6(b)) is observed at the hybridized water-AZO/air-AZO LSPRs wavelength, which strongly depends on the inner radius R and thickness h of the AZO layer. Note that the vibrational resonance of Ladarixin is not prominent in the $\sigma(\lambda)-\lambda$ plots, see Figs. 5.6(a,b), due to the dilute molecular number density. Rather, dominant

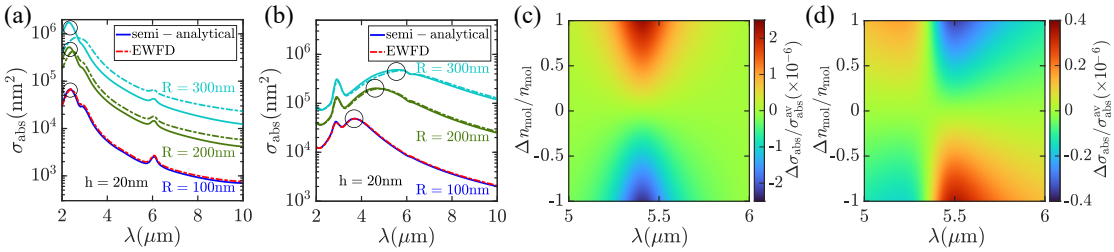


Figure 5.6: (**a**, **b**) Dependence of absorption cross-section $\sigma_{\rm abs}(\lambda)$ of (**a**) Type-1, see Fig. 5.2(a) and (**b**) Type-2, see Fig. 5.2(b) AZO-based nanoshells/nanosphere embedding/embedded in pure aqueous R-Ladarixin with number density $n^{(\rm R)}_{\rm mol} = 10^{-2}$ nm^{-3}, over vacuum wavelength λ for fixed thickness $h = 20$ nm and different radii $R = 100, 00, 300$ nm and the black circles represent surface plasmon-resonances. Dependence of relative VCDDA $\Delta\sigma_{\rm abs}/\sigma^{\rm av}_{\rm abs}$ over λ and enantiomeric imbalance $\Delta n_{\rm mol}/n_{\rm mol}$ for (**c**) Type-1 and (**b**) Type-2 configuration with fixed radius $R = 100$ nm and thickness $h = 20$ nm.

vibrational resonance of water $\lambda_{\rm H_2O} \simeq 3$ μm leads to the absorption peaks in both configurations. Importantly, due to the presence of the CS, we observe plasmon enhanced VCDDA at the vibrational resonance of Ladarixin at $\lambda = 5.4$ μm. The observed VCDDA in the considered system generates from the enantiomeric imbalance of Ladarixin since water and AZO are optically inactive.

We assess the plasmon-enhanced VCDDA through the differential absorption given by

$$\Delta\sigma_{\rm abs} = \sigma^{(s=+1)}_{\rm abs} - \sigma^{(s=-1)}_{\rm abs}, \tag{5.50}$$

where $\sigma^{(s=\pm1)}_{\rm abs}$ represent the absorption cross-section upon RCP ($s = +1$) and LCP ($s = -1$) impinging radiation. Figs. 5.6(c,d) illustrate the results obtained from our semi-analytical approach where we calculate the relative VCDDA defined as

$$\frac{\Delta\sigma_{\rm abs}}{\sigma^{\rm av}_{\rm abs}} = \frac{1}{2}\frac{[\sigma^{(s=+1)}_{\rm abs} - \sigma^{(s=-1)}_{\rm abs}]}{[\sigma^{(s=+1)}_{\rm abs} + \sigma^{(s=-1)}_{\rm abs}]}, \tag{5.51}$$

where $\sigma^{\rm av}_{\rm abs}$ is the average VCD absorption cross-section. The dependence of $\Delta\sigma_{\rm abs}/\sigma^{\rm av}_{\rm abs}$ over the vacuum wavelength λ and relative enantiomeric imbalance $\Delta n_{\rm mol}/n_{\rm mol}$ are shown for Fig. 5.6(c) Type-1 and Fig. 5.6(d) Type-2 configuration with inner radius $R = 100$ nm and thickness $h = 20$ nm. The observed

VCDDA in the considered system originates from the enantiomeric imbalance of Ladarixin which is the only optically active material in the system. Note that the value of relative VCDDA $\Delta\sigma_{\rm abs}/\sigma^{\rm av}_{\rm abs} \sim 10^{-6}$ at the Ladarixin vibrational resonance $\lambda = 5.4$ μm follows the amplitude of CP $|\kappa_{\rm cs}| \sim 10^{-6}$. Moreover, the relative VCDDA becomes zero ($\Delta\sigma_{\rm abs}/\sigma^{\rm av}_{\rm abs} = 0$) when the relative enantiomeric imbalance disappears $\Delta n_{\rm mol}/n_{\rm mol} = 0$ due to the proportionality of the CP over enentiomeric imbalance $\kappa_{\rm cs} \propto \Delta n_{\rm mol}$, which leads to the sign flip of $\Delta\sigma_{\rm abs}/\sigma^{\rm av}_{\rm abs}$ for opposite enatiomeric imbalance, see Fig. 5.6(c,d). Note that in the case of Type-1 configuration, a single peak is observed due to the resonant CP imaginary part $\mathrm{Im}[\kappa_{\rm cs}(\lambda)]$, see Fig. 5.6(c), while for Type-2 configuration, we observe splitting into two opposite peaks arising from the chirality-induced LSPR shift caused by $\mathrm{Re}[\kappa_{\rm cs}(\lambda)]$, see Fig. 5.6(d).

We evaluate the performance of plasmon-enhanced VCD by individual nanostructures through the enhancement factor defined as

$$f_{\rm VCD}(\lambda) = \Delta\sigma_{\rm abs}(\lambda)/\Delta\Sigma_{\rm abs}(\lambda), \tag{5.52}$$

where $\Sigma_{\rm abs}(\lambda)$ represents the VCDDA in the absence of AZO in the nanostructures, which is accomplished by replacing $\epsilon_{\rm AZO}$ with 1 while calculating the VCDDA. Results are illustrated in the Fig. 5.7, where we compare the enhancement factor for type-1 (blue curve) and Type-2 (red curve) configurations in the considered mid-IR regime. In both cases, we calculate $f_{\rm VCD}$ for fixed number density of aqueous R-Ladarixin $n_{\rm mol} = 10^{-2}$ nm^{-3}, inner radius $R = 100$ nm, and shell thickness $h = 20$ nm of the plasmonic nanoshells. We observe that Type-1 and Type-2 plasmonic nanoshells provide an enhancement of VCD by a factor $\simeq 3$ and $\simeq 20$, respectively. Such enhancement by AZO-based LSPRs for plasmon-enhanced CD is comparable with that of SPPs at noble metal interfaces, discussed in Chapter 4.. We emphasize that Type-2 nanostructures are not favorable for sensing purposes

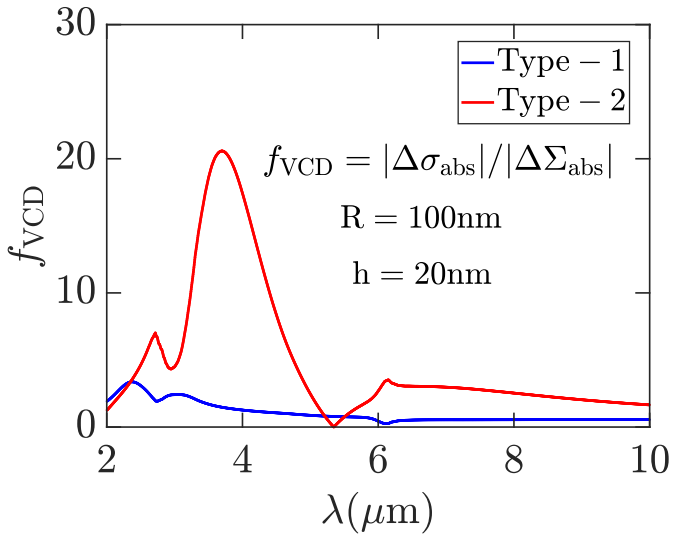


Figure 5.7: VCD enhancement factor $f_{\mathrm{VCD}}(\lambda)$ of the considered AZO-based nanostructures, Type-1 (blue curve) and Type-2 (red curve), as a function of vacuum wavelength λ for fixed inner radius $R = 100$ nm, shell thickness $h = 20$ nm and molecular number density $n_{\mathrm{mol}} = 10^{-2}$ nm^{-3} of aqueous R-Ladarixin.

as the nanoshell core contains the chiral sample, while Type-1 nanostructures are compatible for plamonic sensing since the chiral sample is situated on the AZO-based nanosphere surface. However, both AZO and water exhibit large absorption in the MIR wavelength range, limiting the enhancement of Type-1 nanostructure. One way to exclude the water absorption is to remove the water molecules, leaving only the chiral molecules on the surface of the nanosphere, but a particular enantiomeric form might affect the molecular absorption, which can influence the sensing performance. Furthermore, alternative MIR plasmonic materials can be employed instead of AZO. The optical properties of Indium Tin Oxide (ITO) are quite analogous to those of AZO, and the performance of ITO-based nanoshell regarding enhancement factor is observed to be similar. Another option is provided by Graphene plasmons featuring lower absorption due to the lower count of conduction electron density [185, 199] offering possibilities of developing noble chiroptical sensing techniques based on plasmon-enhanced VCD. However, our electrostatic approach is inadequate to probe such platforms because of the reduced dimensionality of graphene and therefore should be extended for further

investigations to explore graphene-based plasmon enhanced VCD of dilute chiral drug solutions.

5.6 Concluding remarks.

In this chapter, we explore the possibilities of developing a promising platform of plasmon-enhanced VCD of chiral drug solutions utilizing AZO-based plasmonic nanoshells. We demonstrate a semi-analytical approach to evaluate the plasmon-enhanced CD by nanopartcile in the electrostatic/magnetostatic regime. We mainly focus on a realistic chiral drug, aqueous Ladarixin, that has been employed as a dual allosteric inhibitor of CXCL8 (IL-8) receptors, CXCR1 and CXCR2, to cure diabetes, presently in phase 2 and 3 trials. In addition, we have estimated the macroscopic optical parameters of the isotropic chiral drug solution through a hybrid combinational approach based on MD simulation, TDDFT and PMM that we have reported in the previous chapters. Adopting such computational approach along with the radiation-molecule interaction modeling, we determine the optical parameters of the chiral mixture that we incorporate in our theory to evaluate the absorption cross section of the plasmonic nanoshell embedding chiral media. The results obtained from our semi-analytical are validated by comparing them with the EWFD results calculated utilizing the commercial software. The results show very good alignment in the case of nanoshells wiht radii $\leq$ 100 nm. The AZO-based plasmonic nanoshells embedding chiral drugs offer VCDDA enhancement with enhancement factors ranging from 3 to 20 depending on the specific geometry of the nanoshell configurations. We also discuss the possibility of adopting other plasmonic material in MIR range. Our investigation reveals the potential of AZO-based plasmonic nanostructure to probe VCD nanospectroscopy of chiral drugs and offers a promising platform of nanodevices for chiral drug characterization.

Chapter 6

Conclusions

This thesis theoretically demonstrates the modeling of the interaction between electromagnetic radiation and chiral molecules in nanophotonic environments to facilitate the development of innovative chiral sensing techniques. Owing to the inherently weak chiroptical signals, the sensitivity of the characterizations of enantiomeric excess in chiral drug solutions becomes a major concern in pharmaceutical applications. The advancement of contemporary nanofabrication techniques has the potential to significantly overcome the limitations of the measurements of enantiomeric imbalance, enabling efficient designing of novel chiral sensors. This work highlights the opportunities of leveraging nanophotonics to enhance weak chiroptical signals. We focus on realistic pharmaceutical chiral drug solutions and investigate the applications of nanostructured platforms to enhance circular dichroism in nl volume drug solutions. Through theoretical/computational modeling, we demonstrate that plasmonic nanostructures supporting SPP excitations and LSPRs can significantly boost the chiroptical responses. Thanks to the strong near-field enhancements in the vicinity of chiral drug solutions, it is possible to retrieve the enantioselective information in minimal amounts of the drug solutions.

Our study provides comprehensive theoretical insights into enantiosensitive responses of plasmonic nanostructures embedding chiral drug solutions. By impinging circularly polarized light on such structures, we investigate enhanced chirop-

tical light-matter interactions that provide a robust theoretical understanding to optimize the geometry and material properties of nanophotonic devices to obtain efficient chiral signal enhancement employing realistic pharmaceutical drug solutions. These findings offer novel techniques to design highly sensitive chiral sensors that are compatible with real-time analysis. Furthermore, our results open up a window of opportunity to develop compact lab-on-a-chip integration platforms supported by nanophotonics, enabling chiral sensing at low sample volumes.

In summary, we have developed robust analytical and computational methods to model the light-molecule interactions in nanophotonic structures. We have introduced a semi-classical perturbative theory to calculate macroscopic chiroptical responses of dilute drug solutions, incorporating microscopic optical parameters of the chiral drug solutions. The computational approach involves MD simulations, TDDFT and quantum chemical calculations to estimate spectroscopic responses of pharmaceutical chiral drug solutions. Finally, we propose some innovative chiral sensing approaches based on SPPs and LSPRs in plasmonic nanostructures capable of detecting enantiomeric imbalance in nl volume chiral drug solutions.

The original results obtained in this work can be summed up as follows:

- We have investigated the plasmon-enhanced CD spectroscopy of dilute chiral drug solutions utilizing SPPs at the interfaces between noble metals and a Reparixin dissolved in water. The drug solution under consideration consists of a pharmaceutical molecule employed for the treatment of COVID-19 and acute respiratory distress syndrome and patients with community-acquired pneumonia. To calculate the microscopic molecular observables of Reparixin, we have adopted a computational method combining MD simulations, TDDFT, and PMM simulations, leading to the evaluation of time-averaged static and transition electric and magnetic dipole moments. The macroscopic

optical parameters of the isotropic mixture of aqueous Reparixin are determined from the perturbative solution of density matrix equations. We find that SPP excitation facilitates plasmon-induced CDDA enhancement with a factor order of $f_{\mathrm{CDDA}} \simeq 20$ in solutions with sub-nl volume. Our findings are significant to designing innovative integrated schemes for chiroptical sensing of drug solutions.

- We have investigated the potential of AZO-based plasmonic nanoshells for plasmon-enhanced VCD of chiral drug solutions. Our calculations have focused on a realistic chiral drug, aqueous Ladarixin, a dual allosteric inhibitor of CXCL8 (IL-8) receptors, CXCR1 and CXCR2, currently in phase 2 and 3 trials for the treatment of diabetes. By adopting a combination of MD, TDDFT, and PMM simulations, we calculated the macroscopic optical parameters of the isotropic chiral mixture. Moreover, we developed a semianalytical electrostatic/magnetostatic approach enabling the evaluation of the absorption cross-section of plasmonic nanoshells. We corroborate our model by comparing semi-analytical results with EWFD calculations based on commercial software, obtaining excellent agreement for nanoshells with radius ≤ 100 nm. We find that AZO-based plasmonic nanoshells produce VCDDA with a maximum enhancement factor ranging from 3 to 20 depending on the particular nanoshell geometry. Our results shed light on the opportunities offered by AZO-based plasmonic nanostructures for VCD nanospectroscopy of chiral drugs and advanced nanodevices for drug characterization.

6.1 List of publications.

- Plasmon-enhanced circular dichroism spectroscopy of chiral drug solutions, Venturi, M., **Adhikary, R.**, Sahoo, A., Ferrante, C., Daidone, I., Di Stasio, F., ... & Marini, A.,
  The Journal of Chemical Physics, **159**(15), (2023).

- Vibrational circular dichroism of plasmonic nanostructures embedding chiral drugs,
  Adhikary, R., Venturi, M., Salvitti, G., Sahoo, A., Ferrante, C., Benassi, P., Di Stasio, F., Toma, A., Altug, H., Aschi, M. & Marini, A., *Scientific Reports*, **15**(13116), (2025).

† Localization of optical vortices in nonlinear hexagonal multicore fibers,
Khushhali, S., **Adhikary, R.**, Ferrante, C., Antonelli, C., Mecozzi, A., Marini, A., & Roy, S.,
Physical Review A, **110**(1), 013507, (2024).

† Harnessing collisional nonlinearity for enhanced harmonic generation by ultraviolet plasmonic nanoparticles,
Silvestri, M., Venturi, M., Di Muzio, M., **Adhikary, R.**, Ferrante, C., Benassi, P., & Marini, A.,
The Journal of Chemical Physics, **161**(5), (2024).

† Indicates the article is outside the scope of the present thesis.

Bibliography

[1] William Thomson Baron Kelvin. *The molecular tactics of a crystal*. Clarendon Press, 1894. (cited on page 1.)

[2] Laurence D Barron. True and false chirality and parity violation. *Chemical physics letters*, **123**(5):423–427, 1986. (cited on page 1.)

[3] Gareth Thomas. *Fundamentals of medicinal chemistry*. J. Wiley & Sons, New York, N.Y, 2003. (cited on page 2.)

[4] Joseph Gal. Molecular chirality in chemistry and biology: Historical milestones. *Helvetica Chimica Acta*, **96**(9):1617–1657, 2013. (cited on page 2.)

[5] L.C. Cross and W. Klyne. IUPAC COMMISSION ON NOMENCLATURE OF ORGANIC CHEMISTRY. In *Rules for the Nomenclature of Organic Chemistry*, pages 13–30. Elsevier, 1976. (cited on page 2.)

[6] Neil Vargesson. Thalidomide-induced teratogenesis: History and mechanisms. *Birth Defects Research Part C: Embryo Today: Reviews*, **105**(2):140–156, 2015. (cited on page 3.)

[7] John E Mendelson, Dana McGlothlin, Debra S Harris, Elyse Foster, Tom Everhart, Peyton Jacob, and Reese T Jones. The clinical pharmacology of intranasal l-methamphetamine. *BMC clinical pharmacology*, **8**:1–9, 2008. (cited on page 3.)

[8] Tetsuya Nishimura, Kazue Takahata, Yuri Kosugi, Takaaki Tanabe, and Shizuko Muraoka. Psychomotor effect differences between l-methamphetamine and d-methamphetamine are independent of murine plasma and brain pharmacokinetics profiles. *Journal of Neural Transmission*, **124**:519–523, 2017. (cited on page 3.)

[9] R. Craven. Ketamine. *Anaesthesia*, **62**(s1):48–53, December 2007. (cited on page 3.)

[10] Rebecca U McVicker and Niamh M O'Boyle. Chirality of new drug approvals (2013–2022): trends and perspectives. *Journal of Medicinal Chemistry*, **67**(4):2305–2320, 2024. (cited on page 3.)

[11] W H. Brooks, W C. Guida, and K G. Daniel. The significance of chirality in drug design and development. *Current Topics in Medicinal Chemistry*, **11**(7):760–770, 2011. (cited on page 3.)

[12] Lauren A Warning, Ali Rafiei Miandashti, Lauren A McCarthy, Qingfeng Zhang, Christy F Landes, and Stephan Link. Nanophotonic approaches for chirality sensing. *ACS nano*, **15**(10):15538–15566, 2021. (cited on pages 3 and 131.)

[13] Wei Ma, Liguang Xu, Libing Wang, Chuanlai Xu, and Hua Kuang. Chirality-based biosensors. *Advanced Functional Materials*, **29**(1):1805512, 2019. (cited on page 3.)

[14] Hülya Ucar and Hans-Achim Wagenknecht. Dna-templated control of chirality and efficient energy transport in supramolecular dna architectures with aggregation-induced emission. *Chemical Science*, **12**(29):10048–10053, 2021. (cited on page 3.)

[15] Amani Zoabi and Katherine Margulis. Differential interactions of chiral nanocapsules with dna. *International Journal of Molecular Sciences*, **22**(2):584, 2021. (cited on page 3.)

[16] Jihyeon Yeom. Atomic chirality and a materials revolution. *Accounts of Materials Research*, **2**(7):471–476, 2021. (cited on page 3.)

[17] Binghai Yan. Structural chirality and electronic chirality in quantum materials. *Annual Review of Materials Research*, **54**, 2024. (cited on page 3.)

[18] Jing Zhang, M Teresa Albelda, Yu Liu, and James W Canary. Chiral nanotechnology. *Chirality: The Pharmacological, Biological, and Chemical Consequences of Molecular Asymmetry*, **17**(7):404–420, 2005. (cited on page 3.)

[19] Dibyendu S Bag, TC Shami, and KU Bhasker Rao. Chiral nanoscience and nanotechnology. *Defence Science Journal*, **58**(5):626, 2008. (cited on page 3.)

[20] Alexander O Govorov. Plasmon-induced circular dichroism of a chiral molecule in the vicinity of metal nanocrystals. application to various geometries. *The Journal of Physical Chemistry C*, **115**(16):7914–7923, 2011. (cited on pages 4 and 89.)

[21] Alexander O Govorov and Zhiyuan Fan. Theory of chiral plasmonic nanostructures comprising metal nanocrystals and chiral molecular media. *ChemPhysChem*, **13**(10):2551–2560, 2012. (cited on page 4.)

[22] Joshua Vogwell, Laura Rego, Olga Smirnova, and David Ayuso. Ultrafast control over chiral sum-frequency generation. *Science Advances*, 9(33):eadj1429, 2023. (cited on page 4.)

[23] Longfang Ye, Jingyan Li, Felix Ulrich Richter, Yasaman Jahani, Rui Lu, Bo Ray Lee, Ming Lun Tseng, and Hatice Altug. Dielectric tetramer nanores-

onators supporting strong superchiral fields for vibrational circular dichroism spectroscopy. *ACS photonics*, **10**(12):4377–4384, 2023. (cited on page 4.)

[24] P. Fischer, D. S. Wiersma, R. Righini, B. Champagne, and A. D. Buckingham. Three-wave mixing in chiral liquids. *Phys. Rev. Lett.*, **85**:4253–4256, 2000. (cited on page 5.)

[25] M. A. Belkin, S. H. Han, X. Wei, and Y. R. Shen. Sum-frequency generation in chiral liquids near electronic resonance. *Phys. Rev. Lett.*, **87**:113001, 2001. (cited on page 5.)

[26] P. Fischer, A. D. Buckingham, K. Beckwitt, D. S. Wiersma, and F. W. Wise. New electro-optic effect: Sum-frequency generation from optically active liquids in the presence of a dc electric field. *Phys. Rev. Lett.*, **91**:173901, 2003. (cited on page 5.)

[27] P. Fischer and F. Hache. Nonlinear optical spectroscopy of chiral molecules. *Chirality*, **17**:421–437, 2005. (cited on page 5.)

[28] T. Verbiest, M. Kauranen, and A. Persoons. Light-polarization induced optical activity. *Physical Review Letters*, **82**(18):3601, 1999. (cited on page 5.)

[29] J. Zhang, W. Yang, J. Tan, and S. Ye. In situ examination of a charged amino acid-induced structural change in lipid bilayers by sum frequency generation vibrational spectroscopy. *Phys. Chem. Chem. Phys.*, **20**:5657–5665, 2018. (cited on page 5.)

[30] W. Wang and S. Ye. Molecular interactions of organic molecules at the air/water interface investigated by sum frequency generation vibrational spectroscopy. *Phys. Chem. Chem. Phys.*, **19**:4488–4493, 2017. (cited on page 5.)

[31] S. Ye, K. T. Nguyen, S. V. L. Clair, and Z. Chen. In situ molecular level studies on membrane related peptides and proteins in real time using sum frequency generation vibrational spectroscopy. *J. Struct. Biol.*, **168**:61–77, 2009. (cited on page 5.)

[32] L. Fu, J. Liu, and E. C. Y. Yan. Chiral sum frequency generation spectroscopy for characterizing protein secondary structures at interfaces. *J. Am. Chem. Soc.*, **133**:8094–8097, 2011. (cited on page 5.)

[33] S. R. Walter and F. M. Geiger. Dna on stage: Showcasing oligonucleotides at surfaces and interfaces with second harmonic and vibrational sum frequency generation. *J. Phys. Chem. Lett.*, **1**:9–15, 2010. (cited on page 5.)

[34] E. C. Y. Yan, L. Fu, Z. Wang, and W. Liu. Biological macromolecules at interfaces probed by chiral vibrational sum frequency generation spectroscopy. *Chem. Rev.*, **114**:8471–8498, 2014. (cited on page 5.)

[35] J. Vogwell, L. Rego, O. Smirnova, and D. Ayuso. Ultrafast control over chiral sum-frequency generation. *Science Advances*, **9**(33):eadj1429, 2023. (cited on page 5.)

[36] David Ayuso, Andres F Ordonez, and Olga Smirnova. Ultrafast chirality: the road to efficient chiral measurements. *Physical Chemistry Chemical Physics*, **24**(44):26962–26991, 2022. (cited on pages 5 and 88.)

[37] Samuel Beaulieu, Antoine Comby, Dominique Descamps, Baptiste Fabre, GA Garcia, Romain Géneaux, AG Harvey, Francois Légaré, Z Mašín, Laurent Nahon, et al. Photoexcitation circular dichroism in chiral molecules. *Nature Physics*, **14**(5):484–489, 2018. (cited on pages 5 and 88.)

[38] Ofer Neufeld, David Ayuso, Piero Decleva, Misha Y Ivanov, Olga Smirnova, and Oren Cohen. Ultrasensitive chiral spectroscopy by dynamical symmetry

breaking in high harmonic generation. *Physical Review X*, **9**(3):031002, 2019. (cited on pages 5 and 88.)

[39] David Ayuso, Ofer Neufeld, Andres F Ordonez, Piero Decleva, Gavriel Lerner, Oren Cohen, Misha Ivanov, and Olga Smirnova. Synthetic chiral light for efficient control of chiral light–matter interaction. *Nature Photonics*, **13**(12):866–871, 2019. (cited on pages 5 and 88.)

[40] Francesca Calegari, D Ayuso, Andrea Trabattoni, Louise Belshaw, Simone De Camillis, S Anumula, F Frassetto, Luca Poletto, Alicia Palacios, Piero Decleva, et al. Ultrafast electron dynamics in phenylalanine initiated by attosecond pulses. *Science*, 346(6207):336–339, 2014. (cited on page 5.)

[41] Mauro Nisoli, Piero Decleva, Francesca Calegari, Alicia Palacios, and Fernando Martín. Attosecond electron dynamics in molecules. *Chemical reviews*, 117(16):10760–10825, 2017. (cited on page 5.)

[42] Ofer Neufeld and Oren Cohen. Background-free measurement of ring currents by symmetry-breaking high-harmonic spectroscopy. *Physical Review Letters*, 123(10):103202, 2019. (cited on page 5.)

[43] Kai-Jun Yuan, Szczepan Chelkowski, and André D Bandrauk. Photoelectron momentum distributions of molecules in bichromatic circularly polarized attosecond uv laser fields. *Physical Review A*, 93(5):053425, 2016. (cited on page 5.)

[44] Alfredo Gorio, Laura Madaschi, Giorgia Zadra, Giovanni Marfia, Barbara Cavalieri, Riccardo Bertini, and Anna Maria Di Giulio. Reparixin, an inhibitor of cxcr2 function, attenuates inflammatory responses and promotes recovery of function after traumatic lesion to the spinal cord. *Journal of Pharmacology and Experimental Therapeutics*, **322**(3):973–981, 2007. (cited on page 6.)

[45] Alessandro Zanasi, Luigi Lanata, Giovanni Fontana, Federico Saibene, Peter Dicpinigaitis, and Francesco De Blasio. Levodropropizine for treating cough in adult and children: a meta-analysis of published studies. *Multidisciplinary Respiratory Medicine*, 10:1–6, 2015. (cited on page 6.)

[46] G Banderali, E Riva, A Fiocchi, CI Cordaro, and M Giovannini. Efficacy and tolerability of levodropropizine and dropropizine in children with non-productive cough. *Journal of international medical research*, 23(3):175–183, 1995. (cited on page 6.)

[47] Vanessa Castelli, Laura Brandolini, Michele d'Angelo, Cristina Giorgio, Margherita Alfonsetti, Pasquale Cocchiaro, Francesca Lombardi, Annamaria Cimini, and Marcello Allegretti. Cxcr1/2 inhibitor ladarixin ameliorates the insulin resistance of 3t3-l1 adipocytes by inhibiting inflammation and improving insulin signaling. *Cells*, **10**(9):2324, 2021. (cited on pages 6 and 132.)

[48] Lorenzo Piemonti, Bart Keymeulen, Pieter Gillard, Thomas Linn, Emanuele Bosi, Ludger Rose, Paolo Pozzilli, Francesco Giorgino, Efisio Cossu, Luisa Daffonchio, et al. Ladarixin, an inhibitor of the interleukin-8 receptors cxcr1 and cxcr2, in new-onset type 1 diabetes: A multicentre, randomized, double-blind, placebo-controlled trial. *Diabetes, Obesity and Metabolism*, **24**(9):1840–1849, 2022. (cited on pages 6 and 132.)

[49] John David Jackson. *Classical Electrodynamics*. Wiley, New York, 3rd edition, 1999. (cited on pages 11, 99, and 138.)

[50] Julius Adams Stratton. *Electromagnetic Theory*. McGraw-Hill, New York, 1941. (cited on pages 12 and 100.)

[51] Gerald B Folland. *Fourier analysis and its applications*, volume **4**. American Mathematical Soc., 2009. (cited on page 12.)

[52] William W Parson. *Modern optical spectroscopy*, volume **2**. Springer, 2007. (cited on page 16.)

[53] George Gabriel Stokes. On the composition and resolution of streams of polarized light from different sources. *Transactions of the Cambridge Philosophical Society*, **9**:399, 1851. (cited on page 16.)

[54] John Lekner. Optical properties of isotropic chiral media. *Pure and Applied Optics: Journal of the European Optical Society Part A*, **5**(4):417, 1996. (cited on page 18.)

[55] Stephen M Barnett and Robert P Cameron. Energy conservation and the constitutive relations in chiral and non-reciprocal media. *Journal of Optics*, **18**(1):015404, 2015. (cited on page 18.)

[56] Filippo Capolino. *Theory and phenomena of metamaterials*. CRC press, 2017. (cited on pages 18 and 19.)

[57] J. A. A. Kong. *Electromagnetic Wave Theory*. Wiley, New York, 1st edition, 1986. (cited on page 18.)

[58] Ismo Lindell, Ari Sihvola, Sergei Tretyakov, and Ari J Viitanen. *Electromagnetic waves in chiral and bi-isotropic media*. Artech House, 1994. (cited on page 18.)

[59] Cheng-Wei Qiu, Nawaz Burokur, Saïd Zouhdi, and Le-Wei Li. Chiral nihility effects on energy flow in chiral materials. *Journal of the Optical Society of America A*, **25**(1):55–63, 2007. (cited on page 19.)

[60] Laurence D Barron. *Molecular light scattering and optical activity*. Cambridge University Press, 2009. (cited on page 21.)

[61] Kan Yao and Yongmin Liu. Enhancing circular dichroism by chiral hotspots in silicon nanocube dimers. *Nanoscale*, **10**(18):8779–8786, 2018. (cited on page 22.)

[62] John A Schellman. Circular dichroism and optical rotation. *Chemical Reviews*, **75**(3):323–331, 1975. (cited on page 24.)

[63] Prasad L Polavarapu. Kramers- kronig transformation for optical rotatory dispersion studies. *The Journal of Physical Chemistry A*, **109**(32):7013–7023, 2005. (cited on page 24.)

[64] SA Maier. Plasmonics: Fundamentals and applications, 2007. (cited on pages 25 and 27.)

[65] Andreas Otto. Excitation of nonradiative surface plasma waves in silver by the method of frustrated total reflection. *Zeitschrift für Physik A Hadrons and nuclei*, **216**(4):398–410, 1968. (cited on pages 25 and 89.)

[66] Erwin Kretschmann and Heinz Raether. Radiative decay of non radiative surface plasmons excited by light. *Zeitschrift für Naturforschung A*, **23**(12):2135–2136, 1968. (cited on pages 25 and 89.)

[67] Sookyoung Roh, Taerin Chung, and Byoungho Lee. Overview of the characteristics of micro-and nano-structured surface plasmon resonance sensors. *Sensors*, **11**(2):1565–1588, 2011. (cited on page 26.)

[68] Stefan A Maier and Harry A Atwater. Plasmonics: Localization and guiding of electromagnetic energy in metal/dielectric structures. *Journal of applied physics*, **98**(1), 2005. (cited on page 26.)

[69] W Andrew Murray and William L Barnes. Plasmonic materials. *Advanced materials*, **19**(22):3771–3782, 2007. (cited on page 26.)

[70] Yoon Young Lee, Ryeong Myeong Kim, Sang Won Im, Mani Balamurugan, and Ki Tae Nam. Plasmonic metamaterials for chiral sensing applications. *Nanoscale*, **12**(1):58–66, 2020. (cited on page 26.)

[71] Jeffrey N Anker, W Paige Hall, Olga Lyandres, Nilam C Shah, Jing Zhao, and Richard P Van Duyne. Biosensing with plasmonic nanosensors. *Nature materials*, **7**(6):442–453, 2008. (cited on page 27.)

[72] Eleonora Petryayeva and Ulrich J Krull. Localized surface plasmon resonance: Nanostructures, bioassays and biosensing—a review. *Analytica chimica acta*, **706**(1):8–24, 2011. (cited on page 27.)

[73] Lakshminarayana Polavarapu, Jorge Pérez-Juste, Qing-Hua Xu, and Luis M Liz-Marzán. Optical sensing of biological, chemical and ionic species through aggregation of plasmonic nanoparticles. *Journal of Materials Chemistry C*, **2**(36):7460–7476, 2014. (cited on page 27.)

[74] Anthony Stone. *The theory of intermolecular forces*. oUP oxford, 2013. (cited on page 30.)

[75] Jean Louis Calais. Theory of molecular fluids. volume 1: Fundamentals. by c. g. gray and k. e. gubbins, the clarendon press, oxford university press, new york, 1984. *International Journal of Quantum Chemistry*, **38**:497–497, 1990. (cited on page 30.)

[76] M. Born and R. Oppenheimer. Zur quantentheorie der molekeln. *Annalen der Physik*, 389, 1927. (cited on page 33.)

[77] Frank Jensen. *Introduction to computational chemistry*. John wiley & sons, 2017. (cited on pages 33, 38, 42, 43, 44, and 45.)

[78] Darrin M York, Tom A Darden, and Lee G Pedersen. The effect of long-range electrostatic interactions in simulations of macromolecular crystals:

A comparison of the ewald and truncated list methods. *The Journal of chemical physics*, **99**(10):8345–8348, 1993. (cited on page 35.)

[79] Herman JC Berendsen, JPM van Postma, Wilfred F Van Gunsteren, ARHJ DiNola, and Jan R Haak. Molecular dynamics with coupling to an external bath. *The Journal of chemical physics*, **81**(8):3684–3690, 1984. (cited on pages 36 and 60.)

[80] Attila Szabo and Neil S Ostlund. *Modern quantum chemistry: introduction to advanced electronic structure theory*. Courier Corporation, 1996. (cited on page 41.)

[81] W. J. Hehre, L. Radom, P. V. R. Schleyer, and J. A. Pople. *Ab Initio Molecular Orbital Theory*. John Wiley & Sons, New York, 1986. (cited on page 41.)

[82] Raymond McWeeny. *Methods of Molecular Quantum Mechanics*. Academic Press, 1992. (cited on page 41.)

[83] Robert G Parr and Libero J Bartolotti. Some remarks on the density functional theory of few-electron systems. *The Journal of Physical Chemistry*, **87**(15):2810–2815, 1983. (cited on page 41.)

[84] R. G. Parr and W. Yang. *Density-functional Theory of Atoms and Molecules*. Oxford University Press, 1989. (cited on page 41.)

[85] Nathalie Godbout, Dennis R. Salahub, Jan Andzelm, and Erich Wimmer. Optimization of Gaussian-type basis sets for local spin density functional calculations. Part I. Boron through neon, optimization technique and validation. *Canadian Journal of Chemistry*, **70**(2):560–571, February 1992. (cited on page 41.)

[86] Pierre Hohenberg and Walter Kohn. Inhomogeneous electron gas. *Physical review*, **136**(3B):B864–B871, 1964. (cited on page 42.)

[87] Walter Kohn and Lu Jeu Sham. Self-consistent equations including exchange and correlation effects. *Physical review*, **140**(4A):A1133, 1965. (cited on page 42.)

[88] John P Perdew, Adrienn Ruzsinszky, Jianmin Tao, Viktor N Staroverov, Gustavo E Scuseria, and Gábor I Csonka. Prescription for the design and selection of density functional approximations: More constraint satisfaction with fewer fits. *The Journal of chemical physics*, **123**(6):062201, 2005. (cited on page 43.)

[89] J. P. Perdew, E. R. McMullen, and Alex Zunger. Density-functional theory of the correlation energy in atoms and ions: A simple analytic model and a challenge. *Phys. Rev. A*, **23**:2785–2789, Jun 1981. (cited on page 43.)

[90] Seymour H Vosko, Leslie Wilk, and Marwan Nusair. Accurate spin-dependent electron liquid correlation energies for local spin density calculations: a critical analysis. *Canadian Journal of physics*, **58**(8):1200–1211, 1980. (cited on page 43.)

[91] Olle Gunnarsson and Bengt I Lundqvist. Exchange and correlation in atoms, molecules, and solids by the spin-density-functional formalism. *Physical Review B*, **13**(10):4274, 1976. (cited on page 43.)

[92] A. D. Becke. Density-functional exchange-energy approximation with correct asymptotic behavior. *Phys. Rev. A*, **38**:3098–3100, Sep 1988. (cited on pages 43 and 62.)

[93] Chengteh Lee, Weitao Yang, and Robert G. Parr. Development of the colle-

salvetti correlation-energy formula into a functional of the electron density. *Phys. Rev. B*, **37**:785–789, Jan 1988. (cited on pages 43 and 62.)

[94] Axel D. Becke. Density-functional thermochemistry. III. The role of exact exchange. *The Journal of Chemical Physics*, **98**(7):5648–5652, April 1993. (cited on pages 43 and 62.)

[95] Jan Geertsen, Magnus Rittby, and Rodney J Bartlett. The equation-of-motion coupled-cluster method: Excitation energies of be and co. *Chemical Physics Letters*, **164** (1):57–62, 1989. (cited on page 43.)

[96] Rodney J Bartlett. Coupled-cluster theory: An overview of recent developments. *Modern Electronic Structure Theory: Part II*, pages 1047–1131, 1995. (cited on page 43.)

[97] Peter J Knowles and Hans-Joachim Werner. An efficient method for the evaluation of coupling coefficients in configuration interaction calculations. *Chemical physics letters*, **145**(6):514–522, 1988. (cited on page 43.)

[98] Erich Runge and Eberhard KU Gross. Density-functional theory for time-dependent systems. *Physical review letters*, **52**(12):997, 1984. (cited on page 44.)

[99] Hans Martin Senn and Walter Thiel. Qm/mm studies of enzymes. *Current opinion in chemical biology*, **11**(2):182–187, 2007. (cited on page 47.)

[100] Hai Lin and Donald G Truhlar. Qm/mm: what have we learned, where are we, and where do we go from here? *Theoretical Chemistry Accounts*, **117**:185–199, 2007. (cited on page 47.)

[101] Feliu Maseras and Keiji Morokuma. Imomm: A new integrated ab initio+ molecular mechanics geometry optimization scheme of equilibrium

structures and transition states. *Journal of Computational Chemistry*, **16**(9):1170–1179, 1995. (cited on page 47.)

[102] Ulf Ryde. The coordination of the catalytic zinc ion in alcohol dehydrogenase studied by combined quantum-chemical and molecular mechanics calculations. *Journal of computer-aided molecular design*, **10**:153–164, 1996. (cited on page 47.)

[103] Mats Svensson, Stephane Humbel, Robert DJ Froese, Toshiaki Matsubara, Stefan Sieber, and Keiji Morokuma. Oniom: a multilayered integrated mo+ mm method for geometry optimizations and single point energy predictions. a test for diels- alder reactions and pt (p (t-bu) 3) 2+ h2 oxidative addition. *The Journal of Physical Chemistry*, **100**(50):19357–19363, 1996. (cited on page 47.)

[104] Paul Sherwood, Alex H de Vries, Martyn F Guest, Georg Schreckenbach, C Richard A Catlow, Samuel A French, Alexey A Sokol, Stefan T Bromley, Walter Thiel, Alex J Turner, et al. Quasi: A general purpose implementation of the qm/mm approach and its application to problems in catalysis. *Journal of Molecular Structure: THEOCHEM*, **632**(1-3):1–28, 2003. (cited on page 48.)

[105] Hans Martin Senn and Walter Thiel. Qm/mm methods for biomolecular systems. *Angewandte Chemie International Edition*, **48**(7):1198–1229, 2009. (cited on page 48.)

[106] Tommaso Giovannini, Alessandra Puglisi, Matteo Ambrosetti, and Chiara Cappelli. Polarizable qm/mm approach with fluctuating charges and fluctuating dipoles: the qm/fqfμ model. *Journal of chemical theory and computation*, **15**(4):2233–2245, 2019. (cited on page 49.)

[107] Eliot Boulanger and Walter Thiel. Solvent boundary potentials for hybrid qm/mm computations using classical drude oscillators: a fully polarizable model. *Journal of chemical theory and computation*, **8**(11):4527–4538, 2012. (cited on page 49.)

[108] Jay W Ponder, Chuanjie Wu, Pengyu Ren, Vijay S Pande, John D Chodera, Michael J Schnieders, Imran Haque, David L Mobley, Daniel S Lambrecht, Robert A DiStasio Jr, et al. Current status of the amoeba polarizable force field. *The journal of physical chemistry B*, **114**(8):2549–2564, 2010. (cited on page 49.)

[109] Jacek Dziedzic, Yuezhi Mao, Yihan Shao, Jay Ponder, Teresa Head-Gordon, Martin Head-Gordon, and Chris-Kriton Skylaris. Tinktep: A fully self-consistent, mutually polarizable qm/mm approach based on the amoeba force field. *The Journal of Chemical Physics*, **145**(12), 2016. (cited on page 49.)

[110] Daniele Loco, Louis Lagardère, Stefano Caprasecca, Filippo Lipparini, Benedetta Mennucci, and Jean-Philip Piquemal. Hybrid qm/mm molecular dynamics with amoeba polarizable embedding. *Journal of chemical theory and computation*, **13**(9):4025–4033, 2017. (cited on page 49.)

[111] Hans M. Senn and Walter Thiel. Atomistic approaches in modern biology: From quantum chemistry to molecular simulations. In Markus Reiher, editor, *Springer Berlin Heidelberg*, pages 173–290. Springer Berlin Heidelberg, Berlin, Heidelberg, 2007. (cited on page 49.)

[112] Massimiliano Aschi, Riccardo Spezia, Alfredo Di Nola, and Andrea Amadei. A first-principles method to model perturbed electronic wavefunctions: the effect of an external homogeneous electric field. *Chemical physics letters*, **344**(3-4):374–380, 2001. (cited on pages 49 and 51.)

[113] Andrea Amadei, Maira D'Alessandro, Marco D'Abramo, and Massimiliano Aschi. Theoretical characterization of electronic states in interacting chemical systems. *The Journal of chemical physics*, **130**(8), 2009. (cited on pages 49 and 51.)

[114] Laura Zanetti-Polzi, Sara Del Galdo, Isabella Daidone, Marco D'Abramo, Vincenzo Barone, Massimiliano Aschi, and Andrea Amadei. Extending the perturbed matrix method beyond the dipolar approximation: comparison of different levels of theory. *Physical Chemistry Chemical Physics*, **20**(37):24369–24378, 2018. (cited on pages 49, 52, 53, and 56.)

[115] Cheng Giuseppe Chen, Alessandro Nicola Nardi, Andrea Amadei, and Marco D'Abramo. Pymm: An open-source python program for qm/mm simulations based on the perturbed matrix method. *Journal of Chemical Theory and Computation*, **19**(1):33–41, 2022. (cited on page 49.)

[116] Riccardo Spezia, Massimiliano Aschi, Alfredo Di Nola, and Andrea Amadei. Extension of the perturbed matrix method: application to a water molecule. *Chemical physics letters*, **365**(5-6):450–456, 2002. (cited on page 52.)

[117] Marco D'Abramo, Massimiliano Aschi, and Andrea Amadei. Theoretical modeling of uv-vis absorption and emission spectra in liquid state systems including vibrational and conformational effects: Explicit treatment of the vibronic transitions. *The Journal of Chemical Physics*, **140**(16), 2014. (cited on pages 52 and 57.)

[118] Cheng Giuseppe Chen, Alessandro Nicola Nardi, Mauro Giustini, and Marco D'Abramo. Absorption behavior of doxorubicin hydrochloride in visible region in different environments: A combined experimental and computational study. *Physical Chemistry Chemical Physics*, **24**(19):12027–12035, 2022. (cited on page 52.)

[119] Matteo Capone, Abhishek Sirohiwal, Massimiliano Aschi, Dimitrios A Pantazis, and Isabella Daidone. Alternative fast and slow primary charge-separation pathways in photosystem ii. *Angewandte Chemie International Edition*, **62**(16):e202216276, 2023. (cited on page 52.)

[120] Herman JC Berendsen, David van der Spoel, and Rudi van Drunen. Gromacs: A message-passing parallel molecular dynamics implementation. *Computer physics communications*, **91**(1-3):43–56, 1995. (cited on page 58.)

[121] Alpeshkumar K. Malde, Le Zuo, Matthew Breeze, Martin Stroet, David Poger, Pramod C. Nair, Chris Oostenbrink, and Alan E. Mark. An Automated Force Field Topology Builder (ATB) and Repository: Version 1.0. *Journal of Chemical Theory and Computation*, **7**(12):4026–4037, December 2011. (cited on page 58.)

[122] Giovanni Bussi, Davide Donadio, and Michele Parrinello. Canonical sampling through velocity rescaling. *The Journal of chemical physics*, **126**(1), 2007. (cited on page 60.)

[123] Berk Hess, Henk Bekker, Herman JC Berendsen, and Johannes GEM Fraaije. Lincs: a linear constraint solver for molecular simulations. *Journal of computational chemistry*, **18**(12):1463–1472, 1997. (cited on page 60.)

[124] Andrea Amadei, Antonius B. M. Linssen, and Herman J. C. Berendsen. Essential dynamics of proteins. *Proteins: Structure, Function, and Bioinformatics*, **17**(4):412–425, December 1993. (cited on pages 60 and 61.)

[125] M. J. Frisch, G. W. Trucks, H. B. Schlegel, G. E. Scuseria, M. A. Robb, J. R. Cheeseman, G. Scalmani, V. Barone, B. Mennucci, G. A. Petersson, H. Nakatsuji, M. Caricato, X. Li, H. P. Hratchian, A. F. Izmaylov, J. Bloino, G. Zheng, J. L. Sonnenberg, M. Hada, M. Ehara, K. Toyota,

R. Fukuda, J. Hasegawa, M. Ishida, T. Nakajima, Y. Honda, O. Kitao, H. Nakai, T. Vreven, J. A. Montgomery Jr., J. E. Peralta, F. Ogliaro, M. Bearpark, J. J. Heyd, E. Brothers, K. N. Kudin, V. N. Staroverov, T. Keith, R. Kobayashi, J. Normand, K. Raghavachari, A. Rendell, J. C. Burant, S. S. Iyengar, J. Tomasi, M. Cossi, N. Rega, J. M. Millam, M. Klene, J. E. Knox, J. B. Cross, V. Bakken, C. Adamo, J. Jaramillo, R. Gomperts, R. E. Stratmann, O. Yazyev, A. J. Austin, R. Cammi, C. Pomelli, J. W. Ochterski, R. L. Martin, K. Morokuma, V. G. Zakrzewski, G. A. Voth, P. Salvador, J. J. Dannenberg, S. Dapprich, A. D. Daniels, O. Farkas, J. B. Foresman, J. V. Ortiz, J. Cioslowski, and D. J. Fox. *Gaussian 09, Revision E.01*. Gaussian, Inc., Wallingford CT, 2013. (cited on page 62.)

[126] Brent H Besler, Kenneth M Merz Jr, and Peter A Kollman. Atomic charges derived from semiempirical methods. *Journal of computational chemistry*, **11**(4):431–439, 1990. (cited on page 62.)

[127] Jerome V Moloney and Alan C Newell. Nonlinear optics. *Physica D: Nonlinear Phenomena*, **44**(1-2):1–37, 1990. (cited on page 68.)

[128] R. W. Boyd. *Nonlinear Optics*. Academic Press, 3rd edition, 2008. (cited on pages 69, 71, and 77.)

[129] Claude Cohen-Tannoudji, Jacques Dupont-Roc, and Gilbert Grynberg. *Atom-photon interactions: basic processes and applications*. John Wiley & Sons, 1998. (cited on pages 69 and 70.)

[130] John Weiner and P.-T. Ho. *Light—Matter Interaction: Fundamentals and Applications*. Wiley, 1 edition, April 2003. (cited on page 71.)

[131] Daniel Manzano. A short introduction to the lindblad master equation. *Aip advances*, **10**(2), 2020. (cited on page 72.)

[132] Steven S Andrews. Using rotational averaging to calculate the bulk response of isotropic and anisotropic samples from molecular parameters. *Journal of chemical education*, **81**(6):877, 2004. (cited on pages 78 and 79.)

[133] Lukas Ohnoutek, Ji-Young Kim, Jun Lu, Ben J Olohan, Dora M Răsădean, G Dan Pantoș, Nicholas A Kotov, and Ventsislav K Valev. Third-harmonic mie scattering from semiconductor nanohelices. *Nature Photonics*, **16**(2):126–133, 2022. (cited on pages 78, 79, and 131.)

[134] Cholleti Vijay Kumar, Pavan Kumar Vasa, Y Ravindra Kumar, Pasula Aparna, and Padi Pratyusha. Enantiomeric separation of s-epichlorohydrin and r-epichlorohydrin by capillary gas chromatography with fid detector. *American Journal of Analytical Chemistry*, **7**(11):772–784, 2016. (cited on page 88.)

[135] Helmut Duddeck and Edison Díaz Gómez. Chiral recognition of ethers by nmr spectroscopy. *Chirality: The Pharmacological, Biological, and Chemical Consequences of Molecular Asymmetry*, **21**(1):51–68, 2009. (cited on page 88.)

[136] Michael Lämmerhofer. Chiral recognition by enantioselective liquid chromatography: mechanisms and modern chiral stationary phases. *Journal of Chromatography A*, **1217**(6):814–856, 2010. (cited on page 88.)

[137] Nisha Shukla, Nathaniel Ondeck, and Andrew J Gellman. Quantitation of enantiospecific adsorption on chiral nanoparticles from optical rotation. *Surface science*, **629**:15–19, 2014. (cited on page 88.)

[138] Steven S Wesolowski and Don E Pivonka. A rapid alternative to x-ray crystallography for chiral determination: Case studies of vibrational circular dichroism (vcd) to advance drug discovery projects. *Bioorganic & medicinal chemistry letters*, **23**(14):4019–4025, 2013. (cited on pages 88 and 131.)

[139] PJ Stephens and MA Lowe. Vibrational circular dichroism. *Annual Review of Physical Chemistry*, **36**(1):213–241, 1985. (cited on page 88.)

[140] Yiqiao Tang and Adam E Cohen. Optical chirality and its interaction with matter. *Physical review letters*, **104**(16):163901, 2010. (cited on page 88.)

[141] Yiqiao Tang and Adam E Cohen. Enhanced enantioselectivity in excitation of chiral molecules by superchiral light. *Science*, **332**(6027):333–336, 2011. (cited on page 88.)

[142] Ershad Mohammadi, KL Tsakmakidis, Amir-Nader Askarpour, Parisa Dehkhoda, Ahad Tavakoli, and Hatice Altug. Nanophotonic platforms for enhanced chiral sensing. *Acs Photonics*, **5**(7):2669–2675, 2018. (cited on page 88.)

[143] Giovanni Pellegrini, Marco Finazzi, Michele Celebrano, Lamberto Duò, and Paolo Biagioni. Surface-enhanced chiroptical spectroscopy with superchiral surface waves. *Chirality*, **30**(7):883–889, 2018. (cited on page 88.)

[144] Cameron Gilroy, Shun Hashiyada, Kensaku Endo, Affar S Karimullah, Laurence D Barron, Hiromi Okamoto, Yoshihiko Togawa, and Malcolm Kadodwala. Roles of superchirality and interference in chiral plasmonic biodetection. *The Journal of Physical Chemistry C*, **123**(24):15195–15203, 2019. (cited on page 88.)

[145] Ershad Mohammadi, Ahad Tavakoli, Parisa Dehkhoda, Yasaman Jahani, Kosmas L Tsakmakidis, Andreas Tittl, and Hatice Altug. Accessible superchiral near-fields driven by tailored electric and magnetic resonances in all-dielectric nanostructures. *Acs Photonics*, **6**(8):1939–1946, 2019. (cited on pages 88 and 89.)

[146] Ershad Mohammadi, Andreas Tittl, Kosmas L Tsakmakidis, TV Raziman,

and Alberto G Curto. Dual nanoresonators for ultrasensitive chiral detection. *ACS photonics*, **8**(6):1754–1762, 2021. (cited on page 89.)

[147] Maxim L Nesterov, Xinghui Yin, Martin Schä ferling, Harald Giessen, and Thomas Weiss. The role of plasmon-generated near fields for enhanced circular dichroism spectroscopy. *Acs Photonics*, **3**(4):578–583, 2016. (cited on page 89.)

[148] Zhiyuan Fan and Alexander O Govorov. Plasmonic circular dichroism of chiral metal nanoparticle assemblies. *Nano letters*, **10**(7):2580–2587, 2010. (cited on page 89.)

[149] Joseph M Slocik, Alexander O Govorov, and Rajesh R Naik. Plasmonic circular dichroism of peptide-functionalized gold nanoparticles. *Nano letters*, **11**(2):701–705, 2011. (cited on page 89.)

[150] Zhijian Hu, Dejing Meng, Feng Lin, Xing Zhu, Zheyu Fang, and Xiaochun Wu. Plasmonic circular dichroism of gold nanoparticle based nanostructures. *Advanced Optical Materials*, **7**(10):1801590, 2019. (cited on page 89.)

[151] Suntak Park, Gwansu Lee, Seok Ho Song, Cha Hwan Oh, and Pill Soo Kim. Resonant coupling of surface plasmons to radiation modes by use of dielectric gratings. *Optics letters*, **28**(20):1870–1872, 2003. (cited on pages 89 and 98.)

[152] Herman L Offerhaus, B Van den Bergen, M Escalante, Franciscus B Segerink, Jeroen P Korterik, and NF Van Hulst. Creating focused plasmons by noncollinear phasematching on functional gratings. *Nano letters*, **5**(11):2144–2148, 2005. (cited on pages 89 and 98.)

[153] Paul Drude. Zur elektronentheorie der metalle. *Annalen der physik*, **306**(3):566–613, 1900. (cited on page 90.)

[154] N. W. Ashcroft and N. D. Mermin. *Solid State Physics*. Harcourt College Publishers, 1st edition, 1976. (cited on page 90.)

[155] C. Kittel. *Introduction to Solid State Physics*. Wiley, New York, 7th edition, 1996. (cited on pages 90, 91, and 92.)

[156] M. Fox. *Optical Properties of Solids*. Oxford University Press, 1st edition, 2001. (cited on page 91.)

[157] P. B. Johnson and R. W. Christy. Optical constants of the noble metals. *Physical Review B*, **6**:4370–4379, 1972. (cited on page 91.)

[158] A. Rakic, A. Djurišić, J. Elazar, and M. Majewski. Optical properties of metallic films for vertical-cavity optoelectronic devices. *Applied Optics*, **37**, 1998. (cited on pages 91 and 94.)

[159] J. D. Jackson and R. F. Fox. *Classical Electrodynamics*. Wiley, 3rd edition, 1999. (cited on page 91.)

[160] S. A. Maier. *Plasmonics: Fundamentals and Applications*. Springer, 1st edition, 2007. (cited on page 94.)

[161] G. I. Stegeman, R. F. Wallis, and A. A. Maradudin. Excitation of surface polaritons by end-fire coupling. *Optics Letters*, **8**(7):386–388, 1983. (cited on page 98.)

[162] J. A. Stratton. *Electromagnetic Theory*, volume **33**. John Wiley & Sons, 1st edition, 2007. (cited on page 98.)

[163] L. Novotny and B. Hecht. *Principles of Nano-Optics*. Cambridge University Press, 1st edition, 2006. (cited on pages 99 and 100.)

[164] Matteo Venturi, Raju Adhikary, Ambaresh Sahoo, Carino Ferrante, Isabella Daidone, Francesco Di Stasio, Andrea Toma, Francesco Tani, Hatice Altug,

Antonio Mecozzi, et al. Plasmon-enhanced circular dichroism spectroscopy of chiral drug solutions. *The Journal of Chemical Physics*, **159**(15), 2023. (cited on page 103.)

[165] AG Schott. Schott optical glass data sheets. https://refractiveindex.info/download/data/2017/schott_2017-01-20.pdf, 2017. (cited on page 111.)

[166] B. Ung and Y. Sheng. Interference of surface waves in a metallic nanoslit. *Optics express*, **15**(3):1182–1190, 2007. (cited on pages 118, 119, 126, and 127.)

[167] Won Jin Choi, Keiichi Yano, Minjeong Cha, Felippe M Colombari, Ji-Young Kim, Yichun Wang, Sang Hyun Lee, Kai Sun, John M Kruger, André F de Moura, et al. Chiral phonons in microcrystals and nanofibrils of biomolecules. *Nature Photonics*, **16**(5):366–373, 2022. (cited on page 131.)

[168] Hatice Altug, Sang-Hyun Oh, Stefan A Maier, and Jiří Homola. Advances and applications of nanophotonic biosensors. *Nature nanotechnology*, **17**(1):5–16, 2022. (cited on page 131.)

[169] Andreas Tittl, Aleksandrs Leitis, Mingkai Liu, Filiz Yesilkoy, Duk-Yong Choi, Dragomir N Neshev, Yuri S Kivshar, and Hatice Altug. Imaging-based molecular barcoding with pixelated dielectric metasurfaces. *Science*, **360**(6393):1105–1109, 2018. (cited on page 131.)

[170] Joen J Hermans, Lambert Baij, Mark Koenis, Katrien Keune, Piet D Iedema, and Sander Woutersen. 2d-ir spectroscopy for oil paint conservation: Elucidating the water-sensitive structure of zinc carboxylate clusters in ionomers. *Science Advances*, **5**(6):eaaw3592, 2019. (cited on page 131.)

[171] Zhihao Ren, Zixuan Zhang, Jingxuan Wei, Bowei Dong, and Chengkuo Lee. Wavelength-multiplexed hook nanoantennas for machine learning en-

abled mid-infrared spectroscopy. *Nature Communications*, **13**(1):3859, 2022. (cited on page 131.)

[172] Yiming Ma, Bowei Dong, and Chengkuo Lee. Progress of infrared guided-wave nanophotonic sensors and devices. *Nano Convergence*, **7**(1):12, 2020. (cited on page 131.)

[173] Yang Chen, Wei Du, Qing Zhang, Oscar Ávalos-Ovando, Jing Wu, Qing-Hua Xu, Na Liu, Hiromi Okamoto, Alexander O Govorov, Qihua Xiong, et al. Multidimensional nanoscopic chiroptics. *Nature Reviews Physics*, **4**(2):113–124, 2022. (cited on page 131.)

[174] Frank Neubrech, Christian Huck, Ksenia Weber, Annemarie Pucci, and Harald Giessen. Surface-enhanced infrared spectroscopy using resonant nanoantennas. *Chemical reviews*, **117**(7):5110–5145, 2017. (cited on page 131.)

[175] Xianglong Miao, Lingyue Yan, Yun Wu, and Peter Q Liu. High-sensitivity nanophotonic sensors with passive trapping of analyte molecules in hot spots. *Light: Science & Applications*, **10**(1):5, 2021. (cited on page 131.)

[176] Hong Zhou, Xindan Hui, Dongxiao Li, Donglin Hu, Xin Chen, Xianming He, Lingxiao Gao, He Huang, Chengkuo Lee, and Xiaojing Mu. Metal–organic framework-surface-enhanced infrared absorption platform enables simultaneous on-chip sensing of greenhouse gases. *Advanced Science*, **7**(20):2001173, 2020. (cited on page 131.)

[177] Di-Di Zhu, You Lv, Si-Ying Li, and Hai-Feng Zhang. Broadband plasmon-induced transparency to a electromagnetically induced absorption conversion metastructure based on germanium. *Annalen der Physik*, **535**(1):2200425, 2023. (cited on page 131.)

[178] Xiaoxia Yang, Zhipei Sun, Tony Low, Hai Hu, Xiangdong Guo, F Javier

García de Abajo, Phaedon Avouris, and Qing Dai. Nanomaterial-based plasmon-enhanced infrared spectroscopy. *Advanced Materials*, **30**(20):1704896, 2018. (cited on page 131.)

[179] Chengkuo Lee, Rohit Radhakrishnan, Chii-Chang Chen, Jing Li, Jayaraj Thillaigovindan, and N Balasubramanian. Design and modeling of a nanomechanical sensor using silicon photonic crystals. *Journal of lightwave technology*, **26**(7):839–846, 2008. (cited on page 131.)

[180] Yuhua Chang, Dihan Hasan, Bowei Dong, Jingxuan Wei, Yiming Ma, Guangya Zhou, Kah Wee Ang, and Chengkuo Lee. All-dielectric surface-enhanced infrared absorption-based gas sensor using guided resonance. *ACS applied materials & interfaces*, **10**(44):38272–38279, 2018. (cited on page 131.)

[181] Chengkuo Lee and Jayaraj Thillaigovindan. Optical nanomechanical sensor using a silicon photonic crystal cantilever embedded with a nanocavity resonator. *Applied optics*, **48**(10):1797–1803, 2009. (cited on page 131.)

[182] Wenfeng Xiang and Chengkuo Lee. Nanophotonics sensor based on micro-cantilever for chemical analysis. *IEEE journal of selected topics in quantum electronics*, **15**(5):1323–1326, 2009. (cited on page 131.)

[183] Che Chen, Daniel A Mohr, Han-Kyu Choi, Daehan Yoo, Mo Li, and Sang-Hyun Oh. Waveguide-integrated compact plasmonic resonators for on-chip mid-infrared laser spectroscopy. *Nano letters*, **18**(12):7601–7608, 2018. (cited on page 131.)

[184] Francesco Bonaccorso, Zhipei Sun, Tawfique Hasan, and Andrea C Ferrari. Graphene photonics and optoelectronics. *Nature photonics*, **4**(9):611–622, 2010. (cited on page 131.)

[185] F Javier García de Abajo. Graphene plasmonics: challenges and opportunities. *Acs Photonics*, **1**(3):135–152, 2014. (cited on pages 131 and 156.)

[186] Gururaj V Naik, Jongbum Kim, and Alexandra Boltasseva. Oxides and nitrides as alternative plasmonic materials in the optical range. *Optical materials express*, **1**(6):1090–1099, 2011. (cited on page 132.)

[187] Jongbum Kim, Gururaj V Naik, Alexander V Gavrilenko, Krishnaveni Dondapati, Vladimir I Gavrilenko, SM Prokes, Orest J Glembocki, Vladimir M Shalaev, and Alexandra Boltasseva. Optical properties of gallium-doped zinc oxide—a low-loss plasmonic material: first-principles theory and experiment. *Physical Review X*, **3**(4):041037, 2013. (cited on page 132.)

[188] Gururaj V Naik, Vladimir M Shalaev, and Alexandra Boltasseva. Alternative plasmonic materials: beyond gold and silver. *Advanced materials*, **25**(24):3264–3294, 2013. (cited on page 132.)

[189] Nathaniel Kinsey, Clayton DeVault, Alexandra Boltasseva, and Vladimir M Shalaev. Near-zero-index materials for photonics. *Nature Reviews Materials*, **4**(12):742–760, 2019. (cited on page 132.)

[190] Xiang-Tian Kong, Runbo Zhao, Zhiming Wang, and Alexander O Govorov. Mid-infrared plasmonic circular dichroism generated by graphene nanodisk assemblies. *Nano letters*, **17**(8):5099–5105, 2017. (cited on page 132.)

[191] Richard Knipper, Thomas G Mayerhöfer, Vladimir Kopecky Jr, Uwe Huebner, and Jürgen Popp. Observation of giant infrared circular dichroism in plasmonic 2d-metamaterial arrays. *Acs Photonics*, **5**(4):1176–1180, 2018. (cited on page 132.)

[192] Francesco Mattioli, Giuseppe Mazzeo, Giovanna Longhi, Sergio Abbate, Giovanni Pellegrini, Erika Mogni, Michele Celebrano, Marco Finazzi, Lam-

berto Duò, Chiara Giuseppina Zanchi, et al. Plasmonic superchiral lattice resonances in the mid-infrared. *Acs Photonics*, **7**(10):2676–2681, 2020. (cited on page 132.)

[193] Cheng Xu, Zhihao Ren, Hong Zhou, Jingkai Zhou, Chong Pei Ho, Nan Wang, and Chengkuo Lee. Expanding chiral metamaterials for retrieving fingerprints via vibrational circular dichroism. *Light: Science & Applications*, **12**(1):154, 2023. (cited on page 132.)

[194] Amy Morren, Aria T Ballance, Flore K Elliott, and Jennifer S Shumaker-Parry. Plasmon-induced vibrational circular dichroism bands of achiral molecules on gold nanostructures with tunable extrinsic chiroptical responses. *The Journal of Physical Chemistry C*, **128**(36):15091–15102, 2024. (cited on page 132.)

[195] COMSOL AB. *Finite-element frequency domain calculations of spherical nanoshells' absorption cross-sections using COMSOL Multiphysics®*. COMSOL AB, Stockholm, Sweden, n.d. www.comsol.com. (cited on pages 132, 152, and 153.)

[196] Craig F Bohren and Donald R Huffman. *Absorption and scattering of light by small particles*. John Wiley & Sons, 2008. (cited on page 136.)

[197] Evgeniy Shkondin, Osamu Takayama, ME Aryaee Panah, Pei Liu, Pernille Voss Larsen, Mikkel Dysseholm Mar, Flemming Jensen, and AV Lavrinenko. Large-scale high aspect ratio al-doped zno nanopillars arrays as anisotropic metamaterials. *Optical Materials Express*, 7(5):1606–1627, 2017. (cited on page 150.)

[198] George M Hale and Marvin R Querry. Optical constants of water in the 200-nm to 200-μm wavelength region. *Applied optics*, 12(3):555–563, 1973. (cited on page 150.)

[199] Andrea Marini, Iván Silveiro, and F Javier García de Abajo. Molecular sensing with tunable graphene plasmons. *Acs Photonics*, 2(7):876–882, 2015. (cited on page 156.)



Funding

This research was supported by funding from the Italian Ministry of University and Research (MUR) under the National Operational Programme (PON) "Research and Innovation" 2014–2020, within the framework of the XXXVII cycle of the Ph.D. programme at the Università degli Studi dell'Aquila. I gratefully acknowledge this support, which made my doctoral studies and research activities possible.